

**NUMERICAL SIMULATION OF LIQUID SLOSHING IN  
RECTANGULAR TANKS USING CONSISTENT PARTICLE  
METHOD AND EXPERIMENTAL VERIFICATION**

**GAO MIMI**

***(B.ENG, SHANGHAI JIAO TONG UNIVERSITY, CHINA)***

**A THESIS SUBMITTED  
FOR THE DEGREE OF DOCTOR OF PHILOSOPHY  
DEPARTMENT OF CIVIL ENGINEERING  
NATIONAL UNIVERSITY OF SINGAPORE  
2011**



## **Acknowledgement**

The author would like to express her sincerest gratitude and appreciation to the following people for their invaluable guidance, advice and encouragement,

Professor Koh Chan Ghee, for his professional guidance, wisdom, advice and continual support throughout the duration of my PhD. There was a time when my world was filled with darkness and I even thought of giving up. It was Professor Koh's great support and encouragement that helped me go through the dark days and accomplish this thesis. His guidance and help are greatly appreciated.

Professor T Balendra, for his invaluable advice and patient help in the study. I am very grateful for his understanding and support in the whole PhD study.

Associate Professor Ang Kok Keng and Professor Choo Yoo Sang, for their suggestions during the qualifying examination which helped me greatly to better define the research focus.

Research Fellow, Dr. Luo Chao for many useful discussions and for his help in the experiments. The thought provoking discussions with him have contributed to the success of the numerical model.

All the staff in the structural engineering laboratory for their kind assistance in providing technical and logistic support for the experimental work.

Dr. Zhang Zhen, Dr. Teng Mingqing and Dr. Duan Wenhui for their insightful discussions and advice.

Finally, to my parents, sisters and brother for their unconditional encouragement and support, without which this thesis would not have been completed successfully.



## Table of Contents

Acknowledgement .....	i
Table of Contents .....	iii
Summary .....	vii
List of Figures .....	ix
List of Tables .....	xvii
Nomenclature .....	xix
Chapter 1 Introduction .....	1
1.1 Overview .....	2
1.2 Sloshing in membrane LNG tank .....	2
1.3 Study of liquid sloshing .....	4
1.4 Research scope and objectives .....	6
1.5 Organization of the thesis .....	7
Chapter 2 Literature Review .....	11
2.1 Research works involving mainly experimental study .....	12
2.2 Analytical study of liquid sloshing .....	14
2.3 Numerical study of liquid sloshing .....	16
2.3.1 Mesh-based methods .....	16
2.3.2 Meshless methods .....	24
2.4 LNG and LNG sloshing .....	28
2.4.1 LNG and its carrier system .....	28
2.4.2 Sloshing phenomena .....	30
Chapter 3 Formulation of Consistent Particle Method .....	37
3.1 Introduction .....	37
3.2 Moving particle semi-implicit method .....	38

3.2.1	Governing equations .....	39
3.2.2	MPS formulation.....	42
3.2.3	Modeling of incompressibility .....	44
3.2.4	Boundary conditions .....	44
3.2.5	Drawbacks of MPS .....	46
3.3	CPM based on Taylor series .....	47
3.3.1	Introduction.....	47
3.3.2	Approximation of gradient and Laplacian by Taylor series .....	50
3.3.3	Main features of CPM.....	54
3.3.4	Performance test of the Laplacian based on Taylor series.....	63
3.4	Concluding remarks .....	67
Chapter 4 Numerical Simulation of Incompressible Free Surface Flows by CPM .....		83
4.1	Introduction.....	83
4.2	Benchmark examples .....	84
4.2.1	Hydrostatic pressure in a static tank .....	84
4.2.2	Dam break with $d / L_w = 2$ .....	86
4.3	Parametric study of CPM.....	87
4.3.1	Influence of weighting functions in weighted least-square solution ...	88
4.3.2	Influence of influence radius .....	90
4.3.3	Influence of particle sizes .....	92
4.3.4	Influence of time step.....	93
4.3.5	Computational cost .....	94
4.4	Numerical simulation of free oscillation of liquid.....	95
4.5	Numerical simulation of violent fluid flows with breaking.....	97
4.5.1	Free oscillation of liquid in a container with large amplitude .....	98

4.5.2	Dam break with $d / L_w = 0.5$ .....	99
4.5.3	Dam break with obstacle.....	103
4.6	Concluding remarks .....	105
Chapter 5 Liquid Sloshing in Rectangular Tanks: Experimental Study and CPM		
Simulation.....		131
5.1	Introduction.....	131
5.2	Experimental setup.....	132
5.2.1	Experimental facilities .....	132
5.2.2	Water Tank.....	133
5.2.3	Shake table .....	133
5.2.4	Wave probes.....	133
5.2.5	Pressure sensor.....	134
5.2.6	Displacement transducer.....	135
5.2.7	High speed camera.....	135
5.2.8	Other considerations .....	135
5.3	Sloshing experiments and comparison with CPM solutions.....	136
5.3.1	Experiments of sloshing waves in high-filling tank .....	138
5.3.2	Experiments of sloshing waves in low-filling tank.....	150
5.3.3	Experiments with sloshing wave impact on the tank ceiling.....	153
5.4	Concluding remarks .....	154
Chapter 6 Conclusions and Future Research .....		189
6.1	Conclusions.....	189
6.2	Future work.....	191
References.....		193
Appendix A: CD for animation files and explanation note .....		207



## Summary

The use of numerical simulation has made an enormous impact on the study of free surface motion of incompressible liquid such as liquid sloshing. Simulating this complex problem has many important applications, ranging from coastal protection and offshore structure design to LNG/oil sloshing on vessels. Furthermore, animated wave motion has great potential in modern movies and computer games where violent liquid motion is featured.

In this context, conventional mesh-based numerical methods have met difficulties in simulating waves involving discontinuity of liquid motion (e.g. wave breaking). Even with some free-surface capturing techniques incorporated, such as marker-and-cell and volume of fluid, mesh-based methods suffer from the problem of numerical diffusion. This is mainly due to the discretization of advection terms in the Navier-Stokes equation in Eulerian formulation. In addition, tracking of free surface requires complex and time consuming algorithm to update the time varying nonlinear boundary.

In recent years, a new generation of computational methods known as meshless (mesh-free) methods has been shown to outperform conventional mesh-based method in dealing with discontinuous fluid motion. Lagrangian meshless methods called particle methods have shown very good potential in dealing with large-amplitude free surface flows, moving interfaces and deformable boundaries. The problem of numerical diffusion does not arise in particle methods. Nevertheless, in many of the existing particle methods such as Smoothed Particle Hydrodynamics (SPH) method and Moving Particle Semi-Implicit (MPS) method, the approximation of partial differential operators requires a pre-defined kernel function. Accuracy is not

necessarily satisfactory when the particle distribution is irregular. In particular, these particle methods tend to give severe and spurious pressure fluctuation.

In this thesis, a new particle method addressing the above-mentioned problems is proposed for 2D large amplitude free-surface motion. Called the Consistent Particle Method (CPM), it eliminates the use of kernel function which is somewhat arbitrarily defined. The required partial differential operators are approximated in a way consistent with Taylor series expansion. A boundary particle recognition method is applied to help define the changing liquid domain. The incompressibility condition of free surface particles is enforced by an adjustment scheme. With these improvements, the CPM is shown to be robust and accurate in long time simulation of free surface flow particularly for the smooth pressure solution without spurious fluctuation.

The CPM is applied to study different 2D free surface flows, i.e. free oscillation of water in static tank, dam break in tank with different water depth-to-height ratios, dam break with obstacle. In the simulation of both gentle and violent free surface motion, the CPM outperforms the original MPS method in both particle distribution and pressure solution.

An important free surface problem, 2D liquid sloshing in rectangular tanks is then studied experimentally and numerically by CPM. A series of sloshing experiments are carried out making use of a hydraulic-actuated shake table. Standing waves in high filling tanks, traveling waves in low filling tanks and breaking waves in a closed tank are well simulated by CPM in terms of free surface profiles and pressure fields. The CPM solution of pressure history shows tremendous improvement compared with MPS results. In all cases considered, the CPM solutions of free surface elevation and pressure are in very good agreement with the experimental results.

## List of Figures

Figure 1-1. An example of prismatic LNG tank (Photo: Business Wire website*) .....	9
Figure 2-1. Effect of liquid density and viscosity in sloshing simulation scanned from Lee et al. (2007b) .....	35
Figure 2-2. The number of LNG ships as at year 2006 scanned from Foss (2007) .....	35
Figure 2-3. The LNG ship orders by containment system scanned from Foss (2007) .....	35
Figure 2-4. Typical permissible filling levels scanned from Lloyd's Register (2008) .....	36
Figure 3-1. Schematic of a typical reference particle with its neighbor particles .....	73
Figure 3-2. Algorithm of the MPS method .....	73
Figure 3-3. (a) The arc boundary recognition method; (b) Example of angle list for particle A and B .....	74
Figure 3-4. Incompressibility adjustment of free surface particles .....	74
Figure 3-5. Candidate list and neighbor list generation .....	75
Figure 3-6. Flowchart of CPM .....	76
Figure 3-7. A center point $\bullet$ surrounded by 24 irregularly spaced points $\ast$ .....	77
Figure 3-8. Comparison of Laplacian using CPM (Eq. (3-31) ), MPS (Eq. (3-16) ) and SPH (Eq. (3-39) ) ( $L_0=0.1$ , Test function $\phi(x, y) = x^4 + y^4$ ) .....	77
Figure 3-9. Convergence test of Laplacian for regular points (Test function $\phi(x, y) = x^4 + y^4$ ) .....	77
Figure 3-10. Convergence test of Laplacian in MPS for irregular points (Test function $\phi(x, y) = x^4 + y^4$ ) .....	78
Figure 3-11. Convergence test of Laplacian in SPH for irregular points (Test function $\phi(x, y) = x^4 + y^4$ ) .....	78
Figure 3-12. Convergence test of Laplacian in CPM for irregular points (Test function $\phi(x, y) = x^4 + y^4$ ) .....	78

Figure 3-13. An example of irregular nodes (1156 in total) in $x$ - $y$ domain $[0.8, 4.2] \times [0.8, 4.2]$ .....	79
Figure 3-14. Analytical and numerical result of Laplacian (Test function $\phi(x, y) = \sin(xy)$ ) .....	80
Figure 3-15. Difference of Laplacian values with analytical result (Test function $\phi(x, y) = \sin(xy)$ ) .....	81
Figure 3-16. Error of Laplacian of different numerical algorithm (Test function $\phi(x, y) = \sin(xy)$ ) .....	82
Figure 4-1. Schematic view of the initial particle distribution for static water tank .	109
Figure 4-2. Time history of hydrostatic pressure at point A by MPS .....	109
Figure 4-3. Time history of hydrostatic pressure at point A with $d=0.2$ m scanned from Khayyer and Gotoh (2008).....	109
Figure 4-4. Time history of hydrostatic pressure at point A with $d=0.2$ m scanned from Khayyer and Gotoh (2009).....	110
Figure 4-5. Comparison of time histories of hydrostatic pressure at point A.....	110
Figure 4-6. Particle distribution at $t=5$ s. ....	111
Figure 4-7. Hydrostatic pressure field of the whole tank of water at $t=5$ s.....	111
Figure 4-8. Geometry and initial particle distribution of the dam break example.....	111
Figure 4-9. Comparison of dam break simulation using MPS with experimental results .....	112
Figure 4-10. Pressure field of the dam break example by MPS method .....	113
Figure 4-11. Pressure field of the dam break example by CPM.....	113
Figure 4-12. Comparison between different weighting function.....	114
Figure 4-13. Comparison of CPM solutions using different weighting functions with experiments .....	114

Figure 4-14. Effect of weighting functions used in CPM.....	115
Figure 4-15. Effect of influence radius used in CPM .....	115
Figure 4-16. Comparison of the leading edge location in CPM solution with published results---experimental: Hirt and Nichols (1981); Lagrangian FEM: Ramaswamy and Kawahara (1987).....	116
Figure 4-17. Effect of particle size used in CPM.....	116
Figure 4-18. Dam break profiles using different particle sizes in CPM .....	117
Figure 4-19. Dam break profiles using different time step $\Delta t$ .....	117
Figure 4-20. CPU time for different operations (a) CPU time of CPM; (b) Fraction over the total time of CPM; (c) Fraction over the total time of MPS .....	118
Figure 4-21. (a) A schematic view of the tank; (b) Initial particle distribution.....	118
Figure 4-22. Comparison of time histories of surface elevation amplitude with published results.....	119
Figure 4-23. Comparison of time histories of surface elevation amplitude results by CPM and MPS .....	119
Figure 4-24. Pressure fields at different time instants for MPS and CPM simulation .....	120
Figure 4-25. Comparison of the free oscillation of liquid for large amplitude.....	121
Figure 4-26. Pressure contours of the free oscillation of liquid by CPM .....	121
Figure 4-27. Pressure contours of the free oscillation of liquid for larger amplitude by CPM .....	122
Figure 4-28. Configuration of the tank in dam break example and the positions of the water depth probes and pressure sensor (Fekken, 1998) .....	122
Figure 4-29. Wave profiles of the dam break example by CPM .....	123

Figure 4-30. Comparison of pressure at Point P1 with published results (Fekken, 1998)	124
Figure 4-31. Pressure contour of dam break by CPM at (a) $t=0.7$ s, (b) $t=1.475$ s and (c) $t=2.95$ s	124
Figure 4-32. Comparison of water heights at the four points with published results (Fekken, 1998)	125
Figure 4-33. Pressure contours of the dam break example by CPM	126
Figure 4-34. Velocity field of the fluid particles of the dam break example by CPM	127
Figure 4-35. Geometry and definition of the dam break with obstacle	128
Figure 4-36. Initial particle distribution of the dam break with obstacle	128
Figure 4-37. Graphical comparisons of the dam break behavior	129
Figure 5-1. The experimental setup	159
Figure 5-2. Tank with pressure sensor mounted	159
Figure 5-3. Experimental apparatus and working principle	159
Figure 5-4. Definition of parameters for liquid sloshing in a rectangular tank	160
Figure 5-5. Fixing tools of rectangular tank on the shake table	160
Figure 5-6. Schematic Diagram and picture of wave probe	160
Figure 5-7. (a) Wave probe mounted to an adjustable stand (b) Calibration of the wave probes	161
Figure 5-8. Calibration results of wave probe 1	161
Figure 5-9. Calibration results of wave probe 2	161
Figure 5-10. Calibration results of wave probe 3	162
Figure 5-11. Experimental installation of pressure sensor	162

Figure 5-12. (a) Devices used for the calibration of pressure sensor (b) calibration of the pressure sensor .....	162
Figure 5-13. Calibration result of the pressure sensor .....	163
Figure 5-14. Displacement transducer and its experimental installation .....	163
Figure 5-15. High speed camera set-up .....	163
Figure 5-16. Securing technique .....	164
Figure 5-17. Displacement signal of shake table (5mm amplitude) .....	164
Figure 5-18. Comparison of free surface elevation at Point P <sub>1</sub> ( $\omega / \omega_0 = 1.0$ ) .....	164
Figure 5-19. Particle distribution simulated by MPS method and comparison with experimental results .....	165
Figure 5-20. Pressure contours simulated by MPS method .....	166
Figure 5-21. Particle distribution of MPS simulation with arc method and IA of free surface particles .....	167
Figure 5-22. Pressure contours of MPS solution with arc method and IA of free surface particles .....	167
Figure 5-23. Comparison of pressure history at Point P <sub>2</sub> ( $\omega / \omega_0 = 1.0$ ) .....	168
Figure 5-24. Particle distribution of CPM simulation .....	169
Figure 5-25. Pressure contours of CPM solution .....	169
Figure 5-26. Comparison of pressure history at Point P <sub>2</sub> ( $\omega / \omega_0 = 1.0$ ) .....	170
Figure 5-27. Comparison of pressure history at Point P <sub>2</sub> ( $\omega / \omega_0 = 1.0$ ) .....	170
Figure 5-28. Comparison of free surface elevation at Point P <sub>1</sub> ( $\omega / \omega_0 = 1.0$ ) .....	170
Figure 5-29. Free-surface elevation vs. time ( $\omega / \omega_0 = 1.0$ ) by CPM .....	171
Figure 5-30. Comparison of free surface elevation at Point P <sub>1</sub> ( $\omega / \omega_0 = 1.1$ ) .....	172
Figure 5-31. Comparison of pressure history at Point P <sub>2</sub> ( $\omega / \omega_0 = 1.1$ ) .....	172

Figure 5-32. Comparison of free surface elevation at Point P <sub>1</sub> ( $\omega / \omega_0 = 1.1$ ).....	173
Figure 5-33. Comparison of pressure history at Point P <sub>2</sub> ( $\omega / \omega_0 = 1.1$ ).....	173
Figure 5-34. Free-surface elevation vs. time ( $\omega / \omega_0 = 1.1$ ) by CPM .....	174
Figure 5-35. Comparison of free surface elevation at Point P <sub>1</sub> ( $\omega / \omega_0 = 0.9$ ).....	175
Figure 5-36. Comparison of pressure history at Point P <sub>2</sub> ( $\omega / \omega_0 = 0.9$ ).....	175
Figure 5-37. Comparison of free surface elevation at Point P <sub>1</sub> ( $\omega / \omega_0 = 0.9$ ).....	175
Figure 5-38. Comparison of pressure history at Point P <sub>2</sub> ( $\omega / \omega_0 = 0.9$ ).....	176
Figure 5-39. Comparison of free surface elevation at Point P <sub>1</sub> ( $\omega / \omega_0 = 0.583$ ) .....	176
Figure 5-40. Comparison of pressure history at Point P <sub>2</sub> ( $\omega / \omega_0 = 0.583$ ) .....	176
Figure 5-41. Comparison of free surface elevation at Point P <sub>1</sub> ( $\omega / \omega_0 = 0.583$ ) .....	177
Figure 5-42. Comparison of pressure history at Point P <sub>2</sub> ( $\omega / \omega_0 = 0.583$ ) .....	177
Figure 5-43. Maximum and minimum free surface elevations vs. excitation frequency .....	178
Figure 5-44. Maximum and minimum hydrodynamic pressure vs. excitation frequency.....	178
Figure 5-45. Maximum and minimum free surface elevations under different excitation amplitudes .....	179
Figure 5-46. Maximum and minimum hydrodynamic pressure under different excitation amplitudes .....	179
Figure 5-47. Maximum and minimum free surface elevations vs. filling depths .....	180
Figure 5-48. Maximum and minimum hydrodynamic pressure vs. filling depths.....	180
Figure 5-49. Standing Wave at the initial stage, $t = 2.75$ s .....	181
Figure 5-50. Traveling wave starts to form, $t = 4.80$ s.....	181
Figure 5-51. Multi-crested waves traveling, $t = 6.10$ s .....	181

Figure 5-52. Hydraulic run-up (before formation of bore), $t = 6.75$ s .....	181
Figure 5-53. Formation of bore, $t = 6.90$ s .....	182
Figure 5-54. Bore splits into multi-crested traveling waves, $t = 7.10$ s .....	182
Figure 5-55. Multi-crested traveling waves, $t = 7.50$ s .....	182
Figure 5-56. Hydraulic run-up, $t = 7.85$ s .....	182
Figure 5-57. Comparison of the free surface elevation at Point $P_1$ .....	183
Figure 5-58. Comparison of the pressure history at Point $P_2$ .....	183
Figure 5-59. Pressure contours for different time instants by CPM .....	184
Figure 5-60. Velocity field of the fluid particles by CPM .....	185
Figure 5-61. Free surface profiles at different time instants. Left: experiments; Right: CPM simulation. ....	186
Figure 5-62. Time history of free surface elevations at the right wall .....	187
Figure 5-63. Pressure contours for different time instants by CPM .....	187
Figure 5-64. Computed pressure history at Point $P_2$ .....	188
Figure 5-65. Computed pressure history at Point $P_1$ .....	188



## List of Tables

Table 2-1. Material properties of LNG in comparison with water .....	33
Table 3-1. Summary and comparison of particle methods .....	71
Table 3-2. Parameters for performance test of Laplacian.....	71
Table 3-3. Parameters for performance test of Laplacian.....	71
Table 4-1. Numerical examples studied in Chapter 4.....	107
Table 4-2. Parameters used in the study of the effect of least-square weighting function .....	107
Table 4-3. CPU time (s) and fraction per time step in CPM.....	107
Table 5-1. Parameters of the tank and liquid for high-filling sloshing.....	157
Table 5-2. Parameters of the tank and liquid for low-filling sloshing .....	157
Table 5-3. Parameters of the tank and liquid for high-filling sloshing with breaking .....	157



## Nomenclature

$A$	amplitude of external excitation
$\mathbf{A}$	matrix used in Eq. (3-21)
$a_1 - a_5$	coefficient used in Eq. (3-28)
$B$	width of the tank
$b_1 - b_5$	coefficients used in Eq. (3-28)
$c_1 - c_5$	coefficients used in Eq. (3-28)
$D$	number of space dimensions
$d$	water depth
$d_1 - d_5$	coefficients used in Eq. (3-28)
$e_1 - e_5$	coefficient used in Eq. (3-28)
$\mathbf{E}$	residual error vector used in Eq. (3-21)
$\ \mathbf{E}\ $	2-norm of $\mathbf{E}$
$\mathbf{f}$	function value vector of fluid particles
$f(x, y)$	differential function of two variables $x$ and $y$
$\mathbf{g}$	body force vector
$H$	height of the tank
$h$	coordinate difference in $x$ direction
$k$	coordinate difference in $y$ direction
$k$ (subscript)	the $k$ -th time step
$L$	length of tank
$L_0$	initial particle distance
$m$	mode number
$N$	number of total particles

$n$	particle number density
$n^*$	temporary particle number density
$n_0$	initial constant particle number density
$p$	pressure
$P(x, y)$	a particle P with coordinate $(x, y)$
$R$	radius of circle around a particle
$r$	particle distance
$\mathbf{r}$	particle coordinate vector
$\mathbf{r}^*$	temporary particle coordinate vector
$r_e$	cut-off radius of influence area
$t, \Delta t$	time, time step
$\mathbf{v}$	particle velocity vector
$\mathbf{v}^*$	temporary particle velocity vector
$V_{\max}$	maximum velocity
$w$	kernel function
$\beta$	parameter used in Eq. 3-19
$\gamma$	coefficient used in Eq. (3-37)
$\eta$	free surface elevation
$\lambda$	coefficient used in Eq. (3-5)
$\nu$	kinematic viscosity of fluid
$\rho$	density of fluid
$\phi(x, y)$	differential function of two variables $x$ and $y$
$\omega$	excitation frequency
$\omega_0$	first natural frequency

## Chapter 1 Introduction

Global growing needs for energy are constantly driving the demand for energy sources such as natural gas. One critical part of the natural gas supply is transportation. When a natural gas source is near the market, it can be transported by pipeline. However, when long distance supply is required, the gas needs to be converted to liquid state for transportation flexibility, which is liquefied natural gas (LNG). LNG is made by cooling natural gas to a temperature of approximately minus 163 degrees Centigrade. At this low temperature, natural gas becomes a liquid and its volume is reduced by more than 600 times. LNG is easier to store and transport than its gaseous form since it takes up much less space. These advantages call for the need for more LNG carriers designed to meet harsher operational requirements.

LNG carriers have usually been operated in fully loaded condition or with a minimum filling of liquid cargo during ballast voyage. Recently however, there has been growing demand for membrane type LNG tanks that can operate with cargo loaded to any filling level. The sloshing induced loads in the tanks at these partial filling levels is the main concern for vessels operated in this manner. Thus, a better physical understanding and numerical modeling of sloshing waves in the partially filled tanks is crucial for the designing of the tank structures and developing mitigation measures and devices to reduce the undesirable effects of sloshing in the LNG carriers and storage tanks. The research findings will then greatly enhance the operational flexibility in LNG transport and delivery as well as safety and cost effectiveness of LNG vessel design.

## **1.1 Overview**

From the viewpoint of competitive energy sources, electricity generation is increasingly dependent on gas which acts as a flexible contributor. The trend comes from the worldwide desire to reduce dependence on nuclear power, coal and oil energy for economic and strategic reasons. Currently the overwhelming majority of gas is supplied by pipelines in the world. Due to geographical constraints, there is a lack of connectivity between pipelines or between countries. As an attractive alternative for flexibility and strategic reasons, gas transportation through vessels becomes a highly desired approach to trade gas all over the world. The conversion of natural gas into a liquid state makes the worldwide gas trade more economical and convenient. LNG is made by cooling natural gas to a temperature of approximately minus 163 degrees Centigrade. LNG makes the long-distance delivery possible, especially for some regions where pipeline transport is not accessible. It is a natural result for energy industry to design and develop more LNG carriers which works under harsher operational requirements. LNG is expected to play an increasing role in the natural gas industry and global energy markets in the next several decades.

## **1.2 Sloshing in membrane LNG tank**

To meet the growing demand, many LNG ships and terminals have been proposed and built. For example, Singapore is building LNG terminal costing about S\$1.5 billion (Energy Market Authority, 2006). There is a trend towards the use of membrane tanks instead of the self supporting storage systems, mainly due to the fact that membrane tanks utilize the hull shape more efficiently. Space utilization is an important consideration on sea vessels. Generally, a membrane-type tank is of prismatic shape (see Figure 1-1 for example) which is more compatible with the shape

of ship hull than other shapes such as sphere. The width and height of a LNG tank are typically around 30m.

LNG carriers are usually operated under the fully loaded condition or with a minimum filling level for the tank cooling-down purpose during the ballast voyage. The typical filling level of the LNG tank is greater than 95 percent or less than 10 percent of the tank height. To overcome this constraint, it would be desired to have large membrane type LNG tanks that can be operated under any filling level. This demand has stemmed from the emergence of a spot energy market for LNG containers. The sloshing load at filling levels other than the fully loaded or ballast condition is the main concern for vessels operated in this manner.

When strong sloshing occurs, liquid moves against the sides of the container with gradually increased surface elevation. The large liquid movement creates highly localized impact pressure on tank walls. If the excitation frequency is near or equal to the natural sloshing frequency, the high dynamic pressures due to resonance may damage the tank walls.

In this context, an academically challenging and practically important aspect is the sloshing-induced loads in the membrane-type tanks. Particularly for partially filled tanks, sloshing can cause both high loads and fatigue upon the containment system and the hull structure of the transportation vessel. Besides, severe sloshing poses a potential threat to the stability of ship motion, thereby restricting the operational flexibility in LNG transport and delivery. Hence research into liquid sloshing is of great importance to the energy industry.

### 1.3 Study of liquid sloshing

Liquid sloshing has been a research subject attracting much attention over the last few decades. There has been a considerable amount of work on the study of liquid sloshing. Most of the early computational studies on liquid sloshing problems were based on linear wave theory, assuming that the free surface elevation is small (Housner, 1957; Abramson, 1996). However, the linear theory will result in big errors in the time-history response when the external excitation is large or near the natural frequency of liquid sloshing. Thus in the last few decades, researchers began to use fully nonlinear wave theory to numerically study and simulate the liquid sloshing in containers. The numerical study of nonlinear liquid sloshing has been actively performed since 1970s. Different numerical methods based on mesh such as finite difference, finite element and finite volume method were applied in the studies (Wu et al., 1998; Koh et al., 1998; Chen and Nokes, 2005).

Mesh-based methods, however, encounter problems when the sloshing amplitude becomes large especially when there are possibilities of free surface breaking, since discontinuity of the domain in such cases can not be modeled in a mesh-based method without the help of other free surface capturing approaches. Although some free surface capturing methods such as Volume of Fluid (Hirt and Nicholls, 1981) and Level Set (Osher and Sethian, 1988) can be used to improve mesh-based methods, they require complex computer programming to solve extra boundary equations in order to capture the time varying free surface and update the computational mesh. Furthermore, problems of numerical diffusion arise owing to the discretization of the advection terms in the Navier-Stokes equation in mesh-based method using Eulerian grids.

Recently there is a growing interest in developing the next generation computational methods, namely meshless methods as alternatives to conventional mesh-based methods. Meshless methods in a Lagrangian description are also named as particle methods. Particle methods have some outstanding advantages which are not possessed by mesh-based methods and are expected to out-perform the conventional mesh-based method in some aspects. For example, particles have a natural ability to represent the coalescence and fragmentation behavior of breaking waves, especially when they are used to simulate free-surface sloshing. The numerical diffusion problem in the conventional mesh-based methods using the Eulerian formulation does not arise in particle methods in which the Lagrangian formulation is adopted. Hence, as a potential algorithm to simulate breaking wave phenomenon, particle methods deserve more research.

Nevertheless, in most of the existing particle methods such as Smoothed Particle Hydrodynamics (SPH) and Moving Particle Semi-Implicit method (MPS), the approximation of partial differential operators is determined by a pre-defined weighting function. The approximation error can be large when the particle distribution is irregular. As a result, existing particle methods such as MPS and SPH suffer from pressure fluctuations especially in fluid problems with long time simulation.

In this study, a new particle method named Consistent Particle Method (CPM) is developed. The required partial differential operators are computed in a way that is consistent with Taylor series expansion. A predictor-corrector algorithm is used to solve the coupled equations efficiently. The Poisson equation of pressure is solved in the context of incompressible flow. A boundary particle recognition method is applied

to help define the changing liquid domain. The proposed method shows better performance both in the accuracy and stability of the scheme compared with the original MPS.

## **1.4 Research scope and objectives**

A better understanding and numerical modeling of sloshing waves is vital to the design of LNG carriers and other similar engineering applications where free surface motion is the main concern. The proposed research mainly addresses a major challenge in such problems, i.e. accurate simulation of nonlinear behavior of sloshing in tank including possible wave overturning and breaking. The key question is how to predict the maximum sloshing motion and maximum hydrodynamic pressure for a given set of external excitations.

The first objective of this thesis is to develop a numerical model and solution strategy suitable for simulating liquid sloshing motion in a moving tank, with specific attention on the potential application to LNG carriers. To achieve this objective, a new particle method in the simulation of free surface flow problem will be proposed and verified by various numerical examples. The numerical simulations by the new particle method will be carried out to investigate the differences in sloshing induced loads on the tank at various filling conditions.

The second objective is to conduct experimental study for partial verification of the numerical model, making use of a shake table facility available in the Structural Engineering Laboratory of National University of Singapore. The experimental results will be compared with the numerical simulation results.

## 1.5 Organization of the thesis

This thesis contains seven chapters as follows.

Chapter 1 introduces the background of LNG and motivation for studying LNG sloshing. An overview of liquid sloshing problems and studies is presented. Based on that, the scope and objectives of this research are defined.

Chapter 2 of the dissertation covers a detailed literature review in the field of liquid sloshing in containers. A summary of the state-of-the-art accomplishments to date is given, including applications and limitations of different numerical methods. The work done on liquid sloshing motion by conventional mesh-based numerical method is mostly confined to a sloshing wave without breaking. Particle methods without mesh are found to be more robust in dealing with large amplitude sloshing with possibility of wave breaking. The advantages and disadvantages of different meshless methods are discussed.

Chapter 3 gives a detailed description of a new method called Consistent Particle Method (CPM). An existing particle method called MPS is introduced first. The limitations of the MPS method are discussed and demonstrated through numerical examples. There are mainly three improvements in the proposed new method compared with other conventional particle method such as MPS and SPH. Firstly, the discretization of derivatives in the Poisson equation of pressure and gradient model in CPM is based on Taylor series expansion. Secondly, a more effective free surface boundary recognition method is introduced, which can greatly improve the stability of the pressure field. Lastly, the problem of imposing an incompressibility condition on

the free surface particles is addressed. Numerical examples are presented in this chapter to demonstrate the capability of the CPM.

In Chapter 4, six numerical examples are tested to show the performance of CPM compared with the existing particle method MPS. The numerical solutions of different free surface flow problems, such as flow due to dam collapse without and with obstacle, are presented based on the proposed CPM and are compared with reference solutions or experimental data. Numerical results using the proposed CPM shows the significant improvement in the pressure field compared with MPS solution.

Chapter 5 gives an experimental verification of the numerical modeling with focus on the liquid sloshing in rectangular tank. Water sloshing under different excitations is studied experimentally and numerically. The proposed CPM is again found to be capable of simulating free surface flows problems. The sloshing wave patterns in rectangular tanks under different filling depths are studied in this chapter. The effects of external excitation frequencies and amplitudes are also investigated. Finally, liquid sloshing at high-filling level with impact on the tank ceiling is studied and simulated.

Lastly, Chapter 6 presents conclusions and suggestions for future work.

A CD is attached containing computer animation files for some selected numerical examples. A brief explanation note is given in Appendix A.

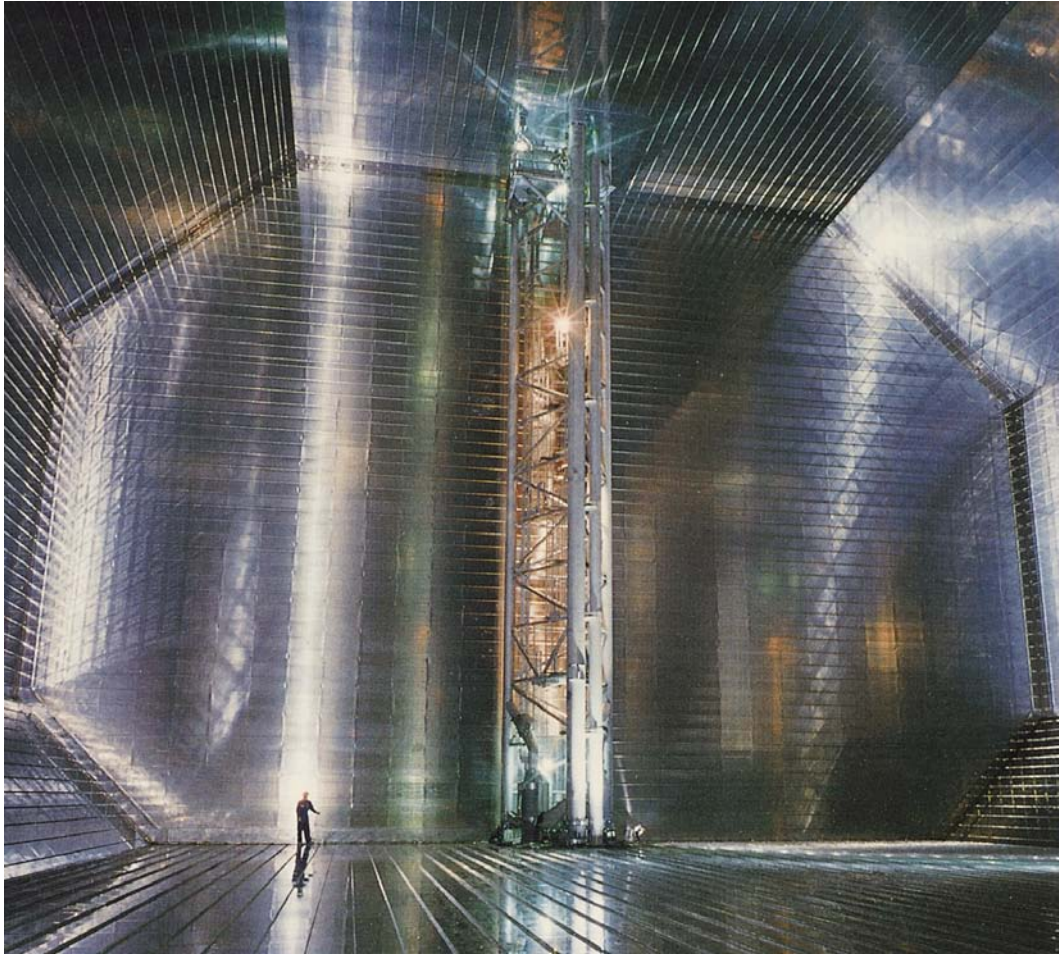


Figure 1-1. An example of prismatic LNG tank (Photo: Business Wire website\*)

\*: <http://www.businesswire.com/multimedia/home/20081217005080/en/1735488/ExxonMobil-Technology-Yields-World%E2%80%99s-Largest-LNG-Carrier>



## Chapter 2 Literature Review

Free surface flow problems, such as wave breaking near shores and moving ships, green water on ship decks, liquid sloshing in containers (e.g. LNG tankers) and interaction of waves with floating structures, have received considerable attention of researchers over the past few decades (Huijsmans et al., 2004; Greco et al., 2005; Lohner et al., 2006). Violent free surface flow has a profound impact on offshore and marine structures (Armenio, 1997; Soulaïmani and Saad, 1998; Apsley and Hu, 2003; Idelsohn et al., 2004). In this thesis, the sloshing phenomenon can be defined as the highly nonlinear motion of the free surface in a moving partially filled tank. Liquid sloshing generates dynamic loads on the structure of the tank and thus is an issue of great concern in the design of membrane-type LNG vessels (Tveitnes et al., 2004). Sloshing loads in liquid transportation tanks affect not only the structure of ships but also their movement and stability on sea waves (Kim et al., 2003). This liquid sloshing may cause loss of human lives, economic and environmental resources owing to the unexpected failure of the vessels.

Liquid sloshing in storage tanks due to wind and earthquake is also a concern in design. Various finite element schemes have been developed to study the seismic response of liquid storage tanks by Brown (1982), Veletsos and Tang (1986) and Rammerstofer et al. (1990). Balendra et al. (1982a, b) and Yi and Natsiavas (1990) studied the mode shapes and natural frequencies of cylindrical storage tanks using the finite element method for the liquid and tank wall.

The sloshing effect coupled with ship motion was studied by Kim et al. (2007). Godderidge et al. (2009) investigated the effect of compressibility of fluid and found

that the inclusion of fluid compressibility has a significant effect on the pressure evolution of a sloshing flow. Kim et al. (2010) studied the fatigue strength of the insulation system of MARK-III type LNG carriers. In contrast to the destructive effect of liquid sloshing in transportation and storages tanks, liquid sloshing in a container, as a vibration absorber, has been found to have a positive effect in suppressing structural vibrations due to external loads. Called tuned liquid dampers (TLDs), they have been used for tall buildings, long span bridges and offshore structures subjected to wind, waves and earthquakes (Modi and Seto, 1997; Modi et al., 2003). Different tank shapes are used in TLDs such as rectangular, cylindrical and U-shaped (Ibrahim, 2005). Koh et al. (1994, 1995) and Shankar and Balendra (2002) proposed multiple TLDs tuned to several natural frequencies of structures. Balendra et al. (1995, 1999) investigated the vibration control effect of tuned liquid column dampers (TLCD) in various buildings. An active control system involving a TLCD is developed by Balendra et al. (2001) for the vibration control of a single-degree-of-freedom tower subjected to wind excitation.

## **2.1 Research works involving mainly experimental study**

Due to the complexity of sloshing, there has been a considerable amount of work carried out to understand the complex sloshing behavior and to design appropriate devices to suppress it. One of the earlier experimental investigations of nonlinear, free-surface standing waves was reported by Taylor (1953) who focused on the wave crest in the center of a rectangular tank. Using different scaled model tanks, Strandberg (1978) conducted experiments to investigate overturning of moving vehicles due to liquid sloshing under different working conditions. It was found that the overturning limit of a half filled tank vehicle could be reduced to half of that of a fully filled tank vehicle where no liquid sloshing occurs.

Wang et al. (1996) experimentally studied the waves in a water-filled circular tank excited by two shakers at opposite sides of the tank. The excitation frequency used was near one of the natural frequencies of sloshing waves. Standing waves as well as breaking waves were observed and investigated in their experiments. Pawell (1997) conducted experimental studies on liquid sloshing interaction with cylindrical tanks subjected to pitching excitation.

Tveitnes et al. (2004) carried out a series of experiments and proposed a simplified load formula for estimation of sloshing load in preliminary design. La Rocca et al. (2005) investigated the problem of sloshing waves of a two-liquid system experimentally and theoretically. The Lagrangian variational approach was used in the mathematical model by applying to the potential formulation of the fluid motion. The theoretical solution of the mathematical model gave good agreement with their experimental results. Rognebakke et al. (2005) conducted a series of tests on a scaled tank. They investigated the high filling impacts by using pressure sensors and analyzing the pressure data statistically. Akyildiz and Unal (2005) investigated the pressure distributions at different locations and three-dimensional (3D) effects on liquid sloshing experimentally. Sloshing in a rectangular tank at a scaled model was studied for various filling levels. Romero et al. (2006) studied lateral sloshing forces within scaled vehicle tanks under high filling levels. Recently Yan et al. (2009) conducted experiments to investigate liquid sloshing in a relatively large size test tank with “Reuleaux triangle” type cross-section. The experiments were performed on the tank with and without laterally placed baffles under three fill conditions.

## 2.2 Analytical study of liquid sloshing

Although experimental study is most direct in obtaining maximum impact pressure due to violent sloshing, some technical issues in the application of experimental data to actual tank designs have not been completely resolved (Kim et al., 2004). For example, the scaling law from model test data to real ships is not clear (Lloyd's Register, 2005). Furthermore, experiments are time consuming and expensive, particularly for large size tanks at real working condition. As an alternative method to experimental approach, analytical methods have been developed for simulation of liquid sloshing.

An analytical model allows understanding of sloshing mechanics and extensive parametric study. Analytical formulation of liquid equations is well documented by many researchers for tanks with various regular geometries. The general equation of liquid motion in closed containers is often simplified by assuming the container rigid and impermeable. Furthermore, the liquid is assumed ideal which is inviscid, incompressible, and irrotational. Capillary or surface tension effects are ignored in a gravitational field.

Stolbetsov (1967) studied the nonlinear sloshing in a rectangular tank due to horizontal excitation theoretically. He used a perturbation technique and presented two types of steady-state solutions. Ockendon and Ockendon (1973) proposed an analytical scheme for resonant sloshing due to external horizontal and vertical excitations. A third order asymptotic solution was derived mathematically. Kim et al. (1996) developed an analytical solution of a partially filled rectangular tank under horizontal and vertical ground excitation. Interaction of the liquid and flexible wall of the tank was taken in to account. Their solutions of two-dimensional (2D) analysis

agreed well with those by other numerical methods. Gavrilova (2004) developed an analytical solution of a cylindrical tank with rigid tank wall using the Bubnov-Galerkin method. The coupling vibration frequency of the system was obtained.

Faltinsen et al. (2000, 2003) studied the liquid sloshing in a square-base tank in frequency domain. The tank was forced under 3D arbitrary motions with frequency close to the lowest natural frequency. In their work, steady-state waves were solved using a Bubnov-Galerkin scheme combined with an asymptotic technique. A quantitative comparison of the free surface elevation using their proposed theoretical method with the experimental results was presented. A sensitivity study of the initial condition was performed. In the work of Faltinsen et al. (2006) the same method was applied in simulation 3D sloshing in a square base tank with emphasis on the swirling waves. Analytical solutions were validated by experiments performed by them with a cubic tank of dimensions 0.6m.

Analytical methods can predict the sloshing waves accurately when the motion is not violent. But wave overturning and breaking cannot be studied analytically. Ideal fluid has to be assumed, i.e. inviscid, irrotational and incompressible. In addition, analytical study of liquid sloshing is often performed for simple boundary conditions. For complex geometry and extensive fluid-structure interaction, analytical solutions are difficult, if not impossible, to obtain.

Hence, for general problems, numerical methods are necessary in the study of fluid problems involving free surfaces (i.e. liquid sloshing) with more complex liquid properties and boundary conditions.

## **2.3 Numerical study of liquid sloshing**

Recent advances in computational methods and computer power make it possible for numerical methods to be applied to study large motion problems of free surface flow. Traditional numerical methods are mesh based, such as Finite Difference Method (FDM), Boundary Element Method (BEM), Finite Volume Method (FVM) and Finite element Method (FEM). The main common feature of these methods is that computation is based on a pre-defined mesh.

### **2.3.1 Mesh-based methods**

There has been a considerable amount of work using mesh-based methods in the simulation of liquid sloshing. Most of the early studies on liquid sloshing problems were based on linear wave theory. Free surface elevation was assumed to be sufficiently small so that the nonlinear effects could be neglected. Abramson (1996) used a linear theory to simulate small amplitude sloshing in a container. Solaas and Faltinsen (1997) adopted a perturbation theory to investigate sloshing in 2D tanks of general shape. Linear theory is not accurate in the time-history response when external excitation is large or near the natural frequency of liquid sloshing. Hence, in recent years, researchers have begun to use fully nonlinear wave theory to numerically study liquid sloshing in containers.

#### **2.3.3.1. Boundary Element Method (BEM)**

Among the numerical methods, the BEM is often used to analyze nonlinear free surface problems. Faltinsen (1978) and Nakayama and Washizu (1981) simulated large amplitude sloshing in 2D rectangular tanks using BEM. Grilli and Svendsen (1990) examined the corner problems (corners of fluid domain were modeled by double-nodes)

and investigated accuracy in the BEM simulation of nonlinear wave flows. Koh et al. (1998) proposed a coupled BEM-FEM scheme to study the fluid-structure interaction during liquid sloshing in a 3D rectangular tank. The tank structure was modeled by FEM while the fluid domain by BEM. Experiments were conducted to validate the proposed numerical scheme. Good agreement in terms of the free surface elevations and hydrodynamic pressures was obtained. Dutta and Laha (2000) analyzed the small amplitude liquid sloshing using a low-order boundary element method. Gedikli and Erguven (2003) adopted variational BEM to investigate the effect of a rigid baffle on the natural frequencies of the liquid in a cylindrical tank. Zhang et al. (2004) developed a fully nonlinear 3D numerical wave tank base on a higher order BEM in the time domain. Numerical examples were presented to show the good performance of their mixed-Eulerian-Lagrangian scheme. Huang et al. (2010) developed a time-domain Green function based BEM to simulate liquid sloshing in tanks. Experiments were conducted to validate the numerical simulation results.

An important feature of the BEM is that only the boundary has to be discretized in order to carry out the integrations. Because the interior of a solution domain is not discretized, there is much less approximation involved in representing the solution variables, making data generation much easier (Fenner, 1983). However, the coefficient matrix in BEM is generally fully populated with non-zero terms, and is not symmetric. It has been pointed out by Bettess (1981) that for simple elements, the FEM is more efficient than BEM in which the mesh is the FEM mesh with internal nodes and elements removed.

#### **2.3.3.2. Finite Difference Method (FDM)**

The FDM is also widely used in the study of liquid sloshing problems. Chen et al. (1996) developed an FDM to simulate large amplitude liquid sloshing in 2D container due to seismic load. Chen and Chiang (2000) used time-independent FDM to study sea-wave induced sloshing in a floating tank. The fluid was assumed to be inviscid, incompressible and irrotational. The coupled interaction effect of sloshing fluid and tank motion was investigated by the FDM. Kim et al. (2004) applied the FDM in simulating violent sloshing flows in 2D and 3D prismatic tanks. The impact pressure on tank ceiling was studied. Numerical solutions were compared with existing experimental data for which favorable agreement was achieved. Frandsen and Borthwick (2003) and Frandsen (2004) developed fully nonlinear FDM solutions based on inviscid flow assumption. The sloshing motions were studied in 2D tanks under both horizontal and vertical external excitations. Gu et al. (2005) coupled the Level Set technique with the finite difference solver to study two-phase flow in a 3D square tank. They found the Level Set method robust in tracking the free surfaces. Valentine and Frandsen (2005) studied 2D sloshing waves in a rectangular tank under horizontal excitation using FDM. The evolutions of sloshing of two-layer and three-layer fluid systems were investigated. Chen and Nokes (2005) developed a novel time dependent FDM for simulation of 2D sloshing motion in a tank. A fully nonlinear model was developed where fluid viscosity was included. The numerical solution of 2D waves was compared with other published results and good agreement was obtained. Lee et al. (2007c) studied the coupling effect of liquid sloshing in LNG tank with ship motion. The FDM with SURF scheme was applied to simulate liquid sloshing. Liu and Lin (2008) studied 3D liquid sloshing in rectangular tanks using FDM. VOF was used to capture the free surface. Wu and Chen (2009) developed a 3D time-independent FDM to study sloshing waves in a square-base tank under coupled

surge-sway motions. Five types of waves under various excitation angles and a wide range of excitation frequencies were presented.

The most attractive feature of FDM is that it is relatively easy to implement. Its basic form is, however, restricted to handle regular shapes and simple boundaries. To handle complicated geometries, FEM is more straightforward to apply (Bathe, 1996).

#### **2.3.3.3. Finite Element Method (FEM) and Finite Volume Method (FVM)**

The FEM has been extensively used in the study and simulation of the liquid sloshing problems. Ikegawa (1974) analyzed sloshing liquid under single component of horizontal excitation using FEM. Nakayama and Washizu (1980) used FEM to analyze nonlinear sloshing of liquid in a 2D rectangular tank subjected to pitching excitations. Wu and Eatock Taylor (1994) developed 2D nonlinear solutions of the free surface flows using FEM. Numerical examples were presented to validate the proposed scheme. Nomura (1994) used the FEM to investigate the interaction between sloshing viscous liquid and rigid body. Wu et al. (1998) gave a broad account of both 2D and 3D sloshing problems based on FEM. In their paper, the potential flow assumption, where the viscosity of the fluid was neglected, was made.

Pal et al. (1999) developed a numerical model to study the dynamics of liquid inside a thin-walled composite cylindrical tank based on FEM. The effect of tank flexibility on the sloshing waves was investigated. Recently, Biswal et al. (2003) developed a finite element formulation to investigate the vibration modes of liquid in a liquid-filled cylindrical tank. But their results were limited to cylindrical tanks. Wave breaking was not included in their works. Pal et al. (2003) studied the effect of the free surface nonlinearity on the coupled response of cylindrical liquid-filled composite container. FEM was used to model both the fluid and structure domain. A mixed-

Eulerian-Lagrangian approach was developed. Ideal fluid was assumed. The results were provided for a cylindrical container using a 2D finite element approach.

Bermudez et al. (2003) used FEM to compute sloshing modes in a container with an elastic baffle. Linear velocity potential formulation in the frequency domain was adopted in their work. Turnbull et al. (2003) developed a  $\sigma$ -transformed FEM for the simulation of 2D free surface wave motions based on potential theory. Forced sloshing in a base-excited rectangular tank was studied with the proposed numerical algorithm. Cho and Lee (2004) simulated a large amplitude liquid sloshing in 2D tanks using fully nonlinear FEM. Sudharsan et al. (2004) studied the large amplitude sloshing in a 2D rectangular tank using FEM. Fluid structural interaction was investigated by the proposed scheme. Ideal fluid was assumed in these works.

Mitra and Sinhamahapatra (2005) studied the coupled slosh dynamics of liquid in containers using pressure based FEM. The analysis was, however, restricted to linear problems where small amplitude wave was assumed. Wang and Khoo (2005) studied nonlinear sloshing in rectangular container under random excitations. FEM solutions were obtained using the fully nonlinear potential wave theory. The spectra of random waves and forces were investigated. The nonlinear effects of the random waves were studied and typical nonlinear features of the waves were captured. Wang et al. (2006) proposed a damping estimation scheme of liquid sloshing with small amplitude based on FEM. The potential wave theory was used in their work. The proposed scheme is not applicable to problems with large sloshing amplitude or large liquid viscosity. Guillot (2006) developed a discontinuous Galerkin FEM and applied it to liquid sloshing problems with shallow water depths. Eatock Taylor et al. (2008) proposed a coupled FE and BE model to study nonlinear transient waves in numerical wave tanks.

A mixed Eulerian-Lagrangian formulation was implemented in quadratic isoparametric elements. Wave overturning was not captured in their numerical model.

Some of the above-mentioned works such as Nakayama and Washizu (1980), Abramson (1996), Solaas and Faltinsen (1997), Dutta and Laha (2000), Gedikli and Erguven (2003) and Wang et al. (2006) concentrated on small amplitude sloshing, while others like Nakayama and Washizu (1981), Cho and Lee (2004), Wang and Khoo (2005), Chen et al. (1996), Frandsen and Borthwick (2003) and Sudharsan et al. (2004) were for relatively large amplitude motions without breaking.

The FVM is widely used in computational fluid dynamics where the solution favors simpler and lower order approximation within each cell (Bucchignani et al., 2004; Ahmadi et al., 2007; Greaves, 2007). Bucchignani (2004) studied 2D sloshing in rectangular tank using FVM based on potential flow. Zhang et al. (2005) developed a FVM code for the numerical simulation of free surface flow in a container. Recently, Ming and Duan (2010) investigated liquid sloshing in rectangular tank using FVM based on unstructured grid. A high order VOF method was adopted in their study to capture the free surface.

Finite element and finite volume analysis can account for complex geometry with relative ease. On the other hand, finite element solution can be time consuming and expensive. In addition, if local nonlinear effects such as overturning and breaking waves are considered, mesh-based methods like FEM, FVM and FDM meet difficulties in simulating waves involving discontinuity of liquid motion. To solve this problem, different interface capturing methods have been proposed by many investigators. Updating of the free surface is a key factor in the identification of the flow domain as well as in the application of free surface boundary conditions. The

error accumulated in the free surface tracking as time progresses may cause numerical instability in the sloshing response (Fletcher, 1991; Chen et al., 1996).

#### **2.3.3.4. Free surface capturing method used in mesh-based methods**

The most well known approaches to capture the free surfaces are PIC (particle-in-cell), MAC (marker-and-cell) and VOF (volume of fluid) methods. The PIC scheme uses particles on the free surfaces and FDM to solve the governing equations (Harlow, 1963). Another similar approach, MAC method, is based on Lagrangian concepts and can treat overturning waves and reentry inception with simple logic. Marker particles which move with the fluid are used in MAC method to track the movement of free surfaces (Harlow and Welch, 1965). MAC has been widely used to solve complex computational fluid dynamic problems (Johnson, 1996). Mikelis and Journee (1984) simulated 2D liquid sloshing using the MAC method. A series of experiments were conducted on scaled tanks in their work. The measured pressures were compared with their numerical transient solution and reasonable agreement was achieved. Armenio and La Rocca (1996) studied the sloshing of water in rectangular containers with the filling depths of liquid in shallow water hypotheses numerically with modified form of MAC method. Experiments were carried out to verify the performance of the numerical solutions.

Though PIC and MAC are flexible and robust, they are quite complicated in programming and need additional storage required for locating the marker particles, and the additional programming complexity to locate the cells containing the free surface. It significantly increases the computational effort especially for 3D cases (Griebel et al. 1998). More recently Hirt and Nicholls (1981) developed the VOF method in capturing the moving boundaries of fluids. VOF method solves an

additional partial differential equation for the volume fraction at each time step besides the conservation equations. This method can define sharp interfaces and is robust. Nevertheless, tracking and reconstruction of free surfaces remains complicated and difficult, especially in three dimensions (Qian et al., 2006). Osher and Sethian (1988) proposed a Level-Set method to deal with moving boundaries. This method also needs to solve an additional level-set function except for the conservation equations.

All of the above free surface capturing methods can properly compute the instantaneous free surface displacement. However, they all require complex computer programming in order to treat the time varying free surface boundary and update the computational mesh. Furthermore, the problem of numerical diffusion arises owing to the discretization of the advection terms in the Navier-Stokes equations in the mesh-based methods using Eulerian grids.

In summary, mesh-based methods are efficient when the sloshing amplitude is small, where several assumptions can be made to help solve the problem. Nevertheless, mesh-based methods have met difficulties in simulating waves involving discontinuity of liquid motion (e.g. wave breaking). These methods may suffer from mesh distortion in problems with extremely large fluid motion if no additional effort of free surface capturing scheme, such as VOF method, is introduced. Even with some free-surface tracking techniques incorporated, mesh-based methods using Eulerian formulations suffer from the problem of numerical diffusion. In addition, tracking of free surfaces require a complex and time consuming algorithm to update the rapidly changing nonlinear boundary. Furthermore, many aforementioned works about liquid sloshing problems are limited to cylindrical tanks because most of the storage tanks are of

cylindrical shape. Little research has been reported on liquid sloshing in rectangular tanks in the context of large motions.

### **2.3.2 Meshless methods**

In recent years, a new generation of numerical methods has been developed, i.e. meshless (mesh-free) methods that outperform conventional mesh-based methods in dealing with discontinuous motion. Meshless methods have been found to have advantages in dealing with problems for large-amplitude free surface flows, moving interfaces, large motion and complex and deformable boundaries. Liquid sloshing with the possibility of wave breaking belongs to the class of large motion problems with a free surface. In particular, meshless methods have good potential in liquid sloshing problems when the sloshing amplitude is large, especially with possible breaking of free surface. The main idea of meshless methods is to obtain numerical solutions of partial differential equations through a set of particles instead of meshes. Since no numerical meshes are needed, multi-scale resolution problems can be modeled with relative ease in meshless methods through adjusting the particle distribution densities over the solution domain. Particles have a natural ability to represent the coalescence and fragmentation behavior of breaking wave, especially when they are used to simulate free-surface sloshing. In addition, the problem of numerical diffusion in mesh-based methods does not arise in Lagrangian formulated particle methods. Hence, with great potential to simulate breaking wave phenomena, meshless methods have recently attracted increasing attention.

Onate et al. (1996) proposed a meshless method called the Finite Point Method using a Lagrangian formulation to solve fluid mechanics problems. Idelsohn et al. (2001, 2003) generalized this meshless idea with finite-element type approximations.

They later proposed a new method called the Particle Finite Element Method (PFEM) using the same meshing technique (Idelsohn et al., 2004). The PFEM method was robust to solve fluid-structure interaction problems with moving free surfaces. However, extra effort was needed to generate a new mesh at each time step, and this made the method inefficient in computation.

Another group of meshless methods using particles to describe the motion of the fluid based on the Lagrangian formulation was developed. The first idea on this approach was proposed by Monaghan (1988, 1994) for the treatment of astrophysical hydrodynamic problems. The method was called Smooth Particle Hydrodynamics (SPH). Many other researchers later generalized this method to solve fluid mechanic problems. For example, Shao and Lo (2003) developed an improved SPH to simulate Newtonian flows with a free surface. They tested the method by a typical 2D dam break example. Souto-Iglesias et al. (2004) simulated sloshing in the anti-roll tanks using SPH. Souto-Iglesias et al. (2006) investigated the sloshing moment amplitudes in a rectangular tank under different rolling frequencies using SPH. Experiments were conducted for validation of the numerical solutions. Very recently Fang et al. (2009) proposed an improved SPH method for simulating free surface flows with viscous fluids. Two enhanced variants were presented. Better accuracy and stability was achieved compared with the original SPH in the work. Delorme et al. (2009) investigated the impact pressure in shallow water sloshing under forced rolling motion experimentally and numerically using SPH. Traveling waves and breaking waves under resonant sloshing condition were observed. A modified SPH scheme was also proposed to study the density effect to the impact pressure. Good agreement in terms of free surface shape and global dynamic of the flow was shown between experimental and numerical results.

In the SPH method, the incompressible flow condition is simulated as the limit of the compressible Navier–Stokes equations with some stiff equation of state (Monaghan, 1988). The compressibility is adjusted by changing the numerical speed of sound in the equation of state, which helps to control density fluctuation to some pre-defined ratio. The incompressible limit is obtained by choosing a very large speed of sound in the equation of state in SPH. However, the large value of the speed of sound restricts the time step to be very small due to the Courant–Friedrichs–Lewy condition (Courant et al., 1967). Furthermore, the compressibility adjustment is case-dependent and it has to be calibrated for every specific fluid dynamic problem.

Perrone and Kao (1975) and Liszka and Orkisz (1980) proposed a so called Generalized Finite Difference (GFD) method for structural problems. Chew et al. (2006) proposed an Arbitrary Lagrangian-Eulerian (ALE) formulation of GFD method and applied it in vortex flow and flows past moving bodies. Tiwari and Kuhnert (2007) presented a meshless method for two-phase incompressible flows named finite pointset method. Nevertheless, neither of these methods has been applied in the study of incompressible free surface flow problems.

A finite point Euler algorithm for aerodynamics was proposed by Batina (1992, 1993). Recently Mendez and Velazquez (2004) applied this method to simulate 2D laminar unsteady flows. Recently, Liu et al. (2005) developed a Lagrangian particle method named finite particle method (FPM) and applied it to modeling incompressible free surface flow problems. Nevertheless, the same approach of imposing the incompressibility condition as that in SPH was adopted in these studies.

Hence, a particle method with more straightforward modeling of incompressible fluid was proposed by Koshizuka and Oka (1996) and Koshizuka et al. (1998). Called the Moving Particle Semi-implicit (MPS) method, it adopts particle number density in

the computation of density parameter. The incompressibility condition is imposed by solving the Poisson equation of pressure.

The MPS method has been applied in many fluid mechanic problems. In comparison with the SPH method, the MPS method showed better stability (Ataie-Ashtiani and Farhadi, 2006). Koshizuka et al. (1998) used MPS to simulate breaking waves. Yoon et al. (1999) proposed a hybrid particle-gridless method for incompressible flows based on MPS and verified their scheme by a liquid sloshing problem in a 2D rigid tank. Zhang et al. (2006) improved the original MPS method and applied it to convective heat transfer problems. Ataie-Ashtiani and Farhadi (2006) improved the stability of MPS and used it to simulate free-surface flows. Shibata and Koshizuka (2007) analyzed ship water impact on a deck. Recently, Lee et al. (2007a) developed a coupled MPS and FEM method to analyze sloshing in tanks with elastic thin walls that undergo large deflection. The results showed that their method could solve current benchmark problems. Sueyoshi et al. (2008) used MPS to simulate wave-induced nonlinear motion of a 2D floating body.

Actually the MPS method evolves from the well-known Marker and Cell (MAC) method (Harlow and Welch, 1965). The predictor-corrector algorithm of MAC is inherited by MPS for solving Poisson equation of pressure. The main difference is that MAC evaluates the Laplace (or Laplacian) operator and gradient operators based on a pre-defined regular mesh while MPS establishes an approximate model of Laplace and gradient operators based on neighbor particles. Based on the transient diffusion model and weight function, Koshizuka and Oka (1996) proposed discrete Laplace and gradient operators to form the basis of MPS. Although subsequent researchers

(Khayyer and Gotoh, 2008, 2009; Zhang et al., 2006) made some modifications, the basic idea of the approximation of these two operators are the same.

Nevertheless, similar to the SPH method, the MPS method employs a smoothing function to approximate a function value and its derivatives. The approximation of partial differential operators is determined with a pre-defined kernel function. The accuracy of the approximation is affected by the particle distribution since the kernel function relies on the inter-particle distance only. As a result, MPS suffers from pressure fluctuations especially in fluid problems with long time simulation.

To address the above-mentioned problems, a new particle method named Consistent Particle Method (CPM) is developed in which the discretization of the equations is based on derivatives consistent with a Taylor series expansion. A two-step algorithm is used to solve the Navier-Stokes equations. The Poisson equation of pressure is solved in the context of incompressible flow. A boundary particle recognition method is applied to help determine the solution domain. Hence, the pressure field is obtained with no spurious pressure fluctuation in the simulation of both gentle and violent free surface flows. This is a great advantage of CPM considering that the pressure solution has not been well simulated in conventional particle methods. The detailed formulation of CPM will be explained in Chapter 3.

## **2.4 LNG and LNG sloshing**

### **2.4.1 LNG and its carrier system**

Natural gas is colorless, odorless, non-corrosive and non-toxic. Liquefied natural gas (LNG) is natural gas that has been cooled to a liquid at  $-260^{\circ}\text{F}$  ( $-162.2^{\circ}\text{C}$ ) at atmospheric pressure. LNG reduces its volume by more 600 times, making it more

economical to store and transport (Foss, 2007). LNG is a liquefied hydrocarbon mixture consisting predominantly of methane ( $\text{CH}_4$ ) with a small admixture of higher hydrocarbons (primarily ethane). For many reasons it is sufficient to consider it to be liquid methane (Webber et al., 2008). The material properties of LNG are listed in Table 2-1 and compared with those of water.

Lee et al. (2007b) performed a parametric sensitivity study on the parameters of sloshing loads in LNG tanks by using a computational fluid dynamics program. They investigated the effect of parameters such as liquid viscosity and density, compressibility and ullage pressure of gas and laminar or turbulence fluid model in the study of sloshing load. They explored the sloshing impact pressure with the liquid property of water and LNG. Figure 2-1 shows the effect of density and viscosity of liquid in simulation of impact pressure of sloshing waves in the work of Lee et al. (2007b). They concluded that the effects of viscosity and density ratio are insignificant, as was also pointed out by Bass et al. (1985). In this context, experimental sloshing tests using water in the laboratory can thus be considered a good approximation of LNG sloshing.

Specially designed tankers (double-hulled ships) are used to transport LNG between terminals. LNG is stored in a containment system within the inner hull at atmospheric pressure and cryogenic temperature ( $-260^\circ\text{F}$ ). There are mainly three types of cargo containment systems used in modern standards, i.e. the spherical (Moss) design, the membrane design and the structural prismatic design. The Moss and membrane design systems are most commonly used historically (Foss, 2007). The Moss design system has better resistance to sloshing forces compared with prismatic membrane type. The tanks in the Moss design, however, do not fit the contour of the

ship's hull, which results in a diseconomy. There is thus a trend towards the use of membrane system in recent years (Foss, 2007). Figure 2-2 shows that 51 percent of LNG ships were membrane design in year 2006. The rising trend towards membrane design is evident in LNG ship orders shown in Figure 2-3, which shows that 85 percent of LNG ships in orders from 2005 to 2010 are membrane design.

#### **2.4.2 Sloshing phenomena**

Earlier LNG vessels were relatively small and employed spherical tanks, hence sloshing influences can be neglected. As pointed by Kim et al. (2004) and Chiu (2006), the spherical tanks of Moss design system are more robust and resistant to the sloshing effects of LNG, while the membrane systems (which are more efficient in hull space usage) are particularly sensitive to sloshing loads. With the increase of the LNG market, there is need to increase the size of tanks for more storage space. This will essentially cause more severe sloshing impacts for partially filled tanks. There are two reasons for violent fluid motion in a tank (Abramson, 2003). One is that the frequency of regular ship motion caused by a sea state is close to the natural frequency of the free surface. The other reason is that the fluid viscosity of LNG for suppressing sloshing motions is very small.

Membrane tanks are potentially susceptible to damage due to strong sloshing since no internal device is used to mitigate fluid motion in a relatively huge space. The characteristics of the free surface in a membrane tank change with the fill level, as described below (Lloyd's Register, 2005).

(1) At the highest fill levels above about  $90\%H$  ( $H$  = maximum height of LNG tank), the vapor space seeks the instantaneous highest point in the tank and this has a major influence on the fluid motion near the surface.

(2) At high fill levels between  $70\%H$  and  $90\%H$ , the free surface takes the form of a standing wave. The oscillatory motion of the surface produces generally vertical velocity components and a shallow contact angle. A consequence is that air and vapor may become trapped between the fluid and tank wall causing a cushioning effect of the sloshing impact.

(3) At intermediate levels (less than  $70\%H$ ), the free surface develops a traveling wave or bore, which is characterized by a high velocity and high impact angle but with low vapor entrapment. Such a wave can transfer a significantly higher impact force to the walls of the tank than a standing wave. Furthermore, cushioning effects due to vapor entrapment are considered to be less likely.

In this study, sloshing in membrane type system is considered. For simplicity a rectangular-shape tank is used to represent the tank in membrane type system. The flexibility of the tank wall, which is commonly assumed rigid in many research works (Ibrahim, 2005; Lloyd's Register, 2008; Chen et al., 2008), is neglected in present study.

It is pointed out by Lloyd's Register (2008) that, in the most recent LNG ships of conventional size (up to 155,000m<sup>3</sup> capacity) filling is permitted for  $70\%H$  and above for higher filling levels ( $H$  is the internal tank height) or  $10\%L_T$  and below for lower filling levels ( $L_T$  is the internal tank length), as illustrated in Figure 2-4. At mid-fill height, ship and tank periods may be close to each other which generally lead to the highest sloshing impacts. Mid-fill heights are therefore not permitted. Recently, however, there has been growing demand for membrane-type LNG tanks that can operate with cargo loaded to any filling level which allow for maximum operational flexibility. The sloshing loads at filling levels other than the fully loaded or ballast

condition is the main concern for vessels operating in this manner. Hence, liquid sloshing around mid-filling is mainly addressed in present study.

Table 2-1. Material properties of LNG in comparison with water

	LNG*	Water ^
Boiling point	111.7 K	373.1 K
Heat of vaporization	510 kJ/kg. K	2257 kJ/kg. K
Dynamic viscosity	$1 \times 10^{-4}$ Pa.s	$1 \times 10^{-3}$ Pa.s
Critical temperature	190.4 K	647 K
Critical pressure	4.6 MPa	22.06 MPa
Density	425 kg / m <sup>3</sup>	1000 kg / m <sup>3</sup>
Phase at room temperature	Gas	Liquid

Source:

\*: Webber et al., (2008) and NIST Chemistry Webbook.

^: [http://en.wikipedia.org/wiki/Properties\\_of\\_water](http://en.wikipedia.org/wiki/Properties_of_water); and Haynes, W. M. ed., (2010).



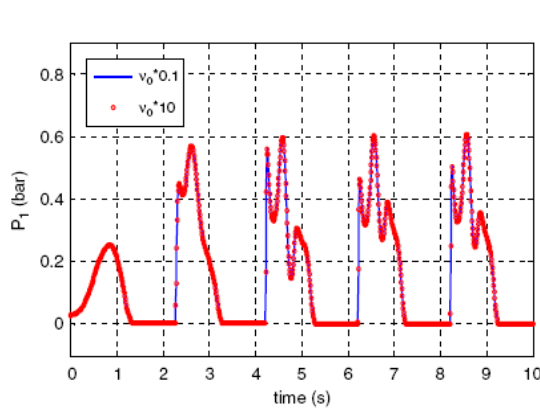


Fig. 9. Time histories of pressure for different kinematic viscosity values (25% fill ratio).

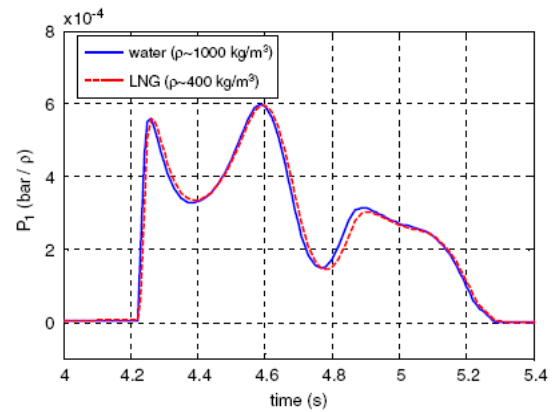
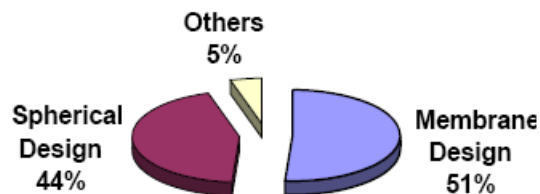


Fig. 10. Time histories of pressure for two different density ratios (25% fill ratio).

Figure 2-1. Effect of liquid density and viscosity in sloshing simulation scanned from Lee et al. (2007b)

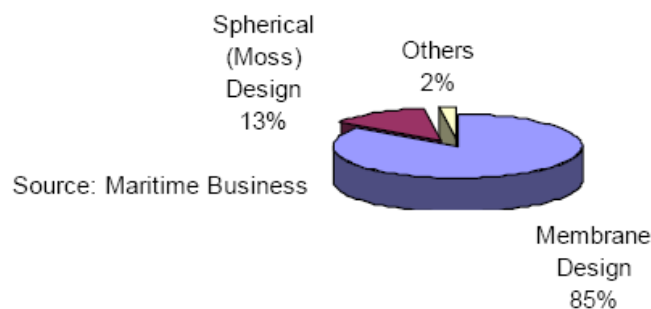
### LNG Fleet Containment System - September 2006 (Number of ships)



Source: Maritime Business Strategies, LLC

Figure 2-2. The number of LNG ships as at year 2006 scanned from Foss (2007)

### LNG Fleet Containment System - Order Book 2005 - 2010 (Number of ships)



Source: Maritime Business

Figure 2-3. The LNG ship orders by containment system scanned from Foss (2007)

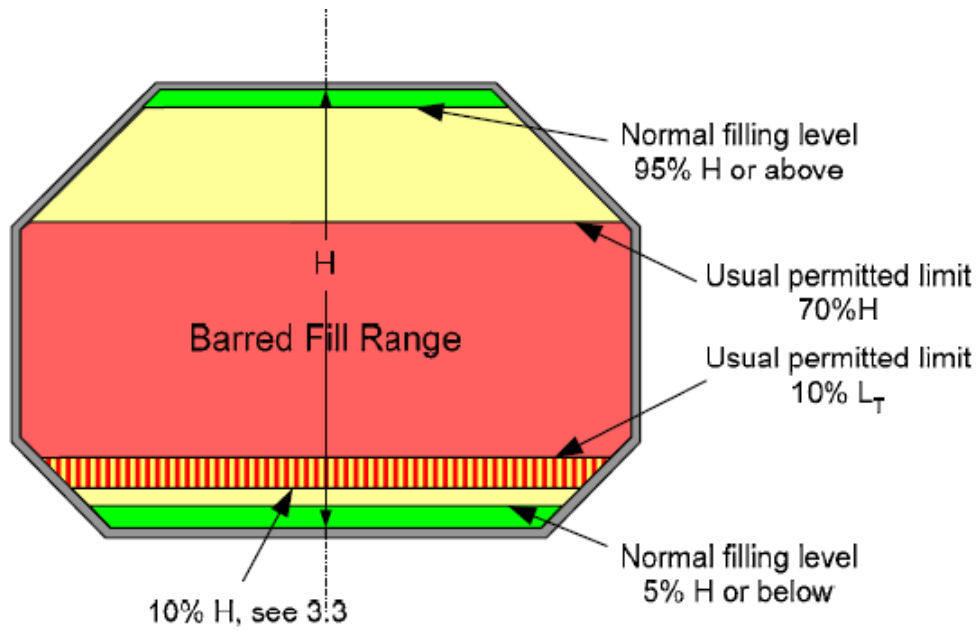


Figure 2-4. Typical permissible filling levels scanned from Lloyd's Register (2008)

## Chapter 3 Formulation of Consistent Particle Method

### 3.1 Introduction

Numerical modeling of highly nonlinear free surface flow is difficult because of the changing boundary condition of free surface, i. e. not only the free surface forms part of boundaries of the computational domain, but also the positions and velocities of the free surface vary with time and are not known a priori. In addition, free surface flow may involve unsteady fragmentation and coalescence processes when wave breaking occurs.

Particle methods in which Lagrangian particles are used to represent the fluid domain becomes appealing in the application of free surface flow problems due to their natural ability in characterization of particle fragmentation and coalescence. Compared with the conventional numerical methods such as FDM and FVM, particle methods show some outstanding advantages which are not possessed by conventional mesh-based methods.

According to the literature review in Chapter 2, we first focus on a promising particle method, i.e. the moving particle semi-implicit (MPS) method, developed by Koshizuka et al. (1995). The method is based on solving a Poisson equation of pressure which is derived from Navier-Stokes equation. By detailed evaluation of the discrete algorithms used in the MPS method, we have found a problem with MPS and another particle method SPH. It is that they rely on a pre-defined kernel function in approximation of the gradient and Laplace operators. Kernel function can cause instability which is often encountered in particle methods (Ataie-Ashtiani and Farhadi, 2006). Besides, even with properly selected kernel function, the pressure solution of

MPS method presents severe fluctuation, as will be shown later in this chapter and subsequent chapters.

A new particle method named Consistent Particle Method (CPM) is therefore proposed to overcome this drawback in the MPS method. Instead of using pre-defined kernel function, the approximations of derivatives in the governing equations are based on Taylor series expansion. In this chapter, the MPS method is first introduced. The new method, CPM, is then proposed with three key improvements over the original MPS. The program codes of MPS and CPM are written in Matlab (v.7.0) and run on computer equipped with Pentium 4<sup>TM</sup> CPU (duo 3.6 GHz).

### **3.2 Moving particle semi-implicit method**

The moving particle semi-implicit (MPS) method was first developed by Koshizuka et al. (1995). It is a Lagrangian method developed for simulating incompressible fluid phenomenon based on Navier-Stokes equation. The fluid is modeled as an assembly of interacting particles. Computational meshes are unnecessary. The governing equations are discretized based on the interaction models of gradient and Laplacian. The pressure field is obtained by solving Navier-Stokes equation in the whole fluid domain. In addition, as no advection term is used in the Lagrangian description in the method, there is no numerical diffusion problem which is present in conventional mesh-based methods.

The MPS method has been applied to a wide range of problems such as hydrodynamics (Koshizuka and Oka, 1996; Ataie-Ashtiani and Farhadi, 2006; Shibata et al., 2009; Gotoh et al., 2005; Sueyoshi et al., 2008), wave breaking (Koshizuka et al., 1998; Khayyer and Gotoh, 2008; Alam et al., 2007), wave impact (Khayyer and Gotoh,

2009), fluid-shell interaction (Lee et al., 2007a) and heat transfer problems (Zhang et al., 2006). Various kernel functions were studied by Ataie-Ashtiani and Farhadi (2006) to improve the stability of the MPS method. Different treatments of the boundary conditions and methods of solving the Poisson equation of pressure were considered to improve the accuracy and stability of the MPS method (Zhang et al., 2006, Khayyer and Gotoh, 2008; Khayyer and Gotoh, 2009). Nevertheless, even with these reported improvements, the problem of pressure fluctuation in long time simulation is still not completely resolved.

The detailed analysis and improvements will be stated in the following section.

### 3.2.1 Governing equations

The governing equations of viscous Newtonian fluid are expressed by the conservation laws of mass and momentum as follows (Lee et al., 2007a):

$$\frac{1}{\rho} \frac{D\rho}{Dt} + \nabla \cdot \mathbf{v} = 0 \quad (3-1)$$

$$\frac{D\mathbf{v}}{Dt} = -\frac{1}{\rho} \nabla p + \nu \nabla^2 \mathbf{v} + \mathbf{g} \quad (3-2)$$

where  $\rho$  is the density of the fluid,  $\mathbf{v}$  the particle velocity vector,  $p$  the pressure,  $\nu$  the kinematic viscosity and  $\mathbf{g}$  the body force (normally the gravity) .

#### Predictor-Corrector algorithm

The computational procedure of the MPS method comprises two steps. The first step is the predictor step in which the velocity field is computed without enforcing incompressibility. In the second step, namely the corrector step, incompressibility is enforced through the calculation of Poisson equation of pressure.

(1) Predictor step. Determine the temporary particle velocities and positions by considering only the body force and viscosity terms in Eq. (3-2).

$$\mathbf{v}^* = \mathbf{v}_k + (\nu \nabla^2 \mathbf{v}_k + \mathbf{g}_k) \Delta t \quad (3-3)$$

$$\mathbf{r}^* = \mathbf{r}_k + \mathbf{v}^* \Delta t \quad (3-4)$$

where  $\Delta t = t_{k+1} - t_k$ ,  $\mathbf{v}_k = \mathbf{v}(x_k, t_k)$ ,  $\rho_k = \rho(x_k, t_k)$ .  $\mathbf{v}_k$  and  $\mathbf{r}_k$  are the particle velocity and position at time  $t_k$ ;  $\mathbf{v}^*$  and  $\mathbf{r}^*$  are the temporary particle velocity and position, respectively.

Incompressibility is not satisfied in this step and the fluid density that is calculated based on the temporary particle position deviates from the constant density.

(2) Corrector step. Pressure computed from Poisson equation of pressure is used to enforce incompressibility.

The momentum equation can be split into

$$\frac{D\mathbf{v}}{Dt} = \frac{\mathbf{v}_{k+1} - \mathbf{v}_k}{\Delta t} = \frac{\mathbf{v}_{k+1} - \mathbf{v}^* + \mathbf{v}^* - \mathbf{v}_k}{\Delta t} = \frac{\Delta \mathbf{v}' + \Delta \mathbf{v}^*}{\Delta t} = -\frac{\nabla p}{\rho} + \nu \nabla^2 \mathbf{v} + \mathbf{g} \quad (3-5)$$

where  $\Delta \mathbf{v}' = \mathbf{v}_{k+1} - \mathbf{v}^*$  and  $\Delta \mathbf{v}^* = \mathbf{v}^* - \mathbf{v}_k$ .

Substituting  $\frac{\Delta \mathbf{v}^*}{\Delta t} = \nu \nabla^2 \mathbf{v} + \mathbf{g}$  from Eq. (3-3) into Eq. (3-5) we can get

$$\frac{\Delta \mathbf{v}'}{\Delta t} = -\frac{\nabla p_{k+1}}{\rho_{k+1}} \quad (3-6)$$

The mass conservation equation can be split into

$$\begin{aligned} \frac{1}{\rho} \frac{D\rho}{Dt} &= \frac{1}{\rho} \frac{\rho_{k+1} - \rho_k}{\Delta t} = \frac{1}{\rho} \frac{\rho_{k+1} - \rho^* + \rho^* - \rho_k}{\Delta t} = \frac{1}{\rho} \left( \frac{\Delta \rho' + \Delta \rho^*}{\Delta t} \right) \\ &= -\nabla \cdot (\mathbf{v}_{k+1} - \mathbf{v}^* + \mathbf{v}^*) = -\nabla \cdot (\Delta \mathbf{v}' + \mathbf{v}^*) \end{aligned} \quad (3-7)$$

The mass conservation equation at the temporary position can be expressed as

$$\frac{1}{\rho} \frac{\Delta \rho^*}{\Delta t} = -\nabla \cdot \mathbf{v}^*$$

Substituting the above equation into Eq. (3-7) gives

$$\frac{1}{\rho} \frac{\Delta \rho'}{\Delta t} = -\nabla \cdot (\Delta \mathbf{v}') \quad (3-8)$$

By combining Eqs. (3-6) and (3-8) the Poisson equation of pressure is obtained (Koshizuka et al., 1998):

$$\nabla^2 p_{k+1} = -\frac{\rho}{(\Delta t)^2} \frac{\rho^* - \rho_{k+1}}{\rho_{k+1}} \quad (3-9)$$

By imposing the new density  $\rho_{k+1} = \rho_0$  on the right side of Eq. (3-9), incompressibility is satisfied at the new time step. In the MPS method, particle number densities  $n^*$  (corresponding to  $\rho^*$ ) and  $n_0$  (corresponding to  $\rho_0$ ) are used in Eq. (3-9) (Koshizuka and Oka, 1996; Koshizuka et al., 1998; Gotoh et al., 2005).

After applying appropriate discretization algorithm for the Laplace operator in Eq. (3-9), a system of linear equations is obtained and can be solved using the existing solver such as incomplete Cholesky decomposition conjugate gradient method (Kershaw, 1978) and Gauss-Seidel method (Ataie-Ashtiani and Farhadi, 2006). In present study the Gauss-Seidel method is adopted.

Once the pressure term is obtained, the new particle velocities can be computed by Eq. (3-6). Finally the new position of the particle is updated by

$$\mathbf{r}_{k+1} = \mathbf{r}_k + \mathbf{v}_{k+1} \Delta t \quad (3-10)$$

The time step is controlled in the computation to satisfy the Courant–Friedrichs–Lewy (CFL) condition (Courant et al., 1967; Ataie-Ashtiani and Farhadi, 2006) as follows,

$$\Delta t \leq 0.2 \frac{L_0}{V_{\max}} \quad (3-11)$$

where  $L_0$  is the initial particle distance and  $V_{\max}$  the maximum particle velocity in the computation.

### 3.2.2 MPS formulation

In MPS, the fluid is represented by a set of particles. Each particle carries a mass  $m$  and moves at velocity  $\mathbf{v}$ . A particle interacts with its neighbor particles covered by an influence radius through a kernel function  $w(r)$ , where  $r$  is the distance between two particles (Figure 3-1).

The most commonly used kernel function applied in the MPS method is the one proposed by Koshizuka and Oka (1996):

$$w(r) = \begin{cases} \frac{r_e}{r} - 1 & 0 \leq r < r_e \\ 0 & r \geq r_e \end{cases} \quad (3-12)$$

where  $r_e$  is the influence radius of the influence area of each particle.  $r_e = (2 \sim 4) \times L_0$  is commonly used in the simulations (Ataie-Ashtiani and Farhadi, 2006; Gotoh et al., 2005) where  $L_0$  is the initial distance between two adjacent particles.

The particle number density for particle  $i$  is then defined as summation of the weights of its neighbor particles (Koshizuka and Oka, 1996; Koshizuka et al., 1998),

$$n_i = \sum_{j \neq i} w(|\mathbf{r}_j - \mathbf{r}_i|) \quad (3-13)$$

The gradient operator is modeled as a weighted average of the gradient vectors between the center particle  $i$  and its neighbor particles. The gradient of the pressure is expressed as (Koshizuka and Oka., 1996),

$$(\nabla p)_i = \frac{D}{n_0} \sum_{j \neq i} \left[ \frac{p_j - p_i}{|\mathbf{r}_j - \mathbf{r}_i|^2} (\mathbf{r}_j - \mathbf{r}_i) w(|\mathbf{r}_j - \mathbf{r}_i|) \right] \quad (3-14)$$

where  $D$  is the number of space dimensions and  $n_0$  the initial constant particle number density. As discussed by Koshizuka et al. (1998), the pressure value of any neighbor particle can be used for  $p_i$  if the distribution of neighbor particles is isotropic. In the above equation,  $p_i'$  is used instead of  $p_i$ . The value of  $p_i'$  is computed by (Koshizuka et al., 1998)

$$p_i' = \min(p_j) \quad \text{for} \{j \mid w(|\mathbf{r}_j - \mathbf{r}_i|) \neq 0\} \quad (3-15)$$

By using the minimum value  $p_i'$  among the neighbor particles within the influence radius  $r_e$ , the inter-particle forces will always be repulsive since  $p_j - p_i'$  is positive. This is good for the numerical stability as pointed out by Koshizuka et al. (1998).

The Laplacian model is proposed by Koshizuka et al. (1998) based on the concept of diffusion, which is in the form:

$$(\nabla^2 p)_i = \frac{2D}{n_0 \lambda} \sum_{j \neq i} [(p_j - p_i) w(|\mathbf{r}_j - \mathbf{r}_i|)] \quad (3-16)$$

where

$$\lambda = \int_V r^2 w(r) dV / \int_V w(r) dV \quad (3-17)$$

In Eq. (3-16), the physical property (such as pressure) of the center particle is distributed to its neighbor particles using a weight function  $w$ . Since diffusion is a

linear process, the distributions from one particle to the others can be superimposed. General concepts of these models can be found in the work of Koshizuka et al. (1998) and Gotoh et al. (2005). The discretization of viscosity components in the viscosity term is the same as that of the Laplacian term shown in Eq. (3-16) (Gotoh et al., 2005).

### 3.2.3 Modeling of incompressibility

In the MPS method, density is represented by particle number density defined in Eq. (3-13). Incompressibility is satisfied by keeping the particle number density constant. By applying particle number density in the right hand side of Eq. (3-9) and imposing  $n_{k+1} = n^0$  (Koshizuka et al., 1998), the Poisson equation of pressure becomes,

$$\nabla^2 p_{k+1} = -\frac{\rho}{(\Delta t)^2} \frac{n^* - n_0}{n_0} \quad (3-18)$$

The computational procedure of MPS is summarized in the flowchart shown in Figure 3-2.

### 3.2.4 Boundary conditions

#### 3.2.4.1 Wall boundaries

In the MPS method, wall boundaries are also modeled by particles. They balance the pressure of the inner fluid particles and prevent them from penetrating the wall (Ataie-Ashtiani et al., 2008). A solid wall boundary is represented by one line of fixed particles. The Poisson equation of pressure is solved on these particles. Furthermore, in order to ensure the particle number density is not truncated near the solid boundaries, several lines of dummy particles are placed outside the wall boundaries. Velocities are

always zero at the solid wall particles and dummy particles so as to retain the non-slip boundary condition.

There are different ways to place the dummy particles. The first one is to use fixed particles which are spaced according to the initial particle configuration (Gotoh and Sakai, 1999). Lo and Shao (2002) used another method involving the so called “ghost particle”, where mirror particles of inner fluid particles adjacent to the wall were used. The fixed particle approach is simpler than the “ghost particle” approach since the ghost particles keep changing their positions every time step. Additional computational cost is required in the ghost particle method to generate dummy boundaries at every time step. Hence in the present study we adopt the fixed particle approach.

In the fixed particle approach, most researchers applied the same pressure for the dummy particles as that of the solid wall particles (Lo and Shao, 2002; Ataie-Ashtiani et al., 2008). As well in ghost particle method, they applied the same pressure for the ghost particle as that of the respective fluid particle (Colagrossi and Landrini, 2003; Molteni and Colagrossi, 2009). However, as pointed out by Delorme et al. (2009), a pressure difference between dummy particles and solid wall particles (or ghost particles and the respective fluid particles) should be introduced to take into account the effect of the gravity field and other body forces. Here in this study, we use the fixed particle approach to place dummy particles and the method of applying pressure for the dummy particles that is discussed by Delorme et al. (2009).

When moving wall boundaries is encountered, the motion of walls is implemented by updating the positions of wall particles at every time step. For liquid sloshing problems in Chapter 5, the tank motion is imposed by this approach.

### 3.2.4.2 Free surface

Since no particle exists outside the free surface, the particle number density of the free surface particles decrease on this boundary. Thus if a particle satisfies Eq. (3-19), it is considered to be free surface particle (Koshizuka et al., 1998).

$$(n^*)_i < \beta n_0 \quad (3-19)$$

where  $\beta$  is a numerical parameter which is usually between 0.8 and 0.99. It is pointed out by Koshizuka and Oka (1996) that the simulation results are not sensitive to the value of  $\beta$  in this range. Fragmentation and coalescence of the fluid can be simulated easily with this simple boundary recognition method. The Dirichlet boundary condition of pressure is applied to the free surface particles.

### 3.2.5 Drawbacks of MPS

Although the MPS method can simulate and represent well the fluid general motion, it produces large pressure fluctuation in the solutions (Khayyer and Gotoh, 2009). Khayyer and Gotoh (2008) pointed out that the spurious pressure fluctuations seem to be unavoidable in the MPS method for incompressible fluid problems. They proposed a corrected MPS algorithm to ensure the momentum conservation of the particles. Their algorithm is further revised by introducing a new source term for the Poisson pressure equation and allowing slight compressibility in their recent work (Khayyer and Gotoh, 2009). They demonstrated the improved performance through several wave breaking cases. However, even with all these improvements, the pressure fluctuation does not vanish especially when large amplitude particle motion appears.

One main reason of the pressure fluctuation in the MPS method is that free surface particles are not accurately recognized. Since free surface particles are detected

by the number density using Eq. (3-19), some in-domain fluid particles with zero or low pressure may be falsely considered as free surface particles when the fluid motion are violent. In this case pressure fluctuation occurs due to incorrect pressure solutions of the whole domain. The pressure fluctuation in turn produces zero or low pressure particles resulting in a vicious cycle.

Another reason of pressure fluctuation lies in the approximation of the Laplacian and gradient model in MPS method. This is a common problem for particle methods such as SPH and MPS in which the partial differential operators are approximated by a pre-defined kernel function. The approximation of these operators is highly dependent on the kernel selected. The accuracy of approximation is not guaranteed when the particle distribution is irregular, as will be demonstrated in Sect. 3.3.4.

This thesis mainly focuses on overcoming the above-mentioned two problems of the pressure fluctuation in fluid flows. A new particle method named Consistent Particle Method (CPM) is proposed in this study. Three main improvements are included, the most important one dealing with the partial differential operators approximated based on Taylor series expansion.

### **3.3 CPM based on Taylor series**

#### **3.3.1 Introduction**

As discussed in the previous section, although the MPS method has been shown to simulate the profile of free surface flow, it has some serious drawbacks for pressure solution. The pressure history shows spurious high fluctuation and sometimes even negative pressure values appear.

In the two popular particles methods MPS and SPH, the discretization of partial derivatives such as Laplace and gradient operators rely on a kernel function defined only according to inter-particle distance. The main problem of using kernel function is that the Laplacian model may become unstable once the distribution becomes irregular. The consistency of the Laplacian and gradient model in conventional particle method such as SPH and MPS is not guaranteed. To overcome the shortcoming, a new method based on Taylor series expansion is proposed.

The method of approximating partial derivatives based on Taylor series expansion is the core algorithm in the generalized finite difference method (GFD). GFD method is a meshless method which is proposed in the early 1970s for structural problems. One of the early investigations was by Perrone and Kao (1975) who studied large deflection response of a flat membrane. Liszka and Orkisz (1980) presented a FIDAM (Finite Difference at Arbitrary Mesh) code based on GFD using moving least-square interpolation, and applied it in structural mechanics. Nevertheless this method has not received much attention possibly because the method does not have the favorable properties such as symmetric positive and well conditioned matrix (Luo and Haussler-Combe, 2002). Luo and Haussler-Combe (2002) developed a GFD based on minimizing global residual and applied in solving solid mechanics problems. Gavete et al. (2003) improved the GFD by using variable radius of influence. The results obtained were compared with other meshless methods. Nevertheless, no application of the method to real problems was presented. Recently Chew et al. (2006) proposed an Arbitrary Lagrangian-Eulerian (ALE) formulation of GFD method. They applied the improved scheme to vortex flow and flows past moving bodies. To our knowledge, however, GFD method has not been used in the study of incompressible free surface flows. The main reason may be that the GFD suffers from ill-conditioning of matrix if

there is poor spatial arrangement of the support particles, which is very likely to occur in free surface flow problems with large particle motions and severe irregularity of particle distribution. Hence the application of GFD in large motion fluid problems with free surface is limited.

By incorporating the incompressibility model of MPS using number density in GFD, we may simultaneously overcome the problem of ill-conditioning in GFD method and improve the approximation accuracy not achieved by MPS method. In this context, we propose a new particle method which combines the merits of GFD in accurate approximation of the gradient and Laplace operators and MPS in obtaining even particle distribution through the modeling of incompressibility. Since in the proposed method the discretization of partial differential operators are consistent with Taylor series expansion, we name it Consistent Particle Method (CPM).

Our algorithm in approximation of differential operators is similar to GFD developed by Perrone and Kao (1975) and Liszka and Orkisz (1980) for structural mechanics. And it resembles the finite point methods of Onate et al. (1996, 2000) and the finite point solver of Mendez and Velazquez (2004). Mendez and Velazquez (2004) pointed out that the evolution of these particle methods (GFD, finite point solver, finite point method and our proposed CPM) leads to a closer resemblance between them. Nevertheless, the main difference between our work and the previous research is that we impose strict incompressibility of free surface flows by computing particle number density and solving Poisson equation of pressure. A free surface recognition method and free surface incompressibility adjustment approach are applied to help define the boundary and impose accurate boundary condition. In this sense, the drawbacks of

low accuracy in some particle methods (such as SPH and MPS) and ill-condition matrix in GFD due to poor spatial particle distribution are resolved.

A brief summary and comparison of particle methods is listed in Table 3-1. As shown in the table, our proposed CPM does not require mesh and pre-defined kernel function. Incompressible fluid is modeled by solving Poisson pressure equation. By incorporating the arc free surface recognition method it can be applied to simulate free surface flow problems.

In this section we present the development of the discretization equations based on Taylor series similar to GFD. The method is first validated through numerical tests of Laplace operator evaluation. The performance of the proposed CPM method in modeling free surface flow will be demonstrated in the next Chapter.

### 3.3.2 Approximation of gradient and Laplacian by Taylor series

For any differentiable function  $f(x, y)$ , the Taylor series expansion around a point  $P(x_0, y_0)$  can be expressed in the form (Gavete et al., 2003)

$$f(x, y) = f_0 + hf_{,x0} + kf_{,y0} + \frac{1}{2}h^2 f_{,xx0} + hkf_{,xy0} + \frac{1}{2}k^2 f_{,yy0} + O(r^3) \quad (3-20)$$

where  $h = x - x_0$ ,  $k = y - y_0$ ,  $f_0 = f(x_0, y_0)$ ,  $f_{,x0} = \frac{\partial f(x_0, y_0)}{\partial x}$ ,  $f_{,y0} = \frac{\partial f(x_0, y_0)}{\partial y}$ ,

$$f_{,xx0} = \frac{\partial^2 f(x_0, y_0)}{\partial x^2}, \quad f_{,xy0} = \frac{\partial^2 f(x_0, y_0)}{\partial x \partial y}, \quad f_{,yy0} = \frac{\partial^2 f(x_0, y_0)}{\partial y^2}, \quad r = \sqrt{h^2 + k^2}.$$

For the reference particle  $P(x_0, y_0)$  with its neighbor particles  $j$  ( $j=1, 2, \dots, N$ ), if the values of the function  $f(x_j, y_j)$  are all known at the neighbor particles, we may truncate the Taylor series to the second order and approximate the derivatives of the

function at the reference particle  $P(x_0, y_0)$  by solving a system of linear equations (Liszka and Orkisz, 1980; Chew et al., 2006).

Writing Eq. (3-20) for each of the neighbor particles, we derive a set of linear equations

$$[\mathbf{A}]\{\mathbf{Df}\} - \{\mathbf{f}\} = 0 \quad (3-21)$$

with

$$[\mathbf{A}] = \begin{bmatrix} h_1 & k_1 & \frac{1}{2}h_1^2 & h_1k_1 & \frac{1}{2}k_1^2 \\ h_2 & k_2 & \frac{1}{2}h_2^2 & h_2k_2 & \frac{1}{2}k_2^2 \\ \vdots & \vdots & \vdots & \vdots & \vdots \\ h_N & k_N & \frac{1}{2}h_N^2 & h_Nk_N & \frac{1}{2}k_N^2 \end{bmatrix} \quad (3-22)$$

$$\{\mathbf{Df}\} = \begin{Bmatrix} f_{,x0} \\ f_{,y0} \\ f_{,xx0} \\ f_{,xy0} \\ f_{,yy0} \end{Bmatrix}, \quad \{\mathbf{f}\} = \begin{Bmatrix} f_1 - f_0 \\ f_2 - f_0 \\ \vdots \\ f_N - f_0 \end{Bmatrix} \quad (3-23)$$

where  $h_j = x_j - x_0$ ,  $k_j = y_j - y_0$  and  $N$  is the total number of particles in the influence area of particle  $P$ .

The minimum number of neighbor particles required in Eq. (3-21) to determine  $\{\mathbf{Df}\}$  vector is five since we are seeking solutions of five unknowns. With exactly five neighbor particles, however, the matrix in Eq. (3-22) is highly susceptible to ill-conditioning due to irregular spatial arrangement of these particles. To overcome this problem, more than five particles can be used in order to improve the accuracy of the approximation (Liszka and Orkisz, 1980). In this case, the over-determined linear equations is solved by minimizing the residual error vector

$$\mathbf{E} = [\mathbf{A}]\{\mathbf{Df}\} - \{\mathbf{f}\} \quad (3-24)$$

We consider the following norm of  $\mathbf{E}$  with weight factors incorporated (Gavete et al., 2003)

$$\|\mathbf{E}\| = \sum_{j=1}^N \left[ f_0 - f_j + h_j f_{,x0} + k_j f_{,y0} + h_j^2 f_{,xx0} + h_j k_j f_{,xy0} + k_j^2 f_{,yy0} \right] w_j \quad (3-25)$$

where  $w_j$  is the weighting function used in the weighted least-square solution of the equation. Incorporating the weight function  $w_j$  in Eq. (3-25) is equivalent to solving the over-determined Eq. (3-21) using the weighted least-square approach. Different least-square weighting functions may be selected (Liszka and Orkisz, 1980; Gavete et al., 2003; Chew et al., 2006).

By minimizing the norm

$$\frac{\partial \|\mathbf{E}\|}{\partial \{\mathbf{Df}\}} = 0 \quad (3-26)$$

a set of five equations with five unknowns is obtained as follows

$$\begin{bmatrix} \sum w_j^2 h_j^2 & \sum w_j^2 h_j k_j & \sum w_j^2 \frac{h_j^3}{2} & \sum w_j^2 h_j^2 k_j & \sum w_j^2 \frac{h_j k_j^2}{2} \\ \sum w_j^2 h_j k_j & \sum w_j^2 k_j^2 & \sum w_j^2 \frac{h_j^2 k_j}{2} & \sum w_j^2 h_j k_j^2 & \sum w_j^2 \frac{k_j^3}{2} \\ \sum w_j^2 \frac{h_j^3}{2} & \sum w_j^2 \frac{h_j^2 k_j}{2} & \sum w_j^2 \frac{h_j^4}{4} & \sum w_j^2 \frac{h_j^3 k_j}{2} & \sum w_j^2 \frac{h_j^2 k_j^2}{4} \\ \sum w_j^2 h_j^2 k_j & \sum w_j^2 h_j k_j^2 & \sum w_j^2 \frac{h_j^3 k_j}{2} & \sum w_j^2 h_j^2 k_j^2 & \sum w_j^2 \frac{h_j k_j^3}{2} \\ \sum w_j^2 \frac{h_j k_j^2}{2} & \sum w_j^2 \frac{k_j^3}{2} & \sum w_j^2 \frac{h_j^2 k_j^2}{4} & \sum w_j^2 \frac{h_j k_j^3}{2} & \sum w_j^2 \frac{k_j^4}{4} \end{bmatrix} \begin{Bmatrix} f_{,x0} \\ f_{,y0} \\ f_{,xx0} \\ f_{,xy0} \\ f_{,yy0} \end{Bmatrix}$$

$$= \begin{pmatrix} \sum f_j w_j^2 h_j - f_0 \sum w_j^2 h_j \\ \sum f_j w_j^2 k_j - f_0 \sum w_j^2 k_j \\ \sum f_j w_j^2 \frac{h_j^2}{2} - f_0 \sum w_j^2 \frac{h_j^2}{2} \\ \sum f_j w_j^2 h_j k_j - f_0 \sum w_j^2 h_j k_j \\ \sum f_j w_j^2 \frac{k_j^2}{2} - f_0 \sum w_j^2 \frac{k_j^2}{2} \end{pmatrix} \quad (3-27)$$

All the elements in the first matrix in Eq. (3-27) depend only on the relative coordinates between the reference particle and its neighbor particles. The main task in this method is to solve the derivatives in Eq. (3-27) for all the particles in the domain. As pointed out by Chew et al. (2006), for stationary boundary problems where all nodes are fixed, one only needs to invert the matrix in Eq. (3-27) once to obtain the derivatives. However, for moving boundary problems, for example, fluid flows with free surface, the matrix needs to be solved for every time step when the particles change positions with time.

The solution of Eq. (3-27) can be expressed as,

$$\begin{Bmatrix} f_{,x0} \\ f_{,y0} \\ f_{,xx0} \\ f_{,xy0} \\ f_{,yy0} \end{Bmatrix} = \begin{bmatrix} a_1 & a_2 & a_3 & a_4 & a_5 \\ b_1 & b_2 & b_3 & b_4 & b_5 \\ c_1 & c_2 & c_3 & c_4 & c_5 \\ d_1 & d_2 & d_3 & d_4 & d_5 \\ e_1 & e_2 & e_3 & e_4 & e_5 \end{bmatrix} \begin{pmatrix} \sum f_j w_j^2 h_j - f_0 \sum w_j^2 h_j \\ \sum f_j w_j^2 k_j - f_0 \sum w_j^2 k_j \\ \sum f_j w_j^2 \frac{h_j^2}{2} - f_0 \sum w_j^2 \frac{h_j^2}{2} \\ \sum f_j w_j^2 h_j k_j - f_0 \sum w_j^2 h_j k_j \\ \sum f_j w_j^2 \frac{k_j^2}{2} - f_0 \sum w_j^2 \frac{k_j^2}{2} \end{pmatrix} \quad (3-28)$$

where the parameters from  $a_1 - a_5$  to  $e_1 - e_5$  are solved from Eq. (3-27).

Hence from Eq. (3-28) the gradient operator is expressed as

$$(\nabla f_0)_x = \sum_{j=1}^N \left[ w_j^2 (a_1 h_j + a_2 k_j + a_3 \frac{h_j^2}{2} + a_4 h_j k_j + a_5 \frac{k_j^2}{2}) \right] (f_j - f_0) \quad (3-29)$$

$$(\nabla f_0)_y = \sum_{j=1}^N \left[ w_j^2 (b_1 h_j + b_2 k_j + b_3 \frac{h_j^2}{2} + b_4 h_j k_j + b_5 \frac{k_j^2}{2}) \right] (f_j - f_0) \quad (3-30)$$

The Laplace operator is obtained as

$$\begin{aligned} (\nabla^2 f)_0 = \sum_{j=1}^N \left\{ w_j^2 \left[ (c_1 + e_1) h_j + (c_2 + e_2) k_j + (c_3 + e_3) \frac{h_j^2}{2} \right. \right. \\ \left. \left. + (c_4 + e_4) h_j k_j + (c_5 + e_5) \frac{k_j^2}{2} \right] \right\} (f_j - f_0) \end{aligned} \quad (3-31)$$

### 3.3.3 Main features of CPM

As mentioned before, the method of computing Laplace and gradient operators based on Taylor series is the core algorithm in the GFD method. The main drawback of the GFD method is the possibility of obtaining ill-conditioned matrix due to poor particle distribution. Since the element in the matrices of Eq. (3-27) is only dependent on the geometrical positions of the reference particle and its neighbors, the distribution of the particles in the domain greatly affects the stability of the algorithm. Ill-conditioned matrix can arise from a variety of causes, such as the total number of neighbor particles less than the number of unknown derivatives in Eq. (3-21) is obtained, extremely close/separation between some particles, and large number of particles aligning in a nearly collinear manner. To overcome this problem, many different approaches have been explored (Luo and Haussler-Combe, 2002; Gavete et al., 2003).

The selection of particles in the neighborhood of the reference particle is a crucial factor affecting the accuracy of approximation. The most commonly used criterion in particle methods is to select the neighbor particles according to their distance from the reference particle (Monaghan, 1994; Shao and Lo, 2003; Koshizuka et al., 1998). It is

simple but fails very often in the GFD method due to the irregular density of particles (Liszka and Orkisz, 1980). Perrone and Kao (1975) presented an “eight segments” method, where the domain around the reference particle is divided equally into eight quadrants. The nearest particle to the reference particle in each quadrant is selected. Liszka and Orkisz (1980) found it too complicated and suggested a simple criterion of “four quadrants”. Gavete et al. (2003) also adopted the same approach as Liszka and Orkisz (1980).

Although the quadrant criterion can improve the performance of the approximation, it cannot completely avoid ill-conditioned matrices. Gavete et al. (2003) suggested variable influence radius for each particle. The residual at each point is obtained first. If ill-conditioned matrix (i.e. large residual value) for any particle is detected, the radius of that particle is increased to capture more neighbor particles. Luo and Haussler-Combe (2002) proposed an improved method based on minimizing global residual with respect to particle parameters. However, they found their results in their method are sensitive to the number of neighbor particles or the size of domain of influence.

Nevertheless, no matter what criteria of particle selection are used, the ill-conditioned matrix cannot be fully avoided due to the irregular density of particles. A possible solution is to generate regular density of particles as used in MPS method where incompressibility is employed by keeping the particle number density constant. Hence, the proposed method is motivated by combining the merits of GFD and MPS in consistent representation of differential operators and producing even particle distribution through the idea of number density, respectively.

### 3.3.3.1 Laplacian and gradient model

According to the derivations in Sect. 3.3.2, the Poisson equation of pressure (see, Eq. (3-18)) can be written as

$$\begin{aligned} (\nabla^2 p)_i = \sum_{j=1}^N \left\{ w_j^2 \left[ (c_1 + e_1)h_j + (c_2 + e_2)k_j + (c_3 + e_3)\frac{h_j^2}{2} \right. \right. \\ \left. \left. + (c_4 + e_4)h_j k_j + (c_5 + e_5)\frac{k_j^2}{2} \right] \right\} (p_j - p_i) = -\frac{\rho}{(\Delta t)^2} \frac{\rho^* - \rho^0}{\rho^0} \end{aligned} \quad (3-32)$$

Incompressibility of the particles inside the fluid domain is satisfied through keeping the density constant. In the MPS method particle number density is used (Koshizuka et al., 1998). In the proposed CPM, the same density computation method is adopted. The Gauss-Seidel method is used to solve the discretized linear equation system of Eq. (3-32). The viscosity term in Eq. (3-3) is also approximated based on the same algorithm in Eq. (3-31).

The gradient model of pressure based on the solution of the first derivatives in Eq. (3-27) is

$$(\nabla p)_{ix} = \sum_{j=1}^N \left[ w_j^2 (a_1 h_j + a_2 k_j + a_3 \frac{h_j^2}{2} + a_4 h_j k_j + a_5 \frac{k_j^2}{2}) \right] (p_j - p_i) \quad (3-33)$$

$$(\nabla p)_{iy} = \sum_{j=1}^N \left[ w_j^2 (b_1 h_j + b_2 k_j + b_3 \frac{h_j^2}{2} + b_4 h_j k_j + b_5 \frac{k_j^2}{2}) \right] (p_j - p_i) \quad (3-34)$$

In the MPS method, the gradient operator defined in Eq. (3-14) with  $p_i$  replaced by  $p_i'$  is shown to be good for the stability of the numerical algorithm (Koshizuka and Oka 1996; Koshizuka et al., 1998). Similarly in our proposed CPM algorithm, a modified gradient model is used as follows

$$(\nabla p)_{ix} = \sum_{j=1}^N \left[ w_j^2 (a_1 h_j + a_2 k_j + a_3 \frac{h_j^2}{2} + a_4 h_j k_j + a_5 \frac{k_j^2}{2}) \right] (p_j - p'_i) \quad (3-35)$$

$$(\nabla p)_{iy} = \sum_{j=1}^N \left[ w_j^2 (b_1 h_j + b_2 k_j + b_3 \frac{h_j^2}{2} + b_4 h_j k_j + b_5 \frac{k_j^2}{2}) \right] (p_j - p'_i) \quad (3-36)$$

where  $p'_i = \min(p_j) \text{ for } \{j \mid w(|\mathbf{r}_j - \mathbf{r}_i|) \neq 0\}$ .

The use of  $p'_i$  improves the stability of the algorithm by imposing the repulsive forces between any pair of particles (Koshizuka et al., 1998). This feature is very important in the algorithm since it reduces the possibility of local accumulation of fluid particles at any time step and hence greatly improves the stability of the algorithm. The stability improvement of the gradient model proposed in Eqs. (3-35) and (3-36) is very significant in moving boundary problems, such as fluid flows with free surface.

The parameter  $w_j$  in the above Laplacian and gradient model is the weighting function used in Eq. (3-25) for the weighted least-square solution of the derivatives. As discussed by researchers using GFD method for the same purpose, three weighting functions are considered: quartic spline and cubic spline functions used by Gavete et al. (2003) and inverse distance weighting coefficients proposed by Liszka and Orkisz (1980). The explanation and comparison of these weighting functions will be presented in Chapter 4.

### 3.3.3.2 Predictor-corrector steps

The same two-step algorithm introduced in Sect. 3.2.1 is used in the CPM method. The algorithm is commonly used in the solution of the Navier-Stokes equation using different numerical method, such as PFEM (Idelsohn et al., 2003) and incompressible SPH (Shao and Lo, 2003).

### 3.3.3.3 Boundary surface recognition

In free surface flow problems, a key consideration is how to recognize free surface boundaries particles. In mesh-based methods like FEM and FDM, the boundary node labels are known a priori. However, in particle methods, a new particle distribution is obtained at each time step. The boundary particles should be recognized before the boundary conditions can be implemented. Hence, in free surface flow problems, the identification of free surface particles is of great importance in obtaining the pressure field accurately. The MPS method uses density threshold in Eq. (3-19) to differentiate the free surface particles. However, as discussed in Sect. 3.2.5, this simple threshold method is not effective in recognizing free surface particles accurately. In addition, the pressure solution is greatly affected by the parameter  $\beta$  as well as the influence radius  $r_e$  defined in the algorithm. Since the pressure values of free surface particles are theoretically zero and hence known, the total number of unknowns in the Poisson equation of pressure excludes the numbers of free surface particles. The density threshold method in recognition of free surface particle will cause great pressure errors when some inner fluid particles are falsely recognized as free surface particles.

Considering this problem, several boundary recognition algorithms may be used to define the boundaries from a collection of particles. Edelsbrunner et al. (1983) proposed a 2D alpha-shape method and later Edelsbrunner and Mucke (1994) developed a 3D alpha-shape method. Idelsohn et al. (2003, 2004) and Idelsohn and Onate (2006) used the alpha-shape method in their proposed PFEM. Dilts (2000) introduced another boundary recognition method named “arc” method. It is tested to be fast and can yield the exact solution. Detailed investigation of the efficiency of the arc

method can be found in a reference (Dilts, 2000). The arc method is used in this study in the CPM simulations since it is easier to implement compared with the alpha-shape method.

The basic idea of arc method can be illustrated in Figure 3-3(a). If any arc of the circle (with radius  $R$ ) around a center particle is not covered by any circle of its neighbors, the center particle is treated as a free surface boundary particle. As shown in the figure, the intersection arc of the center particle covered by the circle of neighbor particle is recorded according to the position of neighbor particle in the form of angle interval of the two interaction points. After that, all the angle intervals covered by the neighbor particles are listed and sorted in ascending order by the left endpoints (either clockwise or anti-clockwise). The angle intervals for the center particle A and B are shown in Figure 3-3(b) for example. The sorted list is then scanned in sequence, looking for gaps between two neighbor angle intervals. If any gap is found, the center particle is considered as a free surface boundary particle. As can be seen in the figure, particle A is recognized as a free surface particle and particle B in-domain fluid particle. A more detailed discussion of the arc method is documented by Dilts (2000).

#### **3.3.3.4 Incompressibility adjustment (IA) of the free surface particles**

The incompressibility condition of fluid particles is imposed by Eq. (3-18), which corrects the temporary particle number densities to the constant  $n_0$ . The number density of free surface particles is less than that of the in-domain fluid particles due to the absence of particles above the free surface. Hence the correction of number density to  $n_0$  is not applicable for the free surface particles since the neighbor particle distributions are truncated. The truncation depends on the radius of influence. Khayyer and Gotoh (2009) noted this problem and proposed a solution method where a

modified source term is used in the right hand side of Eq. (3-18). They compute  $Dn/Dt$  from the derivatives of kernel function  $w$  since number density  $n$  is a function of  $w$ . But the source term in this formulation varies depending on the kernel function used.

Here we proposed a scheme to impose incompressibility condition for the free surface particles explicitly. Since the incompressibility condition is satisfied for all the fluid particles, if the two free surface particles tend to get very close at some time instant, their velocities are modified (as explained below) so that they will not collide. This will greatly improve the stability of the numerical algorithm.

As shown in Figure 3-4, for the two free surface particles  $i$  and  $j$ , their velocities are decomposed into the components normal and tangential to their coordinate vector  $\mathbf{r}_j - \mathbf{r}_i$ . Then we check whether their relative tangential velocity is greater than a criterion shown below

$$(\mathbf{v}_i^t - \mathbf{v}_j^t) \cdot \frac{(\mathbf{r}_j - \mathbf{r}_i)}{|\mathbf{r}_j - \mathbf{r}_i|} \Delta t > \gamma \cdot L_0 \quad (3-37)$$

where  $\mathbf{v}_i^t$  and  $\mathbf{v}_j^t$  are the tangential velocity components of the two particles and  $L_0$  the initial particle distance. The parameter  $\gamma$  is chosen around 0.1-0.3 with the selection of time step  $\Delta t$  according to the condition in Eq. (3-11).

If the condition in Eq. (3-37) is satisfied for any pair of free surface particles, their tangential velocity components will be adjusted as follows

$$\mathbf{v}_i^{t'} = \mathbf{v}_j^{t'} = \frac{\mathbf{v}_i^t + \mathbf{v}_j^t}{2} \quad (3-38)$$

where  $\mathbf{v}_i^{t'}$  and  $\mathbf{v}_j^{t'}$  are the adjusted tangential velocity components of the two particles.

In this way, incompressibility of free surface particles is enforced. The momentum sum of the two particles is still maintained. The proposed algorithm is verified to be able to improve the distribution of the free surface particles so that collision will not occur. It hence improves the stability of the algorithm.

### 3.3.3.5 Selection of neighbor particles

In particle methods, a particle interacts with its neighbor particles in a restricted area within an influence radius  $r_e$  (Figure 3-1). The influence radius is usually much smaller than the solution domain size. For instance, Oger et al. (2006) have pointed out that an influence radius covers 20 neighbor particles provide acceptable results in SPH simulation of a 2D problem. The number of neighbor particles is a small fraction of the total particle number in the solution domain. Identification of the neighbor particles for a center particle requires the computation of distances between all pairs of particles. If  $N$  is the total number of particles in a solution domain, the computational operations for searching neighbor particles are of the order  $N^2$ . The computational cost in selection of neighbor particles is then dominant in the total computation time. Therefore, an efficient neighborhood search algorithm is of great importance in fluid problems with a large number of particles.

Viccione et al. (2008) compared two strategies of neighbor list generation, named Verlet list method and cell-lined list method, and presented a sensitivity study on the efficiency of the two methods. Koshizuka et al. (1998) proposed a candidate list method, which is in principle the same as the Verlet list method in the work of Viccione et al. (2008), to improve the efficiency of MPS method. The candidate list method is shown to be efficient in decreasing the computational time in MPS code.

Here in this thesis we adopted the candidate list method of Koshizuka et al. (1998) because of the simplicity of the approach.

The basic principle of the candidate list method is shown in Figure 3-5. For a given problem with  $N$  particles, two lists are generated. One is for the neighbor particles within the influence radius  $r_e$  and the other is for the candidate particles within the distance of  $r_e + h$ , where  $h$  is an additional distance. The candidate list is updated every  $k$  time steps by searching all  $N$  particles. The neighbor list is updated every time step by searching all the candidate particles in candidate list. The parameter  $k$  and  $h$  are selected properly depending on the motion of the problem so that all neighbor particles within the influence radius should be captured in the candidate list. Koshizuka et al. (1998) have shown that by proper selection of  $k$ , the computational operations of list generation are reduced from the order of  $N^2$  to the order of  $N^{1.5}M^{0.5}$  where  $M$  ( $\ll N$ ) is the number of neighbor particles.

### **3.3.3.6 Distinctive features of CPM**

In summary, there are three distinctive features of the proposed CPM which distinguish CPM from other particle methods.

Firstly, the method establishes discrete equations from derivatives obtained based on Taylor series. The derivatives are solved from the function values of a collection of particles in a weighted least-square approach. The Laplacian and gradient model are established based on the derivatives. The improvement in accuracy of Laplacian model in CPM will be presented in the following section (performance test).

Secondly, a more efficient method (arc method) for free surface particle recognition is adopted in CPM. The arc method can produce more accurate boundary

particle recognition results compared with the density threshold method in MPS. The performance of the arc method will be shown in the sloshing examples in Chapter 5.

Finally, the incompressibility condition of free surface particles is adjusted by an IA scheme. A velocity modification scheme for the free surface particles is adopted to impose incompressibility condition for them explicitly. The accuracy and stability improvements of the arc method and IA scheme will be demonstrated in the following two chapters through numerical examples.

The flowchart of CPM is shown in Figure 3-6, with the three distinctive features highlighted.

### **3.3.4 Performance test of the Laplacian based on Taylor series**

#### **(1). Laplacian at a fixed point**

Based on the algorithm described in Sect. 3.3.2, a simple performance test is presented here to test the accuracy and convergence of the Laplacian model by Taylor series solution. As shown in Figure 3-7, irregularly distributed points are generated by adding random noise (uniform distribution) to the coordinates of 24 regularly spaced points. The random positions are within a radius of  $0.1L_0$  around the original position of regular grid. The operation of randomization is repeated for 50 times and thus 50 groups of irregular distribution are obtained.

For a given function  $\phi(x, y)$ , the Laplacian of this function at the center point (dot shown in Figure 3-7) can be evaluated by Eq. (3-16) in MPS method and Eq. (3-31) in Taylor series method. Different discretization equations of Laplacian are proposed by many researchers in SPH method (Shao and Lo, 2003; Lee et al., 2008). Here for

comparison a typical one shown in the following equation (Shao and Lo, 2003) is investigated.

$$\nabla \cdot \left( \frac{1}{\rho} \nabla \phi \right)_i = \sum_{j \neq i} m_j \frac{8}{(\rho_i + \rho_j)^2} \frac{(\phi_i - \phi_j) \mathbf{r}_{ij} \cdot \nabla_i w(r_{ij})}{r_{ij}^2 + \delta^2} \quad (3-39)$$

where  $m_j$  is the mass of particle  $j$ ,  $\rho_i$  and  $\rho_j$  are the densities of particle  $i$  and  $j$  and  $\delta$  is usually equals to  $0.1r_e$  where  $r_e$  is the influence radius of particle  $i$ .

According to Eqs. (3-16) and (3-39), Laplacian models of MPS and SPH rely on a kernel function  $w(r_{ij})$ . In order to compare the performance of these two discretization models, the same kernel function (Shao and Lo, 2003) is used as follows

$$w(r_{ij}) = \begin{cases} \frac{40}{7\pi r_e^2} \left( 1 - 6 \left( \frac{r}{r_e} \right)^2 + 6 \left( \frac{r}{r_e} \right)^3 \right) & 0 \leq r \leq 0.5r_e \\ \frac{10}{7\pi r_e^2} \left( 2 - 2 \frac{r}{r_e} \right)^3 & 0.5r_e < r \leq r_e \\ 0 & r > r_e \end{cases} \quad (3-40)$$

Therefore 50 corresponding values of Laplacian by each of the three methods can be evaluated based on the parameters listed in Table 3-2. A test function  $\phi(x, y) = x^4 + y^4$  is selected in the study.

As shown in Table 3-2, since the tested function is  $\phi(x, y) = x^4 + y^4$ , the exact value of Laplacian at the point with coordinate (1, 1) is 24. The computed Laplacian values using the three methods are shown in Figure 3-8. The plot of Laplacian using CPM is very close to the exact value. On the contrary, the results of MPS and SPH method have prominent fluctuation. The solution using Taylor series in CPM is more accurate than those of the MPS and SPH methods.

Besides accuracy, convergence is another performance which needs to be tested. Generally speaking, for any numerical method, a finer discretization can help improve the accuracy of simulation. For the same test function  $\phi(x, y) = x^4 + y^4$ , a convergence study of Laplacian using the three methods is performed with different initial point distance  $L_0$ . The convergence test of the three methods in regularly distributed points (without imposing random noise for the coordinates) is first studied with  $L_0$  decreasing from 0.7 to 0.001, as shown in Figure 3-9. One can see in the figure that all the Laplacian value obtained from approximation schemes in the three methods converge to 24 when  $L_0$  becomes smaller. The convergence speed of MPS and SPH seems better than CPM when regular points are used.

The convergence performance in irregular point distribution is then investigated with  $L_0 = 0.2$ ,  $L_0 = 0.1$ ,  $L_0 = 0.01$ , and  $L_0 = 0.001$ . Small random noises are imposed to the neighbor point coordinates. The convergence test results using MPS and SPH are shown in Figure 3-10 and Figure 3-11 respectively. One may observe in the two figures that the Laplacian approximation algorithms in the MPS and SPH methods produce non-convergent solutions since a smaller particle size  $L_0 = 0.001$  results in larger fluctuation of the Laplacian values. In contrast, Figure 3-12 shows the results of convergence performance using the CPM method. The algorithm based on Taylor series presents a good convergence trend: when the particle size is smaller, the plot curve of Laplacian converges to the exact value. Therefore, we can conclude that the approximation algorithms of Laplacian in MPS and SPH method produce convergent solutions only when the particle distribution is regular. The convergence performance is poor when the particles are irregularly distributed. In contrast, the approximation

algorithm in CPM presents good and convergent solutions even for irregular particle distribution.

(2). Laplacian of a 2D surface

Instead of calculating Laplacian at a fixed point with coordinates (1, 1), a more general case is studied here. The parameters used in this case are shown in Table 3-3. A more complicated test function  $\phi(x, y) = \sin(xy)$  is used in this case. The analytical (exact) Laplacian of the test function is  $\nabla^2 \phi(x, y) = -(x^2 + y^2) \sin(xy)$ , which is a smoothed surface in the  $x$ - $y$  domain.

In order to obtain numerical results of the Laplacian by the three methods, a set of regular-grid points (34 x 34) in the domain is first generated. The irregular grid points are then generated by imposing small random noise (random position within a radius of  $0.06 L_0$  around the regular point), as can be seen in Figure 3-13. Based on the point positions and corresponding function values at each point, Eqs. (3-16), (3-31) and (3-39) are used respectively in the three methods to evaluate the Laplacian at the points.

The comparison of three numerical solutions with the exact Laplacian solution in the  $x$ - $y$  domain  $[0.8, 4.2] \times [0.8, 4.2]$  is shown in Figure 3-14. It is shown that the surfaces of Laplacian using MPS and SPH in general agree with the exact solution. However, the surfaces are not smooth and some fluctuations of the Laplacian values appear in certain points. While the surface using Eq. (3-31) in CPM is very smooth and agree very well with the analytical solution.

In order to clearly show the differences of the numerical solutions with the exact solution, the error (i.e. numerical – exact) surfaces of Laplacian are plotted in Figure 3-15. It can be seen that the error of CPM solution is much smaller than the errors of

SPH and MPS. The global error of the numerical results in Figure 3-15 is estimated by the following equation and the values for MPS, SPH and CPM are 0.1323, 0.1041 and 0.01815, respectively.

$$err = \frac{\left\| \nabla^2 \phi(x_i, y_i)_{numerical} - \nabla^2 \phi(x_i, y_i)_{analytical} \right\|_2}{\left\| \nabla^2 \phi(x_i, y_i)_{analytical} \right\|_2} \quad (3-41)$$

A series of particle distributions with random noise is then generated and the global errors are plotted in Figure 3-16. One can see in the figure that the global error of MPS and SPH approximation of Laplacian values are about 13% and 10% while that of CPM is only about 1.8%. It can be concluded that CPM significantly outperforms SPH and MPS in Laplacian approximation for irregular particle distribution.

### 3.4 Concluding remarks

In this chapter, a promising particle method based on Lagrangian formulation named MPS is first studied. The method is based on solving a Poisson equation of pressure which is derived from Navier-Stokes equation (Koshizuka and Oka, 1996). A two-step algorithm is used to solve the coupled governing equations. At the predictor step, temporary particle velocity and position are computed without considering the pressure gradient. At the corrector step, pressure is computed by solving the Poisson equation of pressure. As a driving source, the pressure gradient is then computed and used to update the particles' velocities and positions.

Nevertheless, in MPS (and also some other particle methods such as SPH), a pre-defined kernel function is used to compute gradient and Laplace operators. Since the kernel function is constructed artificially, an accurate solution cannot be guaranteed, especially when the distribution of particles is irregular. Another reason which deteriorates the performance of MPS method is that the free surface particles are not

accurately recognized at every time steps. Since the free surface particles are detected by the number density, some in-domain fluid particles may be considered as free surface particles, particularly when the fluid motion is violent.

In view of the shortcomings of the conventional particle method such as MPS, a more robust particle method CPM is proposed. There are three key features in the proposed method. Firstly, the method establishes discrete equations from derivatives obtained consistent from Taylor series. The performance of the Laplacian model is verified by a numerical test, and comparison with SPH and MPS method is made. It is shown in the test that the approximation of Laplacian in CPM is significantly more accurate than MPS and SPH. Furthermore, the algorithm in CPM shows better convergence performance as the particle distance become smaller.

Secondly, a boundary recognition algorithm named “arc method” is adopted to overcome the shortcomings of the density threshold method used in MPS. The density threshold method cause great pressure errors when some inner fluid particles are falsely recognized as free surface particles (Khayyer and Gotoh, 2009). With the proposed new boundary recognition method, the problem is addressed.

And finally, the incompressibility conditions of the free surface particles are adjusted by a simple scheme. The relative velocity components of any pair of neighbor free surface particles are checked and adjusted if necessary to make sure they will not collide. In this scheme, the momentum conservation of the two particles is still maintained.

The accuracy and stability performance of the proposed CPM scheme will be demonstrated in the following chapters through different free surface flow problems. A

parametric study of some numerical parameters in CPM such as influence radius and particle sizes will also be carried out in the next chapter.



Table 3-1. Summary and comparison of particle methods

Particle Methods	Require mesh (back-ground)?	Require pre-defined kernel?	Applied to Free surface flow?	Incompressibility	Free surface recognition
PFEM	√	-	√	Solve PPE*	Alpha-shape method
SPH	-	√	√	Slightly compressible	State equation ( $\rho \propto p$ )
MPS	-	√	√	Solve PPE	Number density threshold
GFD	-	-	-	Solve PPE	-
Finite particle	-	-	√	Slightly compressible	State equation ( $\rho \propto p$ )
Finite point solver	-	-	-	Pseudo-compressible	-
Finite point method	-	-	-	Solve PPE	-
Finite pointset	-	-	-	Solve PPE	-
CPM	-	-	√	Solve PPE	Arc method

PPE\*: Poisson pressure equation (or Poisson equation of pressure)

Table 3-2. Parameters for performance test of Laplacian

Interaction radius $r_e$	Initial distance $L_0$	Test function $\phi(x, y)$	Kernel function $w(r, r_e)$
$2.1L_0$	0.1	$x^4 + y^4$	Eq. (3-40)

Table 3-3. Parameters for performance test of Laplacian

Interaction radius $r_e$	Initial distance $L_0$	Test function $\phi(x, y)$	Kernel function $w(r, r_e)$
$2.1L_0$	0.1	$\sin(xy)$	Eq. (3-40)



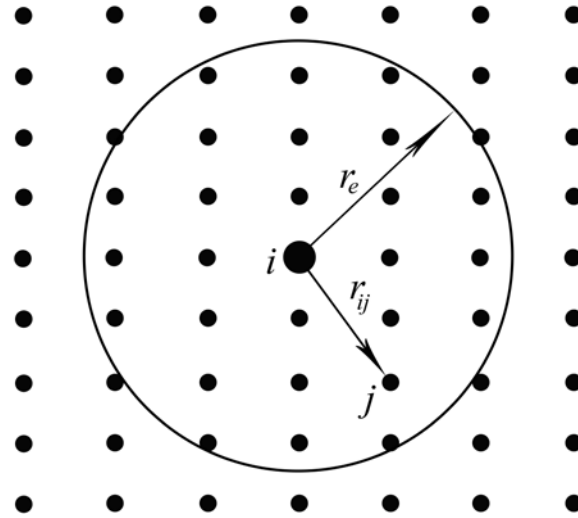


Figure 3-1. Schematic of a typical reference particle with its neighbor particles

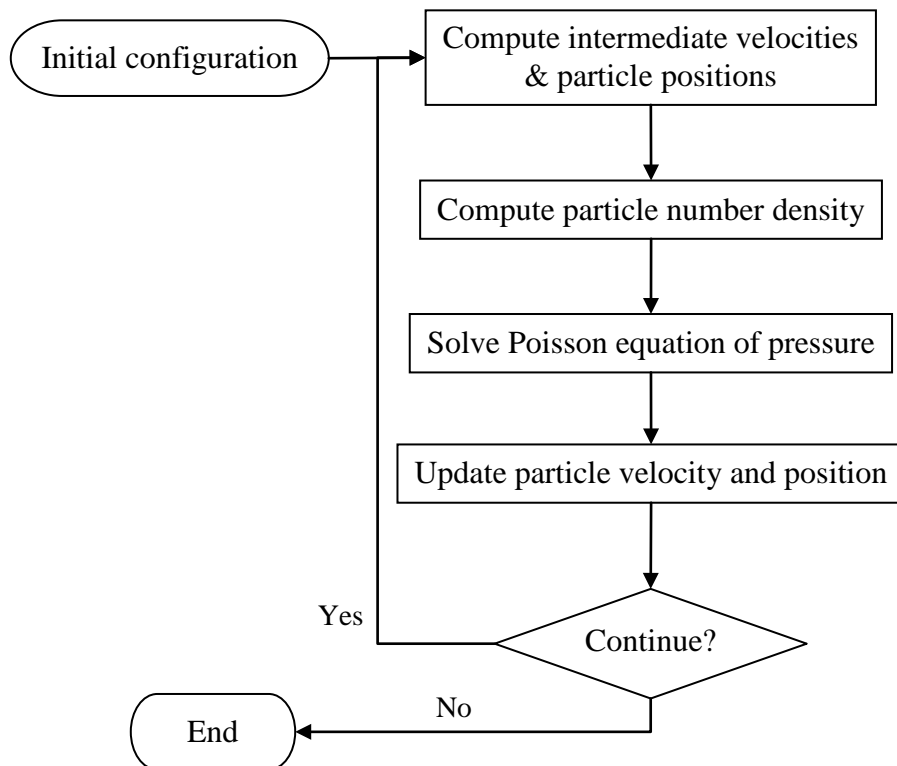
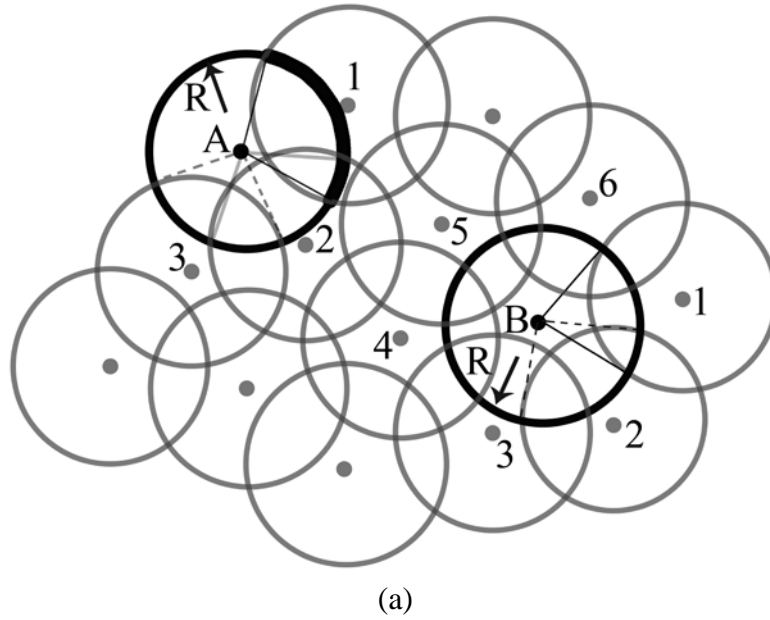


Figure 3-2. Algorithm of the MPS method



Center Particle A			Center Particle B		
Neighbor particle	Range of angle covered (clockwise)	Overlapped with previous arc?	Neighbor particle	Range of angle covered (clockwise)	Overlapped with previous arc?
1	$(0, 0.54\pi)$	N	1	$(0, 0.52\pi)$	Y
2	$(0.42\pi, 0.97\pi)$	Y	2	$(0.27\pi, 0.84\pi)$	Y
3	$(0.81\pi, 1.37\pi)$	Y	3	$(0.64\pi, 1.20\pi)$	Y
			4	$(1.03\pi, 1.58\pi)$	Y
			5	$(1.35\pi, 1.95\pi)$	Y
			6	$(1.59\pi, 2.15\pi)$	Y
Found gap?		Y ( $1.37\pi \sim 2\pi$ )	Found gap?		N
$\therefore$ Particle A: Free surface particle			$\therefore$ Particle B: In-domain particle		

(b)

Figure 3-3. (a) The arc boundary recognition method; (b) Example of angle list for particle A and B

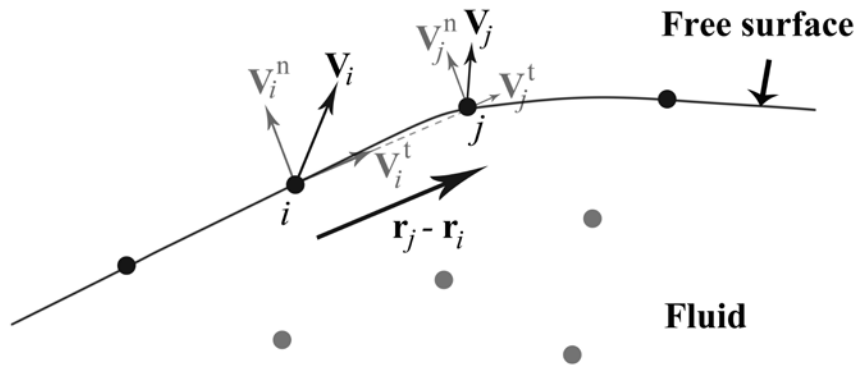


Figure 3-4. Incompressibility adjustment of free surface particles

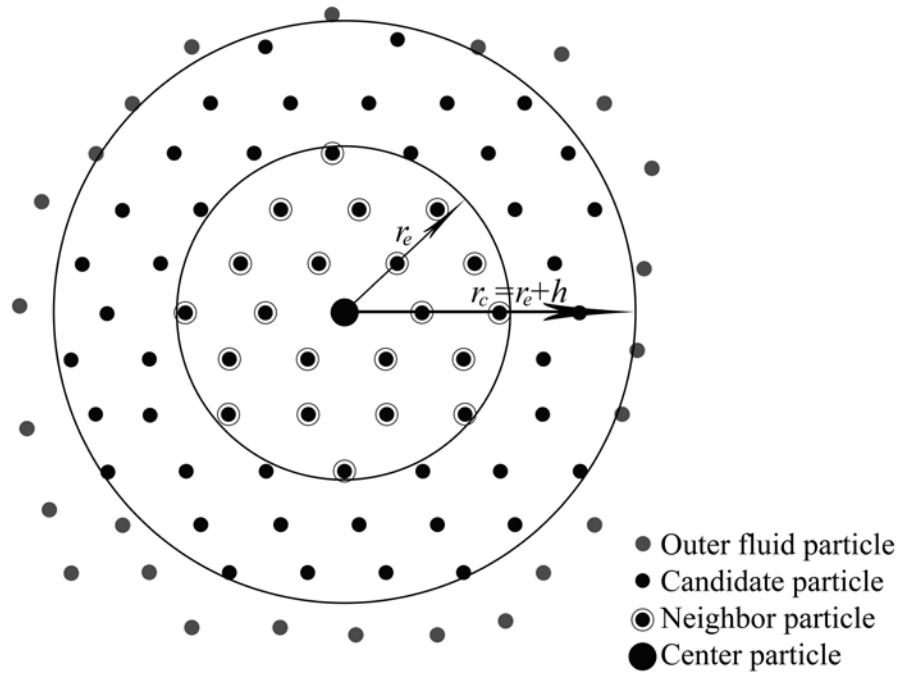


Figure 3-5. Candidate list and neighbor list generation

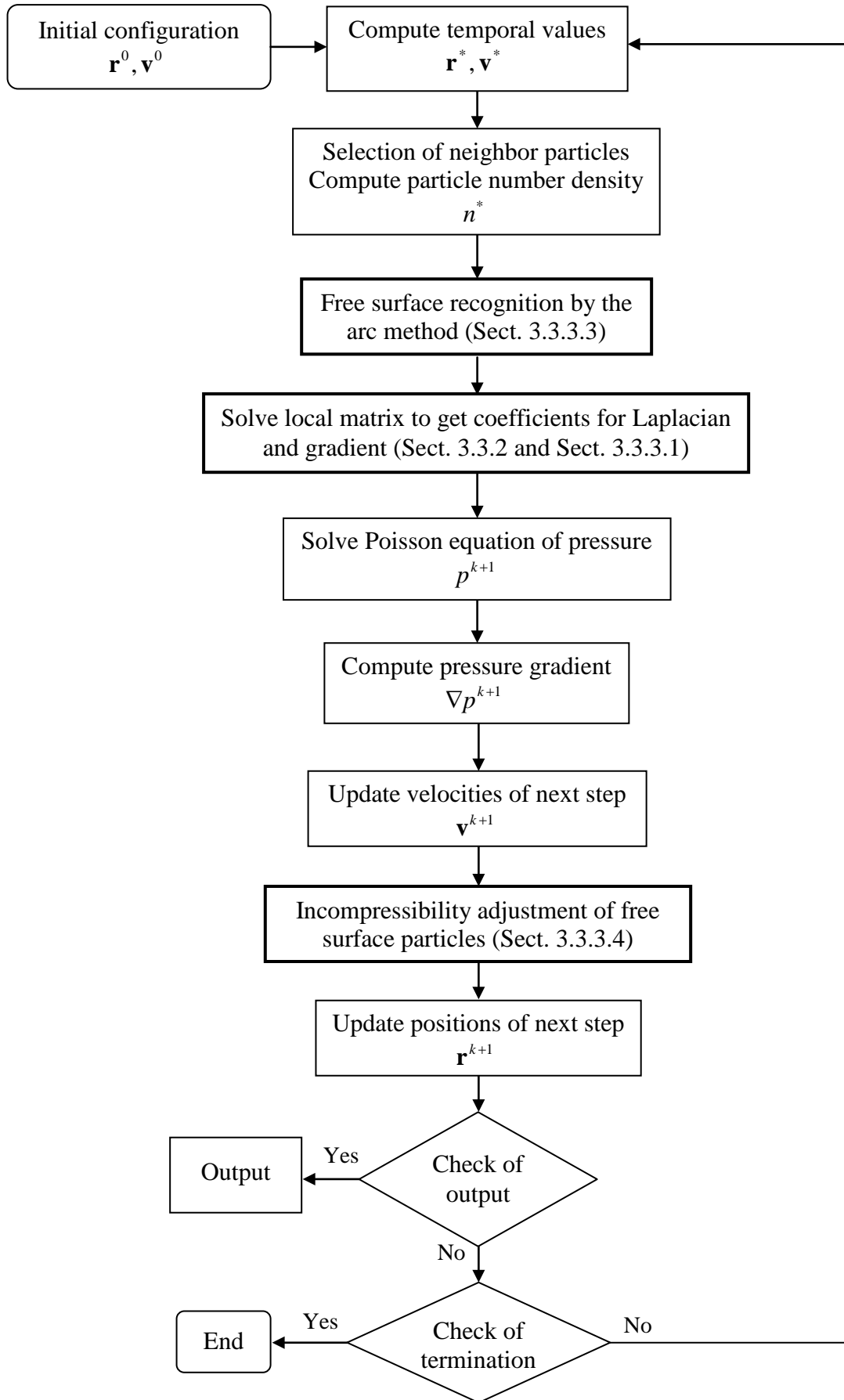


Figure 3-6. Flowchart of CPM

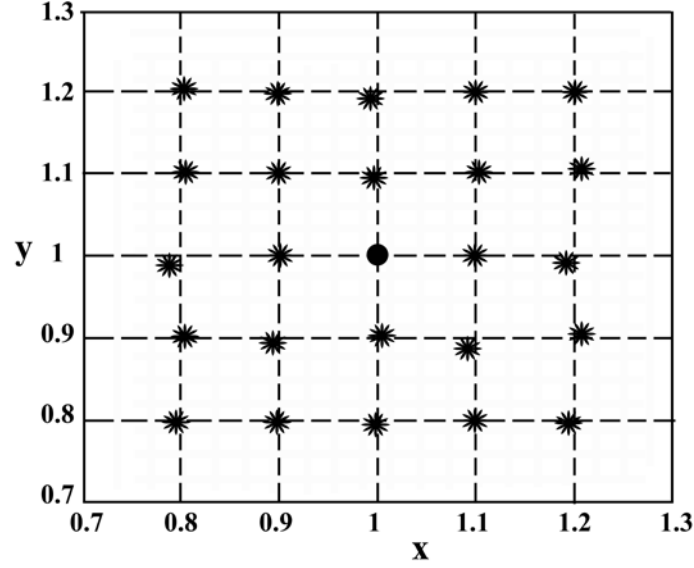
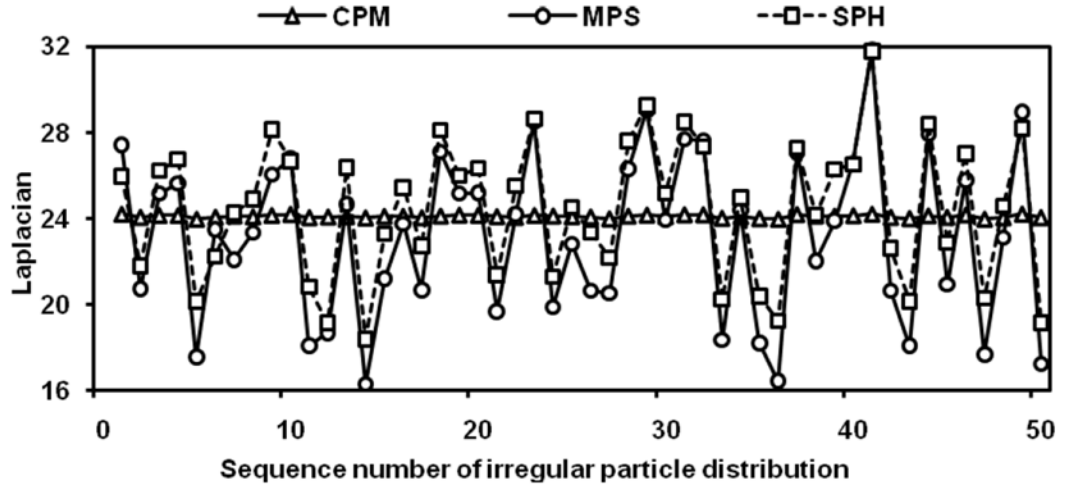
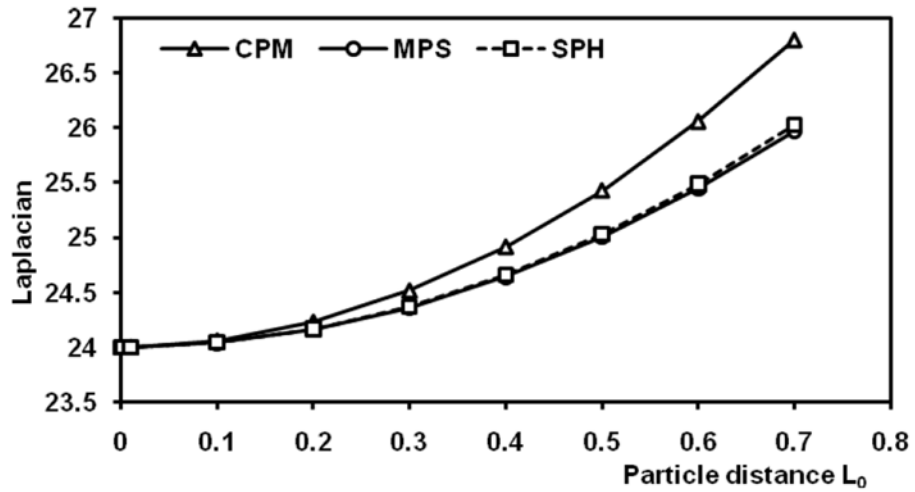
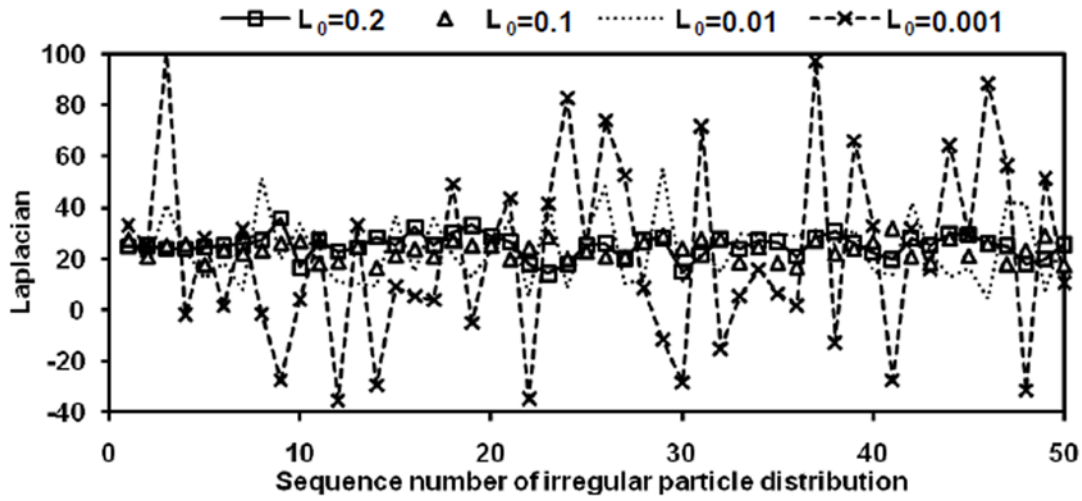
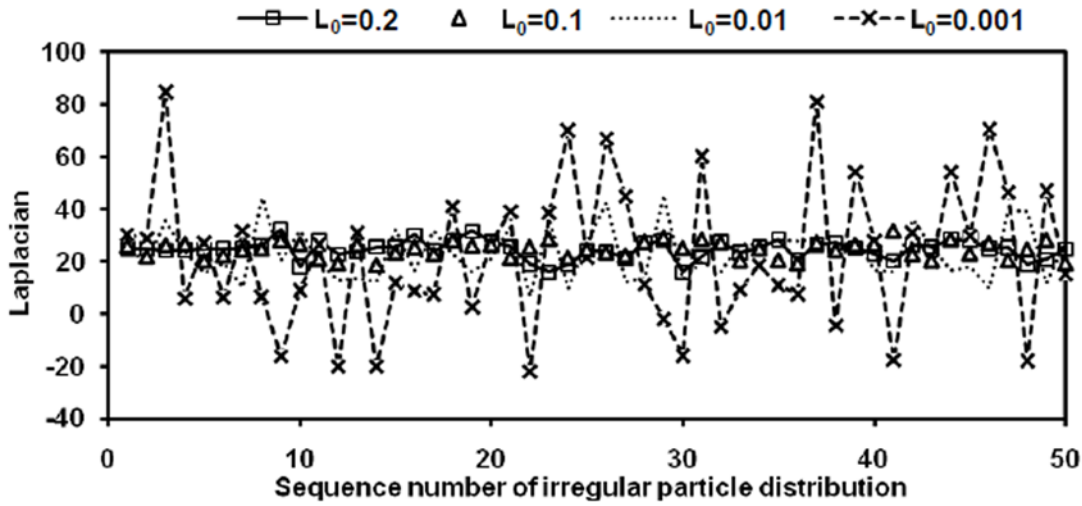
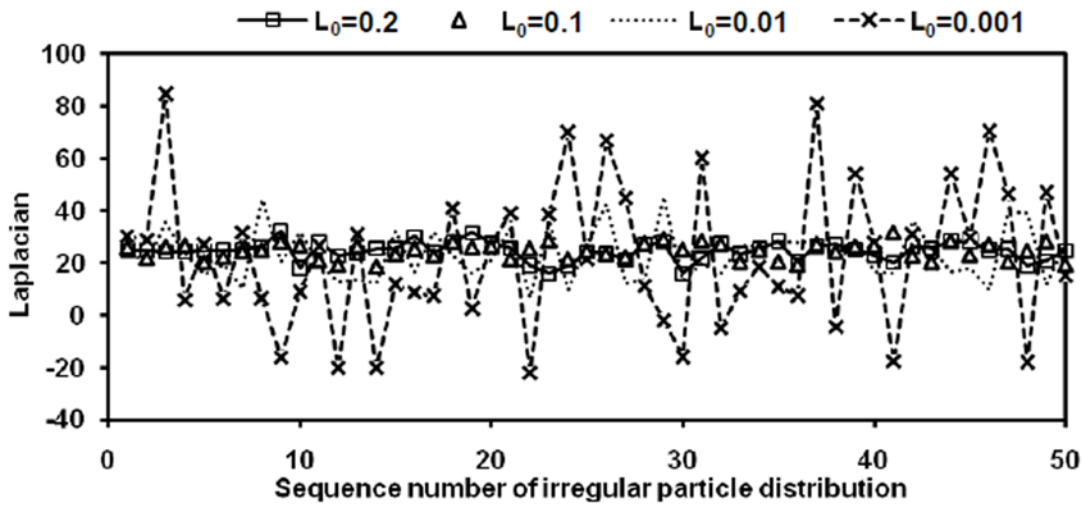

 Figure 3-7. A center point  $\bullet$  surrounded by 24 irregularly spaced points  $*$ 


Figure 3-8. Comparison of Laplacian using CPM (Eq. (3-31)), MPS (Eq. (3-16)) and SPH (Eq. (3-39))

( $L_0=0.1$ , Test function  $\phi(x, y) = x^4 + y^4$ )


 Figure 3-9. Convergence test of Laplacian for regular points (Test function  $\phi(x, y) = x^4 + y^4$ )

Figure 3-10. Convergence test of Laplacian in MPS for irregular points (Test function  $\phi(x, y) = x^4 + y^4$ )Figure 3-11. Convergence test of Laplacian in SPH for irregular points (Test function  $\phi(x, y) = x^4 + y^4$ )Figure 3-12. Convergence test of Laplacian in CPM for irregular points (Test function  $\phi(x, y) = x^4 + y^4$ )

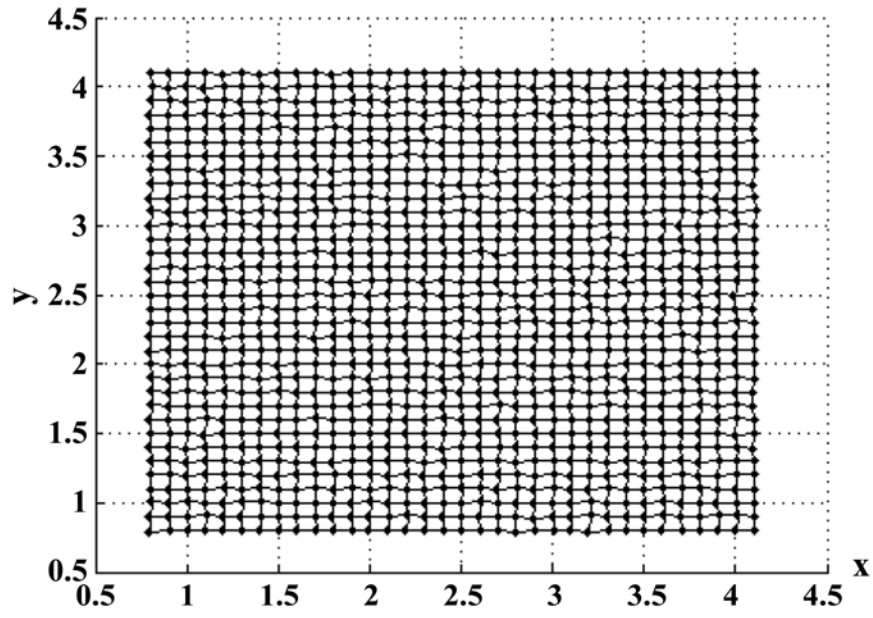


Figure 3-13. An example of irregular nodes (1156 in total) in  $x$ - $y$  domain  $[0.8, 4.2] \times [0.8, 4.2]$

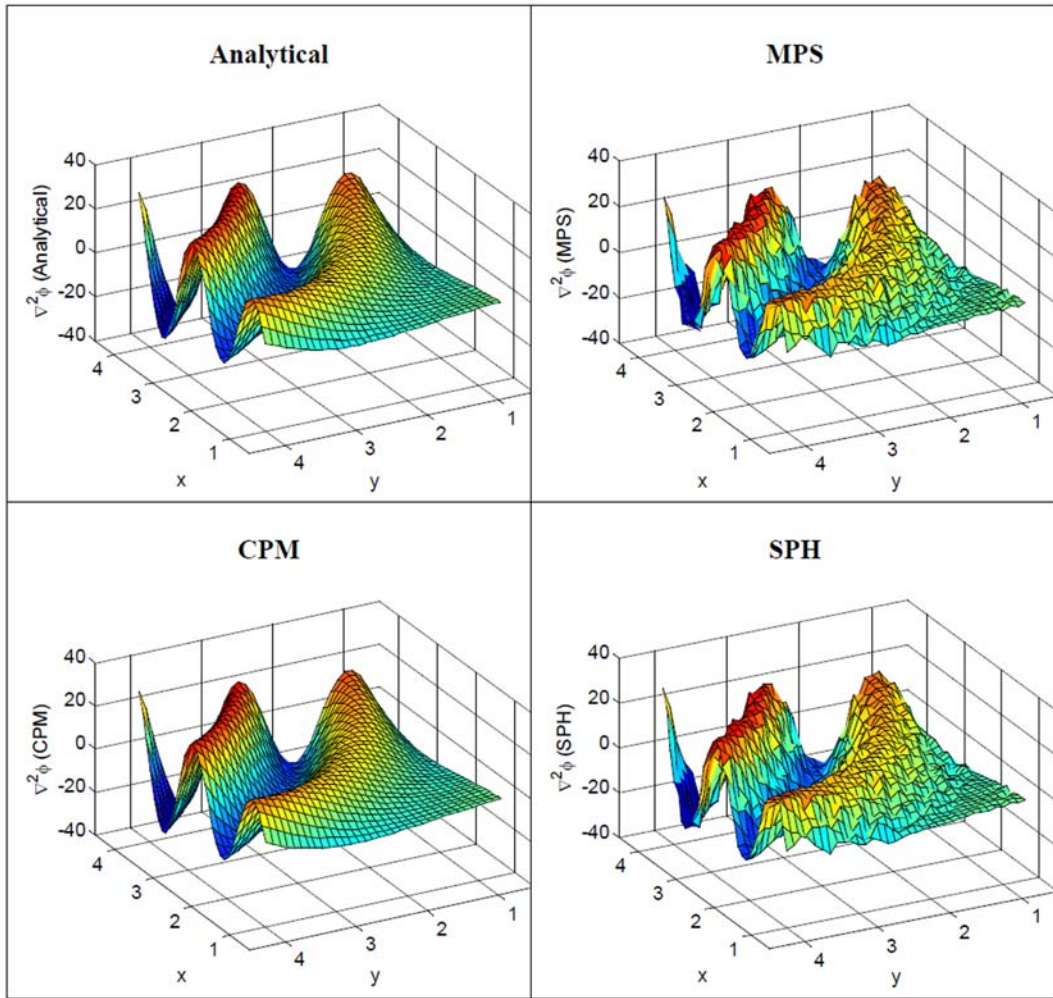


Figure 3-14. Analytical and numerical result of Laplacian (Test function  $\phi(x, y) = \sin(xy)$ )

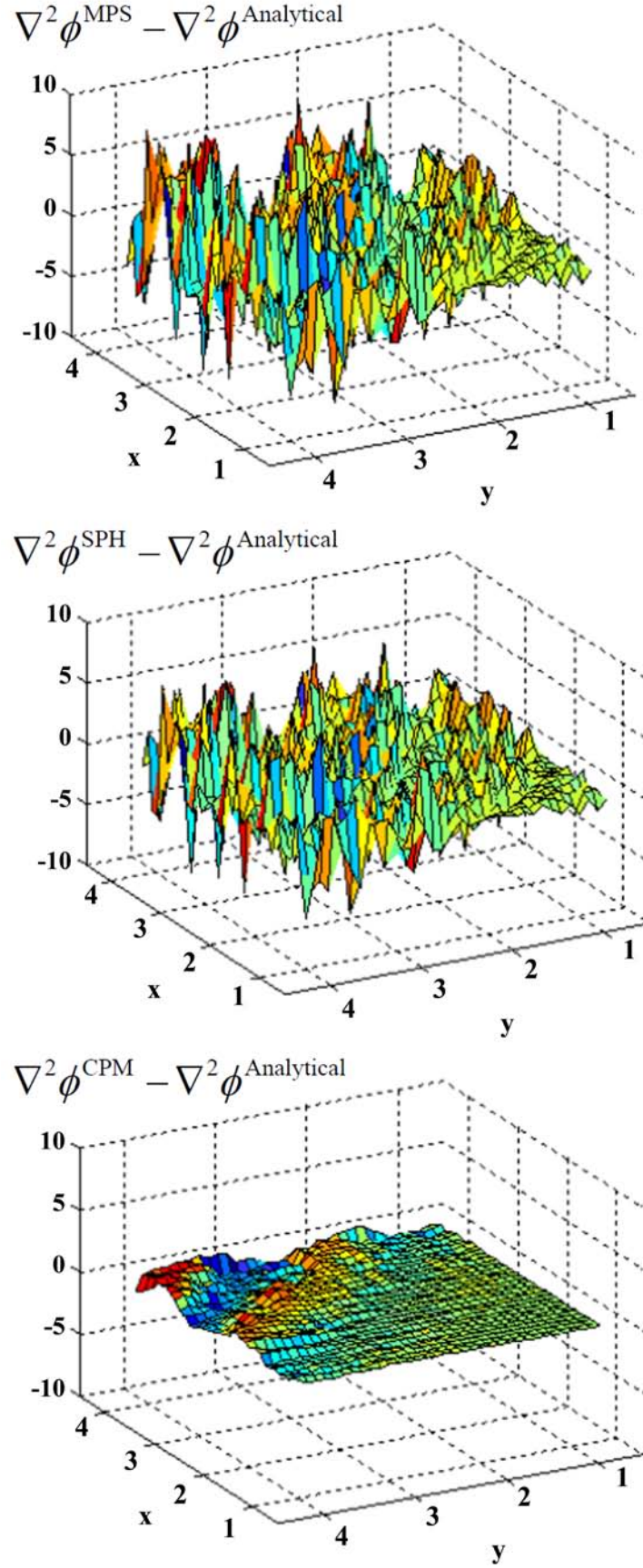


Figure 3-15. Difference of Laplacian values with analytical result (Test function  $\phi(x, y) = \sin(xy)$ )

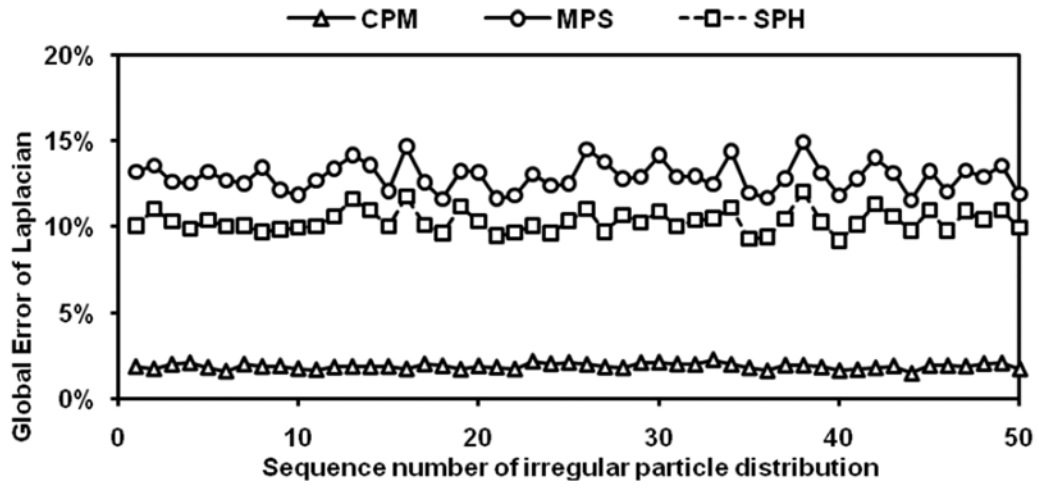


Figure 3-16. Error of Laplacian of different numerical algorithm (Test function  $\phi(x, y) = \sin(xy)$ )

## **Chapter 4 Numerical Simulation of Incompressible Free Surface Flows by CPM**

### **4.1 Introduction**

The CPM formulation presented in Chapter 3 is applied in numerical simulation of free surface flow problems in this chapter. Two benchmark examples, i.e. pressure computation in static tank and dam breaks in tank, are studied using CPM. Comparison of CPM simulation results with MPS solutions is made in terms of free surface motion and pressure contours. A parametric study is performed to investigate the effects of different parameters used in CPM, such as the influence radius, least-square weighting function and initial particle distance. In CPM, the discretization of the governing equation is realized by the derivatives which are solved from the equation based on Taylor series. The weighting function used in the weighted least-square solution of the derivatives plays an important role in the stability and accuracy of the proposed method. Three types of weighting functions are investigated. An investigation of computational cost is performed following the parametric study. Thereafter, different types of free surface flows are investigated and simulated using the proposed CPM. More numerical examples are presented to show the capability of the numerical algorithm and compare the results with published numerical and/or experimental results. Both the MPS and CPM results are generated by the author except some results with given references. All the numerical examples studied in this chapter are summarized in Table 4-1.

## 4.2 Benchmark examples

### 4.2.1 Hydrostatic pressure in a static tank

Water in a static rectangular tank is the simplest free surface problem that can be used to validate the performance of numerical algorithm since the velocities and hydrostatic pressures of all the water particles are known. Starting from assumed initial particle distribution, the two-step dynamic solution algorithm proposed in Chapter 3 is used to simulate the variation of the particles in a static tank without excitation. The velocities of the particles should approach to zero and the pressure of particles is constant hydrostatic pressure when static equilibrium is achieved. In order to check the accuracy of the pressure variation in the MPS method and CPM, the pressure value at a fixed point is computed. The case was first studied by Khayyer and Gotoh (2008) to show the ability of their proposed corrected MPS algorithm. Their results are presented here for comparison.

Figure 4-1 shows a schematic view of the problem and the particle distribution in the initial position. The dark color solid particles represent the fixed particles (solid wall and dummy particles) where velocity is zero. The light color hollow particles are the fluid particles. The water depth considered is 0.3 m. The pressure at a particle (point A in the figure) located at the bottom of the tank is recorded. The initial particle distance is 0.015 m and totally 41x 20 fluid particles are used in the simulation.

The time history of hydrostatic pressure at point A obtained by the MPS method is shown in Figure 4-2. It can be seen that there is a significant pressure fluctuation even in a static water tank. The fluctuation of pressure is so significant that the real pressure history cannot be observed. The same observation and findings has been

reported by Khayyer and Gotoh (2008) for the original MPS method with water depth 0.2 m. The time history of hydrostatic pressure of their results is shown in Figure 4-3. They proposed a corrected MPS algorithm (CMPS) to ensure the momentum conservation of particles and showed that the CMPS reduced the pressure fluctuation, as shown in Figure 4-3. In their more recent work (Khayyer and Gotoh, 2009), the algorithm is further revised by introducing a new source term (MPS-HS) for the Poisson pressure equation and allowing slight compressibility (MPS-WC). Figure 4-4 shows the time history of hydrostatic pressure at point A with these improvements in the work of Khayyer and Gotoh (2009). Although the fluctuation of pressure history is reduced with the combination of these improvements (Figure 4-4), the pressure fluctuation does not vanish especially when large amplitude particle motion appears.

The hydrostatic pressure in the static tank is studied by CPM and the time history of hydrostatic pressure at point A is shown in Figure 4-5. The dashed line represents the pressure solution of CPM. It can be seen in the figure that the solutions using CPM agree very well with the theoretical solution. In contrast, large pressure fluctuation is observed in the original MPS method. The pressure fluctuation problem is eliminated in CPM without resorting to relaxing incompressibility condition or introducing any artificial source term.

Figure 4-6 shows the particle positions of the fluid domain at  $t=5$  s using MPS method and CPM. The fluid particles simulated by the MPS method show uneven distribution especially near the free surface. This is due to its inability to satisfy the incompressibility condition for the free surface particles.

Figure 4-7 shows the comparison of the hydrostatic pressure field at the same time instant. The MPS method presents incorrect pressure field where some particles

with zero pressure (in dashed circle) appear inside the fluid domain. In the CPM simulation, the pressure field is generally smooth and presents a good solution of hydrostatic pressure which increases linearly with respect to the particle depth.

#### 4.2.2 Dam break with $d / L_w = 2$

A schematic view of the problem and initial particle distribution is shown in Figure 4-8. It is a 2D simplification of water dam. The water located on the left is kept still initially by the dam as a barrier. Once the barrier is suddenly removed at  $t=0$  s, the water collapses and starts to flow along the tank bottom. The example was solved by Koshizuka and Oka (1996) both experimentally and numerically by the MPS method. Later it became a benchmark problem to test the validity of Lagrangian formulation in fluid flows. In this section, the results obtained using the MPS method proposed in 2D domain are firstly presented. Viscosity and surface tension effects are neglected.

The geometry ratios of the initial water depth over width and tank length are  $d / L_w = 2$  and  $d / L_T = 0.5$ , where  $d$  is the water depth and  $L_w, L_T$  are the water width and tank length. In this example, the water column is represented by  $18 \times 36$  particles with initial particle distance 0.008 m and the time step is 0.001 s.

Figure 4-9 shows MPS solution of the particle positions at different time instants. Water runs onto the bottom surface until near 0.3 s when it impinges on the right vertical wall. Breaking waves appear at about 0.6 s. As can be seen in the figure, the MPS solution is in very good agreement with the experimental results in the change of free surface profile with time.

Although the flow profile of dam break process is well simulated by MPS method, the pressure field is not. Figure 4-10 shows that the pressure field is not smooth at some time instances. Particles with zero pressure are detected not only on the free surface but also (incorrectly) inside the fluid domain. For example, as we can see in Figure 4-10, some particles inside the fluid domain has low pressure at time  $t=0.2$  s,  $0.5$  s and  $0.9$  s (dark particles in dashed circle) and are recognized falsely as free surface particles for which pressure is set to be zero according to the criterion in Eq. (3-19). Hence, the pressure contours at these time instants are not accurate any more. Furthermore, by checking the pressure values of all the fluid particles, we found that negative pressure value appeared at some time instant. This causes large pressure fluctuation inside the fluid domain.

In contrast, the particle distribution and pressure solutions using CPM are shown in Figure 4-11 at various time instants. The agreement with the experimental results in Figure 4-9 both in the shape of the free surface and time development is excellent. The pressure contours using the CPM method are shown to be much smoother than the MPS solution in Figure 4-10. No zero pressure solution appears inside the fluid domain. This mitigates pressure fluctuation inside the fluid domain.

### **4.3 Parametric study of CPM**

There are several parameters in CPM which affect the stability and accuracy of the simulation results. The first one is the weighting function used in the weighted least-square solution of the derivatives based on Taylor series. Different least-square weighting functions have been proposed (Gavete et al., 2003) and applied in the simulation of problems such as solid mechanics and steady flows. The influence of the weighting functions in free surface flows used in CPM is studied in this section.

Three different weighting functions are analyzed in the study of a simple dam collapse example. Other parameters such as particle size (or initial particle distance) and influence radius are also important in the proposed scheme. The effects of these parameters will also be investigated in this section through the dam break example in Sect. 4.2.2.

#### 4.3.1 Influence of weighting functions in weighted least-square solution

In the solution of the derivatives based on Taylor series, a weighted least-square approach is used. The weighting function used in Eq. (3-25) mainly helps to reduce the distance effect of the particles since Taylor series expansion assumes the particles involved are close. When the distance of the particles used in the Taylor series expansion is too large, the accuracy of the second-order approximation decreases. Hence, it is reasonable to give less weight for particles further away in the least-square solution of Eq. (3-26).

As discussed by researchers who use weighting function in GFD method for the same purpose, the stability of the algorithm is affected by the weighting coefficients in the weighted least-square solution of the derivatives. We will investigate three different weighting functions in CPM: the quartic spline and cubic spline functions used by Gavete et al. (2003), and inverse distance weighting coefficients proposed by Liszka and Orkisz (1980). They are listed as below.

*Quartic Spline* (Gavete et al., 2003)

$$w(r) = \begin{cases} 1 - 6\left(\frac{r}{r_e}\right)^2 + 8\left(\frac{r}{r_e}\right)^3 - 3\left(\frac{r}{r_e}\right)^4 & r \leq r_e \\ 0 & r > r_e \end{cases} \quad (4-1)$$

*Cubic Spline* (Gavete et al. 2003)

$$w(r) = \begin{cases} \frac{2}{3} - 4\left(\frac{r}{r_e}\right)^2 + 4\left(\frac{r}{r_e}\right)^3 & 0 \leq r < 0.5r_e \\ \frac{4}{3} - 4\left(\frac{r}{r_e}\right) + 4\left(\frac{r}{r_e}\right)^2 - \frac{4}{3}\left(\frac{r}{r_e}\right)^3 & 0.5r_e \leq r < r_e \\ 0 & r > r_e \end{cases} \quad (4-2)$$

*Inverse distance* (Liszka and Orkisz, 1980)

$$w(r) = \begin{cases} \frac{1}{r^3} & r \leq r_e \\ 0 & r > r_e \end{cases} \quad (4-3)$$

All the three weighting functions are summarized in Table 4-2 and compared in Figure 4-12. The effects of the three different weighting functions in CPM are investigated using the same dam break example as in Sect. 4.2.2. A total of 18 x 36 fluid particles are used in the model. The initial particle distance is  $L_0=0.008$  m and the radius of influence is selected as  $r_e = 2.5L_0$ .

The CPM solutions using the three least-square weighting functions are shown in Figure 4-13. Agreeable wave profiles and smooth pressure contours can be obtained using all these weighting functions. It is shown that the water profiles using cubic spline weight function progress slightly faster than the experimental results, while the solutions using quartic spline and inverse distance weighting functions agree well with the experiments.

A sensitivity analysis is performed on the weighting functions, where the proportion of number of free surface particles to the total fluid particles ( $N_f$ ) is plotted in Figure 4-14. It can be seen that both the cubic spline and the inverse distance weighting functions can produce stable results. The proportion of free surface particles increases from less than 10% in the beginning of dam break to about 35%

when breaking wave occurs and gradually becomes stable at about 10%. When the quartic spline weighting function is used, the number of free surface particles at some time instants from 0.6 s to 1 s is abnormally high (up to more than 60% of total fluid particles). This means that high fluctuation occurs so that most of the fluid particles are recognized with zero pressure value. However, the fluctuation is suppressed after 2 s and the method still can run until the liquid calms down to be a tank of static liquid.

By comparing the results of three weighting functions in Figure 4-13 and Figure 4-14, we found that the inverse distance weighting function is preferred. The time history of the total number of free surface particle is smooth even when water hits the tank wall and breaking occurs. The reason may be that the inverse distance weighting function preserves a sharper increase when the particle distance decreases, while the weights computed with quartic and cubic spline weighting functions increase much more slowly when particle distance decreases (see Figure 4-12). Hence, very close particle distance or even particle overlap is less likely to happen when the inverse distance weighting function is used. In the subsequent numerical examples, the inverse distance weighting function is therefore used.

#### **4.3.2 Influence of influence radius**

Influence radius  $r_e$  is another important parameter used in CPM. It cannot be too small, otherwise not enough particles are included to obtain the solutions of derivatives. Since in Eq. (3-27) five unknowns are to be determined for the center particle, at least 5 neighbor particles are need. However, the distribution of the five particles may not be satisfactory to avoid ill-conditioned matrix. Therefore more than five particles are included for a stable and convergent solution. The influence radius

cannot be too big either. One reason is that it will increase the computational cost in solving the derivatives from Eq. (3-27). Another important reason is that if  $r_e$  is too large, particles far away are unnecessarily included in the truncated Taylor series expansion which assumes small distance from the center particle.

A sensitivity analysis is performed on the influence radius and the results of the number of free surface particles are shown in Figure 4-15. The minimum influence radius for regularly distributed particles should be  $\sqrt{2}L_0$  because it guarantees minimum particle numbers needed in the solution of the five unknowns. Hence in this study we investigate the different influence radii from  $1.5L_0$  to  $3.1L_0$ . It can be seen in the figure that, numerical instability occurs when the influence radius is  $1.5L_0$ . In this case, the number of free surface particles increases suddenly to a very high number at about 0.2 s when the fluid has not hit the wall yet. In contrast, the number of free surface particles is stable for influence radius from  $1.6L_0$  to  $3.1L_0$ .

Figure 4-16 indicates the location of leading edge of the collapsed water with time using different influence radius. Experimental results presented by Hirt and Nichols (1981) and published numerical solution using Lagrangian FEM by Ramaswamy and Kawahara (1987) are also plotted in the same figure for comparison. It can be seen that, the CPM solution for leading edge of water using influence radius  $1.6L_0$  is slightly slower than the experimental result, while the solution using  $3.1L_0$  is slightly faster than the experimental result. The CPM solutions of leading edge using influence radii from  $1.8L_0$  to  $2.5L_0$  are in good agreement with the experimental results by Hirt and Nichols (1981). Hence, the influence radius needs not be too large

due to the reasons mentioned before. In the later numerical examples in this thesis, either  $2.1L_0$  or  $2.5L_0$  will be used.

### 4.3.3 Influence of particle sizes

In particle methods, the solution domain is represented by particles. The initial particle distance or the so-called “particle size”, is another parameter that needs to be studied. The particle size is, to some extent, the same as the mesh size in mesh-based method. The particle size should not be too large since too few fluid particles will result in an inaccurate representation of liquid motion in the simulation. In theory, the more particles used in representing the domain, the better accuracy of simulation results may be obtained. However, the computational cost increases correspondingly. Therefore, a reasonable particle size should be selected depending on the severity of liquid motion.

In this section, a sensitivity study on the particle size is performed in CPM in terms of the number of free surface particles. As shown in Figure 4-17, five different particle sizes are used in the simulation, which are  $L_0=0.004$  m, 0.006 m, 0.008 m, 0.012 m and 0.016 m respectively. It is expected that decreasing the particle size will result in an increase of the total number of the fluid particles. Hence the number of free surface particles is normalized with respect to the total fluid particles. It is shown in Figure 4-17 that, all the four particle sizes used in the simulation generate stable results. The variations of proportions of free surface particles with time using particle size from 0.004 m to 0.008 m show similar results. When particle size 0.012 m and 0.016 m are used, the proportions of free surface particles are higher than other cases. This means that large particle size presents inaccurate representation of the liquid motion, with large portion of particles recognized as free surface.

The profiles of dam break process using four different particle sizes are shown in Figure 4-18 for different time instants. In the left-most column, solution based on the particle size 0.016 m is too large to capture the detailed wave profile. It is shown that the liquid motion is well represented using the particle size  $L_0 = 0.004$  m. The profile of liquid motion is very similar to the solution based on a smaller particle size  $L_0 = 0.003$  m.

We can conclude that for the dam break case in this study, the particle size  $L_0 = 0.004$  m can be selected as a reasonable value. For other cases with different geometries and liquid motion types, a similar convergence study performed here is needed to help make a choice of suitable particle size. A relatively large particle size should be used first to examine the overall liquid motion. A refined particle size will then be used to model the details of changing free surface profile.

#### 4.3.4 Influence of time step

Similar to the MPS method, a two-step predictor-corrector algorithm is used to solve the governing equation. The time step is controlled by the CFL condition shown in Eq. 3-11. In this section, the choice of time step is studied and discussed by using the same dam break example.

The particle size  $L_0 = 0.004$  m is selected here according to previous section. The maximum fluid velocity  $V_{\max}$  can be estimated as (Lee et al., 2008)

$$V_{\max} = 2\sqrt{gH}$$

where  $H$  is the initial water height. From Eq. 3-11 we can obtain the maximum time step is about  $\Delta t = 0.00025$  s.

Four different time steps are used in this study, which are 0.0002 s, 0.00025 s, 0.0005 s and 0.001 s. The dam break profiles using these time steps are shown in Figure 4-19 for the three time instants. It can be seen that when larger time step are used (0.0005 s and 0.001 s), the particle distributions at  $t=0.3$  s are not well simulated. The solutions diverge due to large particle motion at one time step. When the time step is selected according to the CFL condition in Eq. 3-11, the simulation results are very good. It is shown that the simulation results of water profiles using a smaller time step  $\Delta t=0.00015$  s are practically the same as those for  $\Delta t=0.00025$  s. But the computational cost using smaller time step is higher. Therefore the time step satisfying the CFL condition in Eq. 3-11 is selected in this research.

#### 4.3.5 Computational cost

Compared with MPS, the additional computational cost in CPM lies in the solution of derivatives based on local particle coordinates (See Sect. 3.3.2 and Sect. 3.3.3.1). The computational cost incurred in this operation needs to be investigated. Table 4-3 shows the CPU time per time step for the dam break example in Sect. 4.2.2 with different particle numbers ( $N$ ). The computer used is equipped with Pentium 4<sup>TM</sup> CPU (duo 3.6 GHz). The CPU times of three main operations are listed: generation of neighbor and candidate list ( $t_{\text{list}}$ , see Sect. 3.3.3.5), weighted least-square solving of derivatives ( $t_{\text{WLS}}$ , see Sect. 3.3.2), solving Poisson equation of pressure ( $t_{\text{PPE}}$ , see Sect. 3.3.3.1). The total time cost includes all operations in a time step ( $t_{\text{total}}$ ). The time fraction of the MPS method for four particle numbers is also listed for comparison.

The CPU time and fractions in Table 4-3 are plotted in Figure 4-20 for better presentation visualization of the results. It is shown that when the particle number is small, i.e.  $N=1095$ , the most time consuming part (35%) of CPM is the solving of

derivatives based on Taylor series. The list generation operation only takes up 13%. In MPS method, however, the list generation occupied 41% of the total time (Gotoh et al., 2005). With the increase of particle numbers, the time used in least-square solution of derivatives in CPM reduces from 35% to less than 10% while that of list generation increases from 13% to about 30% of the total time. It can be concluded that computational cost in the addition algorithm of solving derivatives based on local particle coordinates in CPM is not significant in problems requiring large particle number. The time used in solving Poisson equation of pressure in CPM increases with increasing particle number and becomes the dominant part of the total computational time when the particle number is large. This was also pointed out by Koshizuka et al. (1998) in the case of MPS method.

#### **4.4 Numerical simulation of free oscillation of liquid**

After the parametric study performed in the previous section, the CPM can be applied in simulation of various free surface flows. In general the motion of the free surface fluid flows can be classified as fluid motion without wave breaking and with breaking.

Many particle methods have been developed with emphasis on breaking waves, such as SPH, FPM and MPS. However these methods frequently suffer from difficulties in simulation of steady-state fluid motion even without breaking. The pressure fluctuation problem in these particle methods makes the solution unstable if long time simulation is performed, as demonstrated in Sect. 4.2.1 for MPS.

In this section, we will demonstrate the capability of CPM in simulation of fluid motion without breaking, i.e. free oscillation of liquid in a container with small

amplitude. The schematic view of the container used for the analysis is illustrated in Figure 4-21(a). A square liquid column of width  $b$  with initially a sinusoidal free surface profile in a rectangular 2D tank is fixed on ground. The initial velocities of the liquid particles are all zero. The analytical solution is available when the amplitude is small (Radovitzky and Ortiz, 1998). The case was studied by many researchers numerically (Ramaswamy et al., 1986; Ramaswamy, 1990; Radovitzky and Ortiz, 1998; Idelsohn et al., 2004). The initial free surface profile of the liquid column is as follows

$$\eta(x,0) = a \sin \frac{\pi}{b} x \quad (4-4)$$

The initial particle distribution is shown in Figure 4-21(b). In this example we use the same parameters as those adopted by Idelsohn et al. (2004). The initial amplitude of free surface is  $a=0.1$  unit and the square liquid column (in steady-state) is of width  $b=1$  unit. 50 x 53 fluid particles are used to model the water inside the tank. Viscosity is assumed to be negligible.

The time variation of the free surface elevation at  $x = -b/2$  is computed with the MPS method and CPM. The comparison of the free surface elevation with analytical results is plotted in Figure 4-22. The free surface elevation obtained using CPM agrees well with the numerical solution of Idelsohn et al. (2004) using PFEM. Compared with the analytical results, it is seen that both the two numerical solutions exhibit some numerical viscosity. This has been also discussed by Idelsohn et al. (2004). Furthermore, the solution of Idelsohn et al. (2004) using PFEM presents some phase difference compared with the theoretical results, as shown in the figure. In contrast, this phase difference in the solution using CPM method is smaller.

The solution of free surface elevation in the MPS method and CPM are compared in Figure 4-23. The MPS solution exhibits fluctuation after  $t=0.5$  s. After  $t=2$  s the fluctuation becomes so severe that the sinusoidal sloshing profile of free surface cannot be clearly identified. This shows that MPS method fails to produce long time simulation of the free oscillation of liquid.

Figure 4-24 compares the pressure fields at several time instants using MPS, CPM and analytical solutions. Compared with MPS, the CPM solution is much better in terms of free surface and agrees very well with analytical results. Before  $t=1.26$  s the MPS solution for free surface profile agrees with the CPM solution. However, after that the free surface profiles in MPS solution become “volatile”, which makes the recognition of free surface elevation difficult. The MPS solution of pressure contours shows poor performance. There are particles with inaccurate pressure inside the fluid domain in the MPS solution, whereas CPM gives smooth pressure solutions correctly. The drawback of the MPS method in the pressure solution makes it difficult to study the fluid motion for a long time simulation due to the pressure fluctuation problem.

More cases of fluid motion without breaking will be studied in Chapter 5, which focus on sloshing in moving rectangular tank.

## **4.5 Numerical simulation of violent fluid flows with breaking**

Study of violent free surface flow with wave breaking is a challenging problem in fluid dynamics. The fast changing free surface means that the geometry of the solution domain changes with time and the free surface after some time becomes discontinuous. The free surface may break in many parts, and some parts may join

together in one. The fragmentation and coalescence of fluid particles makes numerical simulation difficult especially for conventional mesh-based methods. For this reason many particle methods have been developed and applied in the study of such problems. The most well known ones are SPH and MPS. As discussed before, in conventional particle methods such as MPS, the solution of the pressure field is not satisfactory.

In this section, we will demonstrate the ability of the proposed CPM in modeling this kind of problem, especially with regards to improvement in pressure solutions.

#### **4.5.1 Free oscillation of liquid in a container with large amplitude**

The first case we considered is the same free oscillation of non-viscous water column but with larger initial amplitude. Upon oscillation, the waves may break. Linear analytical solution is not applicable for large wave amplitude.

The amplitude of the initial free surface is one third of the width of square water column in the tank. The same problem is studied by Idelsohn et al. (2004) using PFEM method. Their simulation result is presented here for comparison. In our simulation 39 x 39 fluid particles are used.

Figure 4-25 compares the CPM solution of wave profiles at several time instants with the PFEM solutions obtained by Idelsohn et al. (2004). The general free surface profiles are in good agreement. Breaking particles are captured in both solutions. Nevertheless, there is a large density variation in the PFEM solution of Idelsohn et al. (2004) in Figure 4-25 (a). This large density variation makes differentiation between breaking particles and non-breaking particles difficult and also affects the boundary particle recognition. The error in identifying the free surface particles would, in turn,

affect the pressure solution in the Poisson equation of pressure, thereby further deteriorating the accuracy of PFEM solution.

The CPM simulation solution is shown in Figure 4-25 (b). Breaking particles are observed in the third picture. Compared with the PFEM solution, the CPM solution does not present large density variation inside the fluid domain. As discussed before, this helps improve the simulation accuracy.

The pressure contours at the respective time instants for CPM in Figure 4-25 are shown in Figure 4-26. Again it is seen that the pressure distributions inside the fluid are smooth with no abnormal pressure values in the tank. The pressure field is well represented even when breaking particles appear.

In order to obtain more violent breaking phenomena, an even larger amplitude free oscillation example is investigated. The initial amplitude of free surface is  $a=0.6$  unit. A total of  $27 \times 27$  fluid particles are used. The CPM solution of pressure fields at different time instants is shown in Figure 4-27. It is shown that the larger initial amplitude produce more violent breaking particles from  $t=0.42$  s to 1.02 s. The pressure contours are smooth even when the breaking wave occurs. Furthermore, the free surface particles (with zero pressure) are accurately recognized in CPM. No spurious pressure value in the fluid domain is observed.

#### 4.5.2 Dam break with $d / L_w = 0.5$

To further demonstrate the performance of CPM in the pressure field solution for free surface flow with breaking, a larger dam break example with  $d / L_w = 0.5$  and  $d / L_T = 0.6 / 3.22 \approx 0.186$  is considered. This dam break example is based on an experiment performed by the Maritime Research Institute Netherlands (MARIN). A

schematic view of the example is shown in Figure 4-28. A large tank of 3.22 m in length is used with an open roof. A volume of water with 0.6 m in height and 1.2 m in length was released to flow at the initial time step.

Measurements were performed in the experimental study. As shown in Figure 4-28, four vertical wave probes were used to measure the water elevations at positions H1 to H4. One of the pressure sensors was located at position P1 to capture the pressure value at that point. Details of the experimental study can be found in the references (Fekken, 1998; Kleefsman et al., 2002).

In our numerical model, the initial particle distance is  $L_0=0.01$  m. The kernel size  $r_e = 2.5L_0$  and time step  $\Delta t=0.001$  s are adopted. Viscosity of the liquid is neglected. The animations of CPM simulation of the dam breaking wave profiles, pressure and vector fields are recorded in the attached CD with their respective file names “Dam\_marin\_w.avi”, “Dam\_marin\_p.avi” and “Dam\_marin\_v.avi”.

The water profiles obtained in CPM simulation at different time instants are shown in Figure 4-29. The water flows once the dam breaks at the initial time step and hits the right wall of the tank in less than one second. The water runs up along the right wall and then overturns and falls back ( $t=1.4$  s) before hitting the water body in the tank and generating a big splash ( $t=1.7$  s to  $t=2.1$  s). The splash falls into the tank and the water gradually calms down after that.

Figure 4-30 shows the time history of the computed pressure at point P1 using CPM superimposed on a scanned figure that presents the experimental result of MARIN and numerical solution by Fekken (1998). In the figure, the dashed line represents the experimental results. The pressure solution by CPM agrees reasonably

well with the experimental result before  $t=2$  s. In terms of agreement with the experimental results, the CPM solution is better than the numerical solution of Fekken (1998) who used the software ComFlow developed by MARIN. From  $t=2$  s to  $t=4$  s the pressure in CPM solution is higher than the experimental result.

There are two sharp pressure peaks in the pressure history, as shown in Figure 4-30. The first one occurs at about  $t \approx 0.7$  s when water from the collapsed dam hits the right wall. The second and higher peak appears at  $t \approx 1.5$  s when the overturned breaking wave falls and hits the remaining water body which then exerts additional pressure on the tank wall. Furthermore, there is a gentle peak at  $t \approx 3$  s when the overturned wave fully falls down to the tank bottom and induce a relatively large undulation of water. The undulation hence causes a pressure increase at point P1 due to the moderate water run-up around the wall. It is clear in the figure that, both these three peaks are successfully captured in CPM. In contrast, the numerical result by Fekken (1998) fails to capture the two peaks at  $t \approx 0.7$  s and  $t \approx 3$  s. The pressure contours at the occurrence of these three pressure peaks are shown in Figure 4-31, where high pressures around point P1 are observed.

Figure 4-30 also shows that there is some minor fluctuation of pressure value after water hits the right wall and falls back to water body. It is caused by the impact of breaking particles on wall or main water body. Some of the particles fly outside the solution domain and later fall back to the domain with big velocities. These particles will affect the local pressure distribution of the fluid particles when they fall down and re-join the fluid. This may be mitigated with some special treatment of the flying particles once they separate from the main solution domain. For example, a “particle slip” method is adopted by Losasso et al. (2008) in which ballistic particle threshold is

maintained to differentiate solitary particles that are far from the main fluid body and follow ballistic trajectories. Nevertheless in this study we do not focus on the breaking particles and thus no special action is taken.

Figure 4-32 shows the water heights computed by CPM at the four measure positions, and the results of MARIN and Fekken (1998) are again scanned for comparison. It is shown that, the computed water heights at the four positions in general agree well with the experimental results. The agreement is especially excellent before and long after the water hits the tank wall. During the impact of water on the wall or main water body, i.e. from  $t=1.5$  s to  $t=2.2$  s, some differences between the CPM solution and the experimental results are observed at points H1 and H2. It can be seen that the difference in the maximum height are less than 16% in CPM solution, while in the result of Fekken (1998) the difference is up to 42% at point H2. The agreement of our simulation results with experiments is thus much better than the numerical solution of Fekken (1998).

The water profiles with pressure contours are presented in Figure 4-33 for some representative time instants. It can be seen in the figure that the water hits the wall in less than one second after release from the dam. Large pressure occurs during the hitting of the water on the tank wall. Some water particles break away upon hitting the wall. Some particles roll up along the wall and then overturn and fall back to the main water body. The overturning wave generates high pressure in the fluid when hitting the fluid particles, as shown in the figure for  $t=1.5$  s. The pressure solution approaches hydrostatic pressure field after  $t=2.5$  s since then the water becomes gentle and gradually calms down.

The pressure contours shown in the figures are smooth without any zero pressure values inside the domain. The CPM is shown to be robust in simulation of the violent fluid motion even when the fluid motions are complicated including possible wave breaking. The capability of CPM shown in the numerical examples reveals the great potential of the proposed particle method in the study and simulation of problems in fluid dynamics.

The velocity fields after the dam break at different times in Figure 4-34 shows the fast changing flow motion. At  $t=0.5$  s the velocities of the particles at the left corner are relatively small while those of the particles at the front of the water are large. At  $t\approx 1.0$  s when the water hits the right wall, the vertical velocity components of the particles near the wall are large. From  $t=1.3$  s to  $t=1.5$  s overturning wave is observed, for which the velocity vectors of the particles exhibit the direction of the fluid motion. The overturning wave hits the main water body at  $t\approx 1.5$  s and water splash appears from  $t=1.7$  s to  $t=2.1$  s. Some local violent vortexes of the water are observed at  $t=3.1$  s and  $t=3.5$  s from the velocity fields. The water gradually calms down after  $t=3.5$  s. The velocity results obtained prove the good performance of CPM in the simulation of violent free surface problem with possible water breaking.

#### **4.5.3 Dam break with obstacle**

To further demonstrate the capability of the proposed CPM in simulation of the violent breaking waves, another dam break example is presented in this section. A more violent and complicated fluid motion is generated in this example, owing to the presence of an obstacle in the tank. The dam break examples with and without obstacle can be considered as a simple model of green water flow on the deck of a ship (Fekken, 1998; Lee et al., 2002; Greco et al., 2004; Lohner et al., 2006).

The example was studied experimentally by Koshizuka et al. (1995). A schematic view of the problem is shown in Figure 4-35. The tank geometry is the same as the case studied in Sect. 4.2.2. In addition, an obstacle block with geometry  $h \times 2h$ , where  $h = 24$  mm is used in the experiment, is located at the middle of the tank. The same problem was also studied by Larese et al. (2008) using the PFEM method. Their simulation results are presented here for comparison.

The initial particle distribution of water is shown in Figure 4-36. The initial particle distance  $L_0 = 0.0073$  m and totally  $36 \times 18$  fluid particles are used. The influence radius is  $r_e = 2.5L_0$  and time step is  $\Delta t = 0.0005$ . Viscosity of the liquid is neglected. The obstacle block is modeled as part of the rigid tank wall.

Figure 4-37 shows the water profiles at several time instants after the dam breaks. The left column shows the experimental results of the water profiles captured by camera (Koshizuka et al., 1995). The middle column shows the numerical results by Larese et al. (2008), who used the particle FEM method in their simulation. The right column of Figure 4-37 presents the simulation results by the proposed CPM.

The experimental results show that the water collapses and, at about 0.1 s, water hits the obstacle block, upon which the wave profile changes tremendously. The wave runs up to a high elevation upon impact with the obstacle block. The big water splash then hits the right wall and falls back to the right part of the tank. After that the water flows to the left and gradually calms down.

One can see in the figure that, the simulation results using CPM agree well with the experimental results and PFEM solutions until  $t=0.4$  s. After that, the numerical simulation results of the water profiles differ somewhat from the experiments. It is

shown in Figure 4-37 that, for the experimental results at  $t=0.5$  s, the water particles on the right side of the obstacle are higher than the obstacle. The numerical simulation results of both CPM and PFEM show that the particles fall down towards the tank bottom. The main reason is that there is air entrapped in the overturned waves in the experiment. Since only one fluid is modeled in the numerical simulation, air entrapment is not considered in either of the two numerical methods. However, in the real experiments, air entrapped inside the overturned wave slow the fall of water particles. Therefore a two-phase model is needed if numerical simulation is to be improved.

Nevertheless, the CPM results agree with the experimental results well after the main water body totally fall down to the tank. It can be seen that for  $t=1.0$  s the CPM solution agree with the experimental results much better than the PFEM solutions. The animation of CPM solution for this case is recorded in the attached CD with file name “Dambreak\_obstacle.avi”.

## **4.6 Concluding remarks**

In this chapter, six numerical examples are presented to examine the performance of CPM in simulation of different free surface flow problems.

In the benchmark examples, the MPS method present “volatile” free surface profiles and the solution of pressure field presents inaccurate result with zero pressure inside the fluid domain. In contrast, the CPM solution presents much smoother and accurate pressure contours without volatile free surface.

Different problems of free surface flows are investigated with the proposed CPM. The pressure field is successfully presented in the CPM. No severe pressure

fluctuation appears in the simulation of both gentle fluid motions without breaking and violent free surface flows when the fluid waves are complicated and with the possibility of breaking. The CPM solutions agree very well with published numerical and/or experimental results.

A parametric study is performed to investigate the effects of different parameters in CPM using the dam break example. It is found that the inverse distance weighting function is more suitable for the proposed CPM for better numerical accuracy. The influence radius  $r_e = 2.1L_0$  or  $2.5L_0$  can be used in the simulation of violent fluid motion. The initial particle distance should be chosen according to the geometry and fluid motion types of the specified problem to be studied. The computational cost of CPM is also investigated. It is found that the time used in the addition algorithm of solving derivatives based on local particle coordinates in CPM is not a significant portion when large particle numbers are used.

Table 4-1. Numerical examples studied in Chapter 4

Examples	Source of results and methods used for comparison	
	Source of result	Method
Hydrostatic pressure in a static tank	Khayyer and Gotoh (2008, 2009)	Improved MPS
Dam break with $d / L_w = 2$	Koshizuka and Oka (1996)	Experiment
Free oscillation of liquid with small amplitude	Idelsohn et al. (2004)	Analytical and PFEM
Free oscillation of liquid with large amplitude	Idelsohn et al. (2004)	PFEM
Dam break with $d / L_w = 0.5$	Fekken (1998)	Finite volume method +improved VOF
Dam break with obstacle	Koshizuka et al. (1995) Larese et al. (2008)	Experiment PFEM

Table 4-2. Parameters used in the study of the effect of least-square weighting function

Cases	1	2	3
Weighting function	Eq. (4-1)	Eq. (4-2)	Eq. (4-3)
$r_e$	$2.5 L_0$	$2.5 L_0$	$2.5 L_0$
$L_0$	0.008 m	0.008 m	0.008 m

Table 4-3. CPU time (s) and fraction per time step in CPM

$N$	$t_{List}$ (fraction)		$t_{WLS}$ (fraction)		$t_{PPE}$ (fraction)		$t_{Total}$ (fraction)	
	CPM	MPS	CPM	MPS	CPM	MPS	CPM	MPS
1095	0.052 (0.13)	(0.41)	0.135 (0.35)	/	0.098 (0.25)	(0.07)	0.389 (1)	(1)
1743	0.310 (0.28)	(0.31)	0.236 (0.22)	/	0.338 (0.31)	(0.16)	1.094 (1)	(1)
3471	0.987 (0.30)	(0.30)	0.593 (0.18)	/	1.203 (0.37)	(0.33)	3.275 (1)	(1)
5775	2.960 (0.29)	(0.28)	0.970 (0.09)	/	5.350 (0.52)	(0.49)	10.266 (1)	(1)
9000	9.500 (0.28)		3.050 (0.09)	/	20.01 (0.58)		34.322 (1)	
10730	13.013 (0.26)		4.508 (0.09)	/	29.595 (0.60)		49.530 (1)	



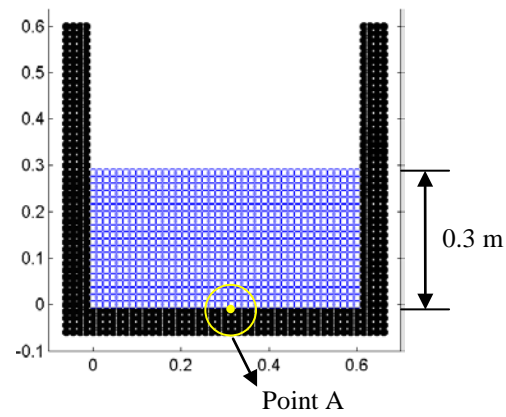


Figure 4-1. Schematic view of the initial particle distribution for static water tank

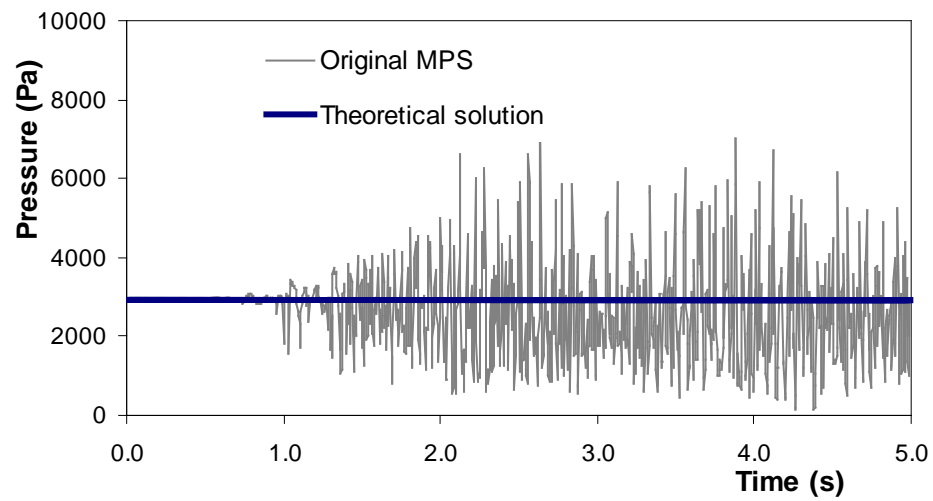


Figure 4-2. Time history of hydrostatic pressure at point A by MPS

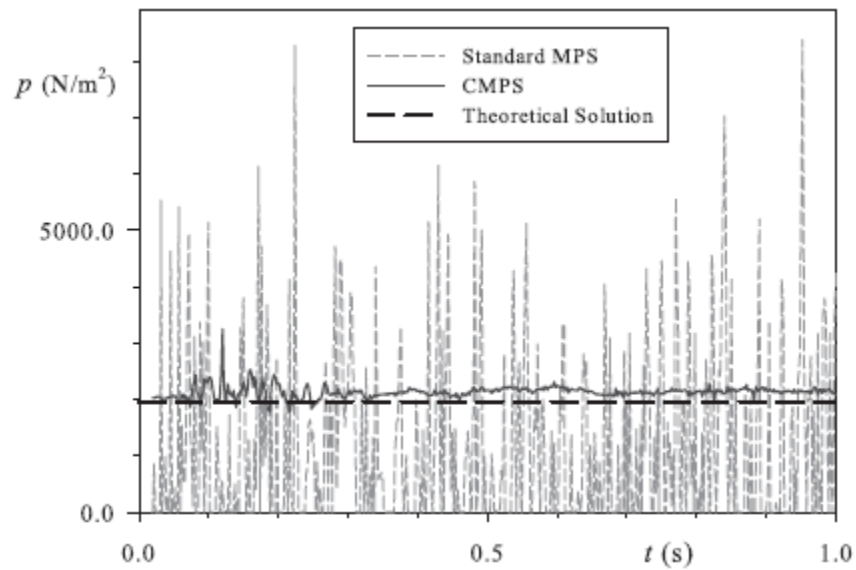


Figure 4-3. Time history of hydrostatic pressure at point A with  $d=0.2$  m scanned from Khayyer and

Gotoh (2008)

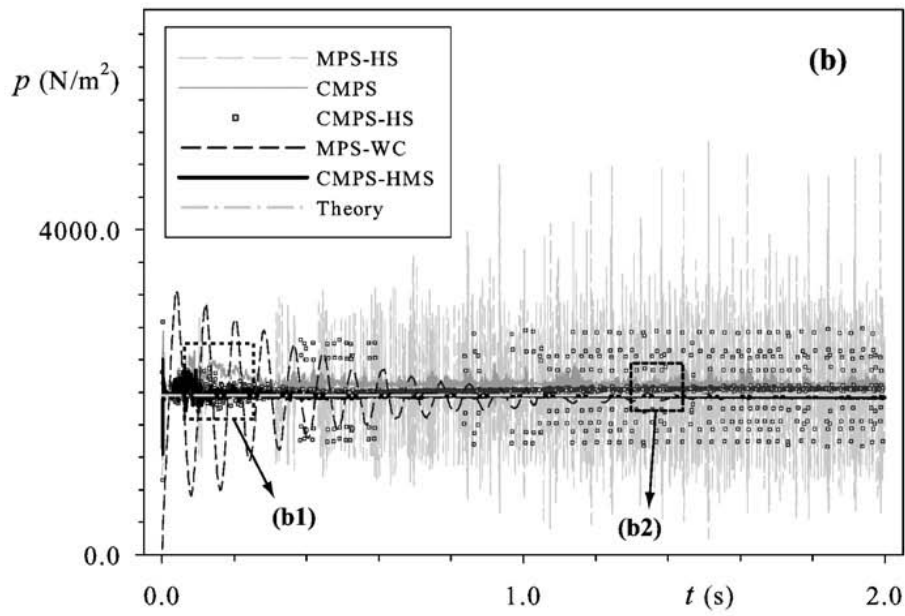


Figure 4-4. Time history of hydrostatic pressure at point A with  $d=0.2$  m scanned from Khayyer and Gotoh (2009)

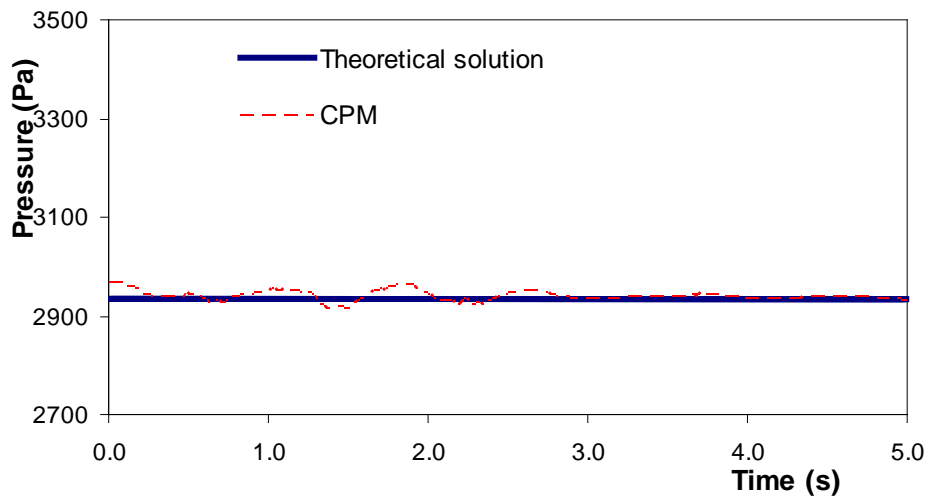


Figure 4-5. Comparison of time histories of hydrostatic pressure at point A

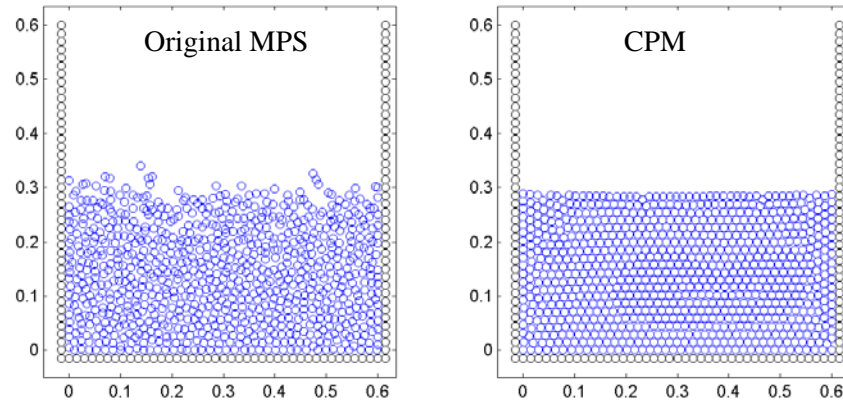


Figure 4-6. Particle distribution at  $t=5$  s.

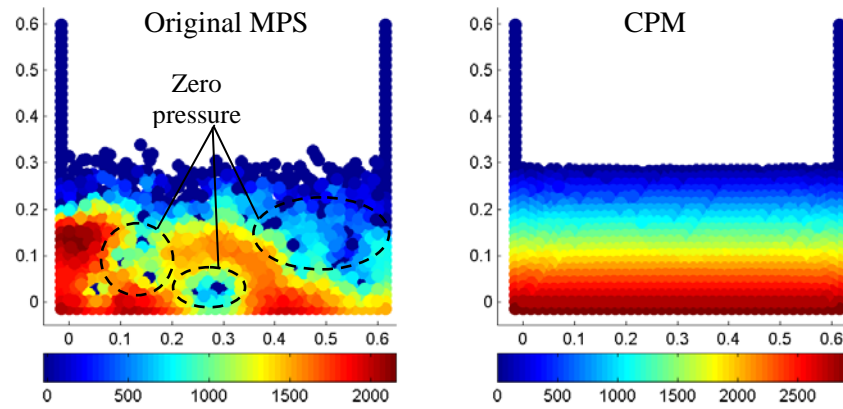


Figure 4-7. Hydrostatic pressure field of the whole tank of water at  $t=5$  s

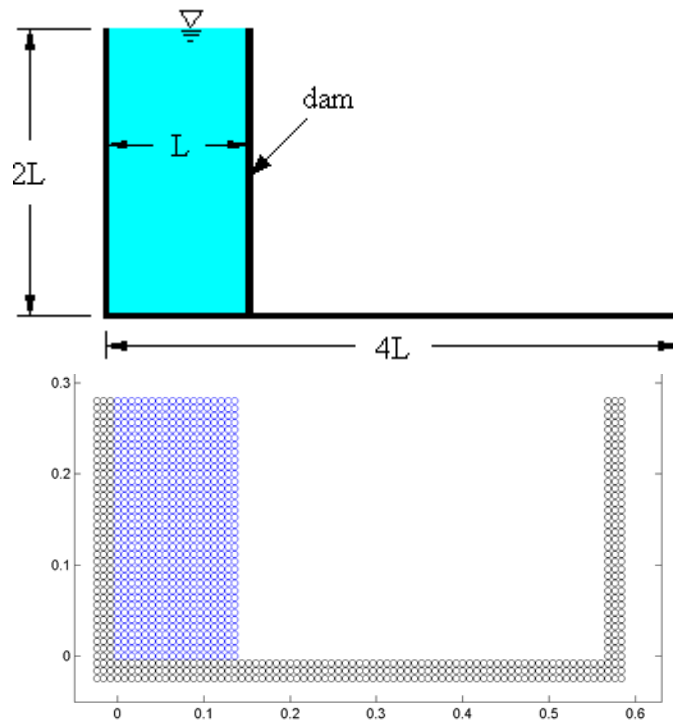


Figure 4-8. Geometry and initial particle distribution of the dam break example

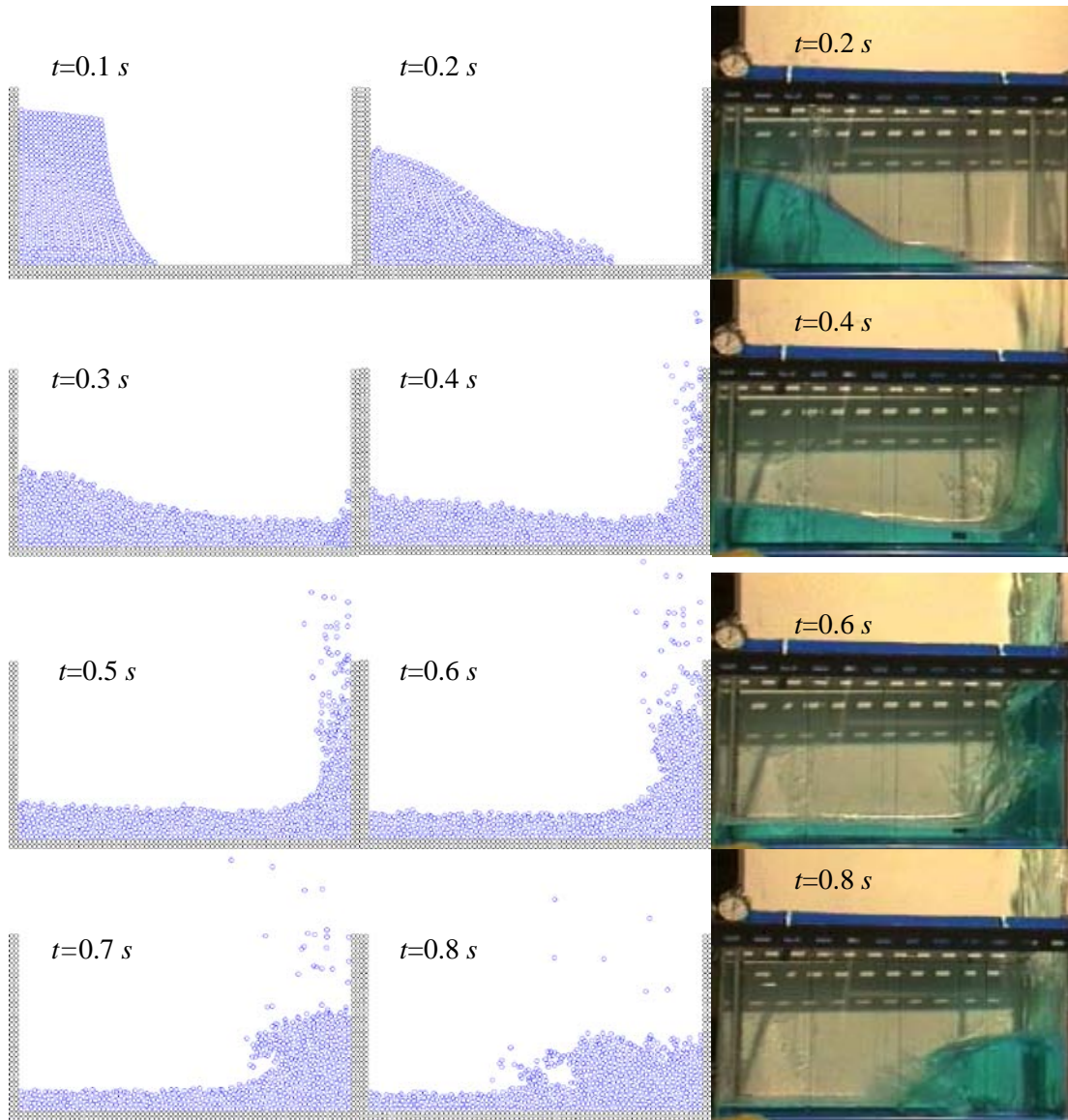


Figure 4-9. Comparison of dam break simulation using MPS with experimental results

Left two Columns: numerical results by MPS; Right Column: experiments (Koshizuka and Oka, 1996)

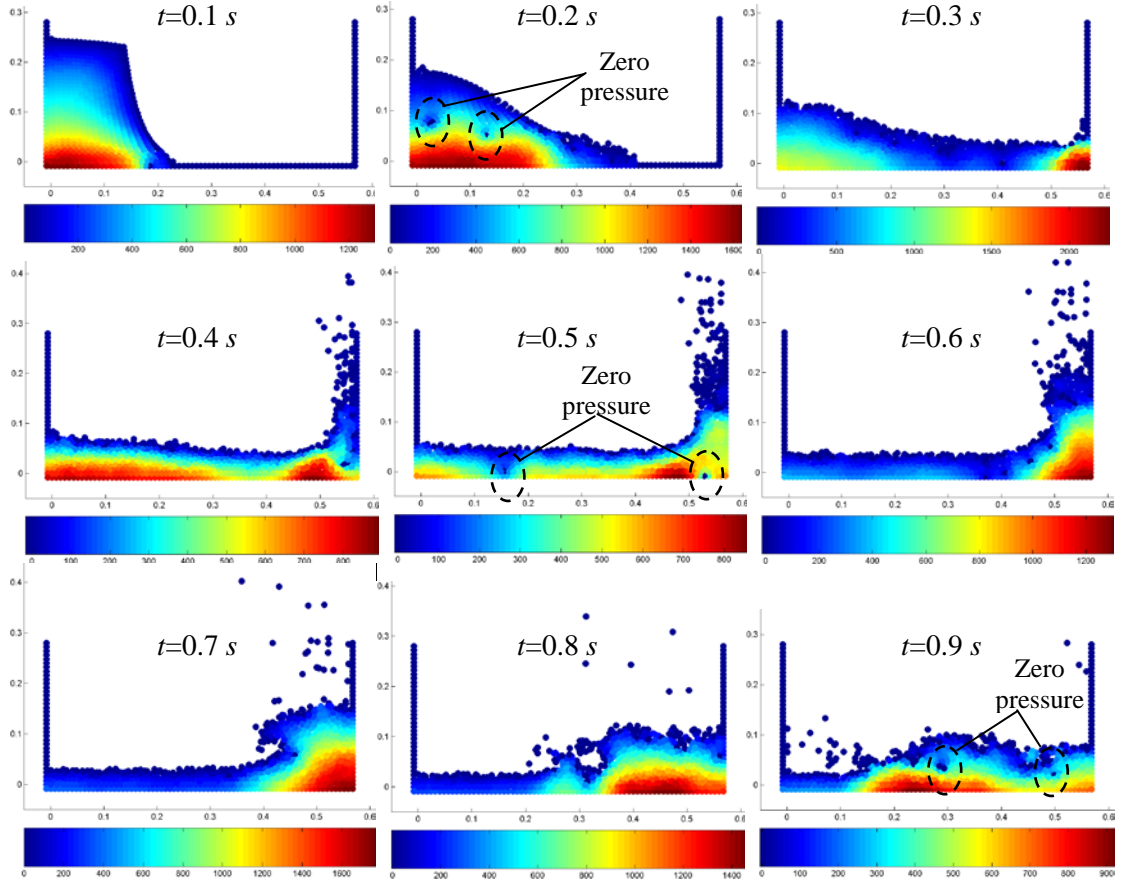


Figure 4-10. Pressure field of the dam break example by MPS method

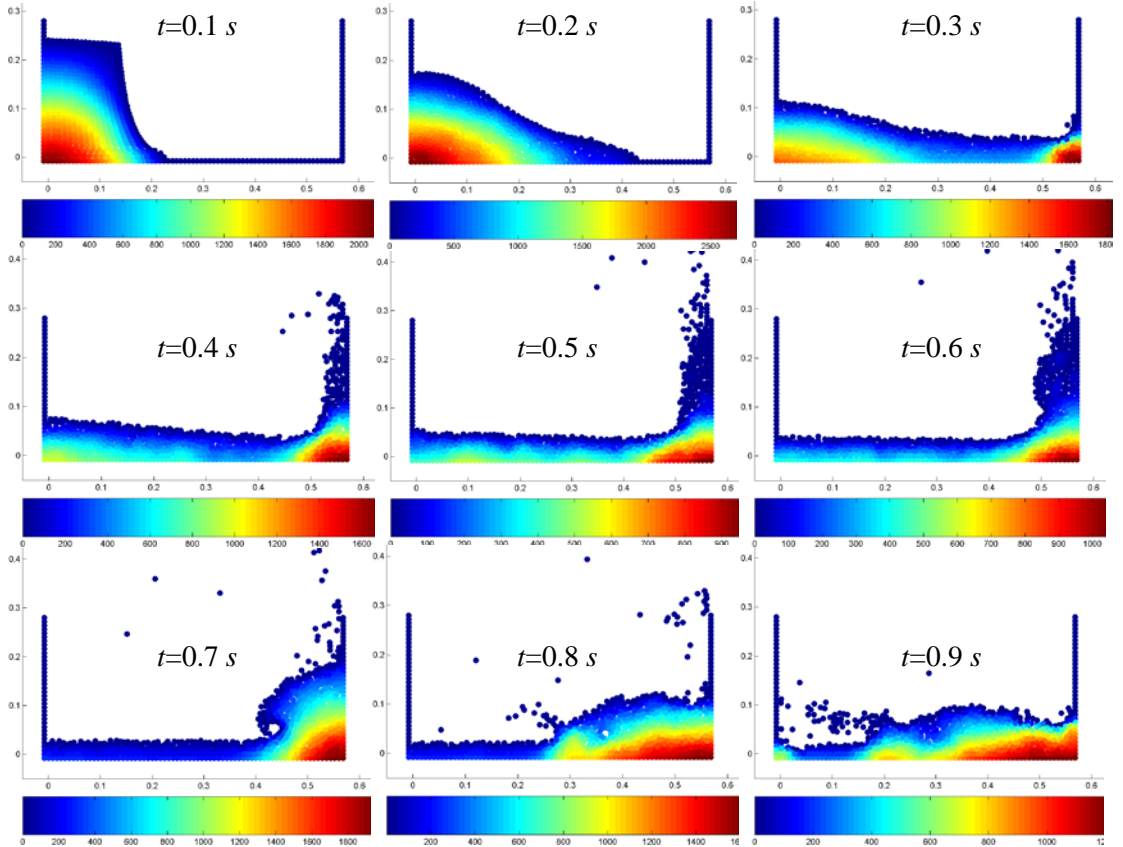


Figure 4-11. Pressure field of the dam break example by CPM

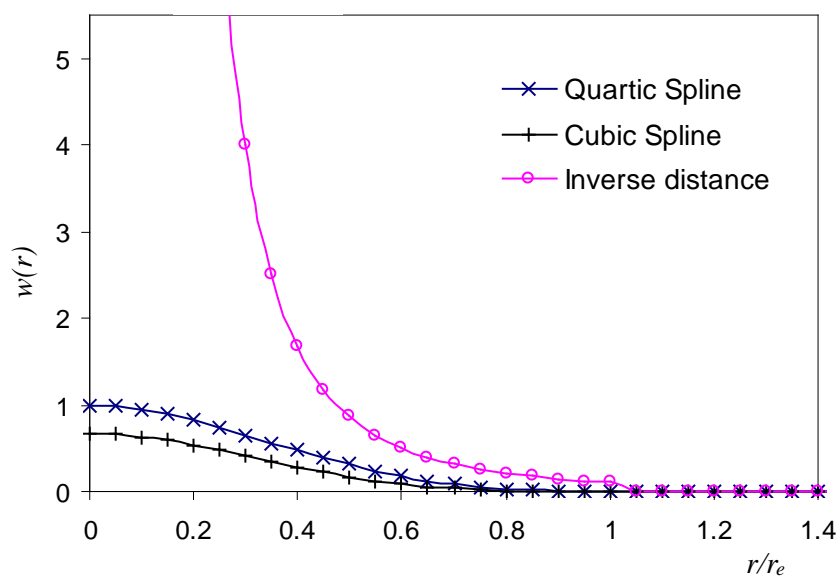


Figure 4-12. Comparison between different weighting function

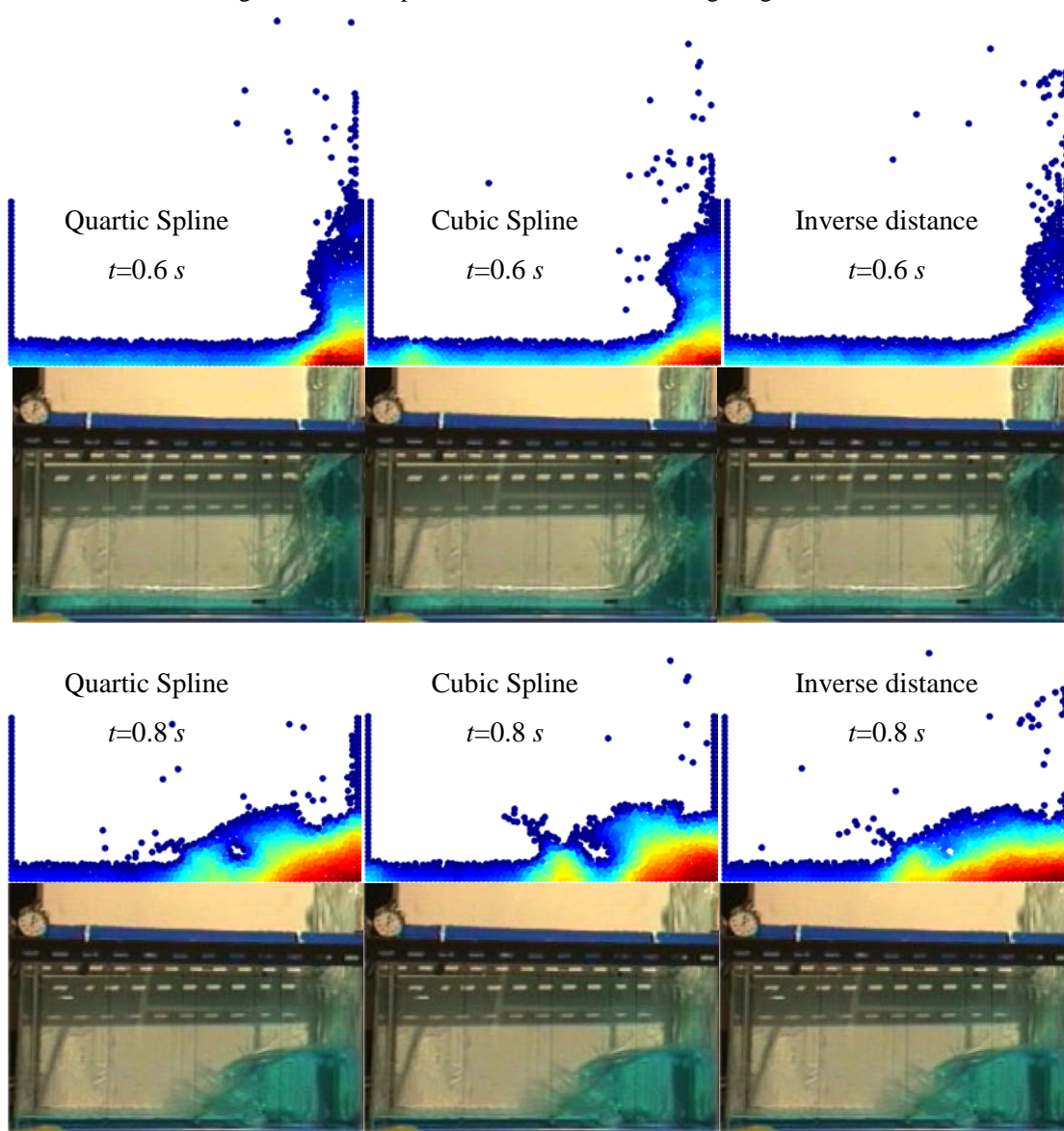


Figure 4-13. Comparison of CPM solutions using different weighting functions with experiments

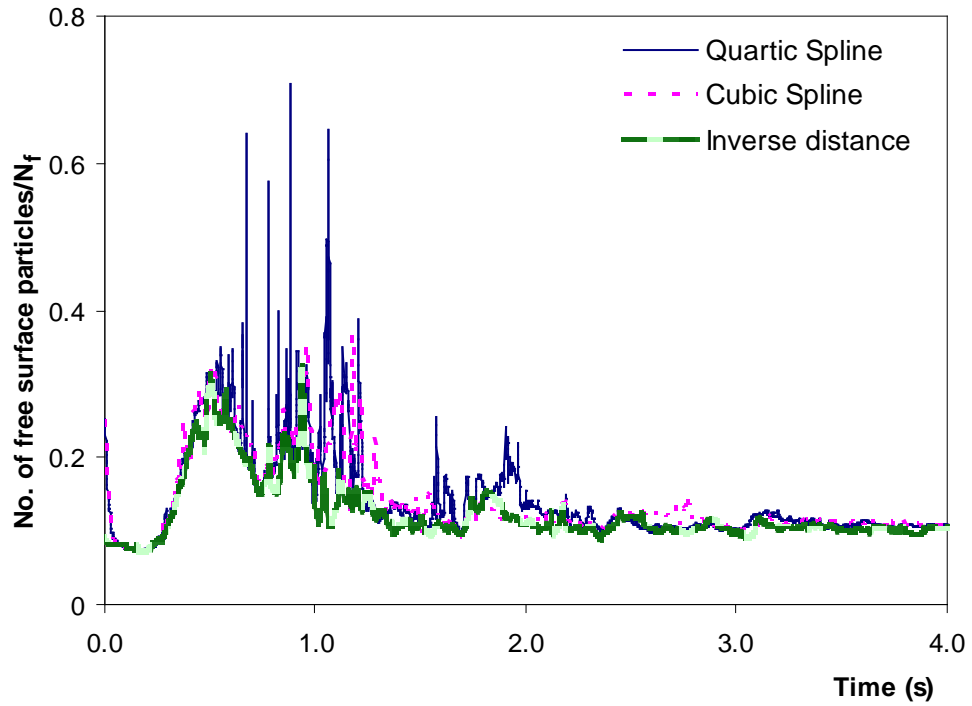


Figure 4-14. Effect of weighting functions used in CPM

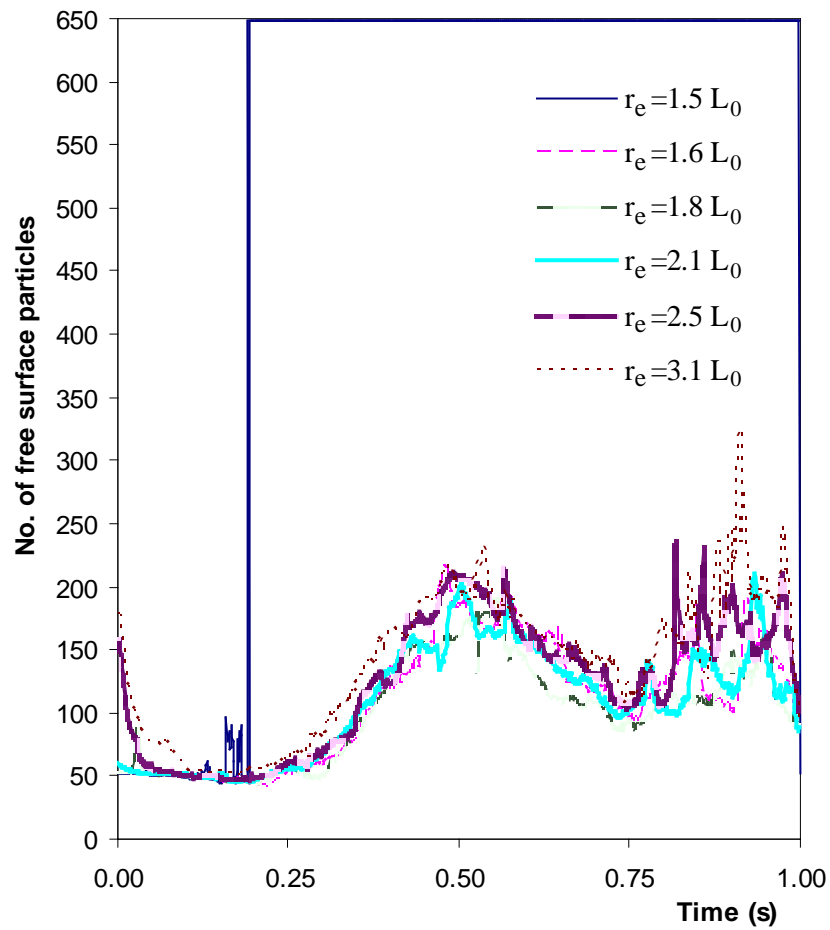


Figure 4-15. Effect of influence radius used in CPM

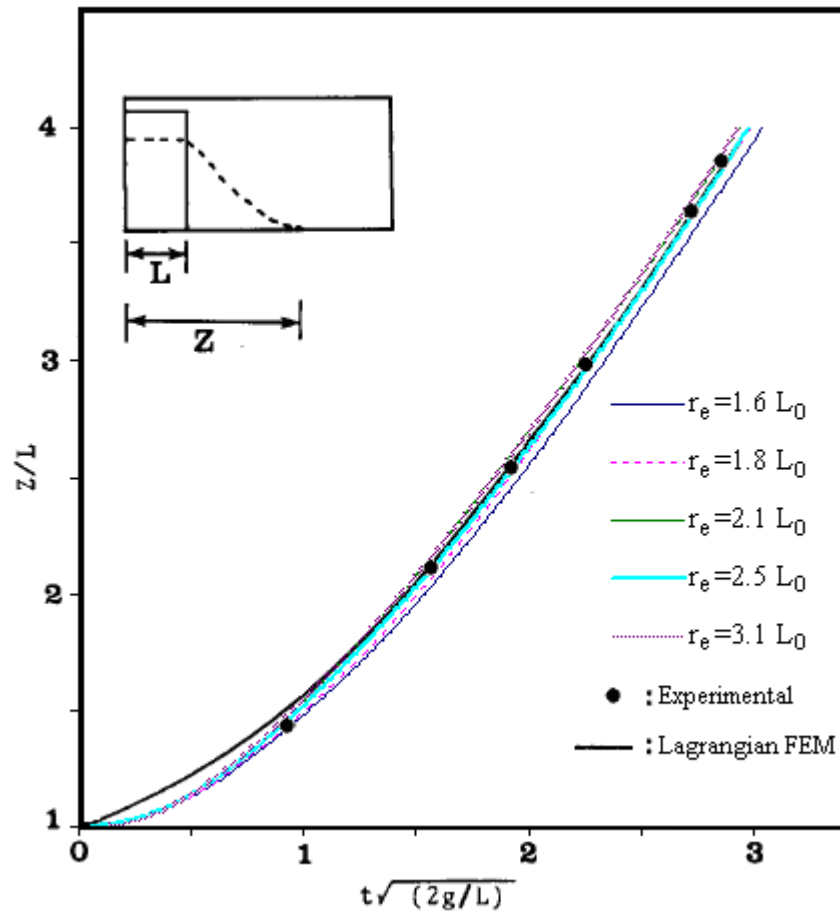


Figure 4-16. Comparison of the leading edge location in CPM solution with published results---  
experimental: Hirt and Nichols (1981); Lagrangian FEM: Ramaswamy and Kawahara (1987)

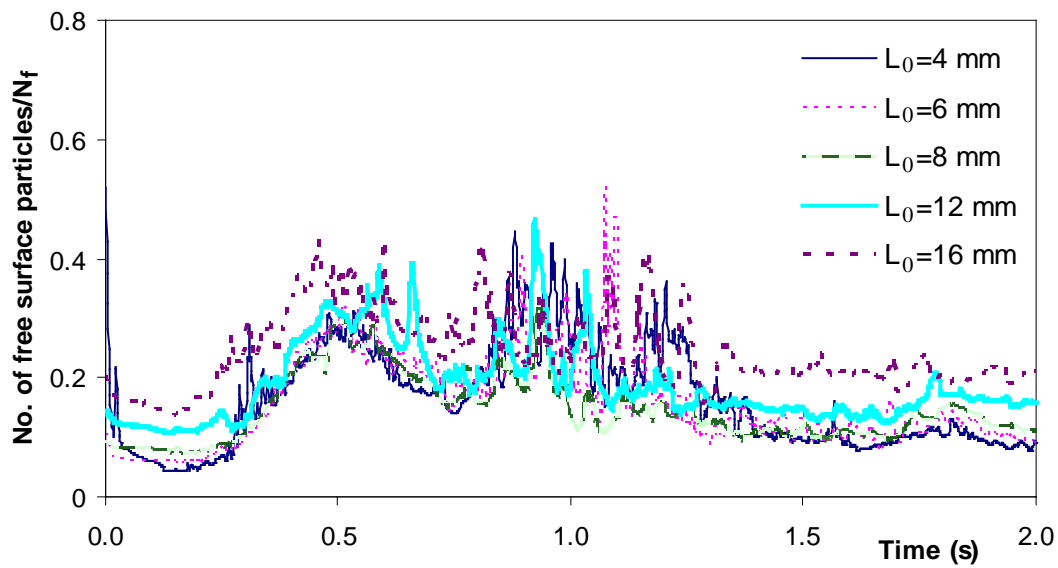


Figure 4-17. Effect of particle size used in CPM

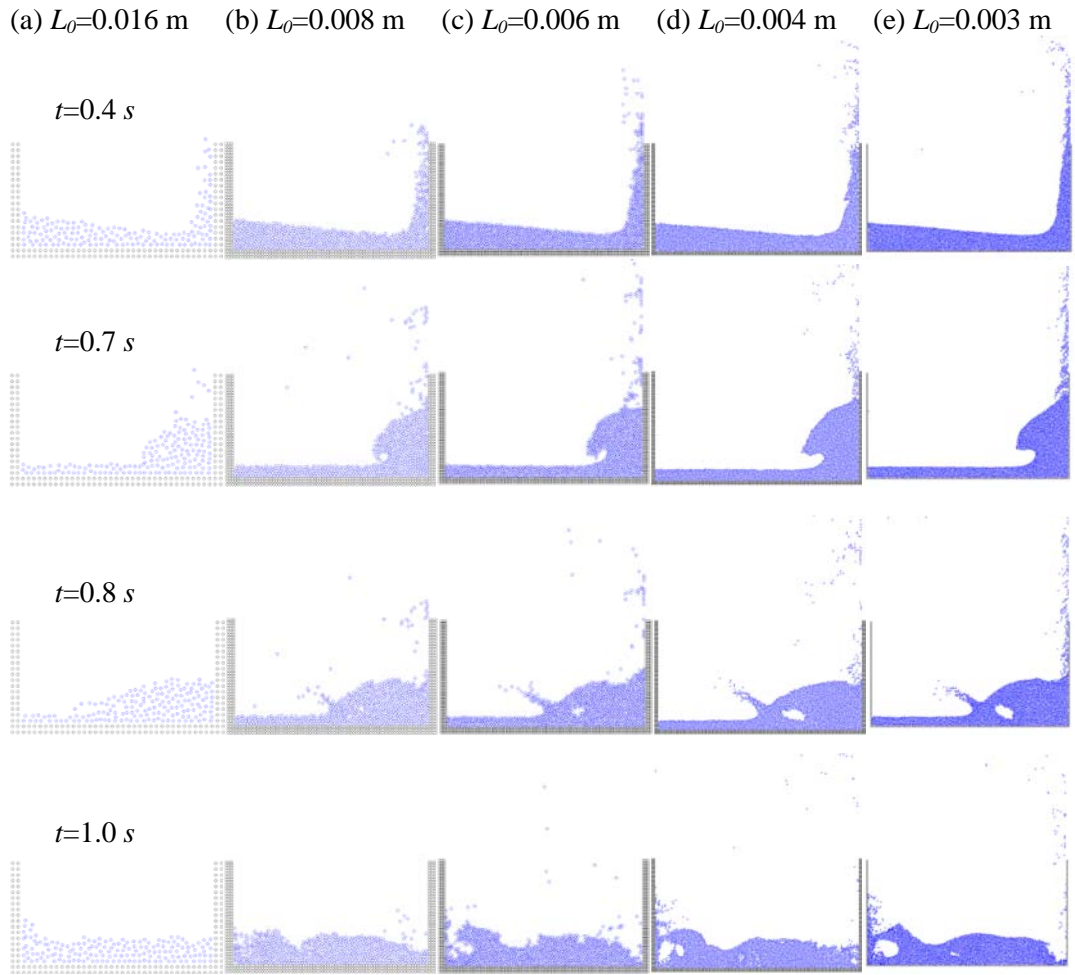


Figure 4-18. Dam break profiles using different particle sizes in CPM

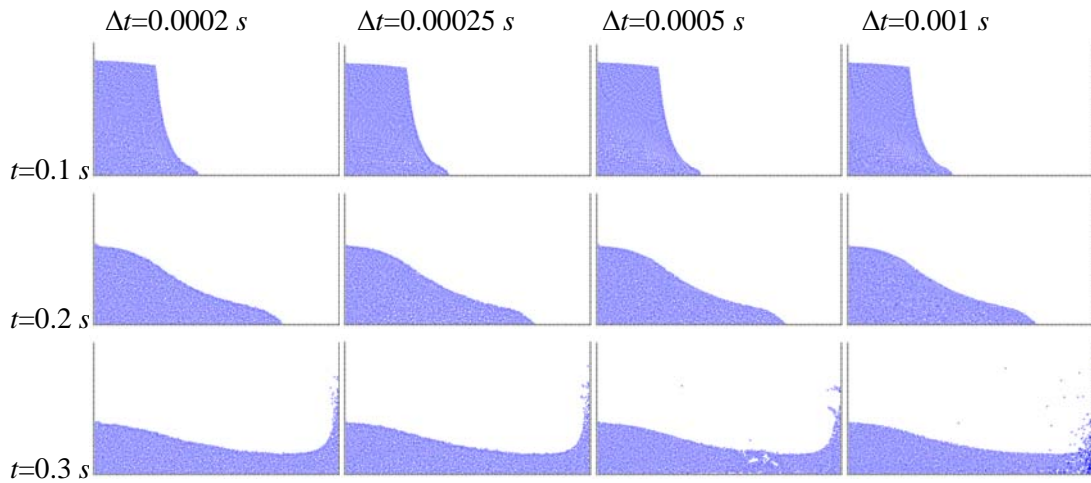


Figure 4-19. Dam break profiles using different time step  $\Delta t$

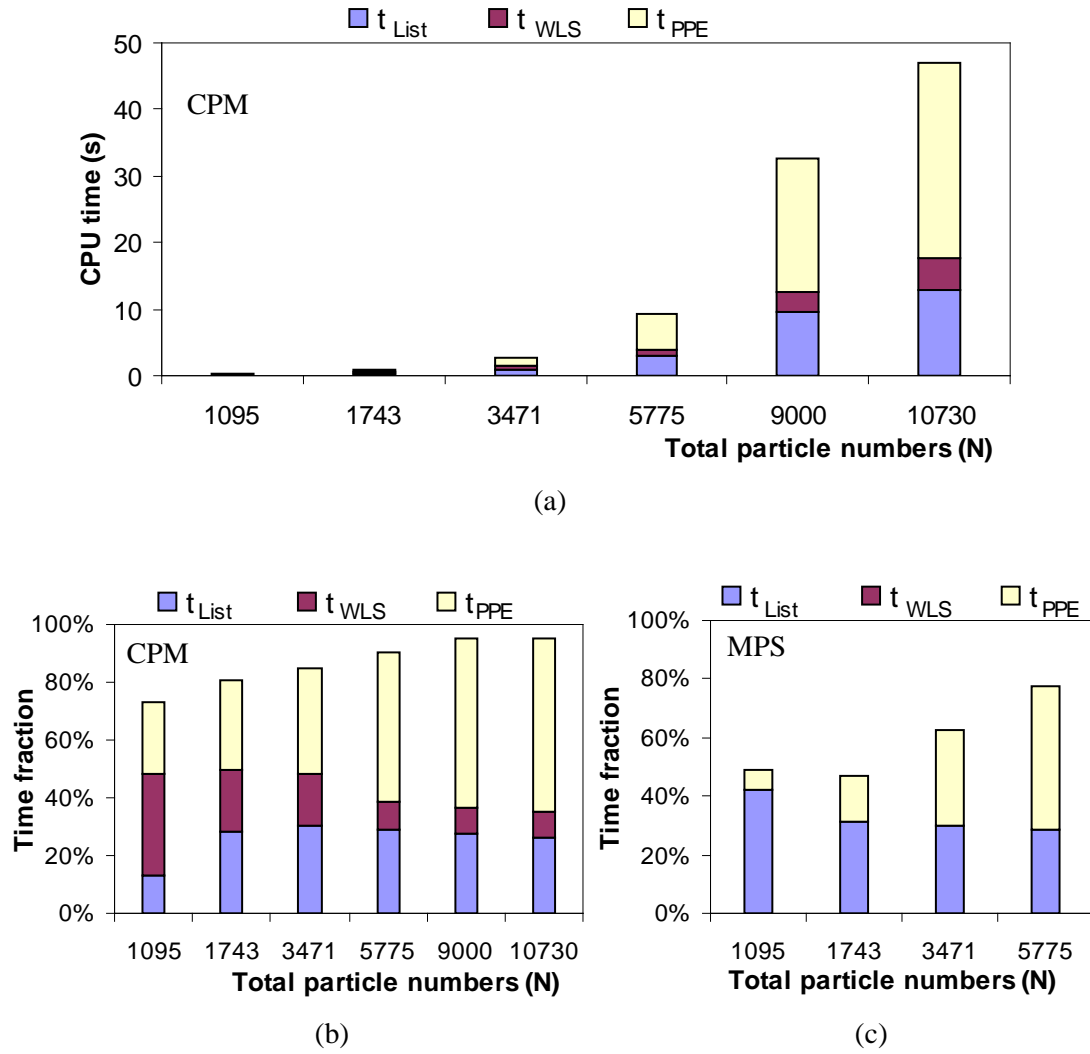


Figure 4-20. CPU time for different operations (a) CPU time of CPM; (b) Fraction over the total time of CPM; (c) Fraction over the total time of MPS

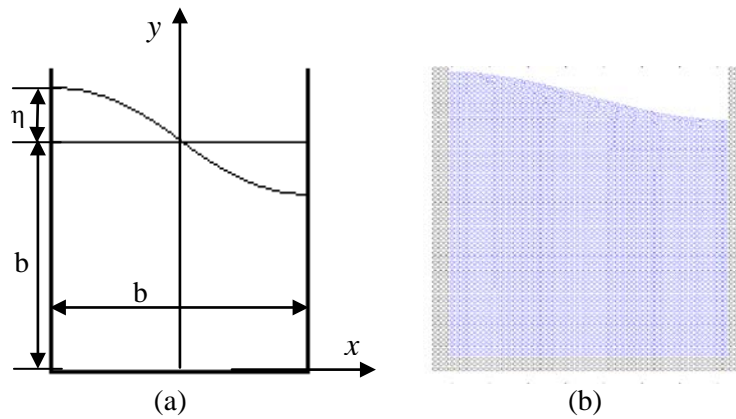


Figure 4-21. (a) A schematic view of the tank; (b) Initial particle distribution

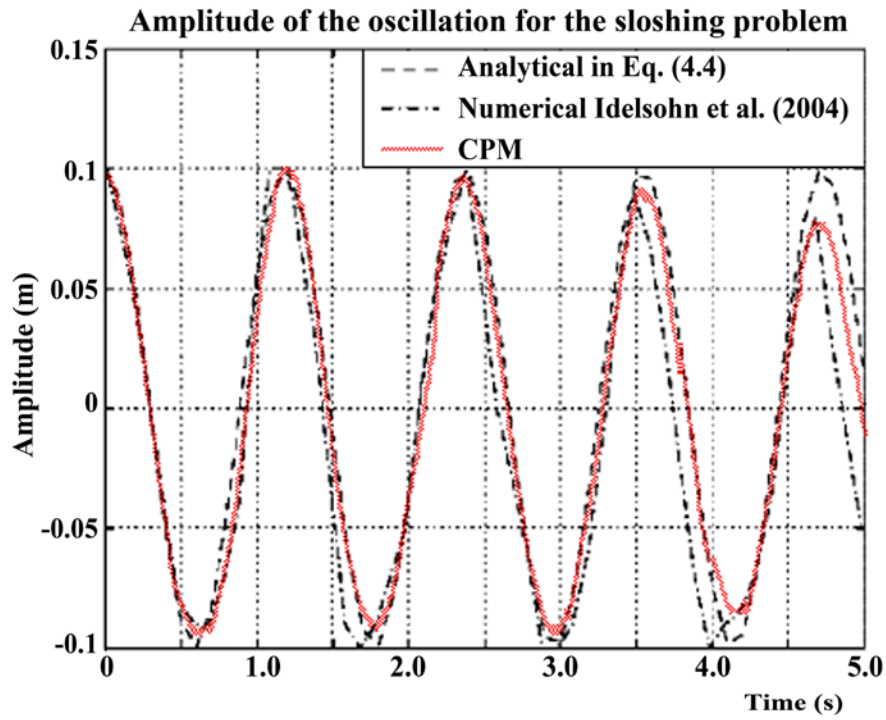


Figure 4-22. Comparison of time histories of surface elevation amplitude with published results

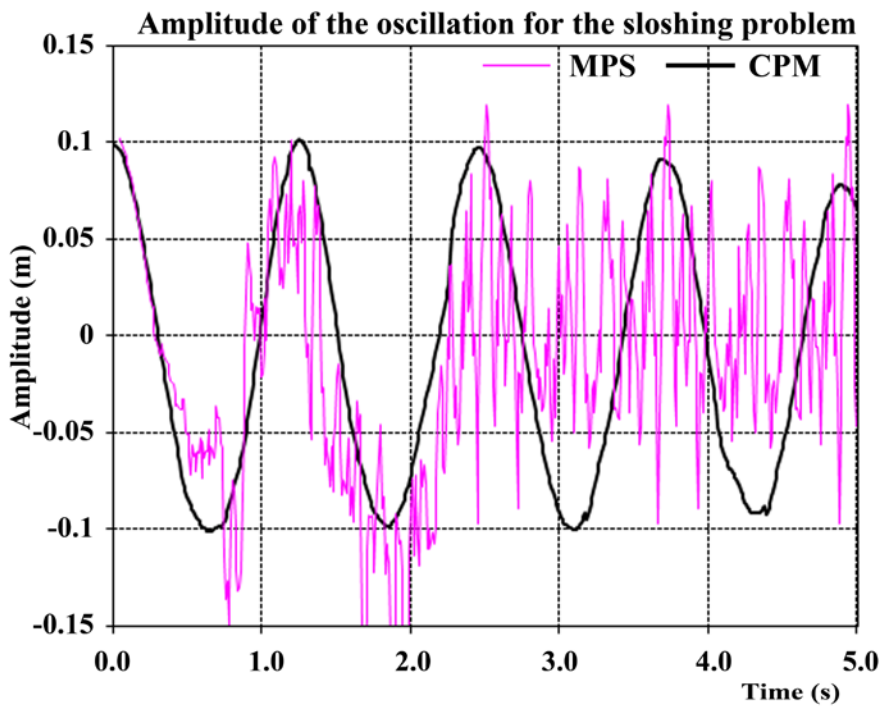


Figure 4-23. Comparison of time histories of surface elevation amplitude results by CPM and MPS

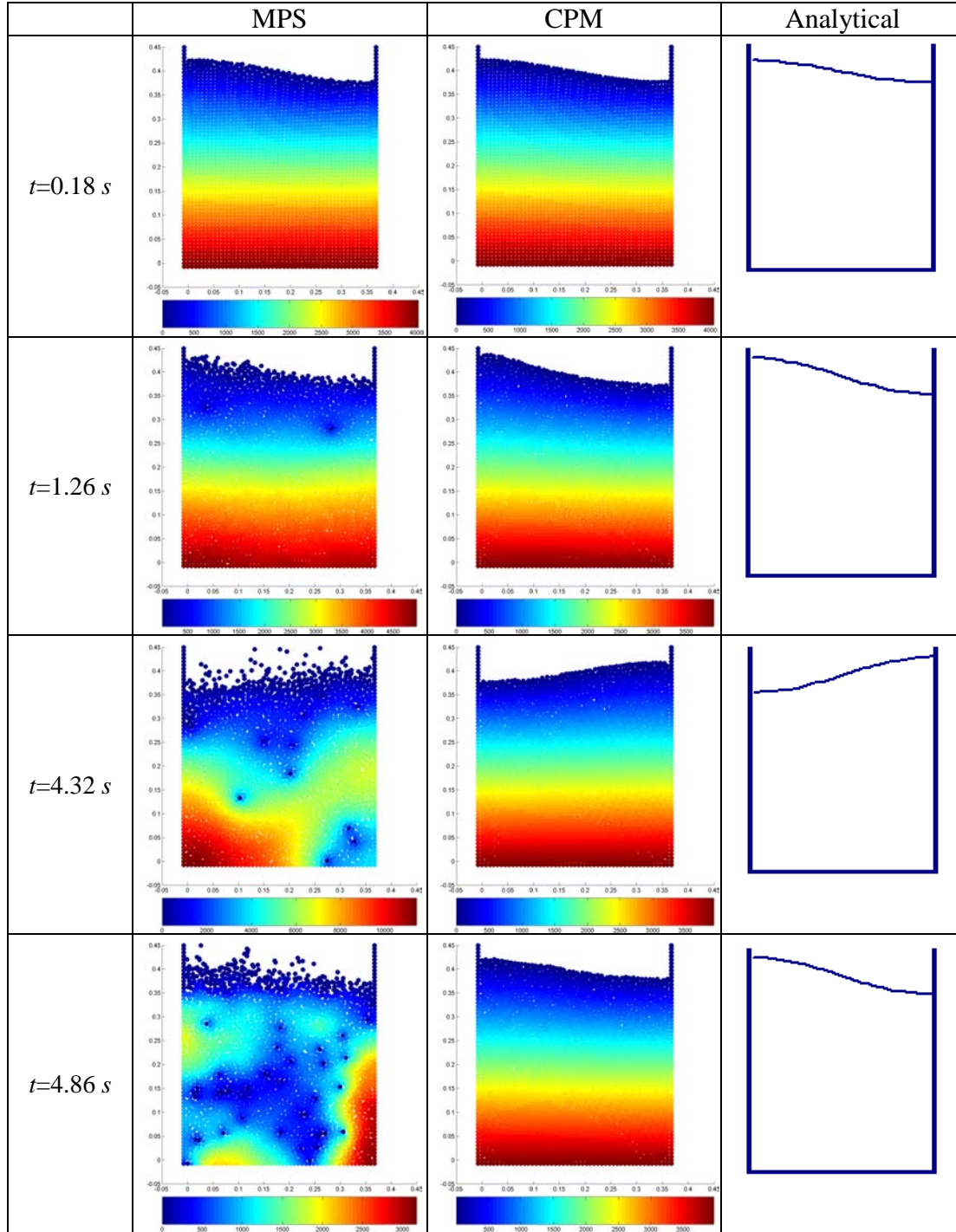


Figure 4-24. Pressure fields at different time instants for MPS and CPM simulation

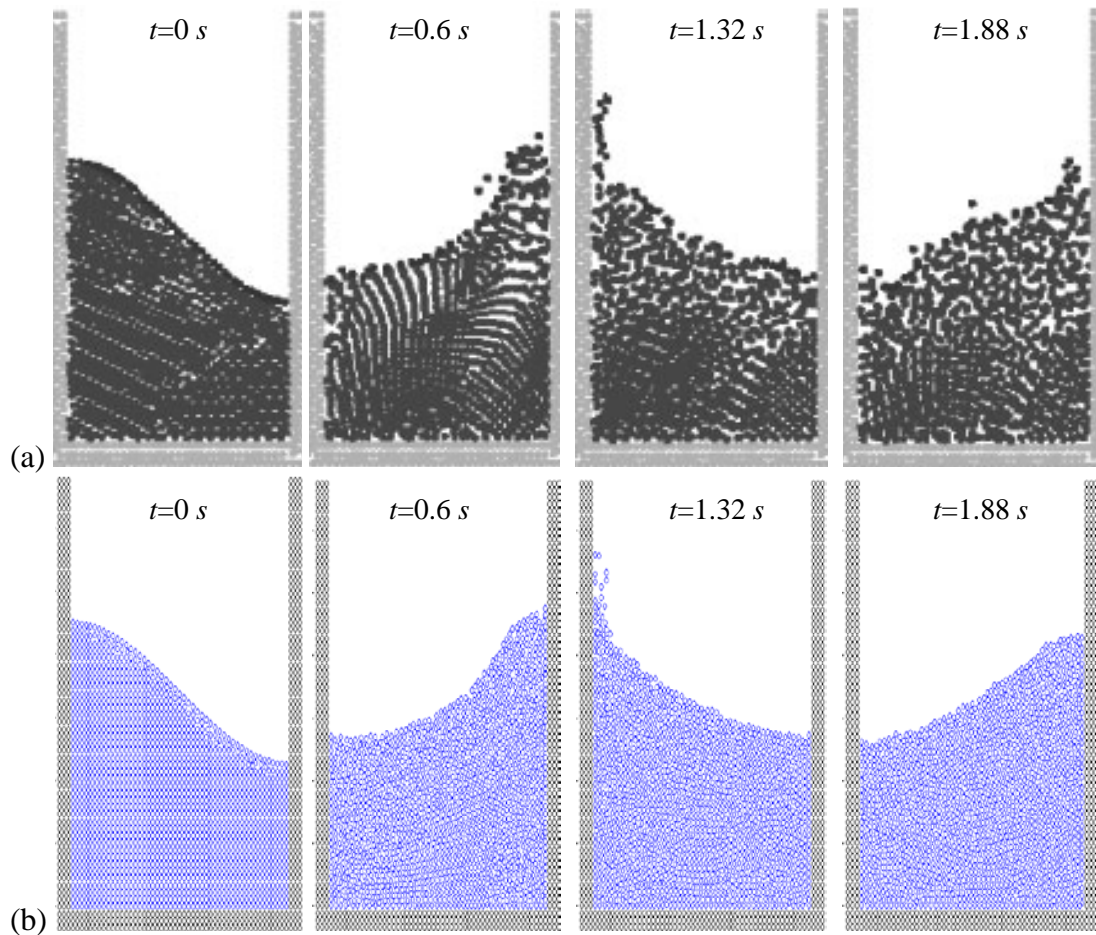


Figure 4-25. Comparison of the free oscillation of liquid for large amplitude

(a) PFEM results by Idelsohn et al. (2004); (b) results by CPM

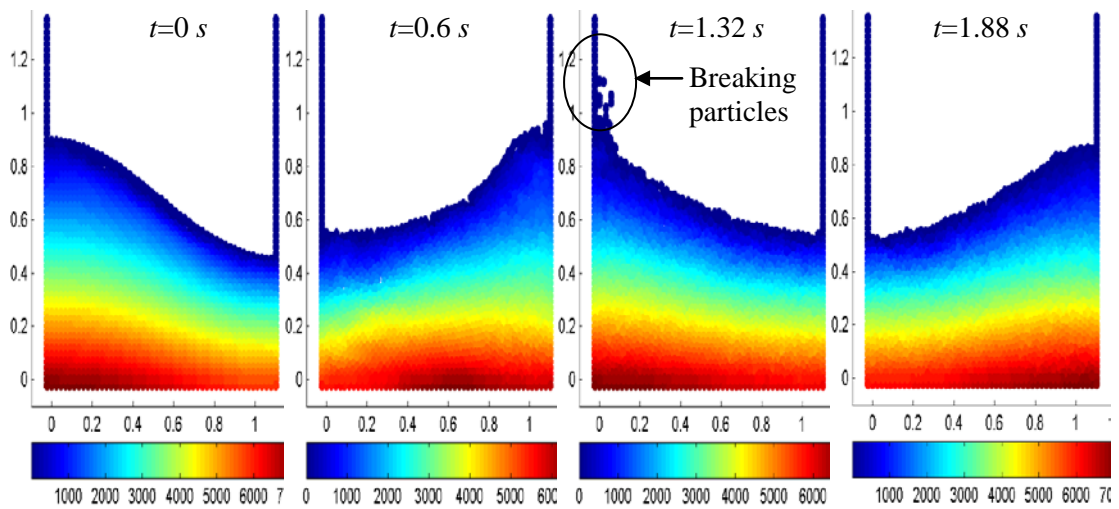


Figure 4-26. Pressure contours of the free oscillation of liquid by CPM

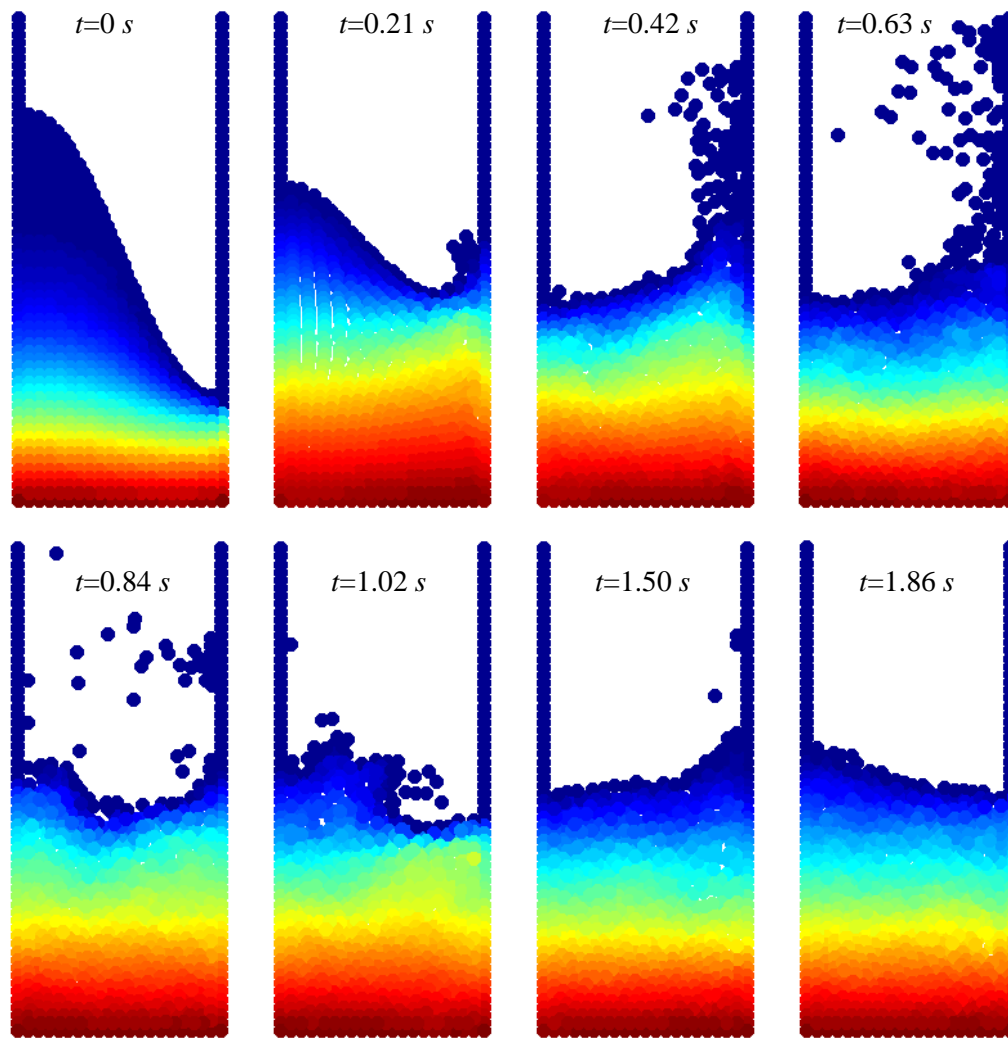


Figure 4-27. Pressure contours of the free oscillation of liquid for larger amplitude by CPM

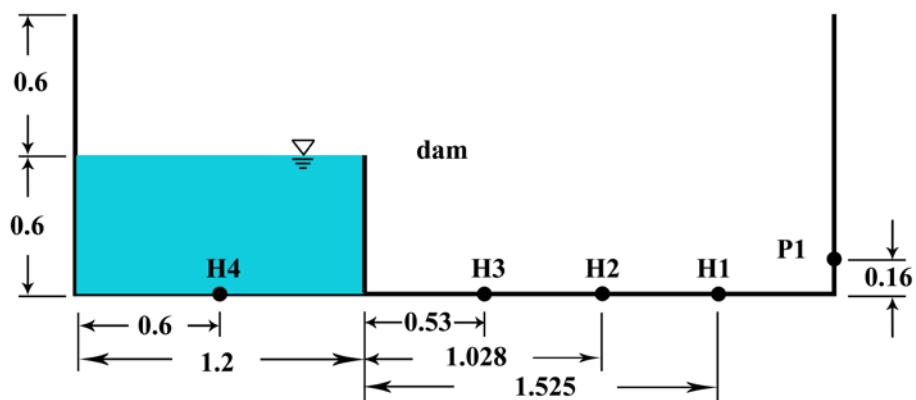


Figure 4-28. Configuration of the tank in dam break example and the positions of the water depth probes and pressure sensor (Fekken, 1998)

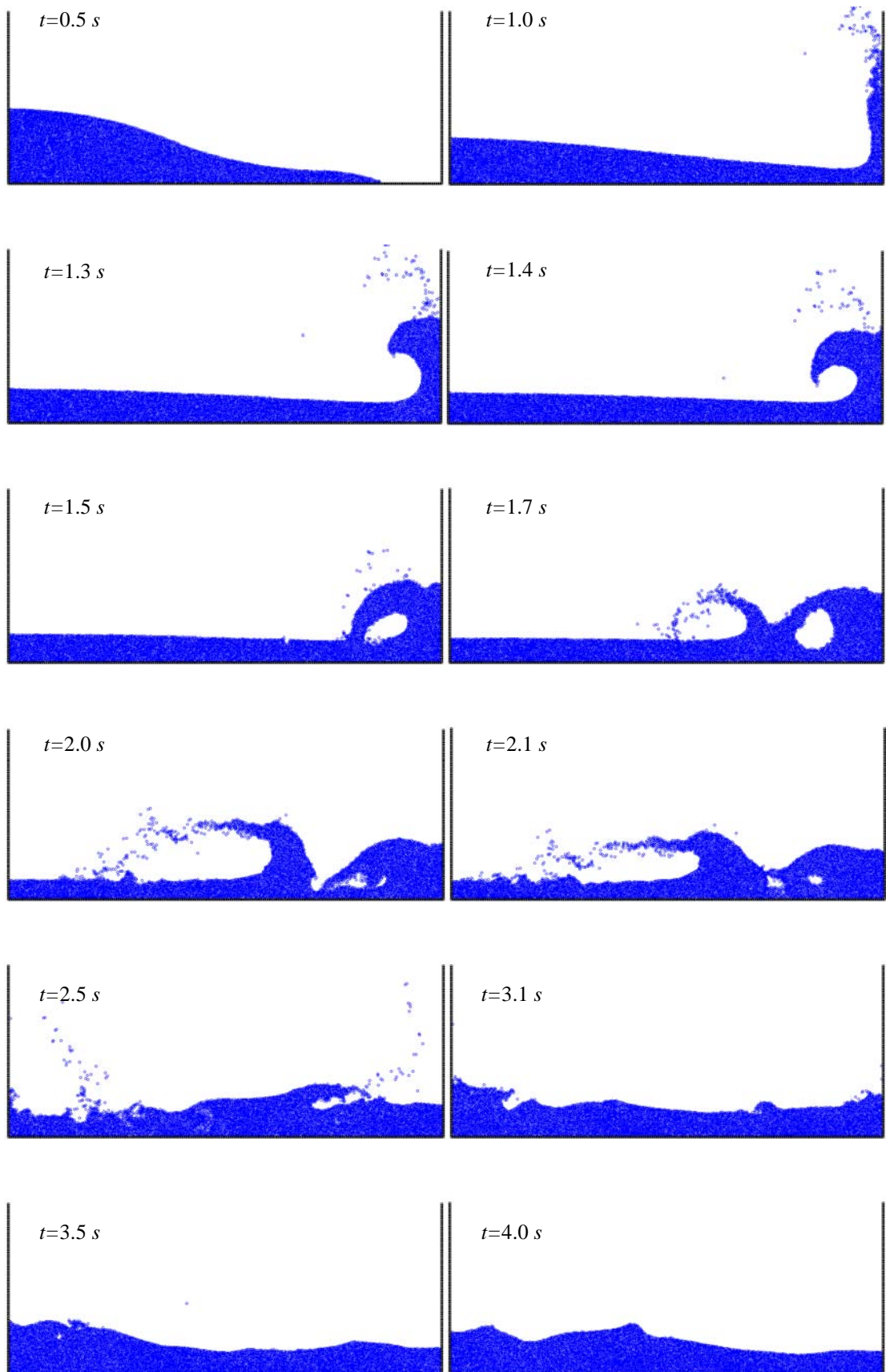


Figure 4-29. Wave profiles of the dam break example by CPM

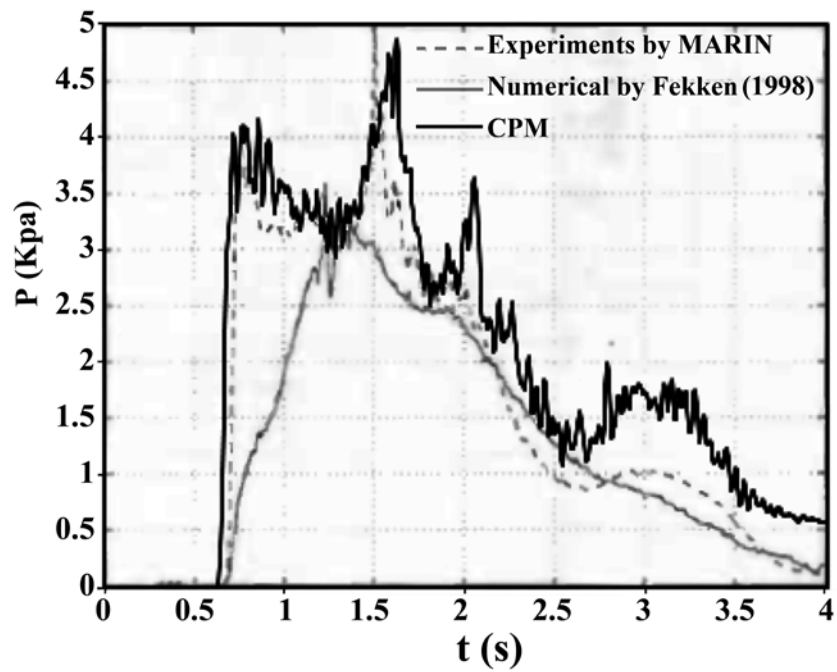
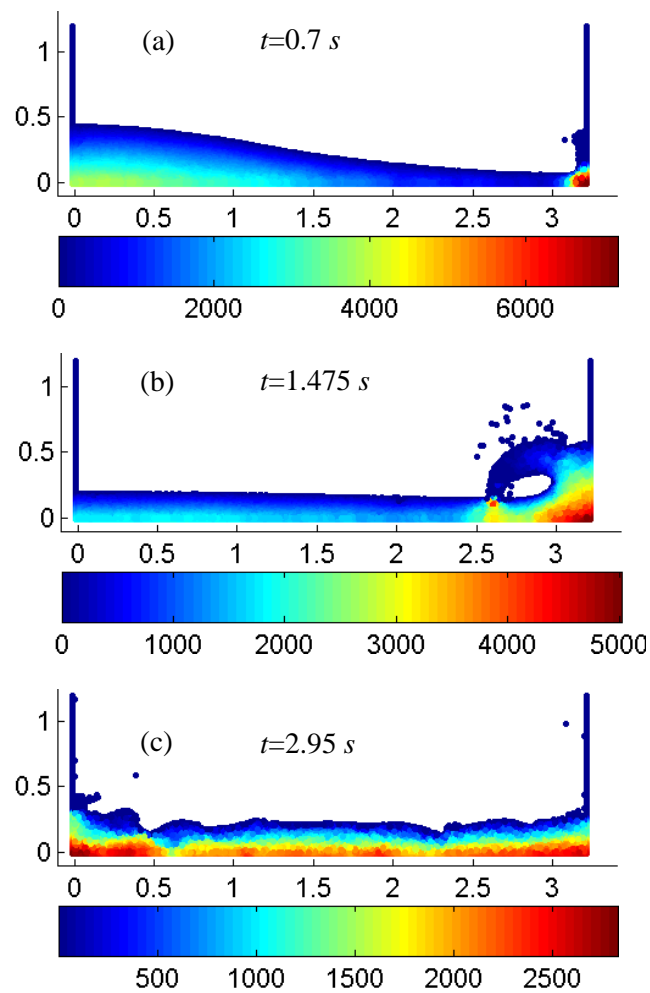


Figure 4-30. Comparison of pressure at Point P1 with published results (Fekken, 1998)

Figure 4-31. Pressure contour of dam break by CPM at (a)  $t=0.7$  s, (b)  $t=1.475$  s and (c)  $t=2.95$  s

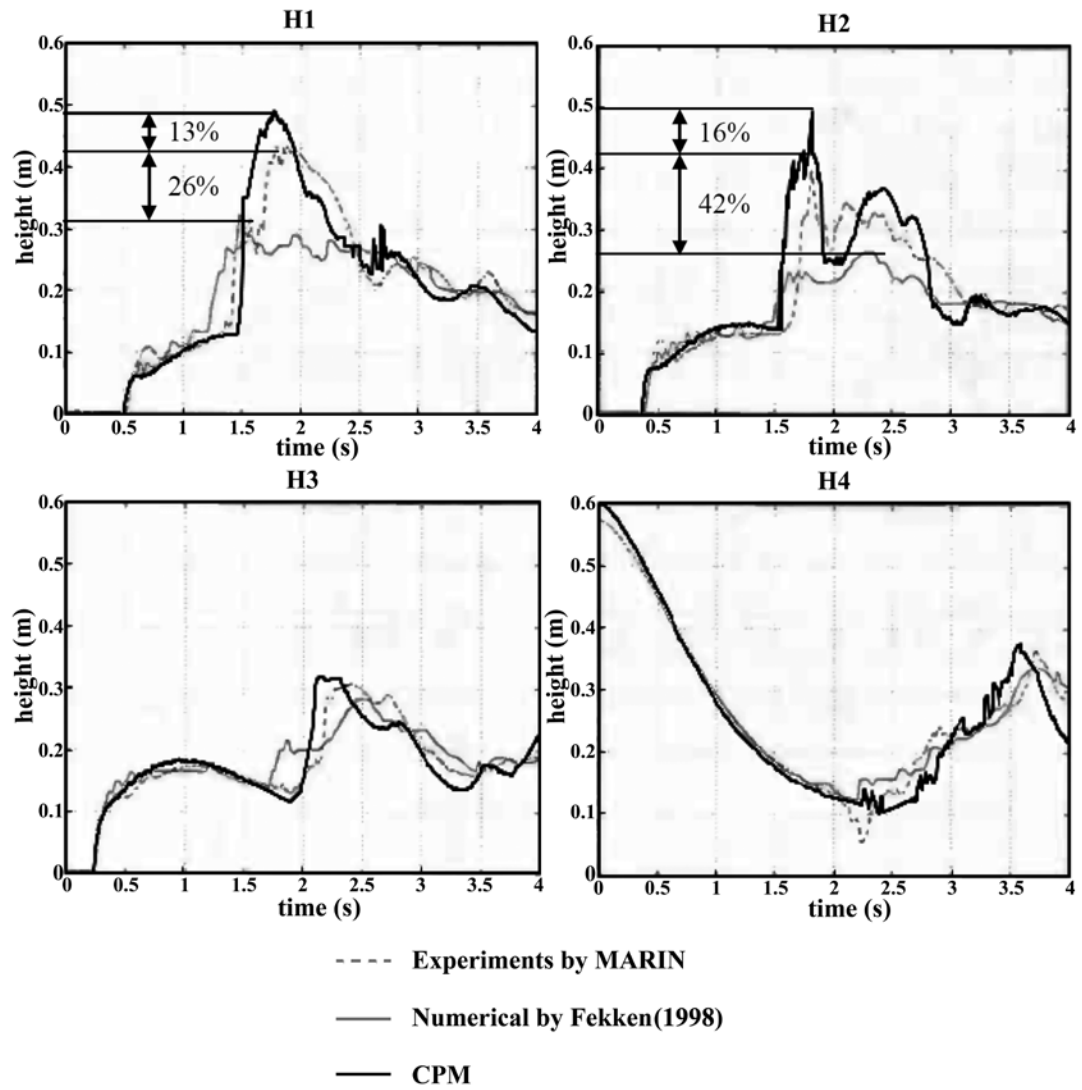


Figure 4-32. Comparison of water heights at the four points with published results (Fekken, 1998)

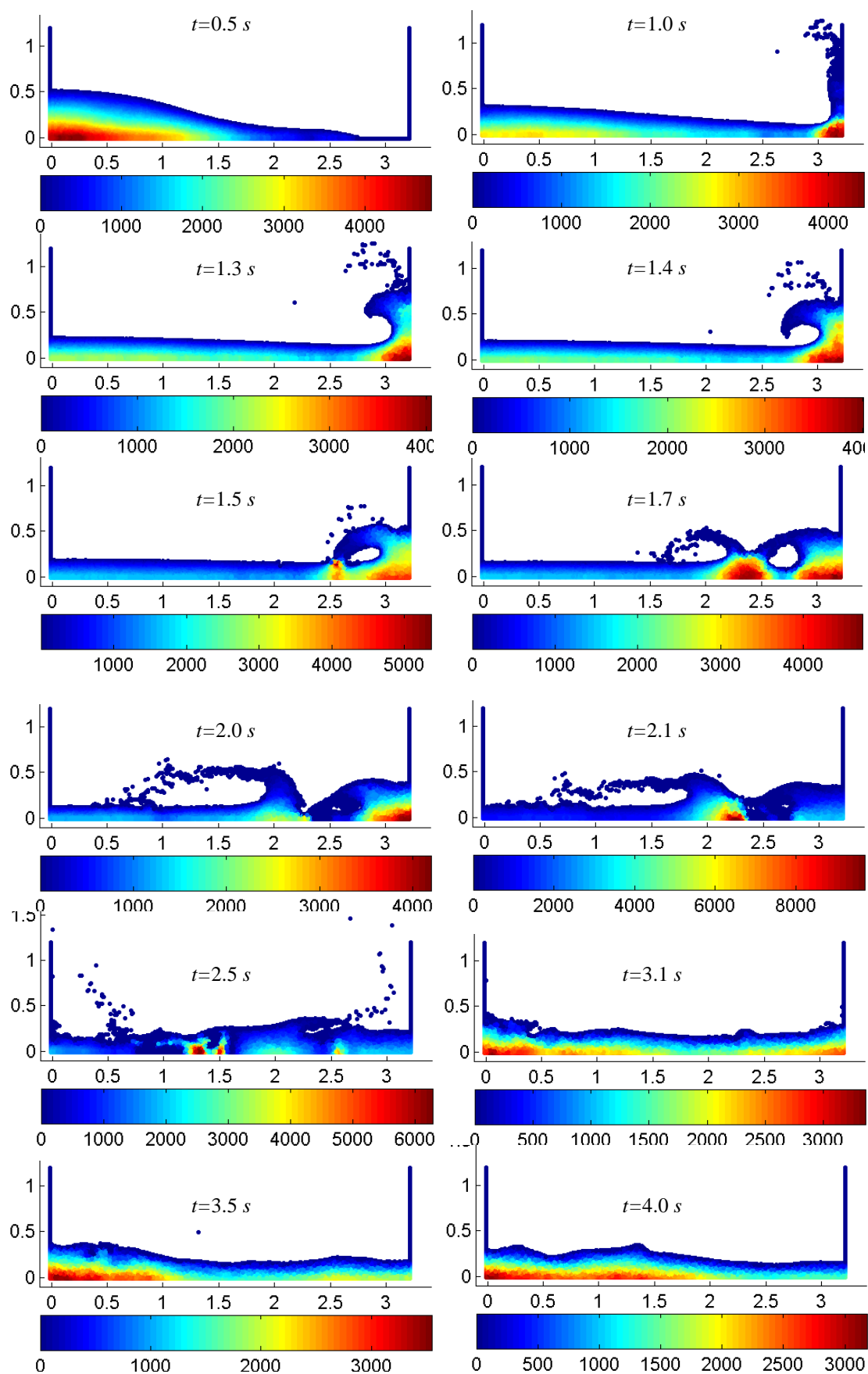


Figure 4-33. Pressure contours of the dam break example by CPM

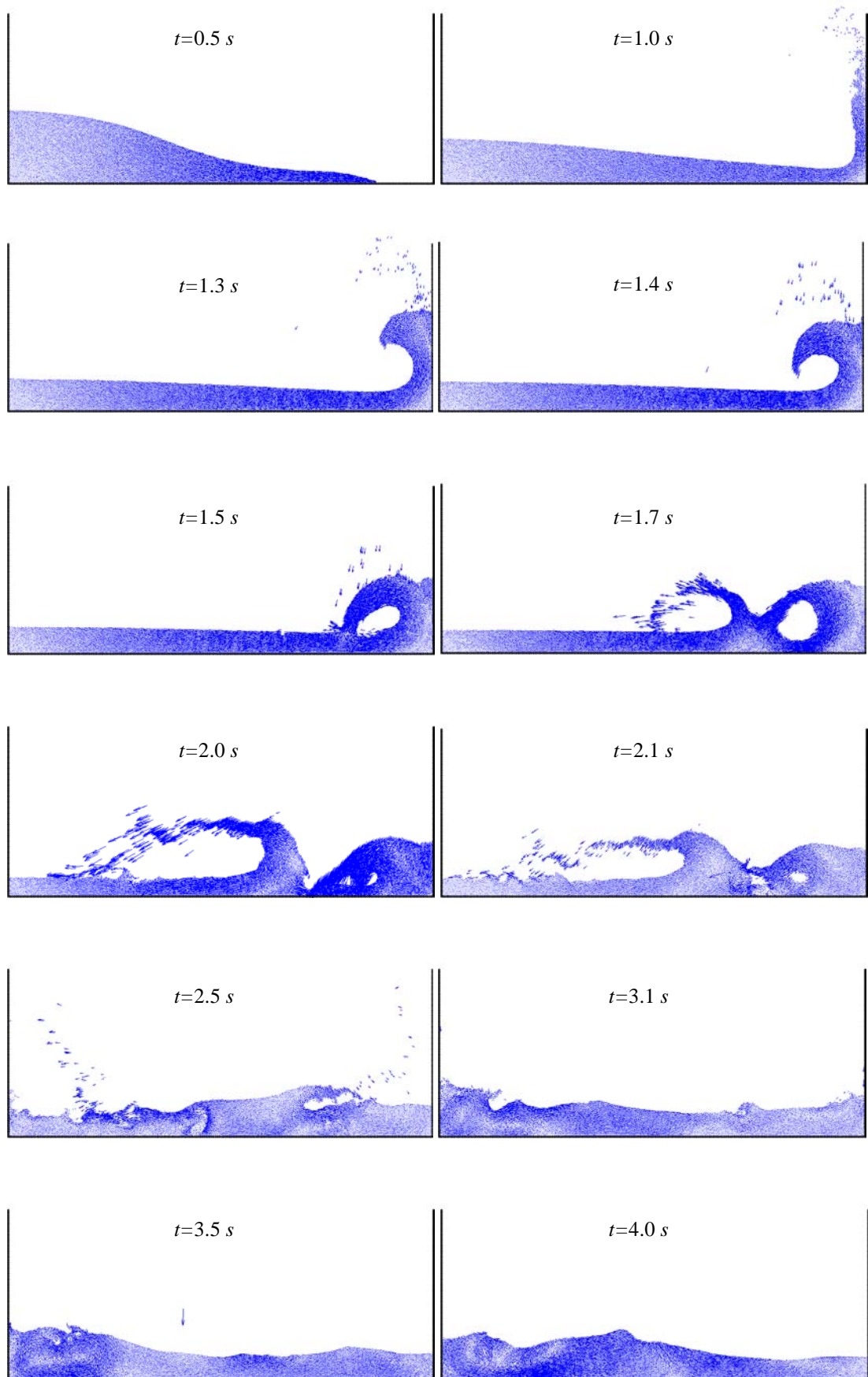


Figure 4-34. Velocity field of the fluid particles of the dam break example by CPM

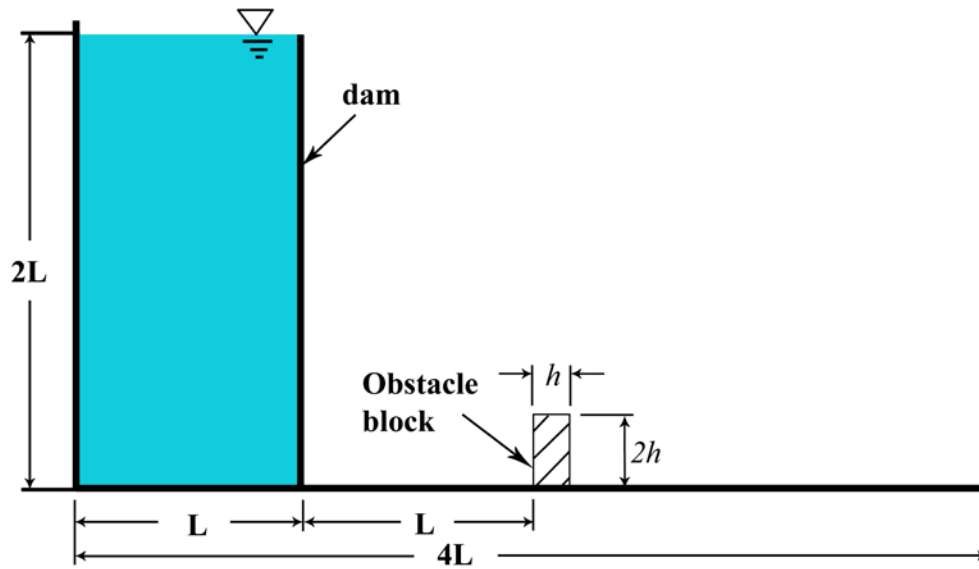


Figure 4-35. Geometry and definition of the dam break with obstacle

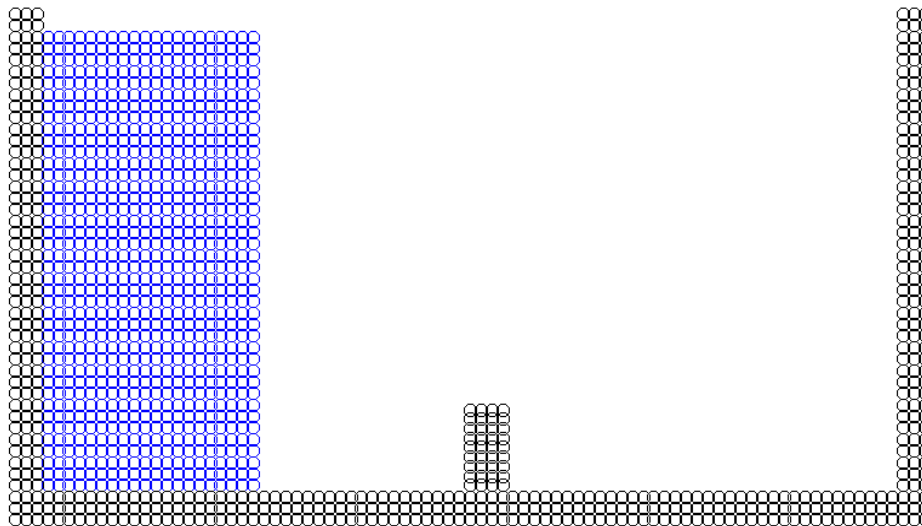


Figure 4-36. Initial particle distribution of the dam break with obstacle

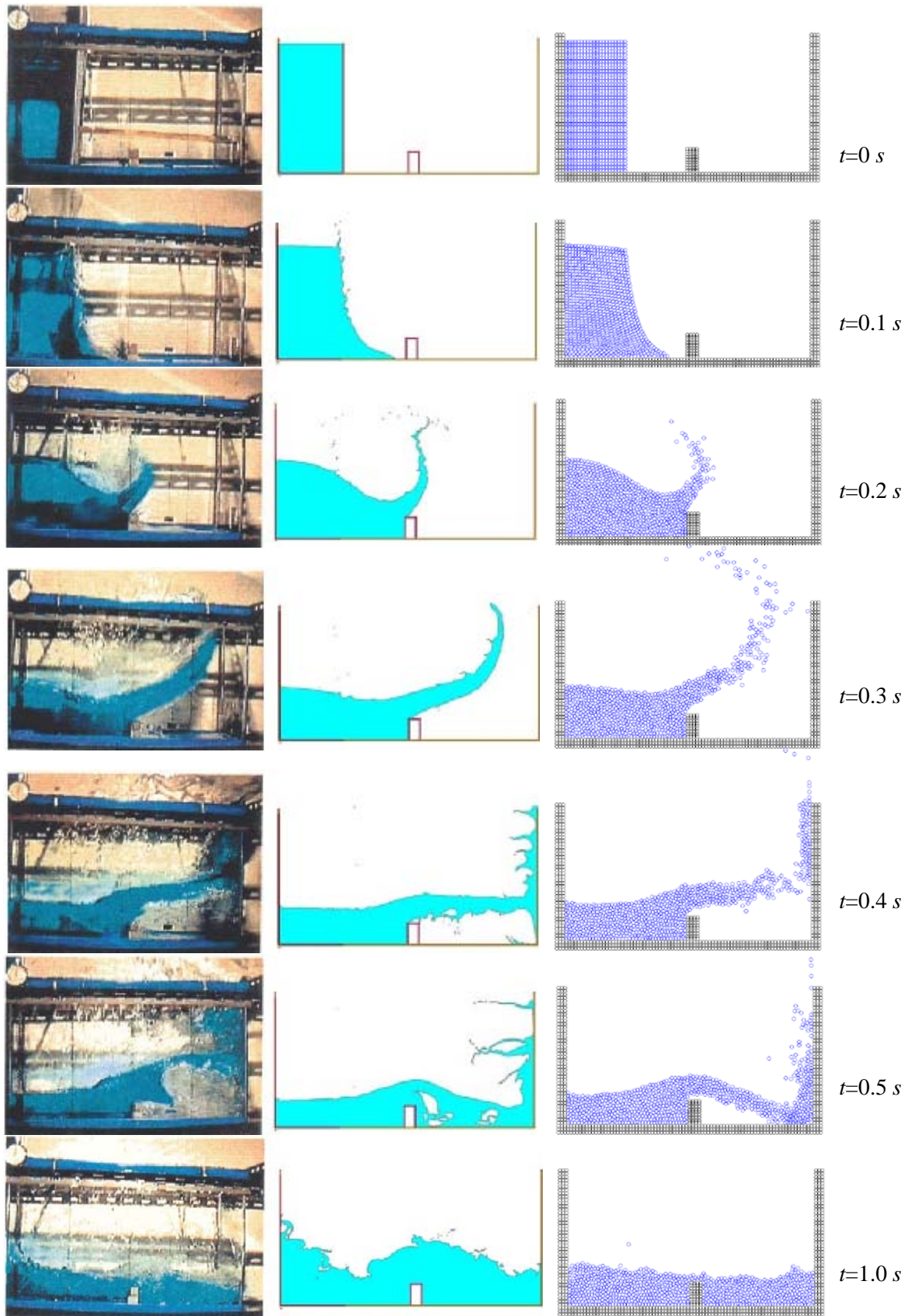


Figure 4-37. Graphical comparisons of the dam break behavior

Left: experimental results by Koshizuka et al. (1995); Middle: PFEM results by Larese et al. (2008);

Right: CPM results



## **Chapter 5 Liquid Sloshing in Rectangular Tanks: Experimental Study and CPM Simulation**

### **5.1 Introduction**

Sloshing is the motion of a liquid with free surface in a partially filled liquid container. The phenomenon is often associated with many engineering problems, and one particular concern is the transportation of LNG in membrane tanks on ships. The basic analysis of liquid sloshing involves the estimation of hydrodynamic pressure distribution, free surface elevations and the natural frequencies of the system. These parameters have a significant effect on the dynamic stability and performance of the moving containers. The high pressures and impact forces created can result in serious implications such as structural deformation within the walls, fatigue of the membrane layer or even structural failure in severe cases. Another repercussion could be the capsizing of the ship, which is caused by the high pressure and as a result, a large overturning moment to cause the instability.

Sloshing is related to the continuously changing free surface. It is difficult to simulate the free surface, especially when nonlinear phenomena such as breaking wave and overturned wave are considered. In this regard, sloshing experiment is essential for understanding and verification of numerical simulating results.

Various experimental studies have been carried out to study dynamic sloshing in rough sea conditions. The most significant experimental study is the one carried out by Lloyd's Register (2008). Damages to containment system in late 1970s and recent NO96 vessels have motivated Lloyd's Register to carry out experimental investigation

to find out the causes. It is concluded that LNG filling depths play a significant role in affecting the structural integrity of cargo containment systems. Another experimental study was carried out by Daewoo Shipbuilding & Marine Engineering Co Ltd (DSME) which was referred to by Chen et al. (2008). DSME has found that high impact pressure is generated at low filling depth of approximately 30%, which is in line with Lloyd's Register's findings.

In this chapter, water sloshing in rectangular tank under lateral excitation is first investigated experimentally. Rectangular tanks with two different sizes are designed to investigate the different aspects of sloshing behavior. Parameters such as water depth and excitation frequencies are varied to study their effects on sloshing. Numerical simulations of typical sloshing cases are then performed using the proposed CPM and the results are compared with the experimental results.

## **5.2 Experimental setup**

### **5.2.1 Experimental facilities**

Figure 5-1 shows the experimental setup. A rectangular tank was mounted on a shake table which was subjected to lateral displacement excitation. The tank made of Plexiglas was partially filled with water. The free surface elevation of water was measured using wave gauges. A pressure sensor was used to measure water pressure on one side wall (see Figure 5-2 for details). A hydraulic actuator generates horizontal motion of the shake table. Its displacement was measured by a displacement transducer mounted on the shake table. All the output signals from the shake-table, wave gauges and pressure sensor were sent to a digital oscilloscope where data can be acquired and stored. The dynamic motion of the fluid was recorded by a high speed

camera located in front of the tank. The overall instrumentation scheme is illustrated in Figure 5-3.

### **5.2.2 Water Tank**

The water tank used in the sloshing experiments is schematically shown in Figure 5-4. The tank with length  $L$  and height  $H$  was filled with water up to the filling depth  $d$ . A wave probe was placed 20 mm from the right wall at Point  $P_1$  to measure the free surface elevation ( $\eta$ ) near that corner. The pressure sensor was located at the left corner of the tank bottom, which is  $P_2$  shown in the figure.

### **5.2.3 Shake table**

A 1.5 m x 1 m shake table driven by a hydraulic actuator (load capacity 25 kN and stroke capacity  $\pm 5$  cm) is used in the sloshing experiments. The shake table can only generate unidirectional lateral excitation (translation in one degree of freedom).

In order to ensure that the excitation from the shake table can be fully transmitted to the tank, the rectangular tank has to be tightly fastened on the shake table. This is done by anchoring the tank against two square steel tubes that are bolted tightly against the shake table (Figure 5-5).

### **5.2.4 Wave probes**

Three capacitance type wave probes (KENEK CHT4-60) were installed to measure the free surface elevation of the sloshing waves. The wave probes worked based on the principle of linear variation of capacitance with water surface change. Capacitor is formed from insulated wire held taut by a supporting rod, with water serving as a “ground” (see Figure 5-6). The capacitance of the wire changes according

to the water surface displacement. Hence, the wave height is obtained by detecting the change in capacitance of wire. Care was to be taken to ensure that the wave probe is installed vertically for accuracy.

Calibration is necessary to obtain conversion coefficient between voltage and water level. Calibration is performed in a deep water bucket, by mounting wave probe on an adjustable stand which allows it to be adjusted up and down as shown in Figure 5-7. The readings are taken at interval of 10 mm from 10 cm to 27 cm of the water height. The calibration results are plotted as shown in Figure 5-8, Figure 5-9 and Figure 5-10 for the three wave probes. As seen in the figures, the calibrated coefficients of the wave probes 1 to 3 are 49.55 mm/v, 47.47 mm/v and 49.85 mm/v, respectively.

### **5.2.5 Pressure sensor**

A WIKA Model S-10 pressure sensor was installed on one side wall at about 20 mm from the bottom of the tank (Figure 5-11). It was used to measure the hydrodynamic pressure response during sloshing. Care was taken to ensure watertightness at the connection point.

Calibration was carried out to obtain the different voltage readings corresponding to the different water pressures. As shown in Figure 5-12, the pressure sensor was mounted at the bottom of a cylindrical container for calibration. A bubble level was used to make sure the cylindrical container was standing vertically. Pressure readings were collected by varying the water level. The calibration result is plotted in Figure 5-13 which shows a calibrated coefficient of 103.87 mm/V. Considering that water density is  $\rho=1000 \text{ kg/m}^3$  and gravity  $g=9.78 \text{ m/s}^2$ , the calibrated coefficient for pressure sensor is 1015.8 Pa/V.

### **5.2.6 Displacement transducer**

The lateral displacement generated by the shake table was measured by using a conductive plastic resistive element type potentiometer 13FLP25A shown in Figure 5-14. The calibration coefficient for the potentiometer is 10.29 mm/V.

### **5.2.7 High speed camera**

As seen in Figure 5-15, a high speed camera (Nikon/Basler A504K) was set up at about 2 m in front of the experimental tank for image capture and connected to a data processor. The camera could record the wave profiles at a maximum frame rate of 500 fps and provided a graphical view of water sloshing. DC lighting was used to provide the necessary brightness. The images taken were selectively digitized to derive the free surface profiles.

### **5.2.8 Other considerations**

Precautions were taken to ensure good accuracy of results during the experiments. Firstly, the water surface was ensured to be stationary before the shake table was started. Secondly, the tank was placed and fastened to align with the motion of the shake table such that 2D water sloshing was obtained (Figure 5-16). The inner surface of the tank was also made smooth to reduce boundary layer effect and minimize 3D effects of sloshing waves. Thirdly, connecting cables were arranged so as not to cross one another and sufficient lag lengths were reserved to avoid cable being stretched when the shake table moved.

### 5.3 Sloshing experiments and comparison with CPM solutions

Liquid sloshing in a tank is a highly nonlinear phenomenon in which the free surface profiles can be considered as a composition of several wave modes. The superposition of the modes depends on the liquid depth, tank geometry and external excitations.

For a rectangular tank, the natural frequency of the fluid can be estimated from linear theories (Su et al., 1982) by the following equation,

$$\omega_m = \sqrt{g \frac{m\pi}{L} \tanh\left(\frac{m\pi}{L} d\right)} \quad (5-1)$$

where  $d$  is the depth of water in the tank,  $L$  the length of the tank,  $m$  the mode number and  $g$  the acceleration due to gravity taken as  $9.78 \text{ m/s}^2$  (gravitation in Singapore, [http://en.wikipedia.org/wiki/Gravity\\_of\\_Earth](http://en.wikipedia.org/wiki/Gravity_of_Earth)).

As seen from the above equation, there exist an infinite number of natural frequencies. However, only the fundamental frequency ( $m=1$ ) is significant for marine engineering application (Su et al., 1982). In our experimental study only the first natural frequency of the first sloshing mode is considered.

It should be noted that resonant sloshing is an ideal scenario difficult to achieve in experiments due to the accuracy in the natural frequency of sloshing. Furthermore, Hill (2003) and Chen and Nokes (2005) pointed out that the first natural frequency is shifted due to the nonlinearity of sloshing and the effect of the viscosity of the fluid. The accuracy of the calculation of the real natural frequency is further decreased by the precision of the parameters used in Eq. (5-1) which were measured during experiments. Therefore, in the following resonant sloshing case, the excitation frequency is close to but is not necessarily exact the natural frequency of liquid

sloshing. Based on the estimation of the first natural frequency, a series of experiments near the resonance frequency were done to investigate violent sloshing phenomenon.

In our experiment study, the shake table displacement is sinusoidal and governed by  $x = A(1 - \cos \omega t)$ , where  $A$  is the amplitude of excitation and  $\omega$  the excitation frequency. Initially we used the excitation displacement  $x = A \sin \omega t$  for  $t \geq 0$ , as many investigators adopted it such as Faltinsen (1978) and Wu et al. (1998). The corresponding velocity is  $u = A\omega \cos \omega t$  in this case. For the shake table given an initial condition with a non-zero velocity, there will be a big initial impulse occurring in a very short time. Using  $x = A(1 - \cos \omega t)$ , the initial velocity  $u = A\omega \sin \omega t$  is zero. This is found to help reduce the initial impulse of the shake table. Ideally, the initial conditions of the shake table should be  $x_{t=0} = 0$ ,  $\dot{x}_{t=0} = 0$  and  $\ddot{x}_{t=0} = 0$ . A more effective way is to introduce ramping function which reduces the influence of the initial velocity and acceleration, as also pointed out by Faltinsen et al. (2000). Nevertheless, in this study we adopted the displacement of shake table  $x = A(1 - \cos \omega t)$  for simplicity. One example of the recorded displacement of the shake table is plotted and shown in Figure 5-17. The excitation amplitude is  $A = 5$  mm and the excitation frequency  $\omega = 6.85$  rad/s (1.09 Hz).

Tap water is used in the experiments and the property of water including viscosity is considered in CPM simulation. The animations of water sloshing by CPM as well as the experiments recorded by high speed camera of most of the cases presented in this chapter (except cases for parametric study) are recorded in the attached CD.

### 5.3.1 Experiments of sloshing waves in high-filling tank

Depending on the liquid filling height in the tank, the sloshing waves can be in the form of a standing wave, a traveling wave or a bore (Wu et al., 1998). Armenio and La Rocca (1996) have found that these three types of wave scenario may all appear depending on the ratio of filling depth over tank length, i.e.  $d/L$ . In this section, experiments are designed to observe the free-surface elevation under relative high filling depth where  $d/L \geq 0.5$  since Chen et al. (2008) and Lloyd's Register (2005) have pointed out that the sloshing is most severe when the filling depth ( $d$ ) is from nearly 50% to 70%  $H$ , where  $H$  is the tank height.

In the study of sloshing in high-filling water tank, a tank with dimension 0.6 m ( $L$ ) x 0.6 m ( $H$ ) x 0.3 m ( $B$ ) is used. The filling depth of the tank is 0.3 m with the ratio  $d/L = 0.5$ . The parameters of the tank and liquid are shown in Table 5-1. The first natural frequency is calculated by Eq. (5-1) as 6.85 rad/s.

With the parameters of the tank and liquid listed in Table 5-1 four different cases are considered with different excitation frequencies. The frequency ratios of the excitation frequency ( $\omega$ ) to the natural frequency ( $\omega_0$ ) of the sloshing system examined in this section are  $\omega/\omega_0 = 1.0, 1.1, 0.9, 0.583$  respectively. The frequency ratios were also used by Wu et al. (1998) in their sloshing study by FEM. In all the four cases, the excitation amplitudes are the same as  $A = 5$  mm.

#### 5.3.1.1 Resonant water sloshing with $\omega/\omega_0 = 1$

When the frequency of the external excitation is close to the natural frequency of the sloshing system, resonant sloshing occurs. The time history of the free surface

elevation at  $P_1$  is shown in Figure 5-18. One can see in the figure that the wave amplitude increases with time until steady state is reached.

The MPS method is first used to simulate the case and the time history of the free surface elevation is plotted in Figure 5-18 for comparison. As can be seen in the figure, the MPS method can reasonably simulate the overall free surface elevations although there is some phase difference as compared with the experimental results. This may be due to the small difference of the excitation frequency assumed in the MPS method from the actual excitation frequency in the experiment. The overall sloshing trend and wave profile can reasonably be modeled in the MPS method. Typical wave profiles at two different time instants ( $t=2.10$  s and  $t=4.35$  s) are shown in Figure 5-19 (b) in comparison with the experimental results presented in Figure 5-19 (a). The general sloshing phenomenon of liquid in the tank is represented fairly well by MPS and agrees with the experimental results. It is seen in the figure that there are some “hot” spots where particles are tightly spaced and some “cold” spots where particles are loosely spaced (see zoom-in figures in Figure 5-19 (c)). These hot spots indicate too high number density and cold spot too low number density, implying that the incompressibility condition is not well enforced.

Nevertheless, as mentioned in Chapter 4, the pressure fluctuation in the MPS method is severe. The pressure contours at the same time instants are shown in Figure 5-20 with local zoom in at the bottom corners. We can see that the pressure distribution in the liquid is not smooth. A large number of particles with zero pressure value occur inside the fluid domain below the free surface (dark points in the zoom-in figures). This greatly affects the pressure field and thus inaccurate pressure distribution is obtained.

As proposed in Chapter 3, there are several ways to improve the pressure fluctuation in the original MPS method. The arc method for free surface particle recognition is the first improvement (Sect. 3.3.3). Another improvement relates to enforcing the incompressibility condition of the free surface particles (Sect. 3.3.3).

The same case of resonant sloshing is studied to demonstrate the effects of the two improvements mentioned above. With the two improvements incorporated in the original MPS method, the sloshing waves are better simulated. Figure 5-21 shows the particle distributions at the same time instants are more regular compared with the original MPS simulation results in Figure 5-19. The hot and cold spots practically disappear in the figure. The pressure contours at these two time instants are plotted in Figure 5-22. Compared with the results shown in Figure 5-20 using the original MPS method, the pressure contours are considerably smoother. The problem of spurious zero pressure inside the fluid domain also vanishes. It can reasonably be inferred that the numerical solution of pressure contour represents the actual one generally well.

Nevertheless, even with the two improvements in the MPS method, the high frequency pressure fluctuation still appears in the time signal of pressure. Figure 5-23 shows the time history of pressure at  $P_2$ . The comparison between the original MPS solution and experimental results is made in Figure 5-23 (a). The pressure fluctuation obtained by the original MPS method is very large with amplitude of fluctuation up to 2-3 times of the actual pressure value. The fluctuation is so severe that it masks the actual trend of the pressure variation due to sloshing. With the arc method for free surface recognition used in the MPS method, the pressure fluctuation is greatly reduced (Figure 5-23 (b)). The amplitude of fluctuation is reduced to less than the actual pressure value. When the incompressibility adjustment (IA) of the free surface

particles is also introduced, the fluctuation of pressure is further reduced (Figure 5-23 (c)). The amplitude of the hydrodynamic pressure can be better estimated in this case.

Now the CPM as proposed in Chapter 3 is used to simulate the same case of resonant sloshing. The particle distribution and pressure contours at the same time instants are shown in Figure 5-24 and Figure 5-25, respectively. It can be seen that the particle distribution in CPM simulation is quite regular even near the free surface. The pressure contours are much smoother compared with those obtained by MPS in Figure 5-22.

The pressure history at  $P_2$  is shown in Figure 5-26. The comparison of the pressure solution with experimental result shows excellent agreement. Due to enforcement of the incompressibility condition for all the fluid particles, there are only some minor fluctuations of the pressure values when the sloshing amplitude becomes large. It can be easily improved by imposing some artificial compressibility of the fluid, as introduced by Hu and Kashiwagi (2004) and Khayyer and Gotoh (2009). In our study we do not implement this since the fluctuation is so minor that it can be neglected. A little phase difference is observed after 6 s. This difference is likely due to the frequency ratio ( $\omega/\omega_0$ ) used in the experiment is not exactly the same as the one assumed in the numerical model.

To show the great improvement achieved by CPM over the original MPS, the pressure solutions are plotted together in Figure 5-27 in comparison with the experimental result. The tremendous improvement of the pressure history in the proposed CPM shows the capability of the new particle method in simulation water sloshing.

The comparison of the free surface elevation at  $P_1$  using the proposed CPM with the experimental result is shown in Figure 5-28. Excellent agreement can be seen in this figure. Again some phase difference after 6 s is also observed, similar to the pressure history in Figure 5-26.

The free surface profiles at different time instants simulated using CPM are shown in Figure 5-29. There is a very good agreement between numerical solutions and experimental results. Standing waves are observed in the tank. The free surface becomes higher and higher with time increase during the resonant sloshing until steady state. Nonlinear sloshing wave with sharp crest and flat trough is observed. It can be seen in Figure 5-29 that the pressure contours exhibits a reasonable trend and without irregular pressures inside the fluid domain. The animations of CPM simulation and experiments of this case are recorded in the attached CD with file name “Slosh\_1\_0.avi”.

#### **5.3.1.2 Water sloshing with $\omega/\omega_0=1.1$**

Besides resonant sloshing, it is interesting to study waves under excitation frequency near natural frequency. As pointed out by Wu et al. (1998), when the external excitation frequency is slightly away from the natural frequency, modulated waves can be obtained. This is also called “beating phenomenon” by some other investigators (Pal et al., 1999; Faltinsen et al., 2000; Cho and Lee, 2004). In order to show this, an excitation frequency ratio  $\omega/\omega_0=1.1$  is considered in this section.

Similar to the resonant sloshing case, an experimental test was performed with  $\omega/\omega_0=1.1$  and excitation amplitude  $A=5$  mm. The MPS method is used first to simulate the sloshing waves. The comparison of the time history of the free surface

elevation using the MPS method and experimental results is shown in Figure 5-30. The beating phenomenon is captured by the wave probe in the experiment. The wave amplitude is modulated with a clear envelop. The period of the envelope is approximately 9.5 times of the period of the sloshing waves. The solutions of the free surface using MPS method in general agree with the experimental results before  $t=4$  s. However, after that the beating waves are not successfully represented. The envelope of the modulated waves cannot be observed. The comparison of the hydrodynamic pressure measured at point  $P_2$  is shown in Figure 5-31. It is again shown that the pressure fluctuation using the original MPS method is very severe.

Next, the CPM is used. The solutions of the free surface and pressure are presented in Figure 5-32 and Figure 5-33, respectively. It is clearly shown that the numerical simulations give excellent agreement with the experimental data, in terms of both the free surface elevation and pressure. In particular, Figure 5-32 shows that the beating phenomenon is successfully captured in the CPM simulation. The period of the envelope of the beating waves agree well with the experiments. In Figure 5-33, the pressure history presents a reasonable trend without obvious spurious fluctuation and matches with the experimental results very well. Some spikes in the experimental results are shown in the figure. This is caused by the shake table for which the hydraulic actuator motion may not be smoothly produced, i.e. it generates sudden acceleration during each start of back and forth motion when the direction of motion is changed.

The free surface profiles at different time instants simulated using CPM are shown in Figure 5-34. It can be seen that standing waves are present in the rectangular tank. Good agreement between numerical solutions and experimental results is found.

With the excitation ratio  $\omega/\omega_0 = 1.1$  in this case, the sloshing wave is modulated at around 7.95 s, when the free surface elevation becomes nearly flat. After that, the wave again becomes higher until it comes to the end of the next beating period. It is also shown in Figure 5-34 that the pressure contours are smooth at every time instant. The animations of CPM simulation and experiments of this case are recorded in the attached CD with file name “Slosh\_1\_1.avi”.

### 5.3.1.3 Water sloshing with $\omega/\omega_0 = 0.9$

Wu et al. (1998) have proved that for the small amplitude sloshing, the frequency of the envelop of the beating waves is governed by  $\Delta\omega = \omega - \omega_0$  and its period is  $2\pi/\Delta\omega$ . That means the excitation frequency ratios  $\omega/\omega_0 = 1.1$  and  $\omega/\omega_0 = 0.9$  would present the same envelope of the beating waves. For large amplitude sloshing however, where nonlinearity affects the natural frequency of the sloshing waves, exactly the same envelopes of the two ratios cannot be obtained. But similar beating waves and close beating frequency are expected.

Hence in this section, we studied the water sloshing waves under external excitation frequency  $\omega/\omega_0 = 0.9$  experimentally and numerically. The numerical solutions using MPS method are shown in Figure 5-35 and Figure 5-36 for free surface elevations and pressure history, respectively. Again the envelope of the beating waves is not represented in the MPS method. The pressure fluctuation shown in Figure 5-36 is large, similar to the results of excitation frequency ratio  $\omega/\omega_0 = 1.1$ .

The simulation results using CPM are shown in Figure 5-37 and Figure 5-38. Both the free surface elevation and the pressure solutions agree well with the experimental results. The envelope of the beating waves is well simulated in the

proposed CPM. Similar to the case with  $\omega/\omega_0=1.1$ , pressure spikes in the experimental result are also shown in Figure 5-36 and Figure 5-38. The free surface profiles at different time instants are very similar to the profiles shown in Figure 5-34 for the excitation ratio  $\omega/\omega_0=1.1$ , and hence these as well as the animation are not presented.

#### **5.3.1.4 Water sloshing with $\omega/\omega_0=0.583$**

The previous three cases study the sloshing waves in 50% filling tank with excitation frequency close to the natural frequency. When the excitation frequency is far away from the natural frequency, the sloshing effect is not significant. An excitation frequency ratio  $\omega/\omega_0=0.583$  used by Wu et al. (1998) is used in the experiment.

The free surface elevation and pressure history based on the original MPS method are shown in Figure 5-39 and Figure 5-40, respectively. The simulation results obtained by the proposed CPM are shown in Figure 5-41 and Figure 5-42. Pressure spikes in experimental results are also observed for  $\omega/\omega_0=0.583$ . Both MPS and CPM can give good agreement with the experiments in term of the free surface elevations. But the CPM simulation gives smoother pressure history compared with MPS method.

It can be seen from Figure 5-41 and Figure 5-42 that the sloshing waves under excitation frequency  $\omega/\omega_0=0.583$  are not significant. The hydrodynamic pressure due to sloshing waves can be neglected compared with the hydrostatic pressure. Hence sloshing under excitation frequency far away from the natural frequency is not a concern in the study of liquid sloshing.

### 5.3.1.5 Parametric study of excitation frequencies at the same filling depth

To further demonstrate the effects of the external excitation frequencies, the maximum free surface elevations of the sloshing waves for different excitation frequencies ( $\omega / \omega_0 = 0.583, 0.9, 1.0, 1.1, 1.417$ ) are plotted in Figure 5-43. Numerical solutions by CPM are also presented for comparison in the figure with dashed lines. For all the cases, the filling depths of the tank are 50%, the excitation amplitudes are  $A=5$  mm.

In order to compare the extreme free surface elevations, the minimum free surface elevations are plotted with their absolute values. In Figure 5-43 it can be seen that the CPM solutions (dashed lines) of the extreme wave elevation agree with the experimental results (solid lines). As expected, the sloshing amplitude of free surface is large when the excitation frequency is close to the natural frequency.

It is interesting to note in Figure 5-43 that the absolute value of the minimum elevation of the sloshing waves is much lower than the maximum elevation. This is a result of wave nonlinearity, where sharp wave crest and flat trough appear in nonlinear waves (Wu et al., 1998; Wang and Khoo, 2005). It is also seen in the figure that the nonlinearity becomes more significant when the sloshing is close to resonance, where the difference between the crest and trough is the largest.

Figure 5-44 plots the maximum and minimum hydrodynamic pressure with different excitation frequencies. Again it can be seen that the CPM solutions agree well with experimental results. As the figure shows, the absolute value of the minimum hydrodynamic pressure is not significantly different from the maximum

hydrodynamic pressure. Nonlinearity of the sloshing waves is less significant in pressure than in wave elevation.

#### **5.3.1.6 Parametric study of excitation amplitudes at the same filling depth**

In real situations, LNG carriers often encounter random waves of different frequencies and amplitudes. Therefore, besides the study of the excitation frequencies, different excitation amplitudes should also be considered in sloshing experiments.

Resonant sloshing with different excitation amplitudes is studied experimentally and numerically. The filling depth of the tank is the same as before, i.e. 50% filling of the tank height. Four different excitation amplitudes, namely 5 mm, 12.5 mm, 15 mm, 20 mm are used in the study. The extreme free surface and pressure are shown in Figure 5-45 and Figure 5-46, respectively. The CPM solutions (dashed lines) are in very good agreement with experimental results (solid lines).

From the maximum and minimum free surface elevations shown in Figure 5-45, one can see that with increasing excitation amplitude, the maximum and minimum free surface elevation increased almost linearly, with the increasing rate of the minimum free surface elevation smaller than that of the maximum. This indicates that as the excitation amplitude increases, nonlinearity of the sloshing wave increases and gives flatter trough.

Figure 5-46 presents the maximum and minimum hydrodynamic pressure with different excitation amplitudes. With larger excitation amplitude, the hydrodynamic pressure increases in an approximately linear manner. The CPM solutions of extreme pressure agree very well with the experimental results.

### 5.3.1.7 Parametric study of filling depths with the same excitation amplitude

As discussed before, the sloshing waves in high-filling level tanks exhibit the standing wave types. The comparison of the sloshing waves under different filling depths is worthy of investigation.

Resonant sloshing with excitation amplitude of 5 mm is studied in this section for five typical filling depths 25%, 50%, 60%, 70%, and 75%. Figure 5-47 shows that the maximum surface elevation occurs between 45% - 70% filling depths. This is in line with the guideline of Lloyd's Register (2008).

Figure 5-48 shows the normalized extreme hydrodynamic pressure versus the ratio of filling depth. The computed solutions by CPM are agreeable with the experimental data. It is interesting to see that the normalized extreme hydrodynamic pressure decreases almost linearly as the filling depth increases. It implies that the proportion of the hydrodynamic pressure decreases in the total pressure when the hydrostatic pressure is large with high filling depth.

### 5.3.1.8 Discussion

In this section, water sloshing in tank with filling depths  $50\%H$  and above are studied experimentally and numerically. The MPS method and the proposed CPM are applied to simulate water sloshing waves. The numerical solutions are compared with experimental results.

The solution of free surface elevation using the MPS method in general agrees with the experimental results. Nevertheless, the MPS solution of pressure history at a fixed position exhibits severe spurious fluctuation. In addition, the particle distribution in MPS simulation shows “hot” spots with particles too densely spaced

and “cold” spots with particles too loosely spaced (see Figure 5-19 and Figure 5-20). This indicates that the incompressibility condition is not satisfactorily enforced. The proposed ways to improve fluctuation in the MPS method, i.e. the arc method for free surface particle recognition and incompressibility adjustment of free surface particles, are proved to some extent to be effective to improve particle distribution (without obvious hot and cold spots) and help mitigate pressure fluctuation amplitude (see Figure 5-21).

The proposed CPM is applied to simulate water sloshing with different excitation conditions. The particle distribution in CPM simulation is regularly spaced with no hot or cold spot observed even near the free surface (Figure 5-24). The pressure contour of CPM solution is quite smooth. Compared with MPS results, the CPM solutions agree better with experimental results in terms of time histories of free surface elevation and especially pressure.

Different parameters which affect the sloshing waves are analyzed. It is concluded that a filling depth of approximately 45%-70% of the tank height produces the highest sloshing pressure and free surface elevation. The larger excitation amplitude produces higher free surface elevation and hydrodynamic pressure. Additionally, for various excitation frequencies, resonant frequency produces the largest free surface elevation and pressure. The conclusions from the research findings are consistent with other published results (Wu et al., 1998; Cho and Lee 2004; Ibrahim, 2005). In addition, the experimental data acquired form a valuable database which could be used to validate numerical models.

### 5.3.2 Experiments of sloshing waves in low-filling tank

Experiments and numerical simulations at partial filling levels in an LNG tank were investigated by many researchers, indicating that the sloshing motion in an LNG tank at the low-filling level is quite different from that experienced at the high-filling level (Ibrahim, 2005). In the low-filling case, a more distinct wave motion is observed in the tank compared with standing wave in high filling level. At the low-filling level, where the filling height is less than 20 percent of tank width (for lateral motion) or length (for longitudinal motion), a phenomenon known as a bore can be observed in the tank (Huang and Hsiung, 1996). The phenomenon can have some practical implications on the carriers. When tank motion is large, the front of the hydraulic run-up becomes steeper, developing a breaking wave. If the bore hits the bulkhead before breaking, large impact pressure can occur and damage the tank. The uniform velocity of the traveling wave also results in a large drag force on the lower part of the pump tower and its supporting system, which is an additional load on the system that must be considered when designing storage tanks on the carriers. Armenio and La Rocca (1996) have reported that, depending on the ratio of fluid depth to breadth of tank, a combination of standing wave, traveling wave and a bore may exist. The same observation was made by Wu et al. (1998) using a FEM simulation. Therefore it is of interest to see the CPM performs in simulating sloshing waves in relatively shallow filling depth.

In this study, a tank with dimension 0.6 m ( $L$ ) x 0.6 m ( $H$ ) x 0.3 m ( $B$ ) is used. The filling depth of the tank is 0.03 m with the ratio  $d/L < 20\%$ . The parameters of the tank and liquid are shown in Table 5-2. The first natural frequency is calculated by Eq. (5-1) according to the tank dimensions and filling condition. Resonant sloshing is

considered with external excitation frequency close to the first natural frequency of the sloshing system. The excitation amplitude used in this study is 0.01 m.

Typical wave profiles at several time instants are shown in Figure 5-49 to Figure 5-56. Good agreement is observed between the CPM solutions and experimental results.

From Figure 5-49 to Figure 5-56, it is observed that traveling wave does not appear immediately after the tank starts to move. Instead, there is a transient period during which the wave changes gradually from a standing wave to a traveling wave (i. e. one wave crest traveling in the tank). After the initial formation of the traveling wave ( $t=4.80$  s), multi-crest traveling waves form ( $t=6.10$  s). At about  $t=6.75$  s the wave crest hits the right wall of the tank and hydraulic run-up of the water appear. The wave then falls back to the tank and results in the formation of bore ( $t=6.90$  s). Bores are formed when a wave travels towards an on-coming wave and superimposes with the on-coming wave. The bore only has a short duration of existence (less than 0.1 s) and splits into multi-crested traveling waves or, in some cases, breaks in the middle of the tank. As seen in the figures, at  $t=6.90$  s, on the left of the bore, the water surface is almost flat and the free surface elevation is very small; and on the right of the bore, the wave elevation is significantly higher. The bore quickly splits into multi-crested traveling waves ( $t=7.1$  s). After that, multi-crested waves travel in the tank and hit the left wall of the tank at  $t=7.85$  s, where the water run-up along the wall of the tank and breaking waves appear when the impact occurs. As can be seen from Figure 5-49 to Figure 5-56, the CPM solutions of water waves agree well with the experimental results.

The long time simulation of this example is performed and the time history of the free surface elevation at  $P_1$  is shown in Figure 5-57. It is shown in the figure that the CPM solution agrees very well with the experimental result. The comparison of pressure history at  $P_2$  is plotted in Figure 5-58. Again very good agreement between numerical simulation and experimental results is observed. The animations of CPM simulation and experiments of this case are recorded in the attached CD with file name “Slosh\_low.avi”.

The pressure contours at different time instants are shown in Figure 5-59. The pressure field of the liquid is smooth and stable. In addition, large total pressure occurs beneath the crest of the traveling waves and travels with the crest of the wave. Furthermore, when the wave peaks reaches the wall, the pressure around the wall is as expected larger than the hydrostatic pressure.

In order to illustrate the bore formation more clearly, the velocity fields of the particles are shown in Figure 5-60 at the time when a bore is generated. It is shown in the figure, at  $t=6.75$  s the first crest of the traveling wave hits the right wall of the tank. Breaking particles appear during the impact. After that the water particles fall back to the main water body with velocities in the reverse direction ( $t=6.80$  s). The wave then travels towards the second wave crest and superimposes with this on-coming wave, as shown in the figure (from  $t=6.80$  s to  $t=6.90$  s). The superimposed wave elevation becomes highest at  $t=6.90$  s, where bore formation is clearly observed. After that the two wave crests split (at about  $t=6.95$  s) and travel in opposite directions (from 6.95 s to 7.10 s) until the second wave crest impacts with the tank wall and reverses its direction of travel.

### 5.3.3 Experiments with sloshing wave impact on the tank ceiling

In the previous sections, liquid sloshing in deep and shallow water depths are studied numerically and experimentally, with the main focus on resonant sloshing. Breaking wave on the tank ceiling due to sloshing is not investigated since the two tanks used in the experiments are open. In order to investigate the breaking waves, a closed tank is built and breaking waves on the tank ceiling is studied.

A closed rectangular tank with dimension 0.57 m ( $L$ ) x 0.3 m ( $H$ ) x 0.3 m ( $B$ ) was build. The parameters of the tank and liquid are shown in Table 5-3. The filling depth of the tank is 60% which is 0.18 m. Sloshing waves under resonant excitation is considered with external excitation amplitude is 10 mm.

Figure 5-61 shows the free surface profiles of the liquid at different time instants inside the tank. The comparison between numerical simulation and experimental results shows good agreement. As shown in the figure, under resonant excitation frequency, the sloshing waves become higher and higher. Finally the wave reaches the top of the tank and breaking waves appear. It can be seen in the figure that the numerical solution successfully captures the appearance of breaking waves through breaking particles. The particle separation due to breaking and coalescence after falling back to the fluid is well represented by the proposed CPM. The animations of CPM simulation and experiments of this case are recorded in the attached CD with file name “Slosh\_breaking.avi”.

Since a closed tank was used in the experiment to study wave impacts onto the tank top, no wave probe could be inserted to measure the free surface elevation. Video camera was thus used in the experiment to record the wave profile. A transparent template with regular grid of 1 cm interval was glued to the front face of the tank to

facilitate measurement of free surface elevation. Hence the free surface elevation at the right wall of the tank could be obtained. The free surface elevation data is plotted in Figure 5-62 and compared with the CPM solution. It is shown in the figure that the CPM solution agrees very well with the experimental result. The free surface elevation gets higher and higher and quickly reaches to a constant value 0.3, which corresponds to the ceiling height of the tank.

Figure 5-63 plots the pressure contours at four representative time instants. It is shown in the figure that, the numerical simulation results present satisfactory pressure field. The pressure contours are smooth even when breaking waves occur. One can observe in the figure that when sloshing waves reach the tank ceiling, the impact pressure generated at the corner of the tank ceiling become high (at 4.56 s and 8.44 s).

Due to the sensor constraint, we did not measure the impact pressure at the tank ceiling. The CPM solutions of pressure history at the two corners of the left wall (marked in Figure 5-63) are shown in Figure 5-64 (left bottom corner  $P_2$ ) and Figure 5-65 (left ceiling corner  $P_1$ ). By comparing the two figures it can be seen that the impact pressure at ceiling corner  $P_1$  is very high (about 1700 Pa) and even larger than the hydrodynamic pressure at bottom corner  $P_2$ . More severely, the impact occurs in very short time instant, as shown in Figure 5-65. Impact pressure due to sloshing is another important aspect which should be addressed in future study.

## **5.4 Concluding remarks**

In this chapter, sloshing waves in rectangular tanks are studied experimentally and numerically.

Sloshing in deep water exhibits nonlinear standing waves. The highest free surface elevation and largest hydrodynamic pressure are observed when resonance occurs. Larger excitation amplitude produces higher free surface elevation and hydrodynamic pressure. A filling depth of approximately 45%-70% $H$  produces the highest sloshing pressure and free surface elevation. Sloshing in low-filling tank produces traveling waves which lead to the formation of bore when they superpose one another. Breaking waves with high impact pressure at the tank ceiling appear due to violent liquid sloshing in a closed tank.

The MPS solution of pressure history in liquid sloshing exhibits severe spurious fluctuation. The proposed two ways to improve pressure fluctuation in MPS method, i.e. the arc method for free surface particle recognition and incompressibility adjustment of free surface particles, are shown effective to improve particle distribution and help suppress pressure fluctuation amplitude.

The CPM simulation of liquid sloshing presents evenly distributed particle distribution without hot or cold spot. The formation of the bore in low-filling sloshing and breaking waves with smooth pressure contours are successfully demonstrated in CPM simulation. The pressure contour of CPM solution is smooth even when breaking occurs. Compared with MPS results, the CPM solutions agree much better with the experimental results particularly in terms of particle distribution and pressure.



Table 5-1. Parameters of the tank and liquid for high-filling sloshing

$L$	Length of tank	0.6 m
$d$	Still water depth	0.3 m
$H$	Height of tank	0.6 m
$\rho$	Density of water	1000 kg/m <sup>3</sup>
$\mu$	Dynamic viscosity of water	1x 10 <sup>-3</sup> Pa.s
$g$	Gravity	9.78 m/s <sup>3</sup>
$\omega_0$	First natural frequency	6.85 rad/s

Table 5-2. Parameters of the tank and liquid for low-filling sloshing

$L$	Length of tank	0.6 m
$d$	Still water depth	0.03 m
$H$	Height of tank	0.6 m
$\rho$	Density of water	1000 kg/m <sup>3</sup>
$\mu$	Dynamic viscosity of water	1x 10 <sup>-3</sup> Pa.s
$g$	Gravity	9.78 m/s <sup>3</sup>
$\omega_0$	First natural frequency	2.825 rad/s
$A$	Excitation amplitude	0.01 m

Table 5-3. Parameters of the tank and liquid for high-filling sloshing with breaking

$L$	Length of tank	0.57 m
$d$	Still water depth	0.18 m
$H$	Height of tank	0.3 m
$\rho$	Density of water	1000 kg/m <sup>3</sup>
$\mu$	Dynamic viscosity of water	1x 10 <sup>-3</sup> Pa.s
$g$	Gravity	9.78 m/s <sup>3</sup>
$\omega_0$	First natural frequency	6.393 rad/s
$A$	Excitation amplitude	0.01 m



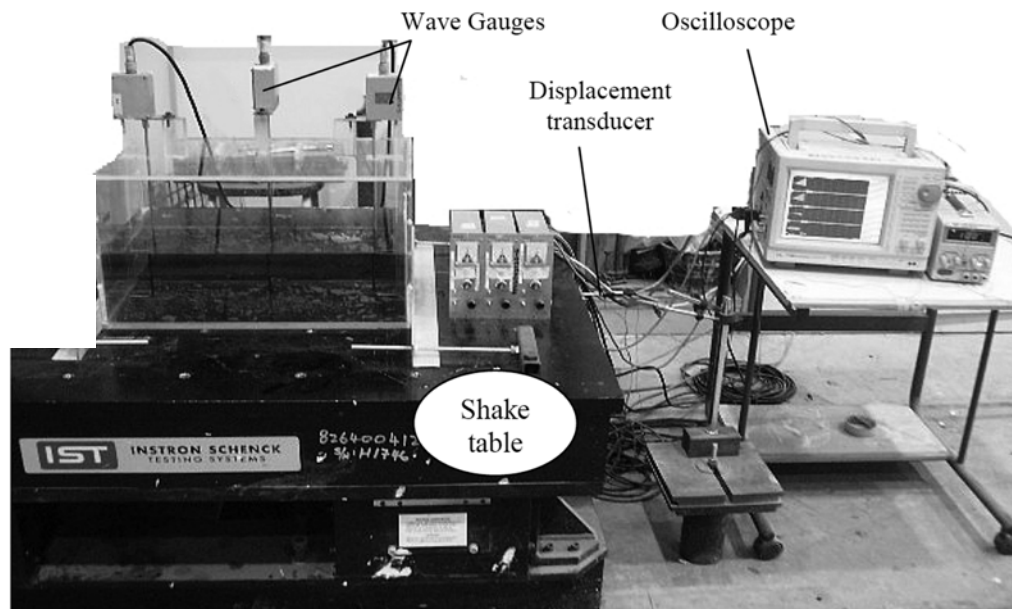


Figure 5-1. The experimental setup

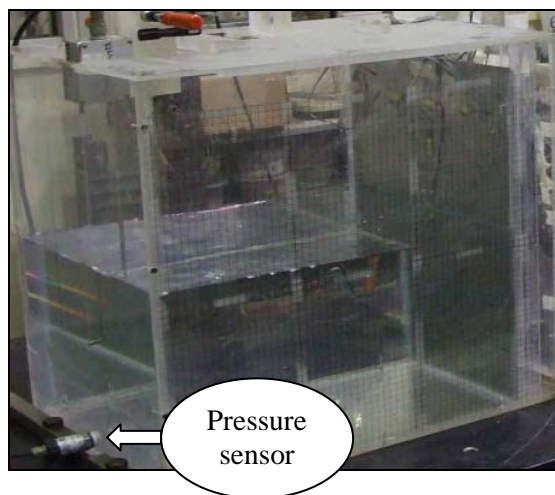


Figure 5-2. Tank with pressure sensor mounted

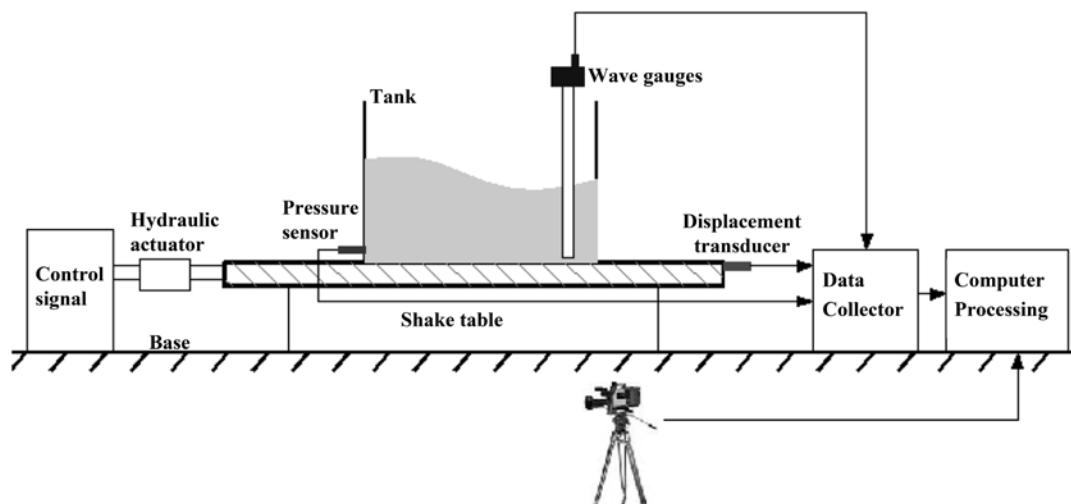


Figure 5-3. Experimental apparatus and working principle

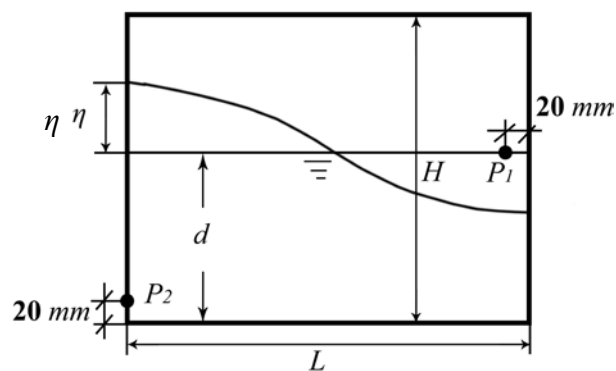


Figure 5-4. Definition of parameters for liquid sloshing in a rectangular tank

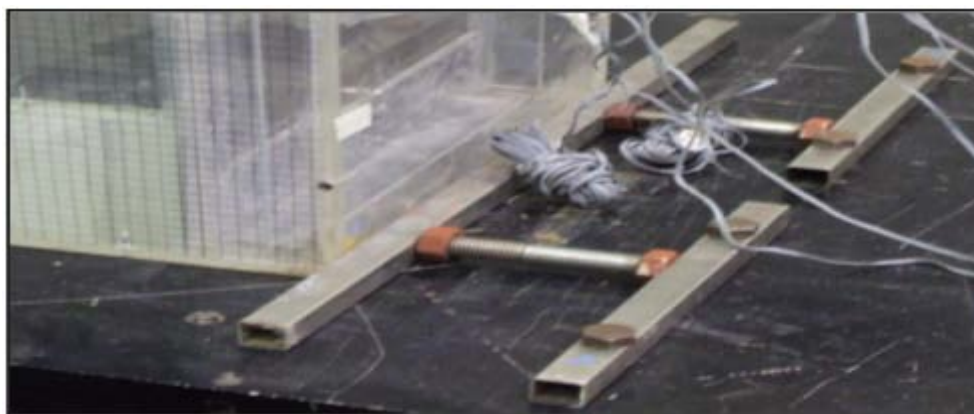


Figure 5-5. Fixing tools of rectangular tank on the shake table

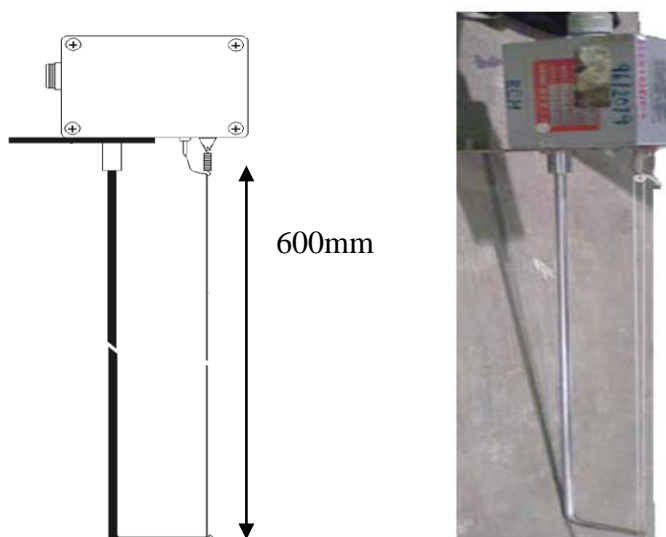


Figure 5-6. Schematic Diagram and picture of wave probe

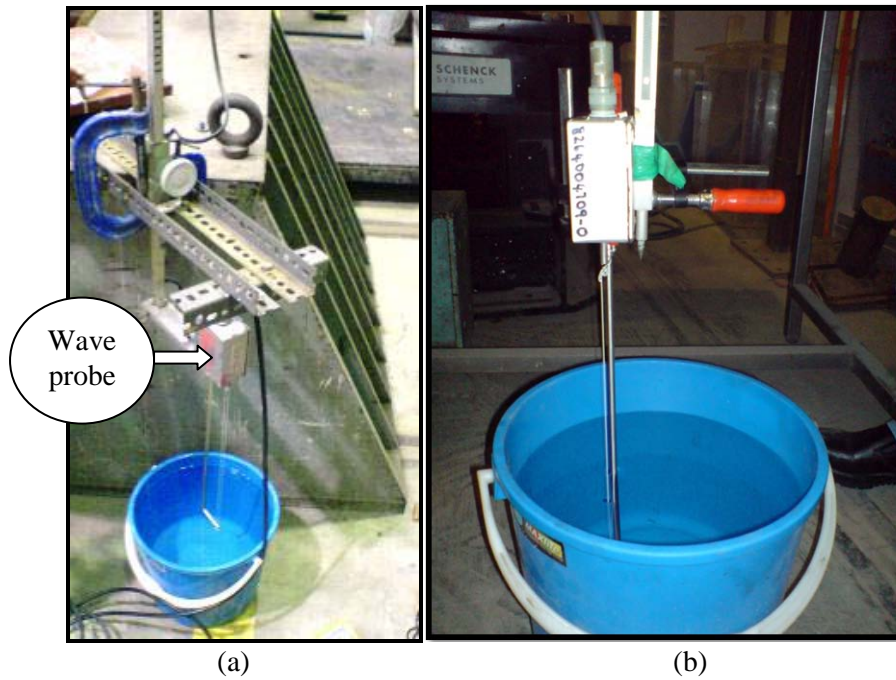


Figure 5-7. (a) Wave probe mounted to an adjustable stand (b) Calibration of the wave probes

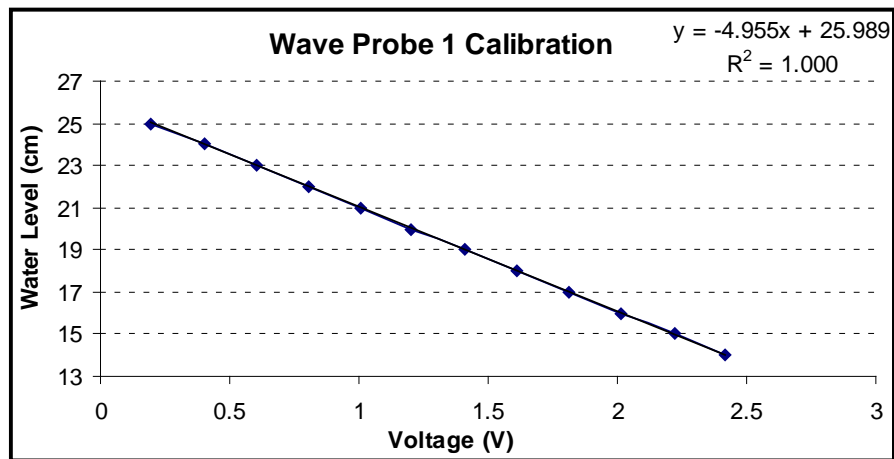


Figure 5-8. Calibration results of wave probe 1

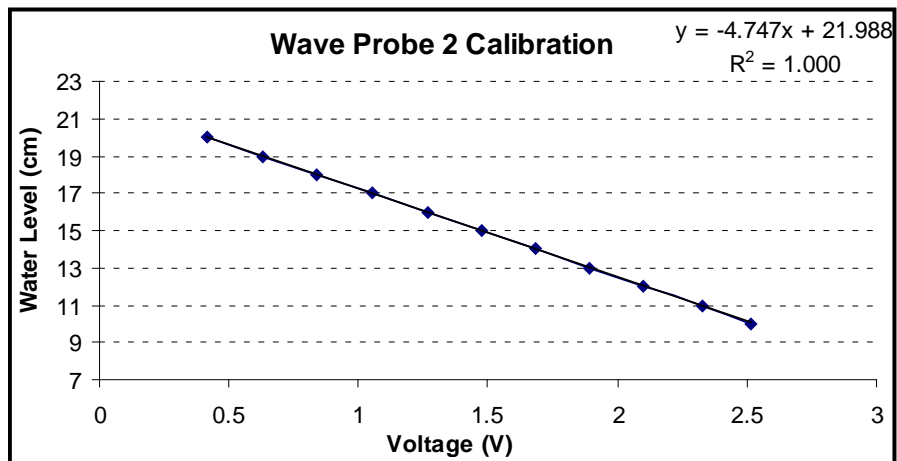


Figure 5-9. Calibration results of wave probe 2

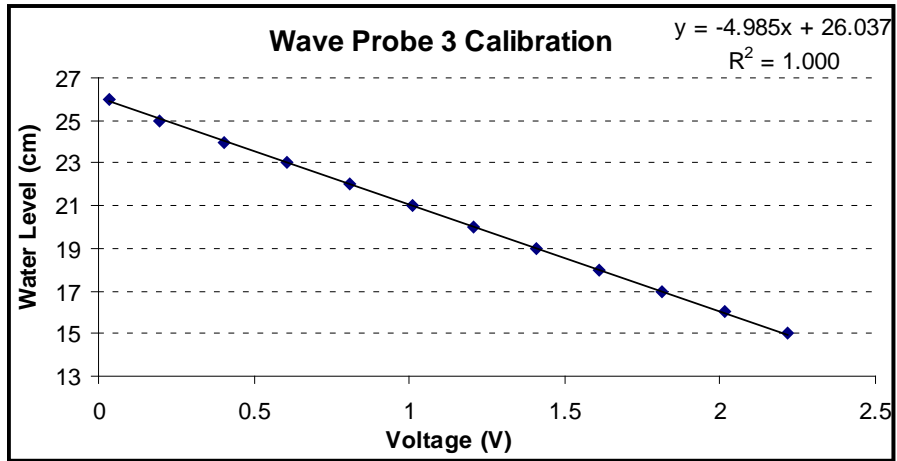


Figure 5-10. Calibration results of wave probe 3

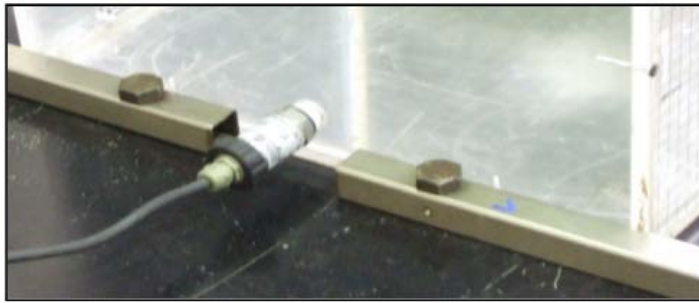


Figure 5-11. Experimental installation of pressure sensor

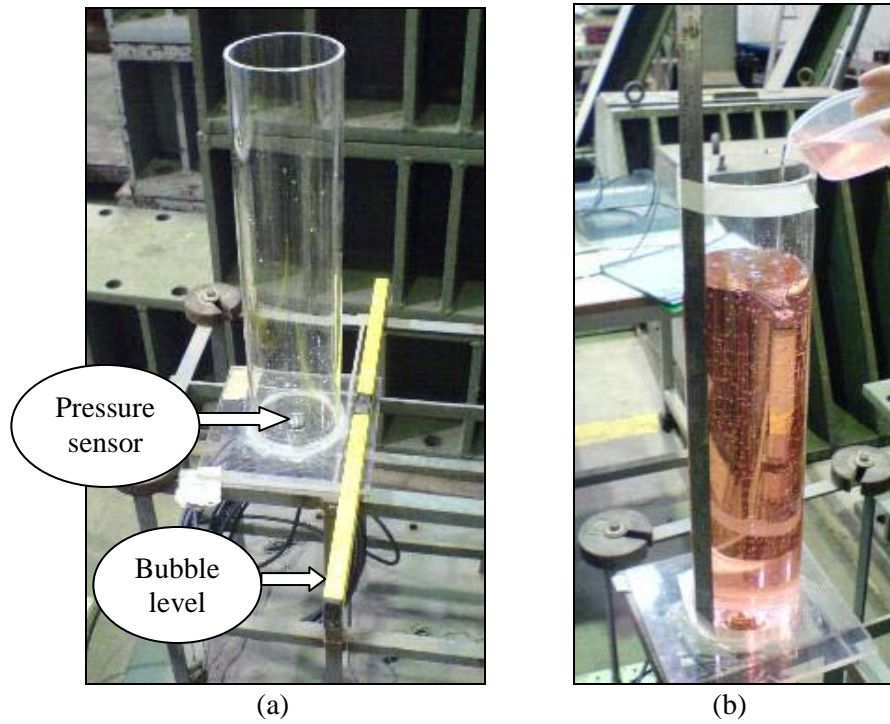


Figure 5-12. (a) Devices used for the calibration of pressure sensor (b) calibration of the pressure sensor

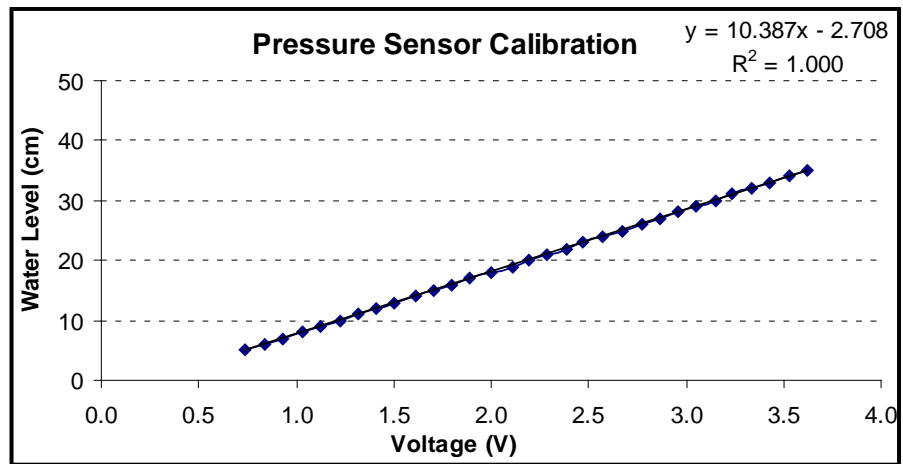


Figure 5-13. Calibration result of the pressure sensor

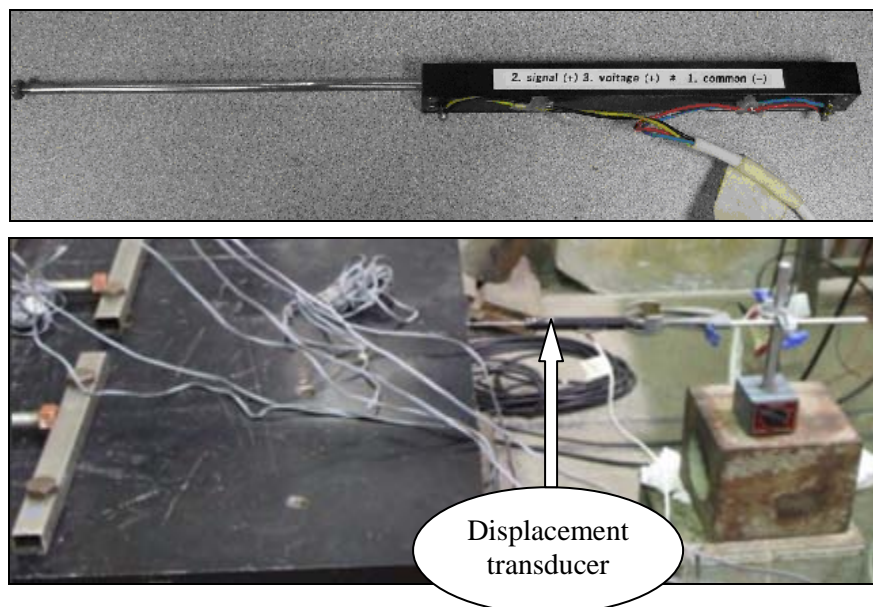


Figure 5-14. Displacement transducer and its experimental installation



Figure 5-15. High speed camera set-up

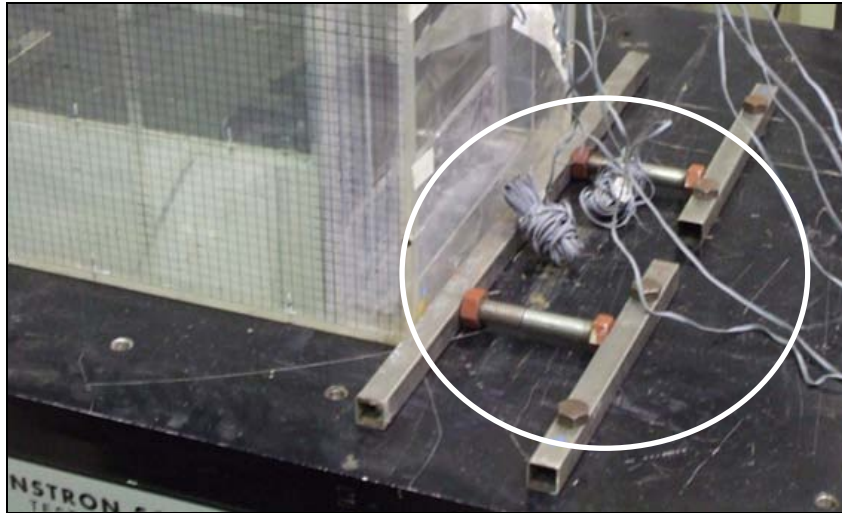


Figure 5-16. Securing technique

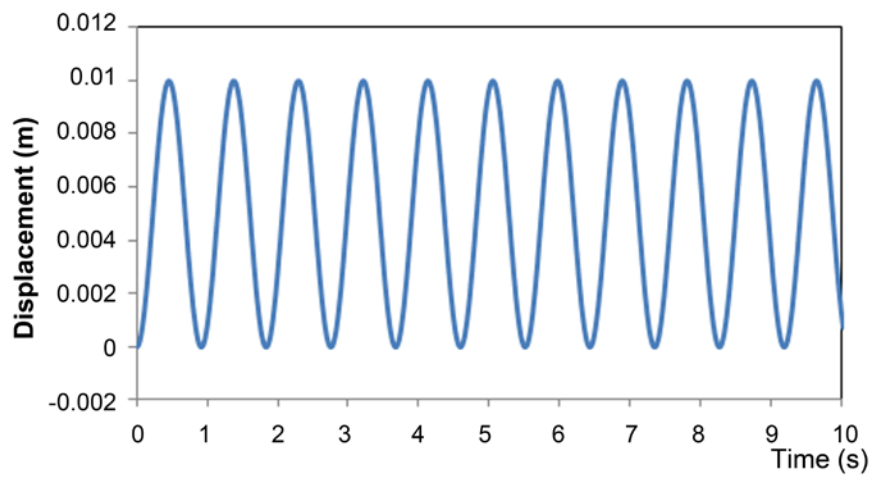


Figure 5-17. Displacement signal of shake table (5mm amplitude)

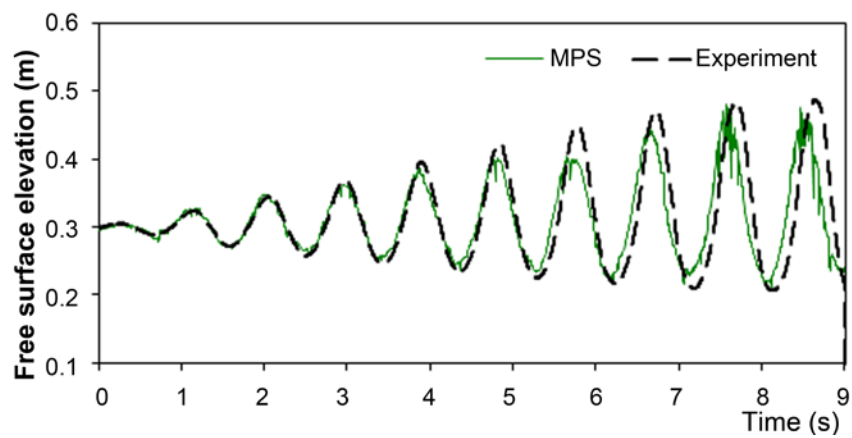


Figure 5-18. Comparison of free surface elevation at Point  $P_1$  ( $\omega / \omega_0 = 1.0$ )

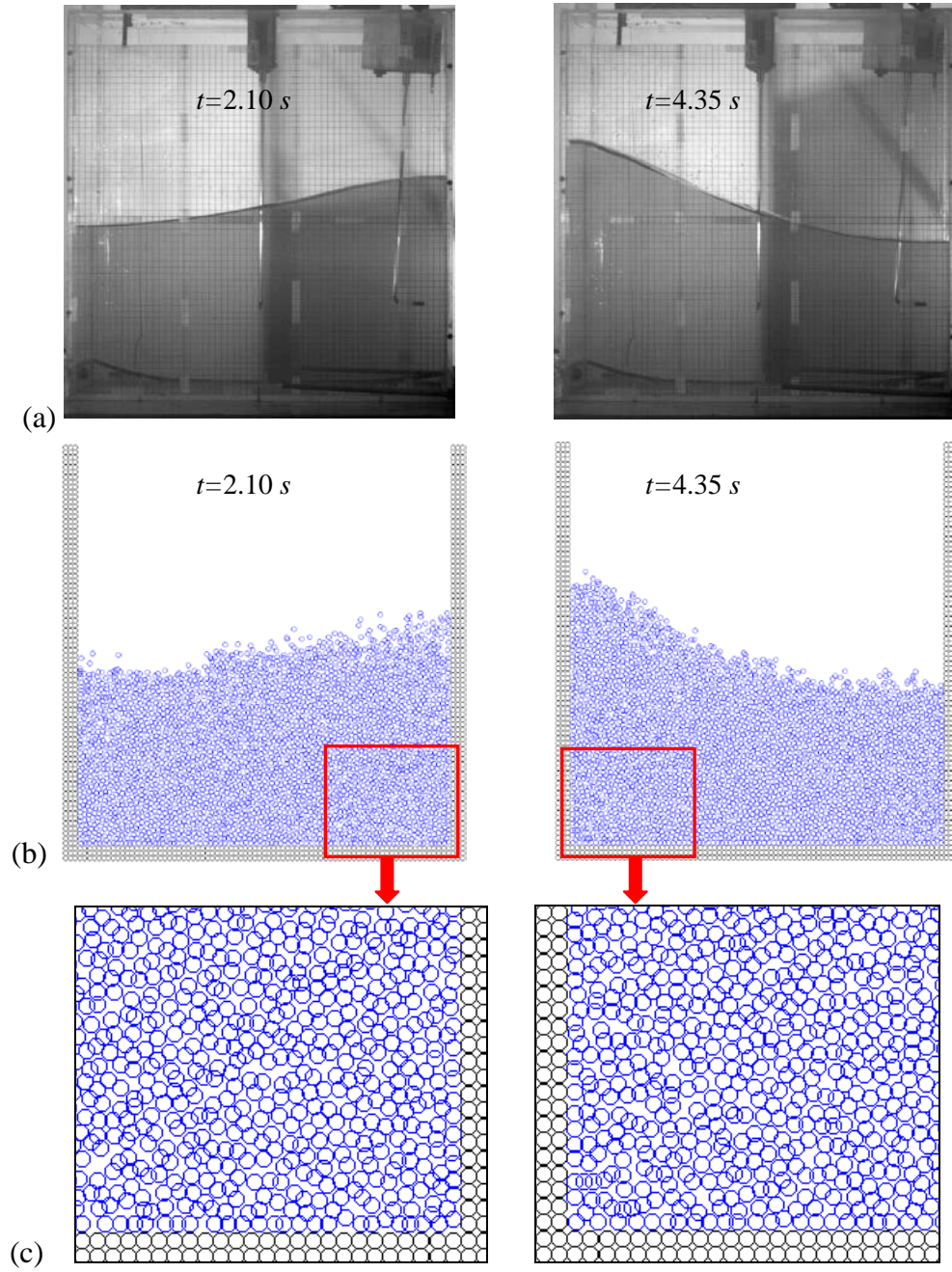


Figure 5-19. Particle distribution simulated by MPS method and comparison with experimental results

(a) Experimental results; (b) MPS results; (c) zoom in of part in (b)

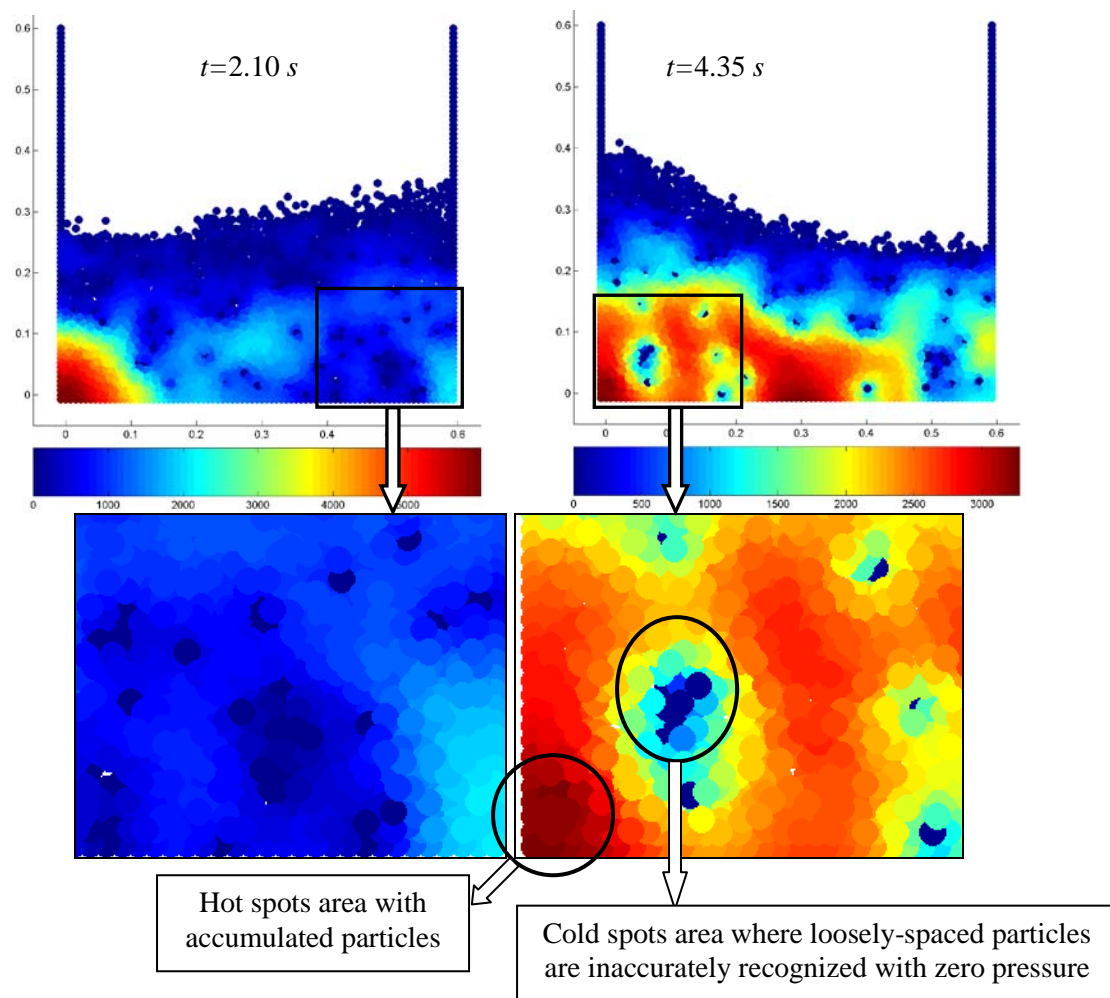


Figure 5-20. Pressure contours simulated by MPS method

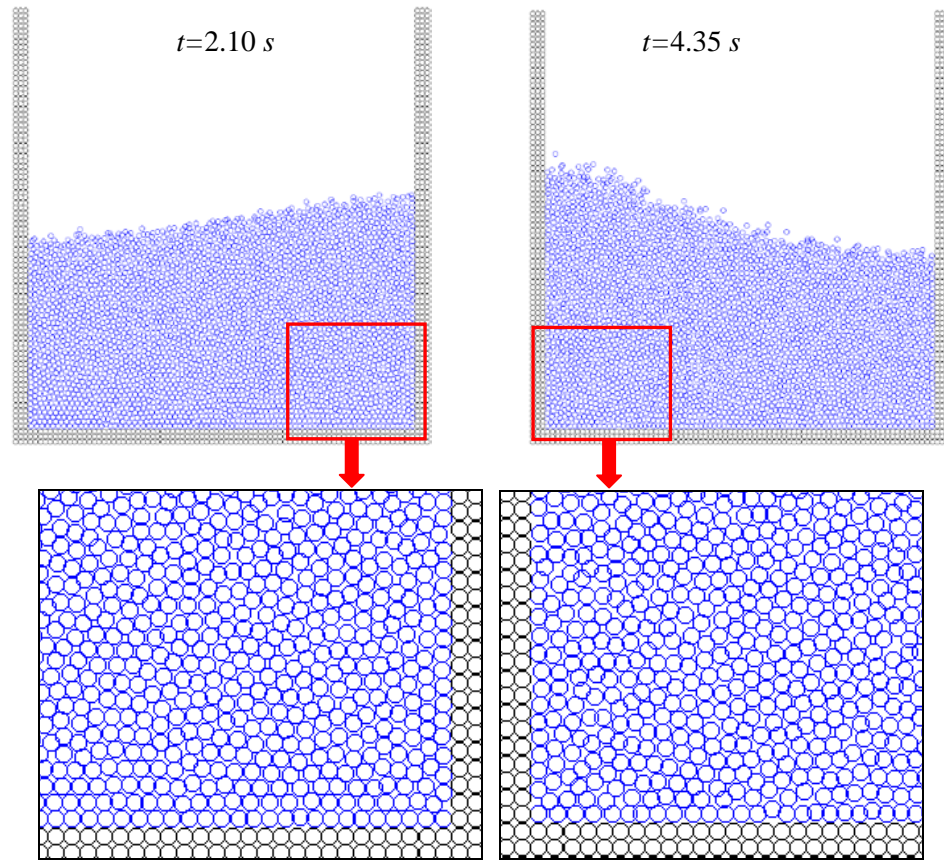


Figure 5-21. Particle distribution of MPS simulation with arc method and IA of free surface particles

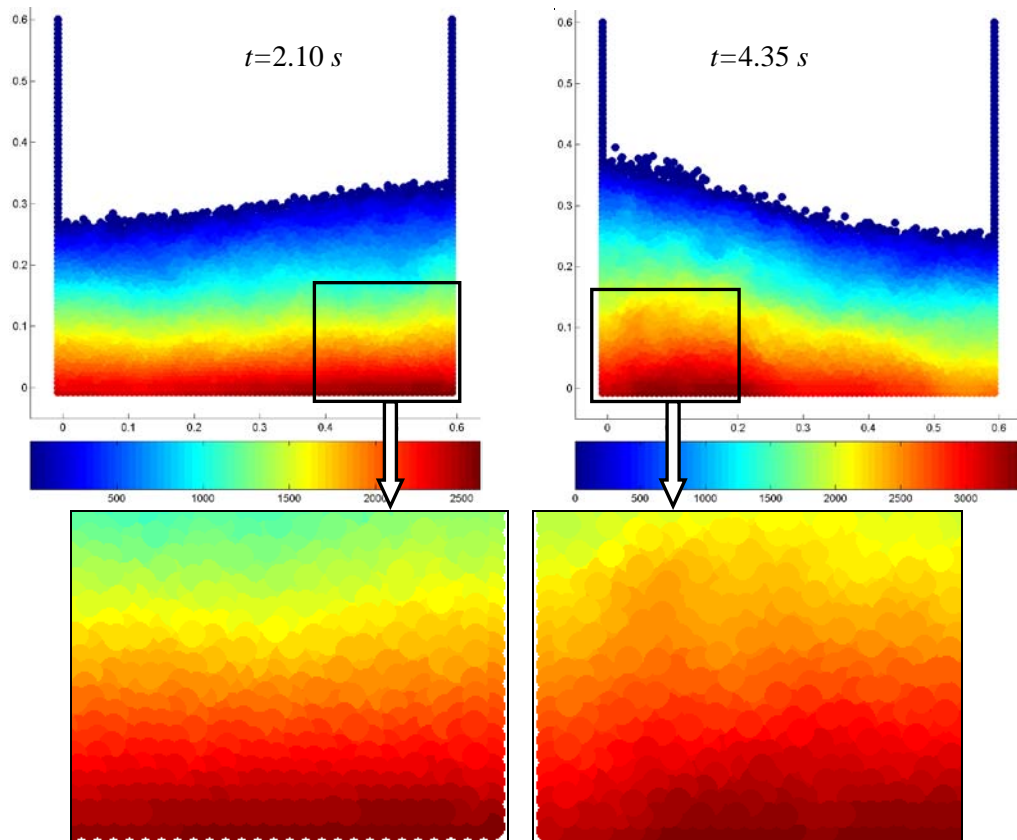


Figure 5-22. Pressure contours of MPS solution with arc method and IA of free surface particles

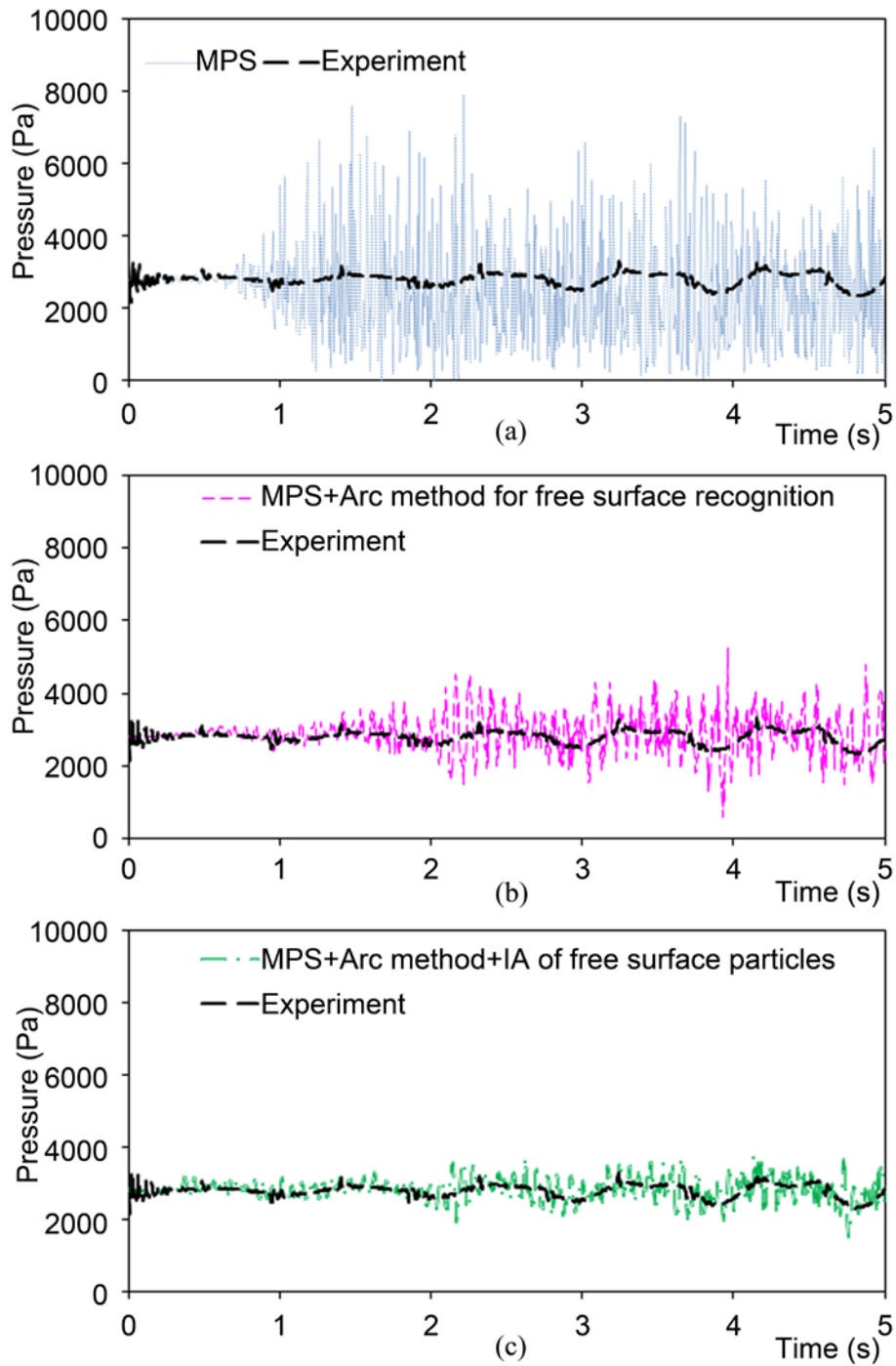


Figure 5-23. Comparison of pressure history at Point  $P_2$  ( $\omega / \omega_0 = 1.0$ )

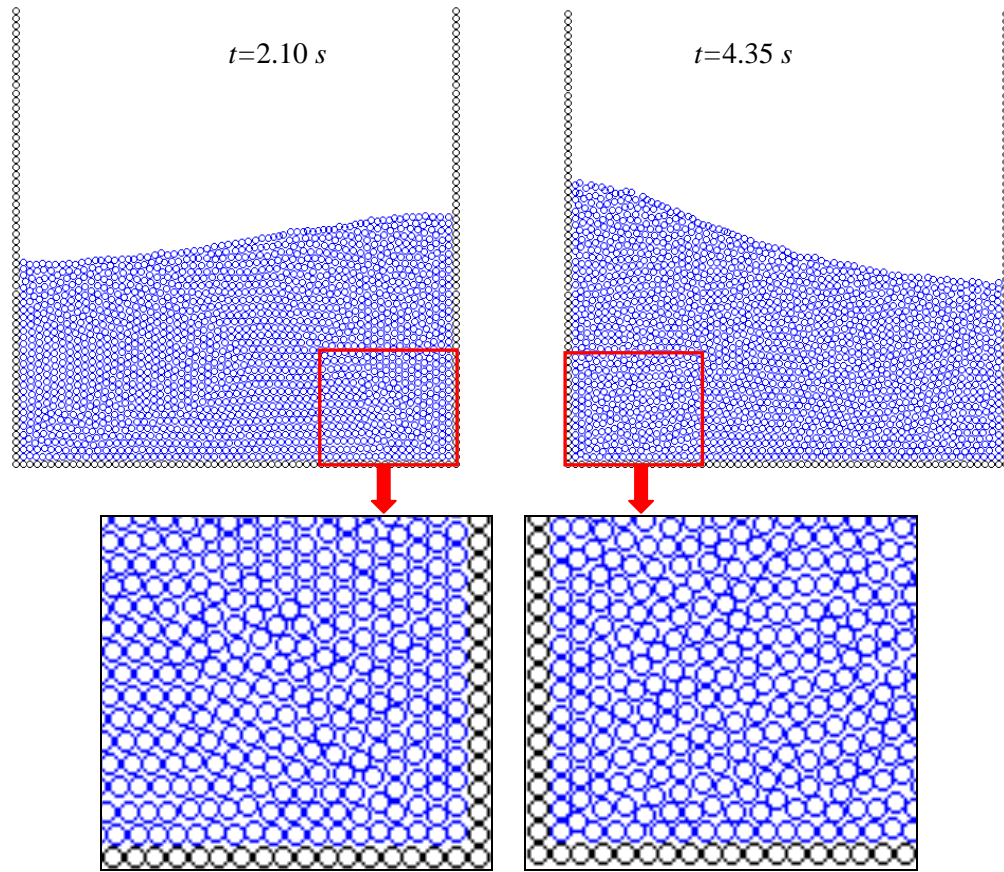


Figure 5-24. Particle distribution of CPM simulation

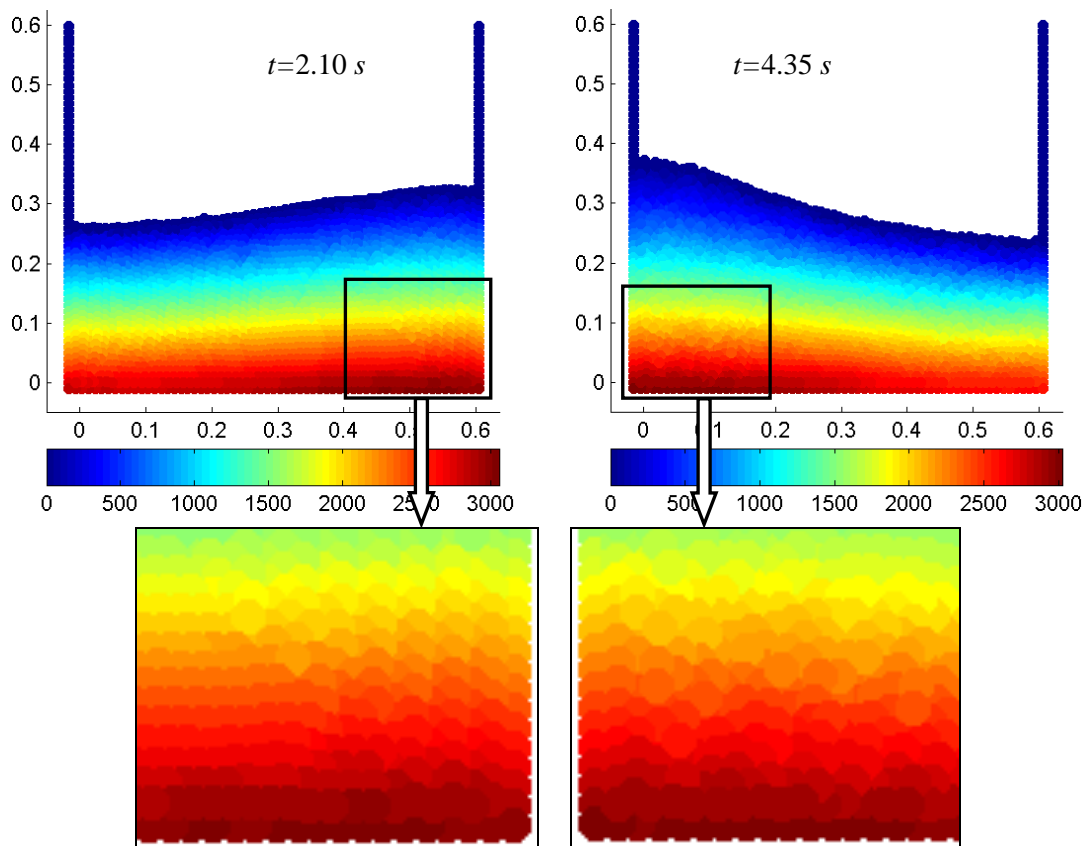


Figure 5-25. Pressure contours of CPM solution

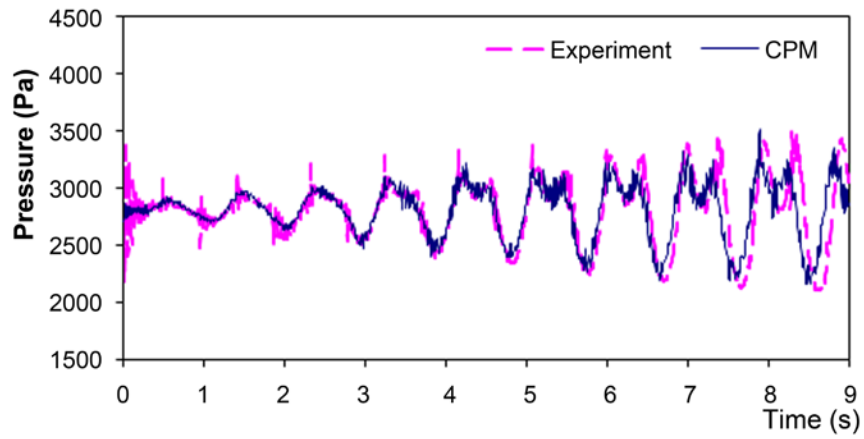


Figure 5-26. Comparison of pressure history at Point  $P_2$  ( $\omega / \omega_0 = 1.0$ )

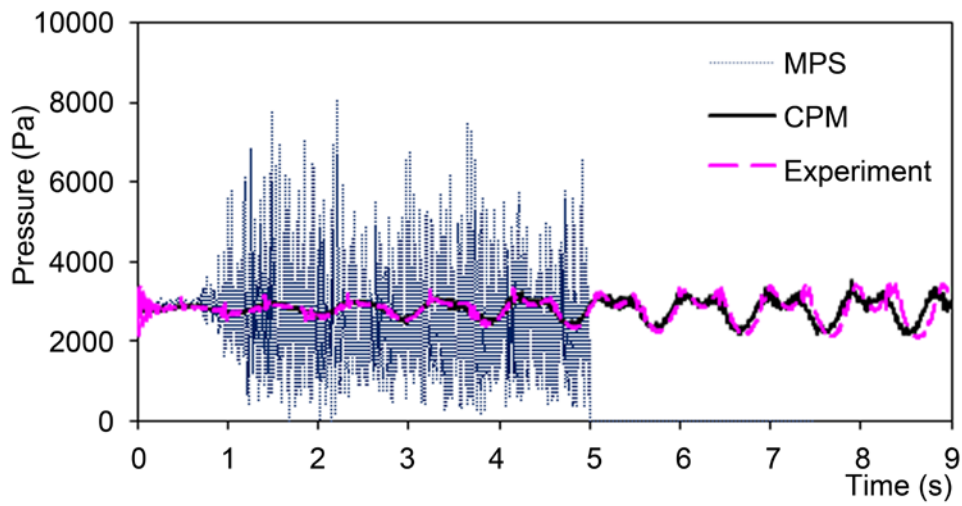


Figure 5-27. Comparison of pressure history at Point  $P_2$  ( $\omega / \omega_0 = 1.0$ )

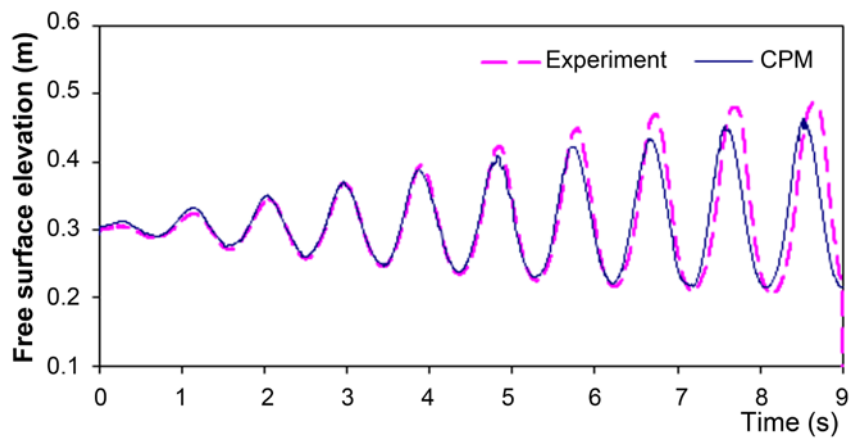


Figure 5-28. Comparison of free surface elevation at Point  $P_1$  ( $\omega / \omega_0 = 1.0$ )

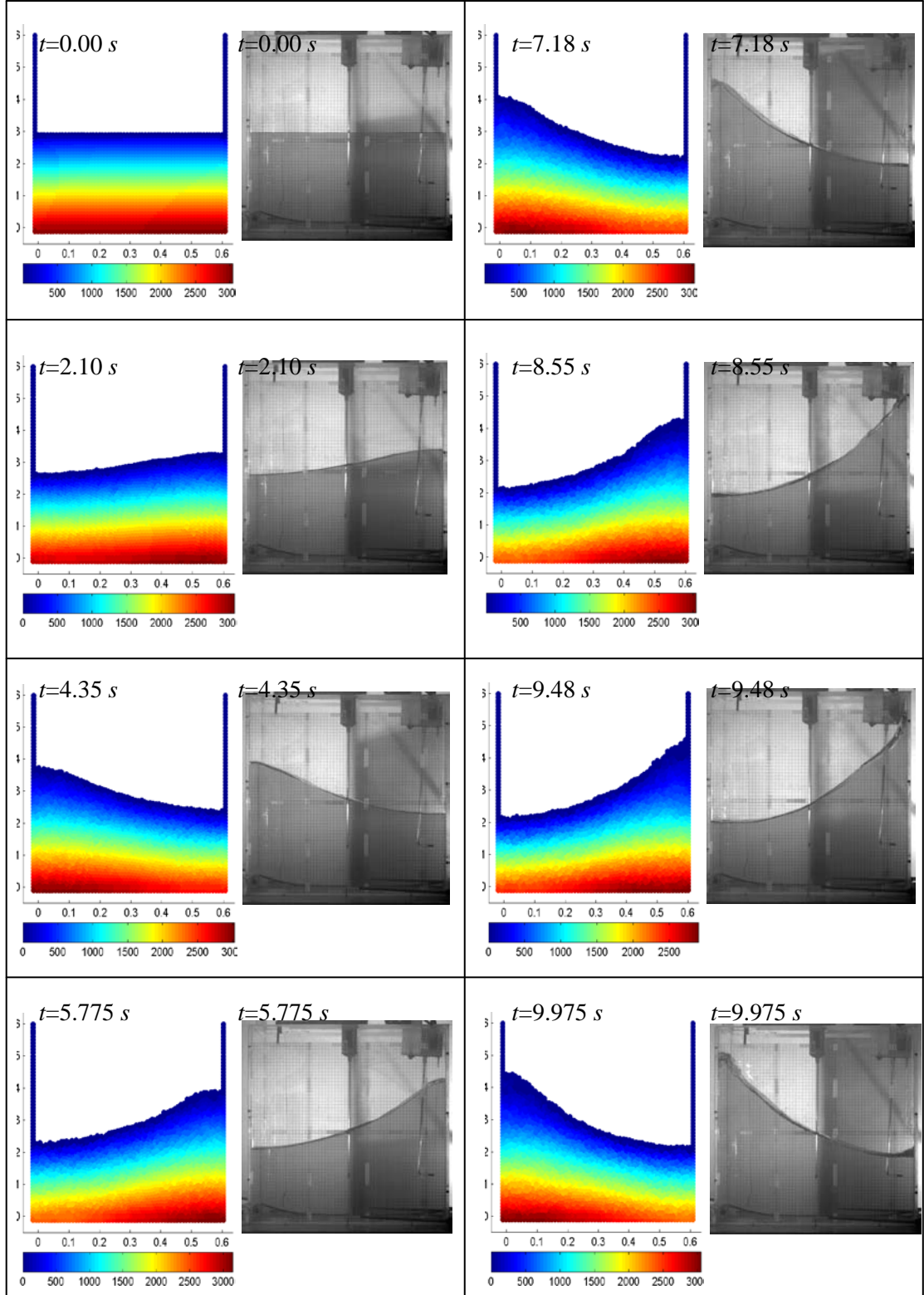


Figure 5-29. Free-surface elevation vs. time ( $\omega/\omega_0 = 1.0$ ) by CPM

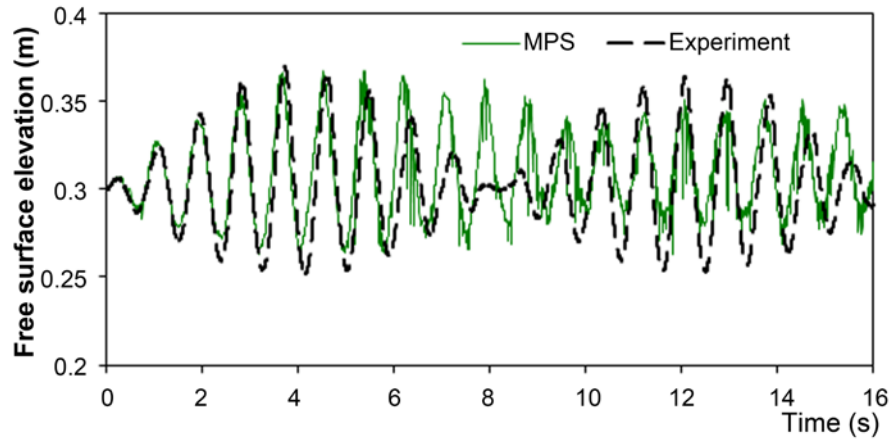


Figure 5-30. Comparison of free surface elevation at Point  $P_1$  ( $\omega / \omega_0 = 1.1$ )

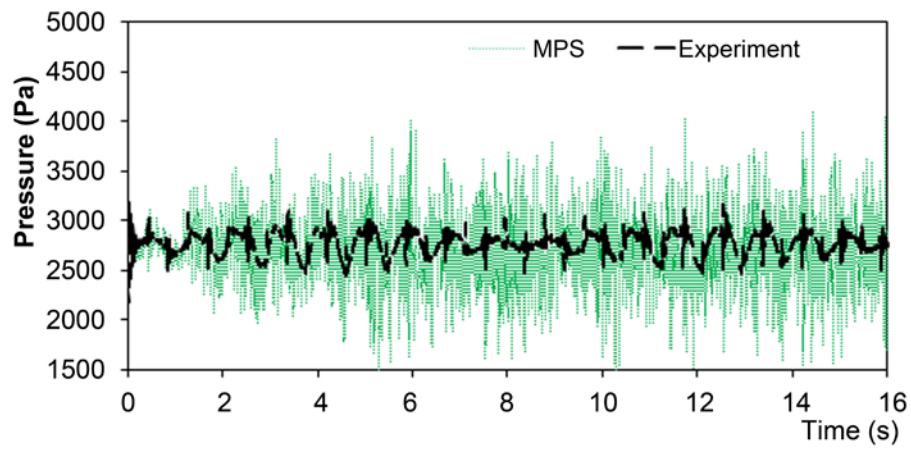


Figure 5-31. Comparison of pressure history at Point  $P_2$  ( $\omega / \omega_0 = 1.1$ )

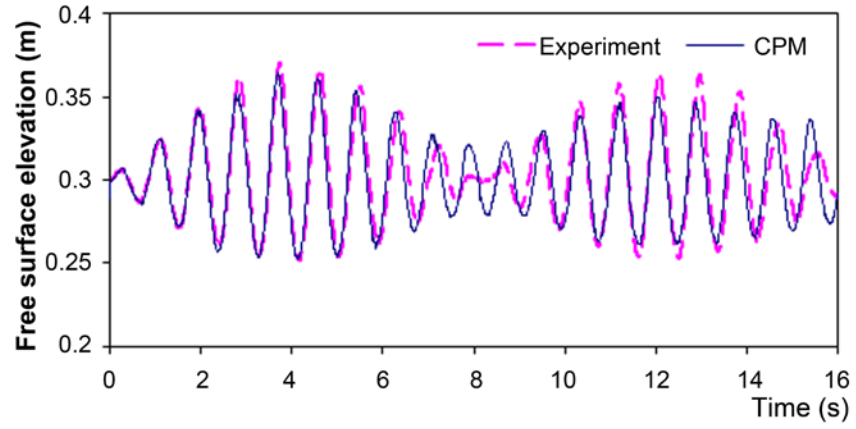


Figure 5-32. Comparison of free surface elevation at Point  $P_1$  ( $\omega / \omega_0 = 1.1$ )

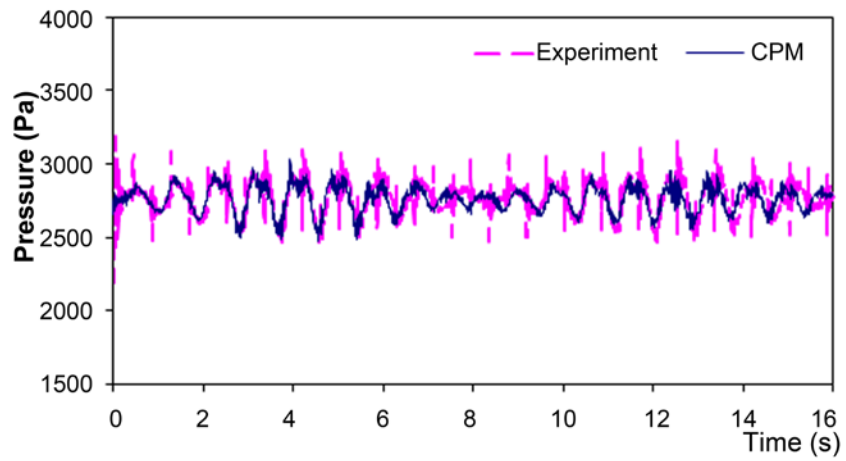


Figure 5-33. Comparison of pressure history at Point  $P_2$  ( $\omega / \omega_0 = 1.1$ )

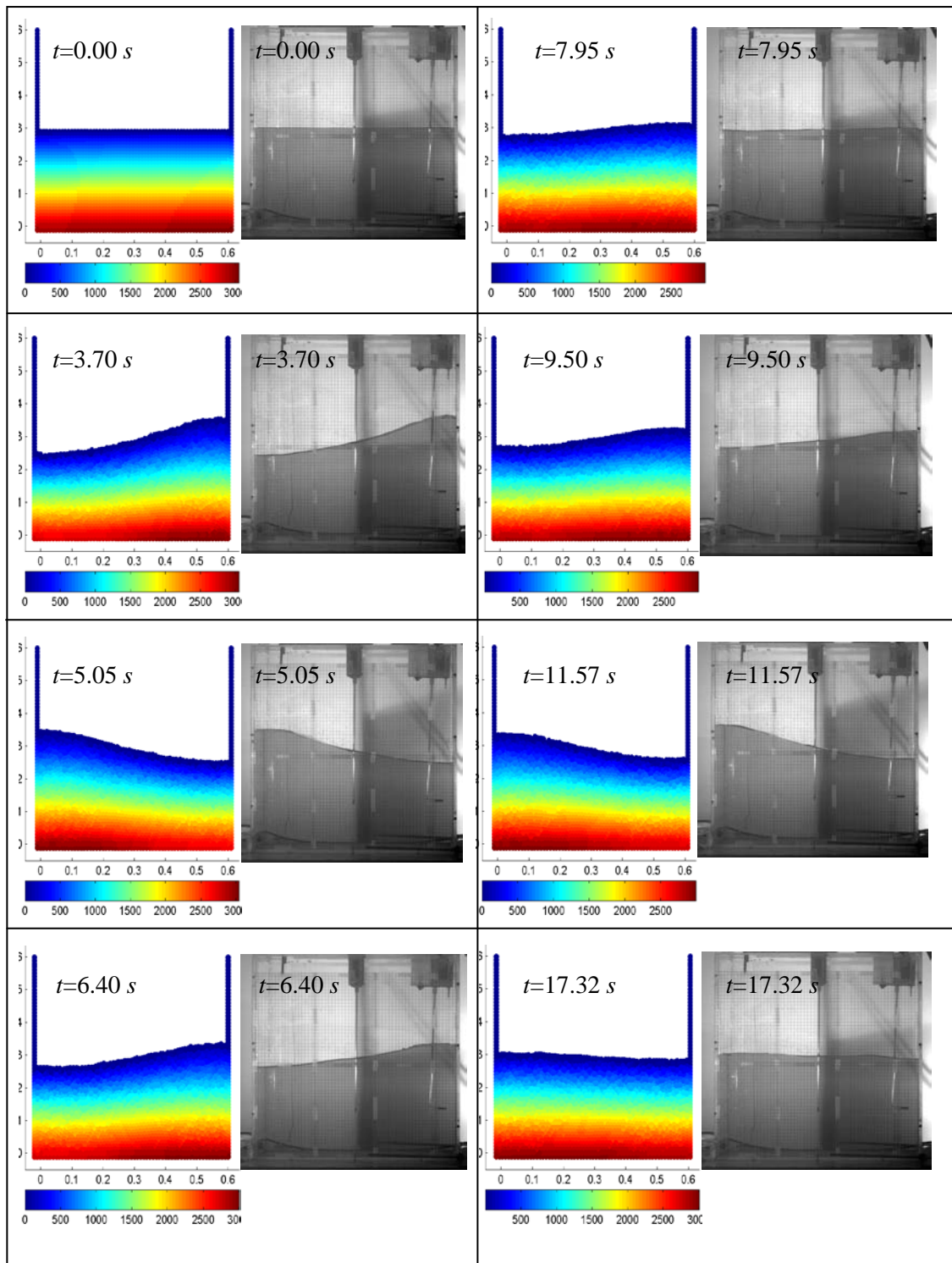


Figure 5-34. Free-surface elevation vs. time ( $\omega/\omega_0 = 1.1$ ) by CPM

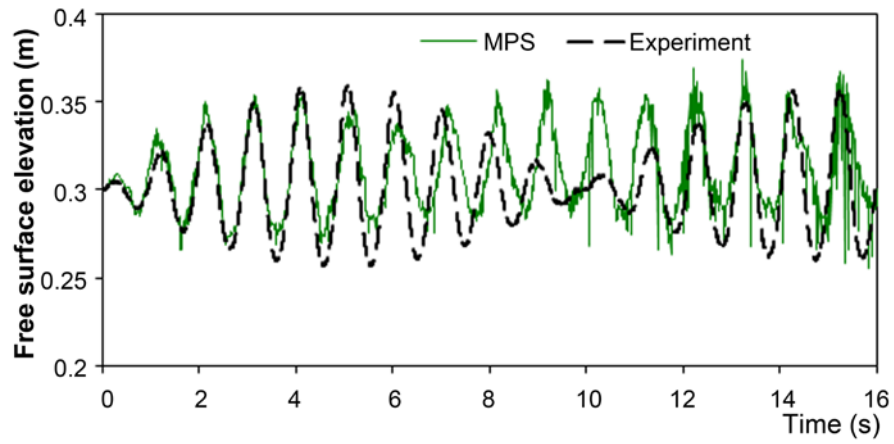


Figure 5-35. Comparison of free surface elevation at Point  $P_1$  ( $\omega / \omega_0 = 0.9$ )

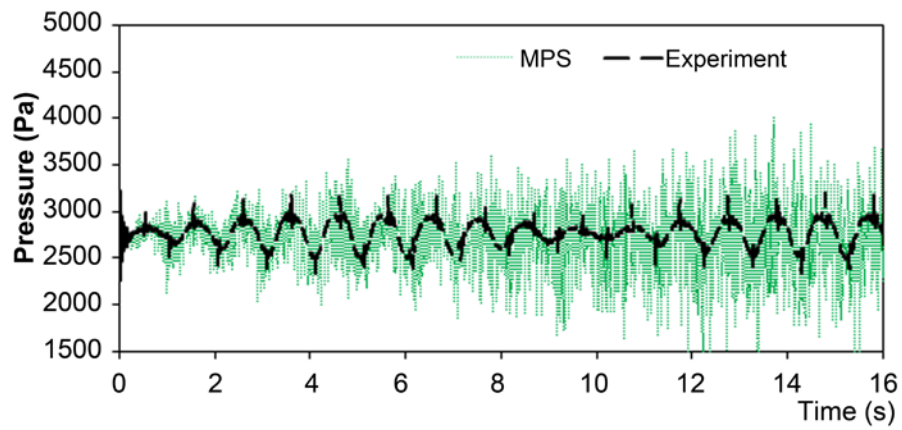


Figure 5-36. Comparison of pressure history at Point  $P_2$  ( $\omega / \omega_0 = 0.9$ )

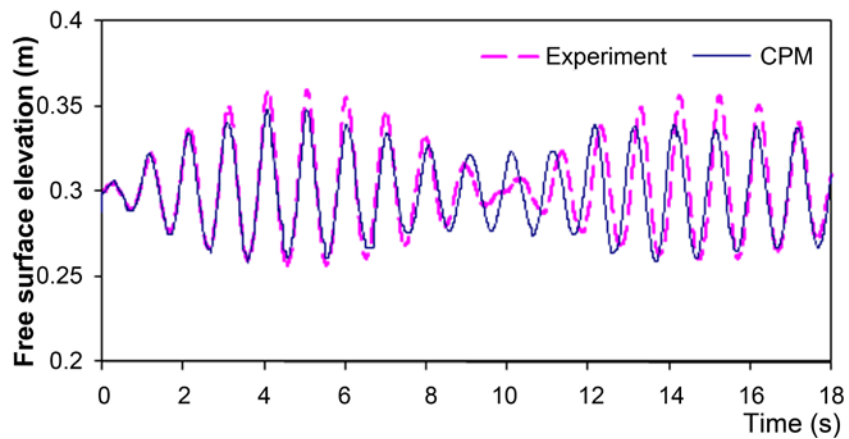


Figure 5-37. Comparison of free surface elevation at Point  $P_1$  ( $\omega / \omega_0 = 0.9$ )

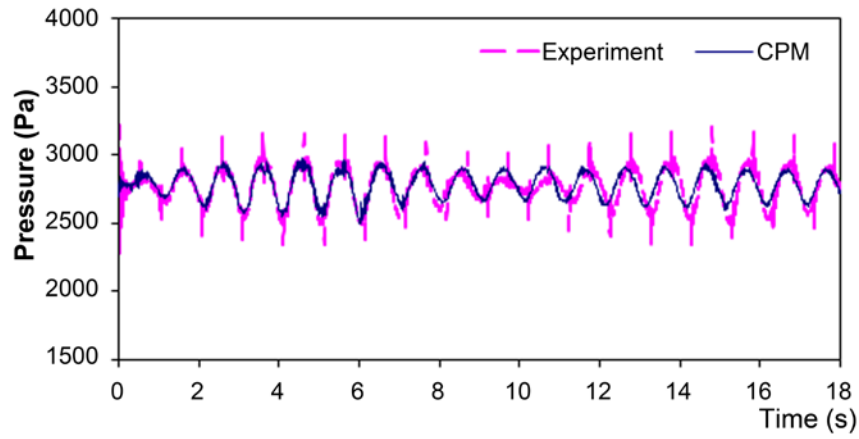


Figure 5-38. Comparison of pressure history at Point  $P_2$  ( $\omega / \omega_0 = 0.9$ )

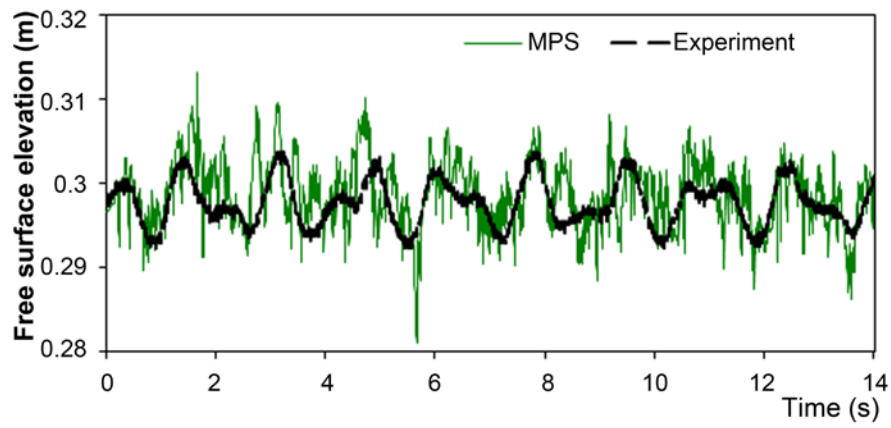


Figure 5-39. Comparison of free surface elevation at Point  $P_1$  ( $\omega / \omega_0 = 0.583$ )

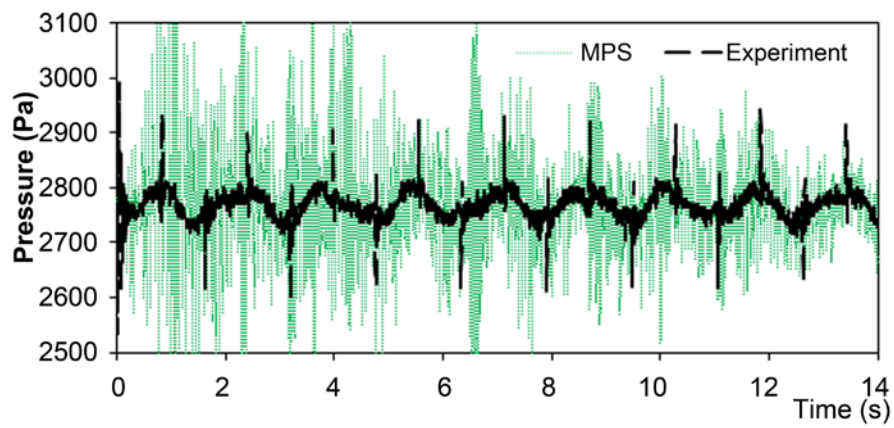


Figure 5-40. Comparison of pressure history at Point  $P_2$  ( $\omega / \omega_0 = 0.583$ )

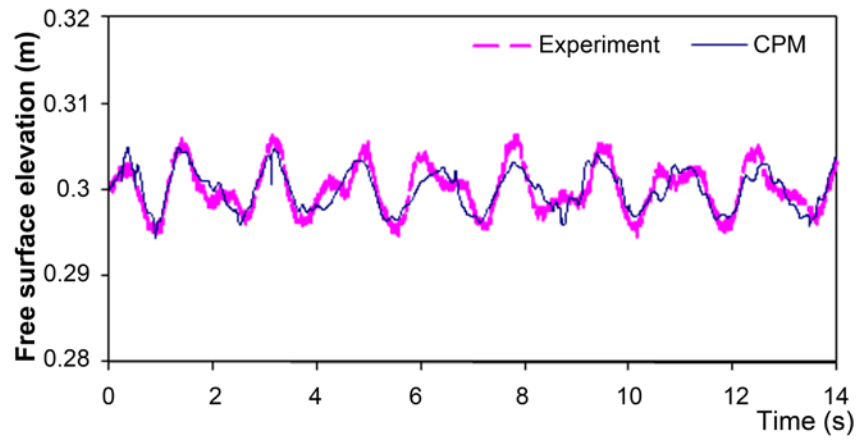


Figure 5-41. Comparison of free surface elevation at Point  $P_1$  ( $\omega / \omega_0 = 0.583$ )

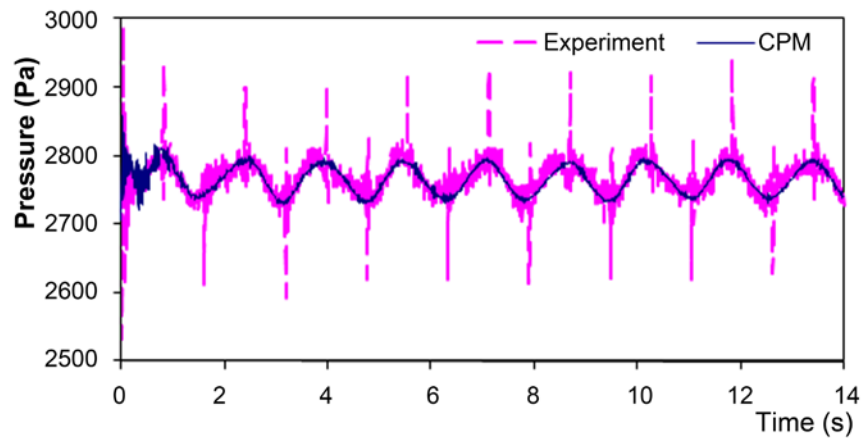


Figure 5-42. Comparison of pressure history at Point  $P_2$  ( $\omega / \omega_0 = 0.583$ )

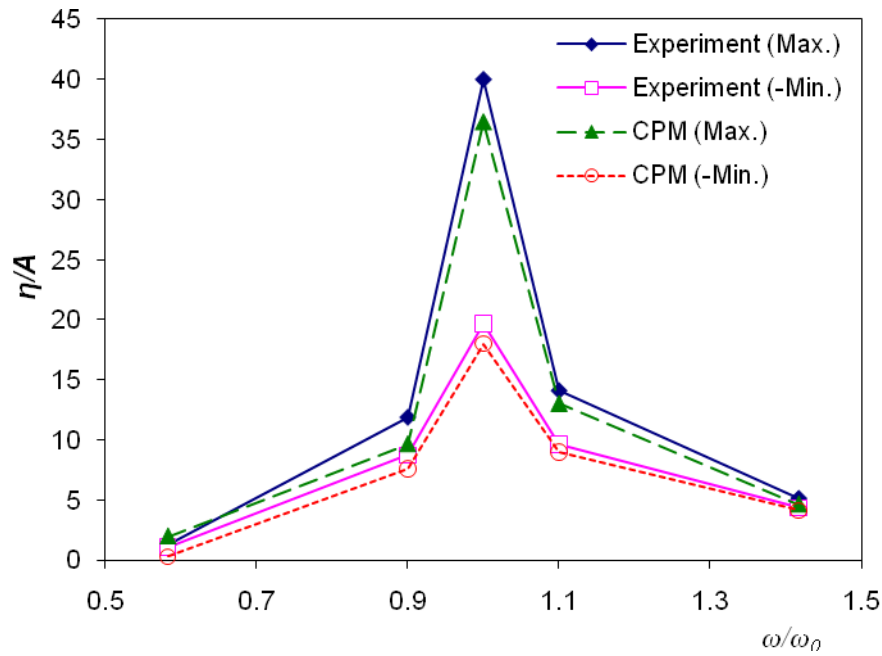


Figure 5-43. Maximum and minimum free surface elevations vs. excitation frequency

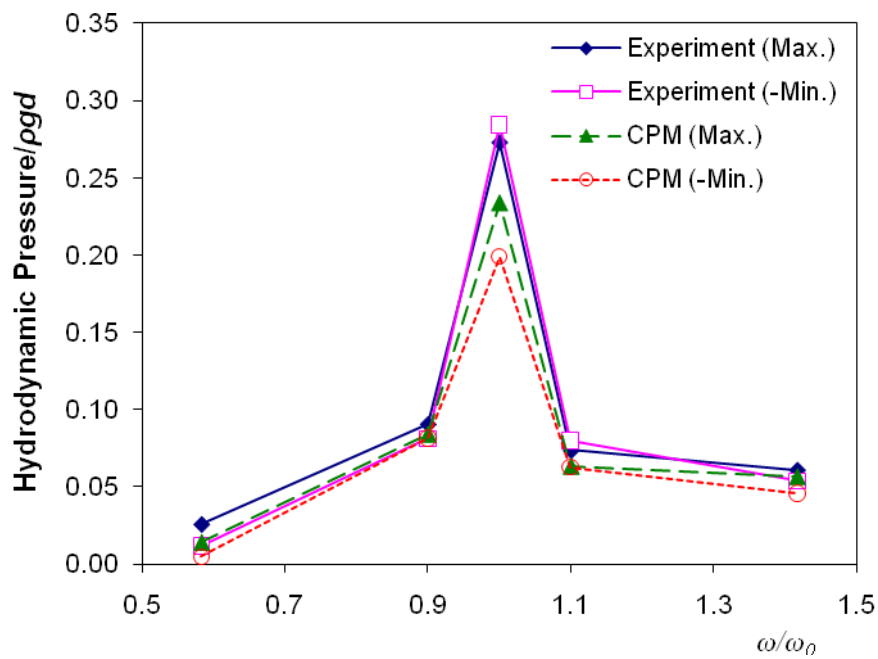


Figure 5-44. Maximum and minimum hydrodynamic pressure vs. excitation frequency

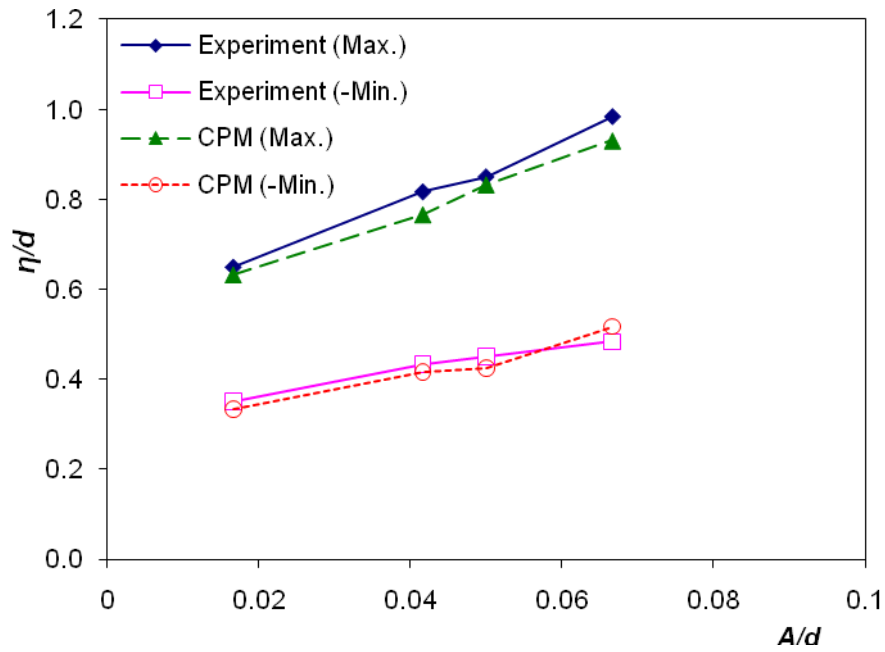


Figure 5-45. Maximum and minimum free surface elevations under different excitation amplitudes

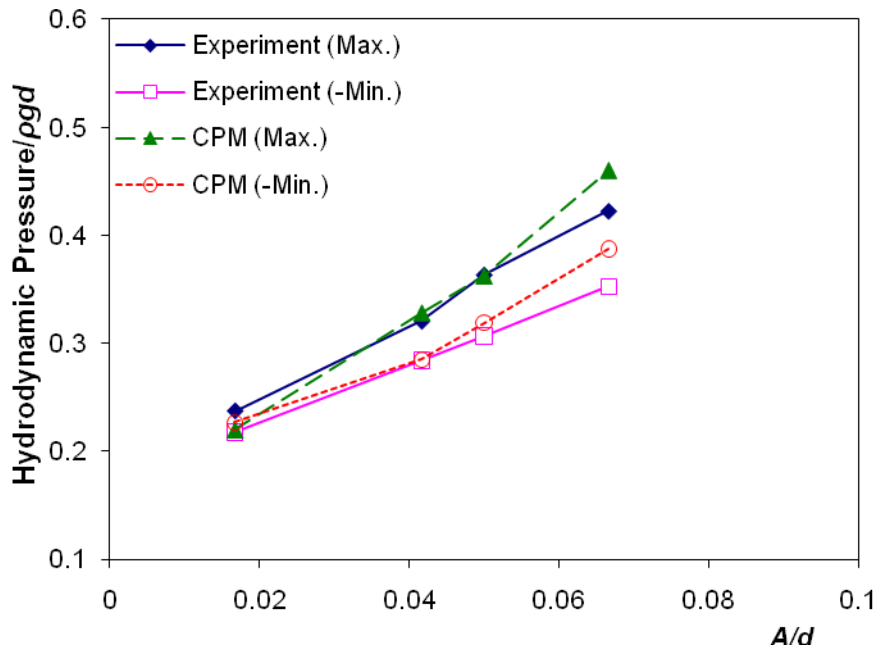


Figure 5-46. Maximum and minimum hydrodynamic pressure under different excitation amplitudes

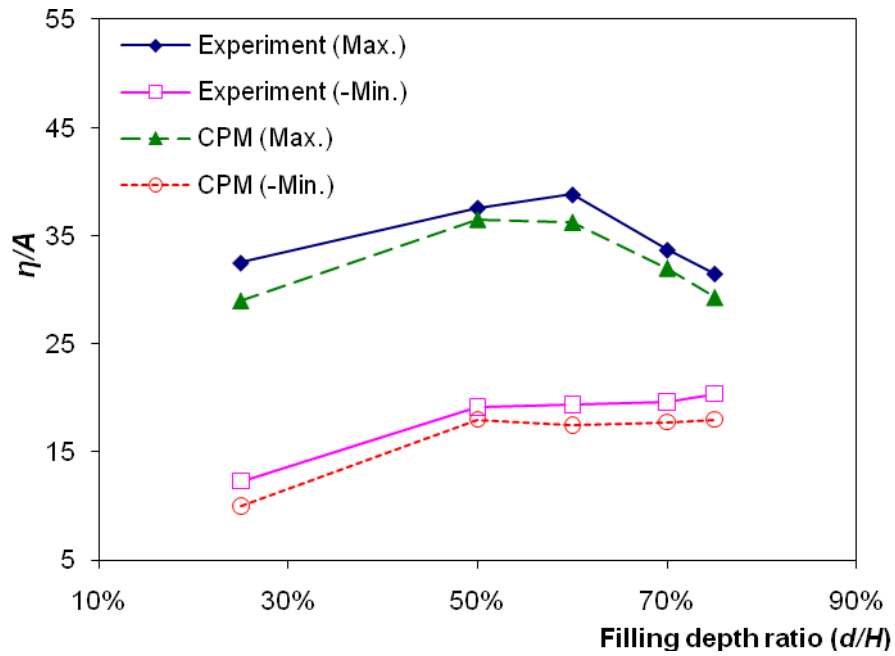


Figure 5-47. Maximum and minimum free surface elevations vs. filling depths

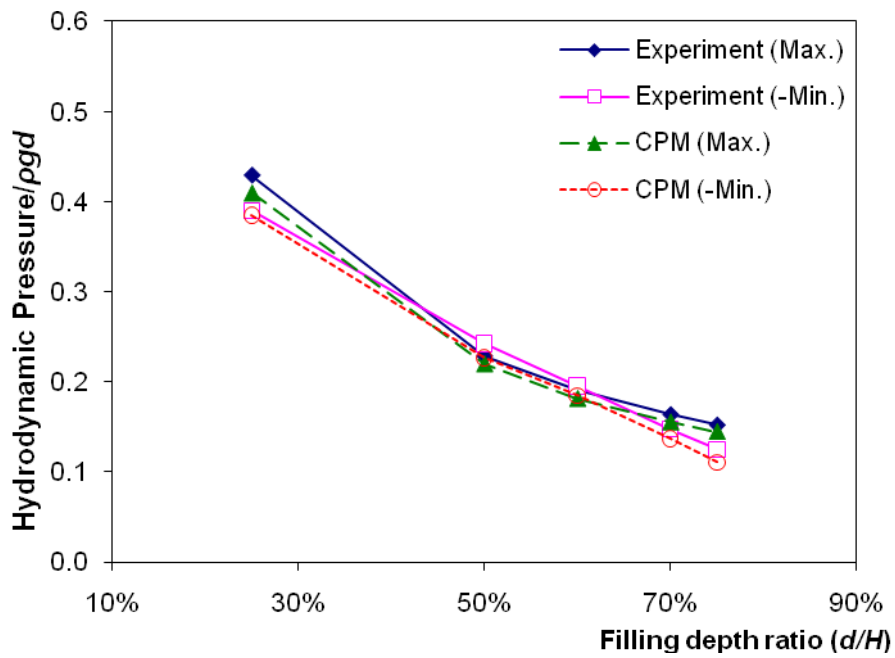


Figure 5-48. Maximum and minimum hydrodynamic pressure vs. filling depths

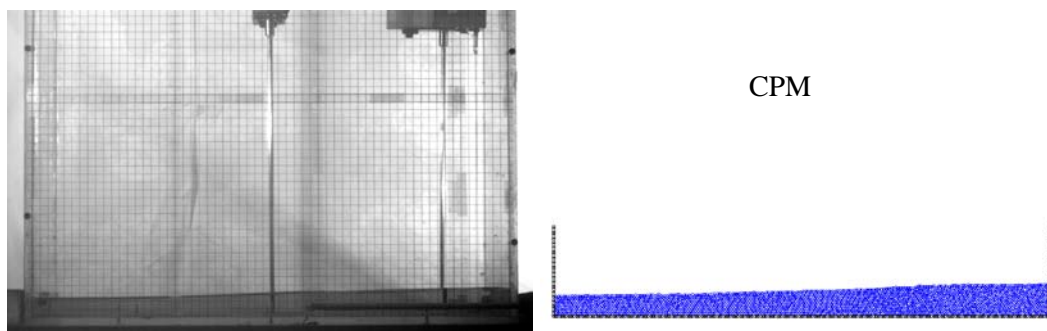


Figure 5-49. Standing Wave at the initial stage,  $t = 2.75$  s

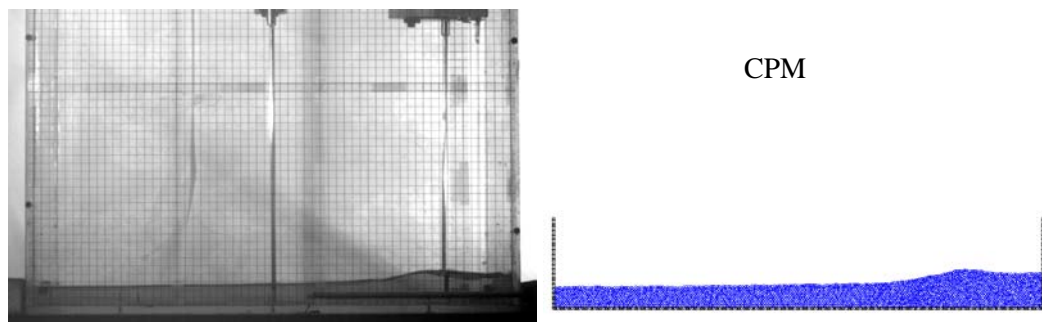


Figure 5-50. Traveling wave starts to form,  $t = 4.80$  s

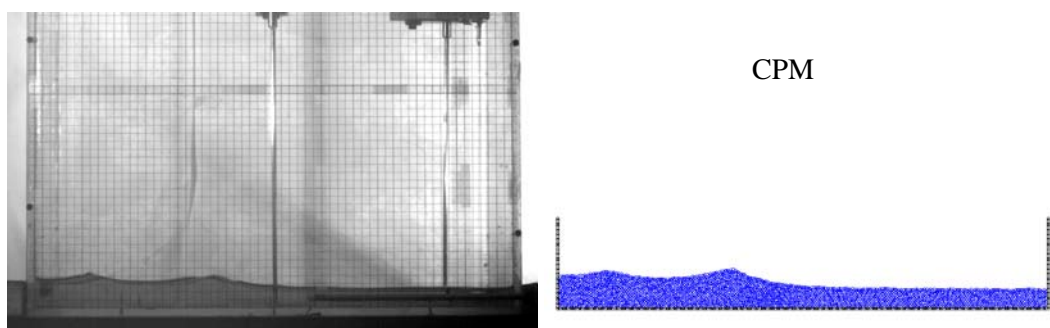


Figure 5-51. Multi-crested waves traveling,  $t = 6.10$  s

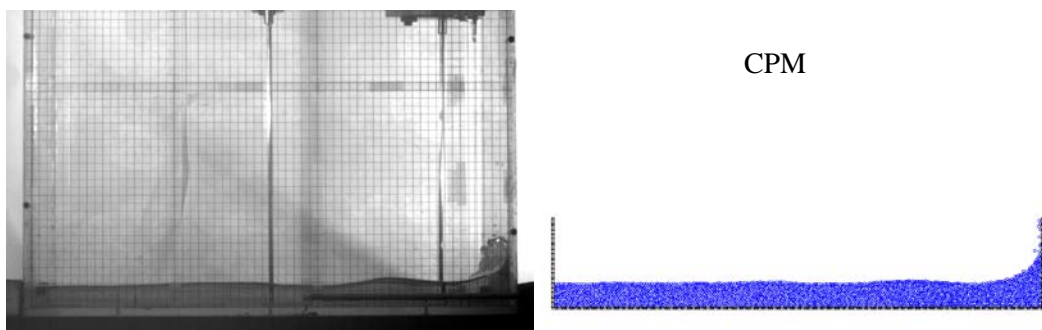


Figure 5-52. Hydraulic run-up (before formation of bore),  $t = 6.75$  s

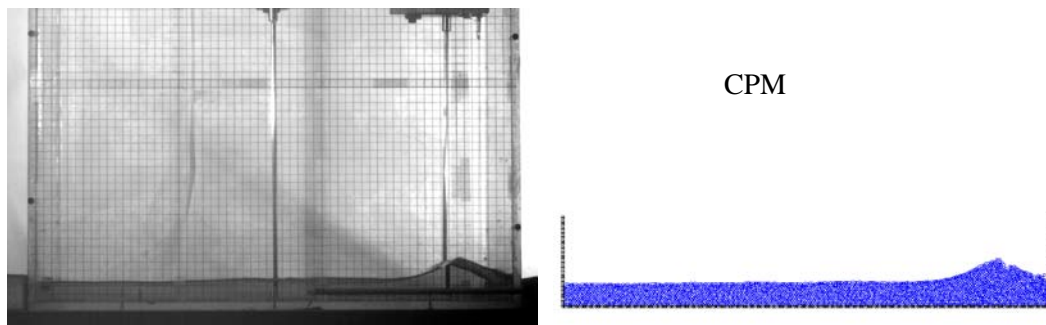


Figure 5-53. Formation of bore,  $t = 6.90$  s

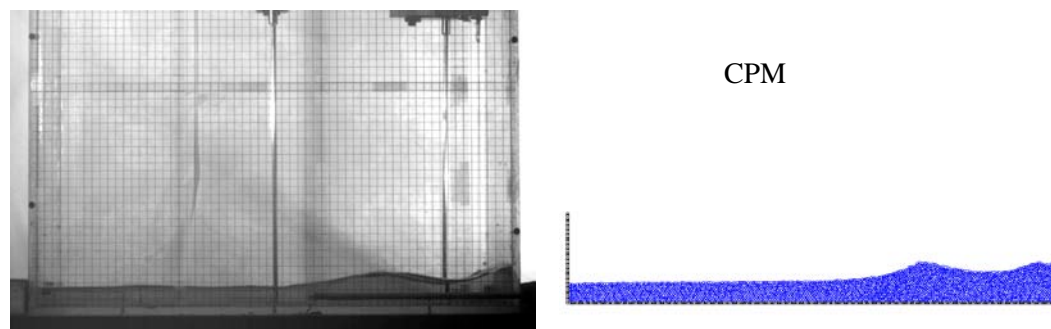


Figure 5-54. Bore splits into multi-crested traveling waves,  $t = 7.10$  s

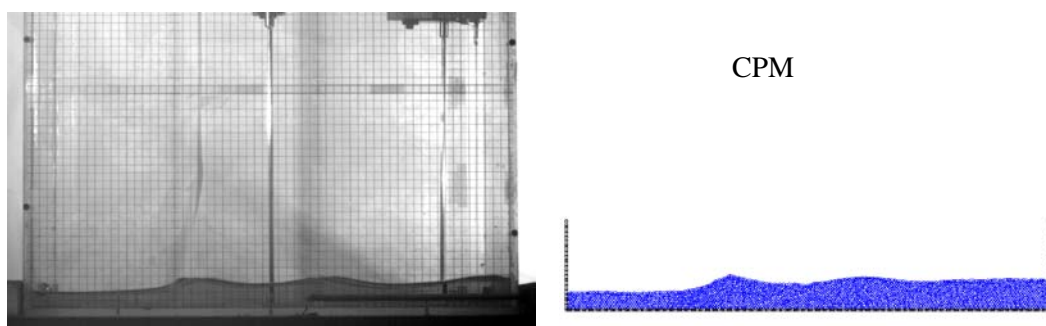


Figure 5-55. Multi-crested traveling waves,  $t = 7.50$  s

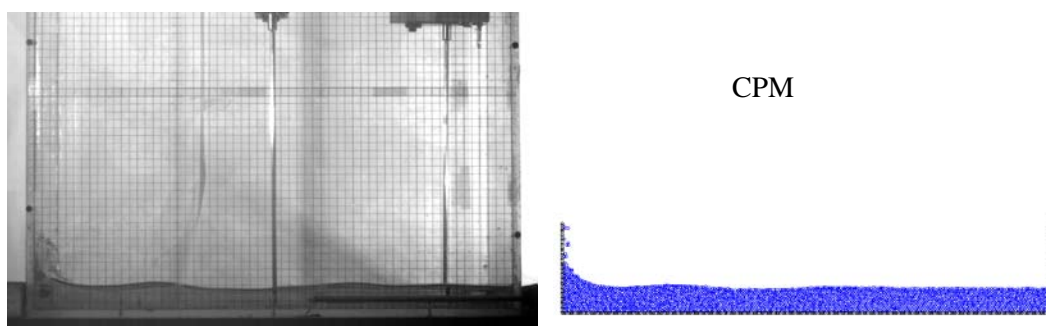


Figure 5-56. Hydraulic run-up,  $t = 7.85$  s

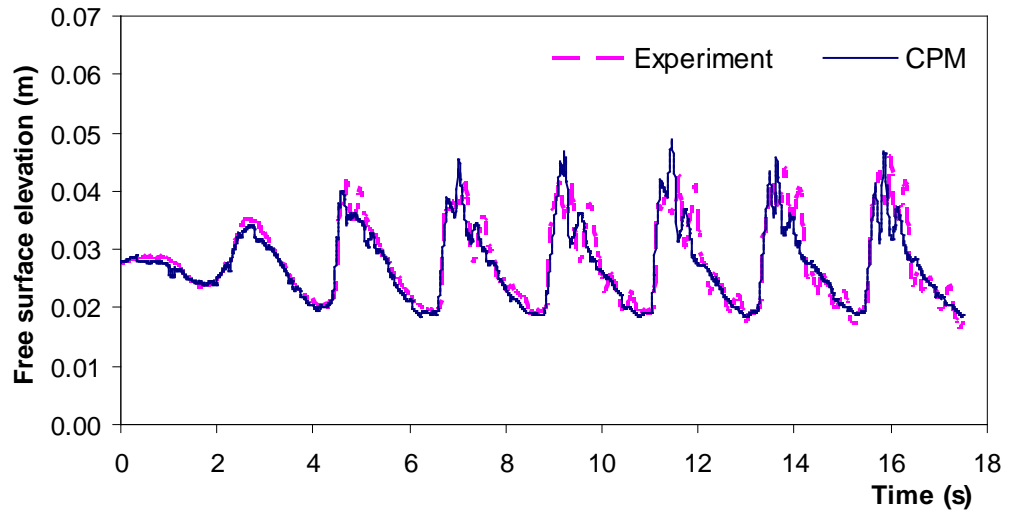


Figure 5-57. Comparison of the free surface elevation at Point  $P_1$

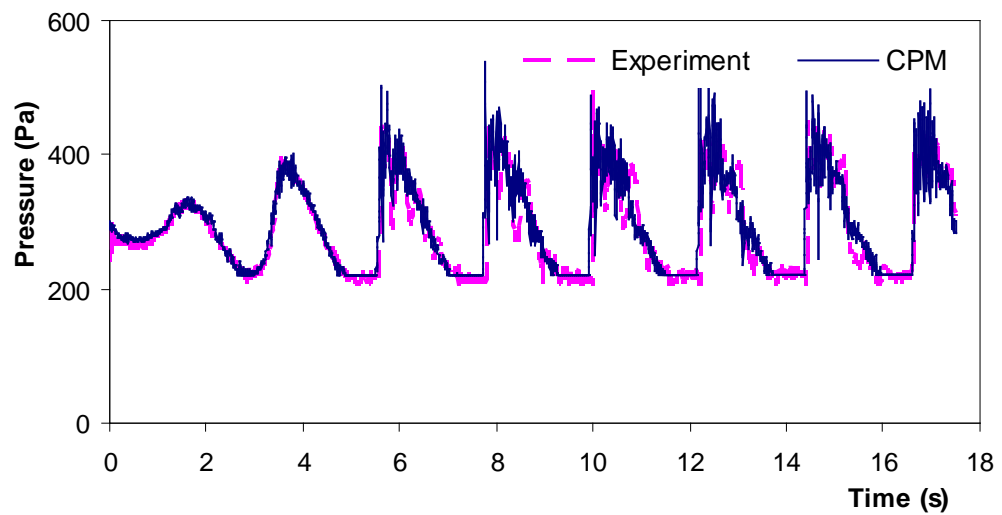


Figure 5-58. Comparison of the pressure history at Point  $P_2$

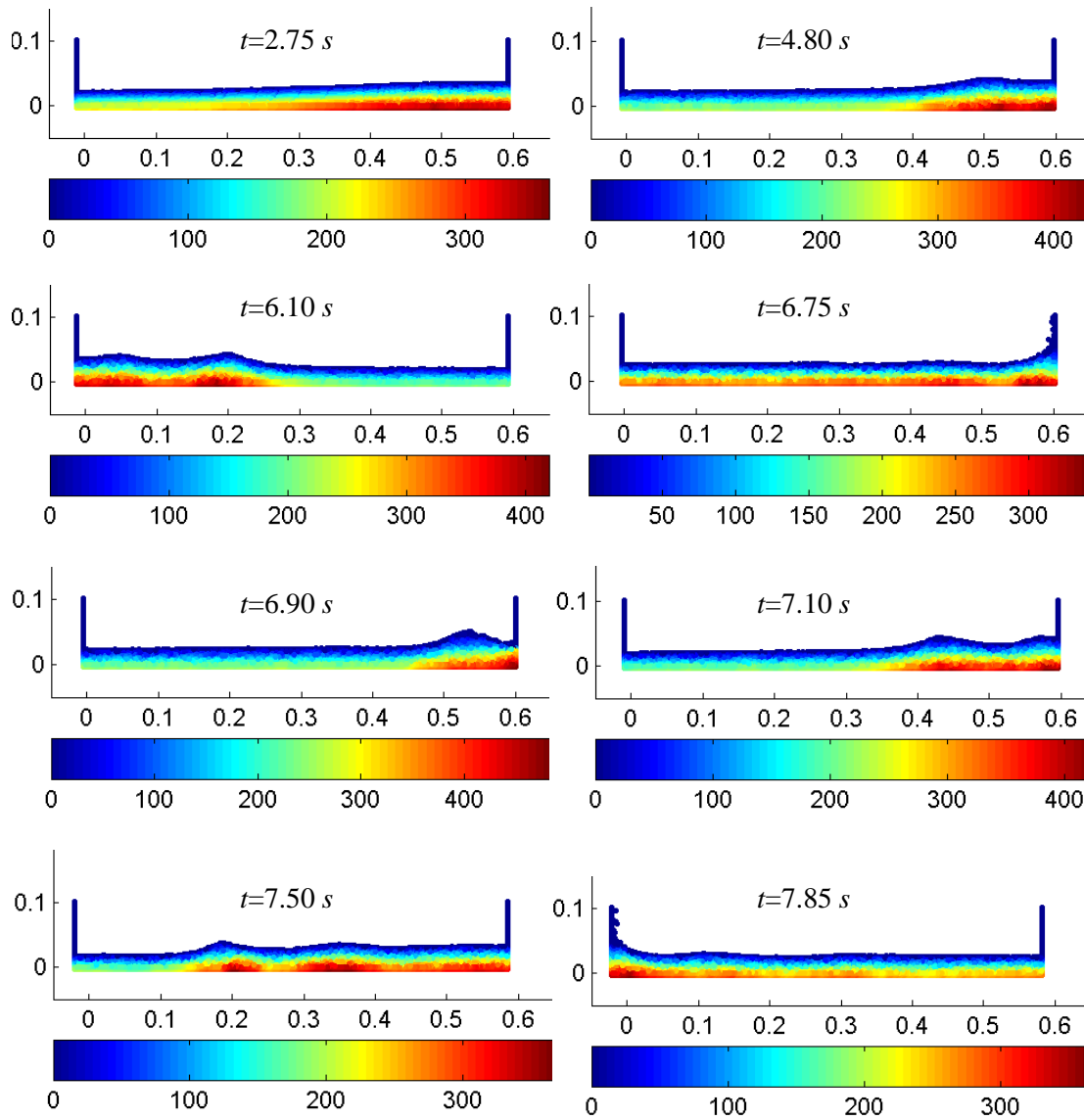


Figure 5-59. Pressure contours for different time instants by CPM

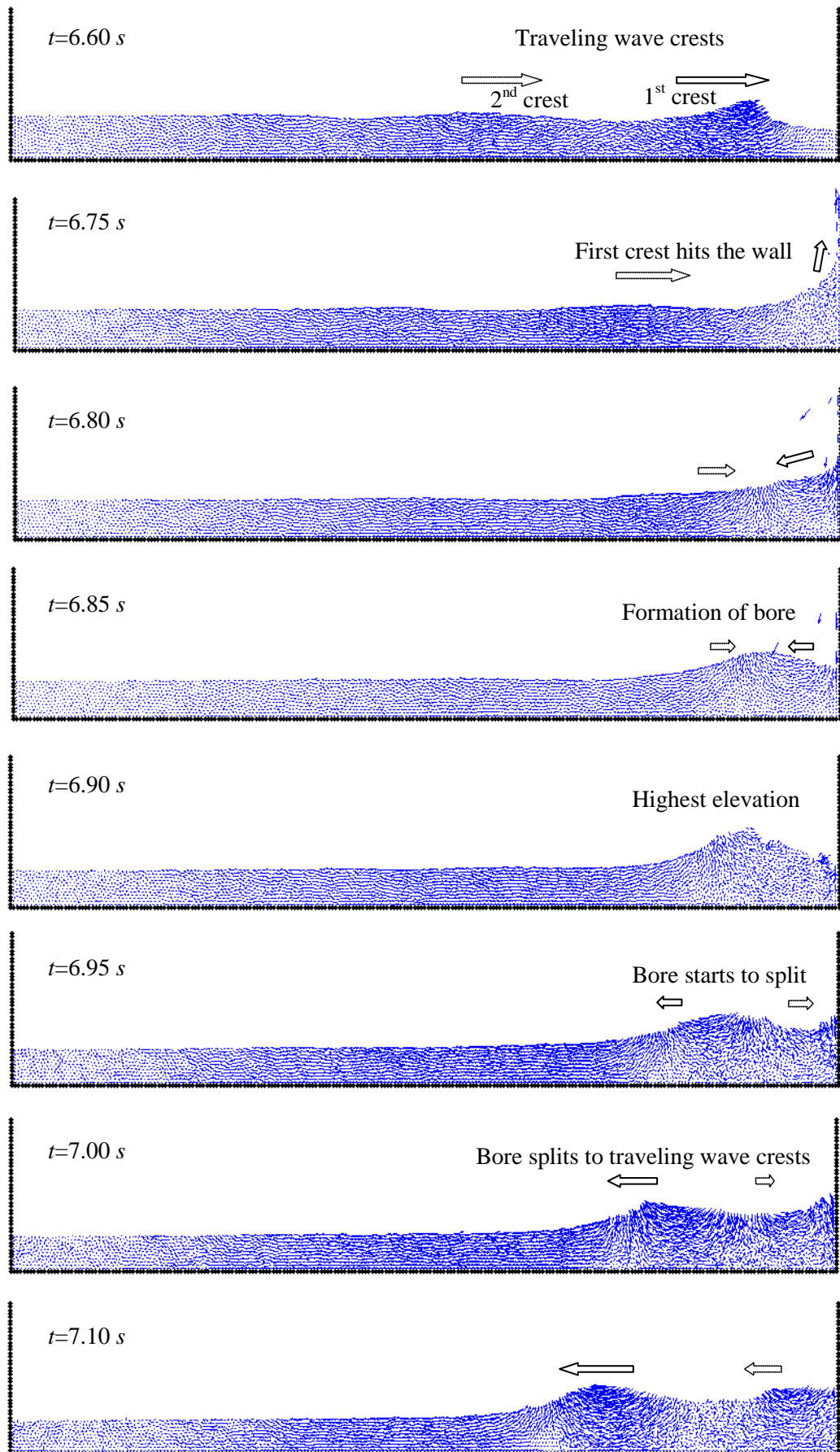


Figure 5-60. Velocity field of the fluid particles by CPM

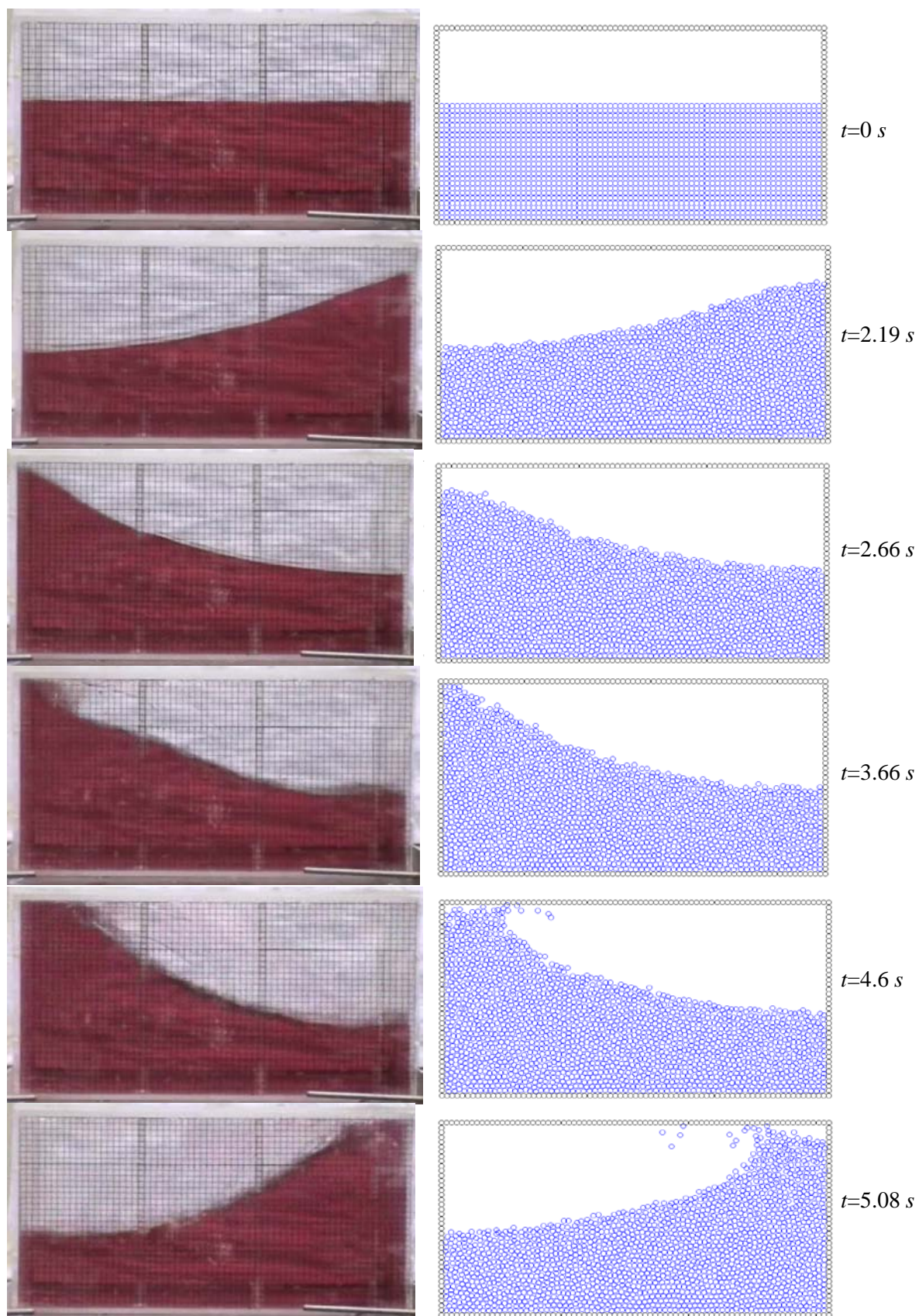


Figure 5-61. Free surface profiles at different time instants. Left: experiments; Right: CPM simulation.

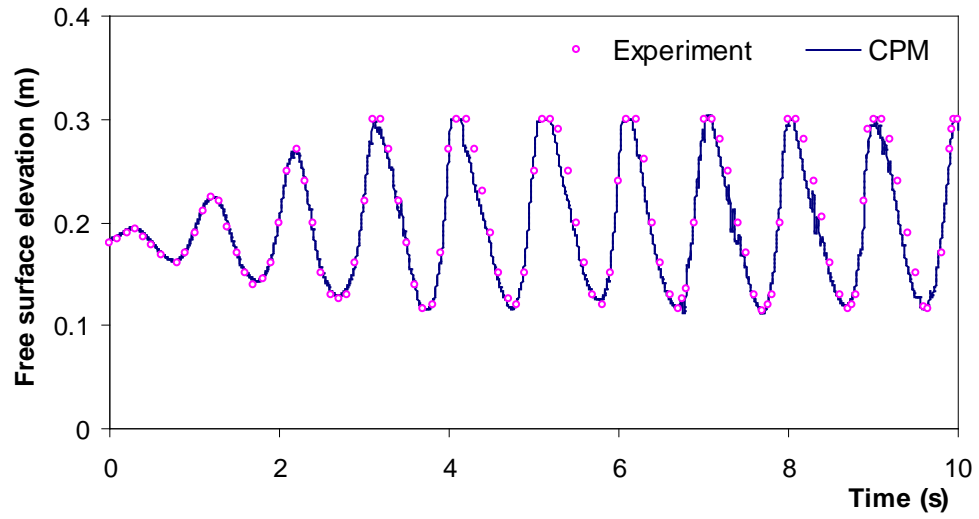


Figure 5-62. Time history of free surface elevations at the right wall

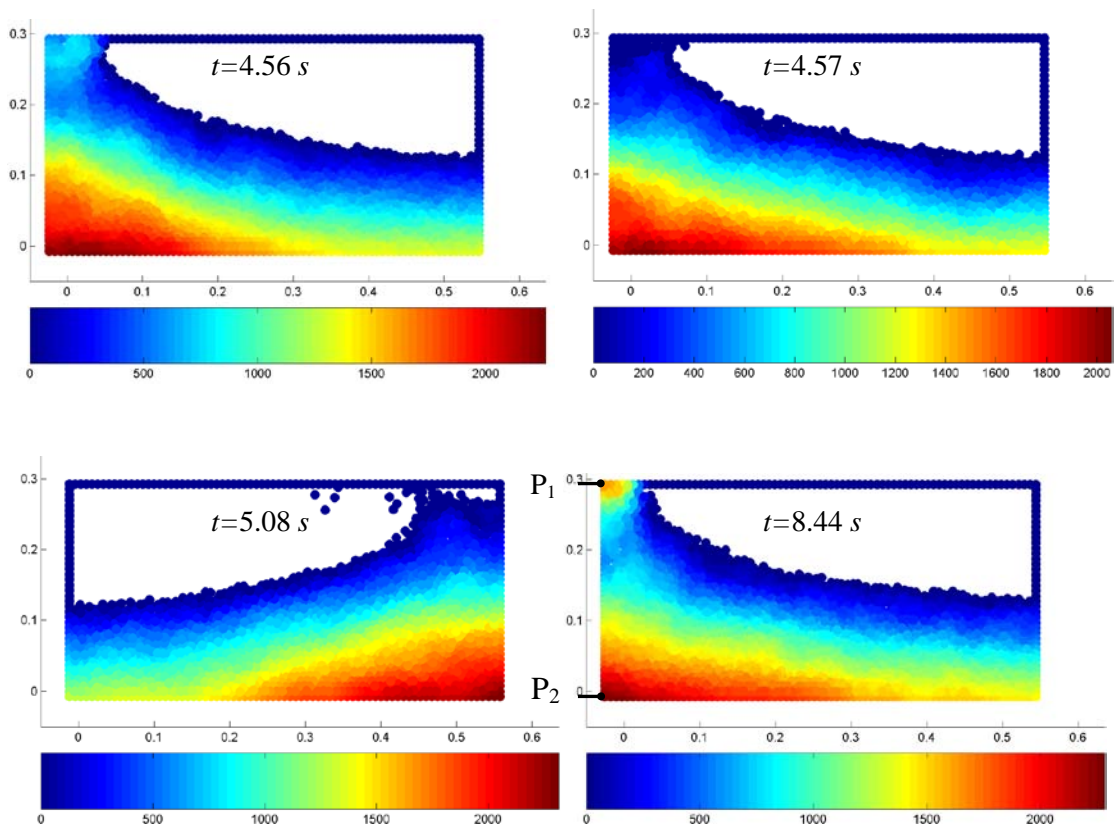


Figure 5-63. Pressure contours for different time instants by CPM

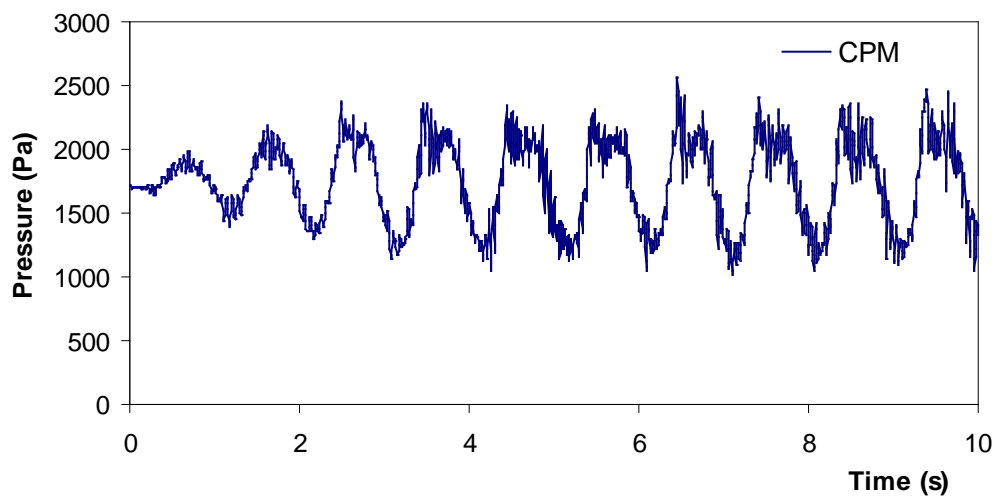


Figure 5-64. Computed pressure history at Point P<sub>2</sub>

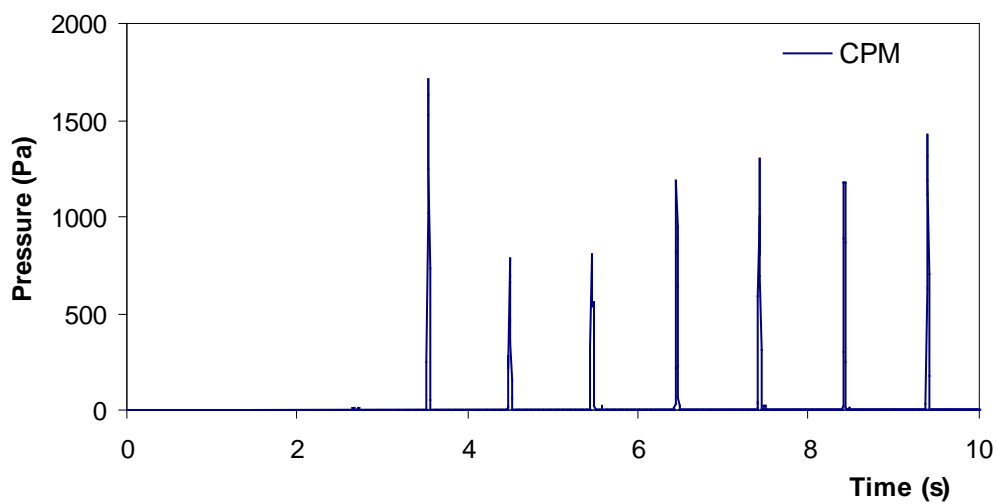


Figure 5-65. Computed pressure history at Point P<sub>1</sub>

## Chapter 6 Conclusions and Future Research

### 6.1 Conclusions

In this thesis, a new particle method named CPM is developed and applied to simulate incompressible free surface flows. The CPM is Lagrangian particle method which solves the Navier-Stokes equations in a semi-implicit time stepping scheme. There are three main features in CPM compared with other particle methods such as SPH and MPS as follows.

(1) The discretization of Laplace operator needed in the Poisson equation of pressure and gradient model are consistent with Taylor series expansion. As a result, the approximation of Laplacian in CPM gives much better accuracy and convergence compared with MPS and SPH methods, particularly when the particles are not regularly spaced.

(2) A free surface particle recognition method (arc method) is applied to capture the free surface more accurately. The arc method produces more accurate boundary particle recognition results compared with the density threshold method in MPS.

(3) The incompressibility condition of the free surface particles is enforced by an adjustment scheme. The scheme is shown to be able to improve the distribution of the free surface particles and hence improves the stability of the algorithm.

These improvements are shown to be beneficial in improving numerical stability of the algorithm and in particular resolve the problem of spurious pressure fluctuation. A benchmark dam break example is first presented to demonstrate the performance of CPM in comparison with the MPS method. The CPM solution shows remarkably

better particle distribution and smoother pressure contours than the MPS solution. The CPM solution also agrees well with published experimental results both in terms of free surface profiles and its development over time. A parametric study is performed to investigate the effects of different parameters used in CPM. The inverse distance weighting function is found to be suitable in the weighted least-square solution of derivatives in CPM. The initial particle distance ( $L_0$ ) is dependent on the geometry and fluid motion type which may require a convergence study by starting with a coarse distribution of particles. The influence radius  $r_e = 2.1L_0$  or  $r_e = 2.5L_0$  is recommended as a good compromise between capturing sufficient particles for accuracy of derivatives and computational efficiency in the simulation of both gentle and violent fluid motion. In terms of computational efficiency, the time used in the addition time required to solve derivatives based on local particles in CPM is not significant particularly in problems with large particle numbers.

The performance of CPM is demonstrated by more numerical examples, i.e. hydrostatic pressure computation in a static tank, free oscillation of liquid in a container, dam break in large rectangular tank and dam break in a tank with obstacle block. In all these examples, the CPM solution of free surface profiles agree very well with published numerical and/or experimental results. For the dam break problems without and with obstacle, the pressure solutions of CPM agree well with experimental results. No severe pressure fluctuation appears even in violent free surface motion with wave breaking. This is a great advantage of the CPM since conventional particle methods (such as SPH and MPS) tend to give severe and spurious pressure fluctuation particularly in long time simulation.

The proposed CPM is thereafter applied to study liquid sloshing in rectangular tanks. Experiments were conducted on rectangular tanks partially filled with water, making use of a 1.5 m x 1 m shake-table. Sloshing waves in high and low filling levels are investigated. Parametric studies with respect to excitation frequency, excitation amplitude and filling depths are performed experimentally and numerically. Standing waves, traveling waves and breaking waves in different filling depths are well captured by CPM. The CPM simulation of liquid sloshing presents evenly distributed particle distribution without hot or cold spot and smooth pressure contour even when breaking occurs. Compared with MPS results, the CPM solutions agree much better with the experimental results particularly in terms of particle distribution and pressure.

In summary, the proposed CPM is shown to be robust and accurate in simulation of incompressible free surface flows in all the cases considered, in terms of free surface profile, wave motion and breaking, particle distribution and pressure, especially the good solution of the pressure field.

## **6.2 Future work**

In this study, incompressible free surface flow problems are considered and simulated by CPM. The capability of CPM in other kinds of fluid motion, such as two-phase flow, has not been addressed. Further work should be conducted to identify the effectiveness of the proposed CPM in simulation of sloshing involving two phase fluids (e.g. water and air).

While the proposed CPM has shown great potential in 2D simulation, more works are needed to extend it to 3D free surface flow problems, such as strong waves

impacting on coastal and offshore objects. Flow motions with more complicated boundaries and excitation conditions should also be tested so as to fully exploit the research and commercial potential of the CPM.

In addition, due to the facility constraint of the shake-table in the water sloshing experiments, only unidirectional regular excitation signal was used. Multi-degree of freedom movements of the tank can be applied in future study. Furthermore, more complicated or irregular external excitation signals may be investigated. Different tank shape other than rectangular tank should be studied in future to better model the real tank geometry.

Lastly, rigid tank wall has been assumed in the study of liquid sloshing, which means there is no deformation of the wall under the liquid pressure during the sloshing procedure. This may not be true in the real tank situation, e. g. in membrane LNG tanks. Fluid-structure interaction should be considered in such a case to account for the effects of tank flexibility.

---

## References

- Abramson, H. N. (1996). The dynamic behaviour of liquids in moving containers, *Report of NASA SP*, 106.
- Abramson, H. N. (2003). Dynamics of contained liquids: A personal odyssey, *Applied Mechanics Reviews*, 56(1), R1-R7.
- Ahmadi, A., Badiei, P. and Namin, M. M. (2007). An implicit two-dimensional non-hydrostatic model for free-surface flows, *International Journal for Numerical Methods in Fluids*, 54, 1055-1074.
- Akyildiz, H. and Unal, E. (2005). Experimental investigation of pressure distribution on a rectangular tank due to the liquid sloshing, *Ocean Engineering*, 32(11-12), 1503-1516.
- Alam, A., Kai, H. and Suzuki, K. (2007). Two-dimensional numerical simulation of water splash phenomena with and without surface tension, *Journal of Marine Science and Technology*, 12, 59-71.
- Apsley, D. D. and Hu, W. (2003). CFD simulation of two- and three-dimensional free-surface flow, *International Journal for Numerical Methods in Fluids*, 42, 465-491.
- Armenio, V. (1997). An improved MAC method (SIMAC) for unsteady high-Reynolds free surface flows, *International Journal for Numerical Methods in Fluids*, 24, 185-214.
- Armenio, V. and La Rocca, M. (1996). On the analysis of sloshing of water in rectangular containers: Numerical study and experimental validation, *Ocean Engineering*, 23(8), 705-739.
- Ataie-Ashtiani, B. and Farhadi, L. (2006). A stable moving-particle semi-implicit method for free surface flows, *Fluid Dynamics Research*, 38(4), 241-256.
- Ataie-Ashtiani, B., Shobeyri, G. and Farhadi, L. (2008). Modified incompressible SPH method for simulating free surface problems, *Fluid Dynamics Research*, 40, 637-661.
- Balendra, T., Ang, K. K., Paramasivam, P. and Lee, S. L. (1982a). Seismic design of flexible cylindrical liquid storage tanks, *Earthquake Engineering and Structural Dynamics*, 10, 477-496.
- Balendra, T., Ang, K. K., Paramasivam, P. and Lee, S. L. (1982b). Free vibration analysis of cylindrical liquid storage tanks, *International Journal of Mechanical Sciences*, 24(1), 47-59.
- Balendra, T., Wang, C. M. and Cheong, H. F. (1995). Effectiveness of tuned liquid column dampers for vibration control of towers, *Engineering Structures*, 17(9), 668-675.

- Balendra, T., Wang, C. M. and Rakesh, G. (1999). Vibration control of various types of buildings using TLCD, *Journal of Wind Engineering and Industrial Aerodynamics*, 83, 197-208.
- Balendra, T., Wang, C. M. and Yan, N. (2001). Control of wind-excited towers by active tuned liquid column damper, *Engineering structures*, 23 (9), 1054-1067.
- Bass, R. L., Bowles, E. B., Trudell, R. W., Navickas, J., Peck, J. C., Yoshimura, N., Endo, S. and Pots, B. F. M. (1985). Modeling criteria for scaled LNG sloshing experiments, *Transactions of the ASME*, 107, 272-280.
- Bathe, K. J. (1996). *Finite Element Procedures*, Prentice Hall Englewood Cliffs, New Jersey.
- Batina, J. T. (1992). A gridless Euler/Navier-Stokes solution algorithm for complex two dimensional applications, *NASA Technical Memorandum*, 107631.
- Batina, J. T. (1993). A gridless Euler/Navier-Stokes solution algorithm for complex aircraft applications, *AIAA paper 93-0333, 31st Aerospace Sciences Meeting and Exhibition*, Reno, NV, USA.
- Bermudez, A., Rodriguez, R., and Santamarina, D. (2003). Finite element computation of sloshing modes in containers with elastic baffle plates, *International Journal for Numerical Methods in Engineering*, 56(3), 447-467.
- Bettess, R. (1981). Operation counts for boundary integral and finite element methods, *International Journal for Numerical Methods in Engineering*, 15, 306- 308.
- Biswal, K. C., Bhattacharyya, S. K., and Sinha, P. K. (2003). Free-vibration analysis of liquid-filled tank with baffles, *Journal of Sound and Vibration*, 259(1), 177-192.
- Brown, S. J. (1982). A survey of studies into the hydrodynamic response of fluid coupled cylinders, *ASME Journal of Pressure Vessel Technology*, 104(1), 2-20.
- Bucchignani, E. (2004). A numerical study of non-linear dynamics in a tank for aerospace applications, *Applied Numerical Mathematics*, 49, 307-318.
- Bucchignani, E., Stella, F. and Paglia, F. (2004). A partition method for the solution of a coupled liquid-structure interaction problem, *Applied Numerical Mathematics*, 51, 463-475.
- Chen, B. F. and Chiang, H. W. (2000). Complete two-dimensional analysis of sea-wave-induced fully non-linear sloshing fluid in a rigid floating tank, *Ocean engineering*, 27, 953-977.
- Chen, B. F. and Nokes, R. (2005). Time-independent finite difference analysis of fully non-linear and viscous fluid sloshing in a rectangular tank, *Journal of Computational Physics*, 209, 47-81.
- Chen, W., Haroun, M. A., and Liu, F. (1996). Large amplitude liquid sloshing in seismically excited tanks, *Earthquake Engineering and Structural Dynamics*, 25(7), 653-669.

- Chen, Y. G., Djidjeli, K. and Price, W. G. (2008). Numerical simulation of liquid sloshing phenomena in partially filled containers, *Computers and Fluids*, 38, 830-842.
- Chew, C. S., Yeo, K. S., and Shu, C. (2006). A generalized finite-difference (GFD) ALE scheme for incompressible flows around moving solid bodies on hybrid meshfree-Cartesian grids, *Journal of Computational Physics*, 218, 510-548.
- Chiu, C. H. (2006). Commercial and technical considerations in the developments of offshore liquefaction plant, *Proceedings of the 23rd World Gas Conference*, Amsterdam 2006.
- Cho, J. R. and Lee, H. W. (2004). Non-linear finite element analysis of large amplitude sloshing flow in two-dimensional tank, *International Journal for Numerical Methods in Engineering*, 61(4), 514-531.
- Colagrossi, A. and Landrini, M. (2003). Numerical simulation of interfacial flows by smoothed particle hydrodynamics, *Journal of Computational Physics*, 191, 448-475.
- Courant, R., Friedrichs, K. and Lewy, H. (1967). On the partial difference equations of mathematical physics, *IBM Journal*, 215-234 (English translation of the 1928 German original).
- Delorme, L., Colagrossi, A., Souto-Iglesias, A., Zamora-Rodriguez, R. and Botia-Vera, E. (2009). A set of canonical problems in sloshing, Part I: Pressure field in forced roll—comparison between experimental results and SPH, *Ocean Engineering*, 36, 168-178.
- Dilts, G. A. (2000). Moving least square particle hydrodynamics II: Conservation and boundaries, *International Journal for Numerical Methods in Engineering*, 48, 1503-1524.
- Dutta, S. and Laha, M. K. (2000). Analysis of the small amplitude sloshing of a liquid in a rigid container of arbitrary shape using a low-order boundary element method, *International Journal for Numerical Methods in Engineering*, 47(9), 1633-1648.
- Eatock Taylor, R., Wu, G. X., Bai, W. and Hu, Z. Z. (2008). Numerical wave tanks based on finite element and boundary element modeling, *Journal of Offshore Mechanics and Arctic Engineering*, 130, 031001.
- Edelsbrunner, H., Kirkpatrick, D. G. and Andseidel, R. (1983). On the shape of a set of points in the plane, *IEEE Transactions on Information Theory*, IT-29(4), 551-559.
- Edelsbrunner, H. and Mucke, E. P. (1994). Three-dimensional alpha shapes, *ACM Transactions on Graphics*, 13(1), 43-72.
- Energy Market Authority (2006). Integrated summary report for proposed Singapore LNG terminal, Singapore, Aug 2006.
- Faltinsen, O. M. (1978). A numerical non-linear method of sloshing in tanks with two dimensional flow, *Journal of Ship Research*, 18(4), 224-241.

- Faltinsen, O. M., Rognebakke, O. F. and Timokha, A. N. (2003). Resonant three-dimensional nonlinear sloshing in a square-based basin, *Journal of Fluid Mechanics*, 487, 1-22.
- Faltinsen, O. M., Rognebakke, O. F. and Timokha, A. N. (2006). Transient and steady-state amplitudes of resonant three-dimensional sloshing in a square base tank with a finite fluid depth, *Physics of Fluids*, 18, 012103.
- Faltinsen, O. M., Rognebakke, O. F., Lukovsky, I. A. and Timokha, A. N. (2000). Multidimensional modal analysis of nonlinear sloshing in a rectangular tank with finite water depth, *Journal of Fluid Mechanics*, 407, 201-234.
- Fang, J., Parriaux, A., Rentschler, M. and Ancy, C. (2009). Improved SPH methods for simulating free surface flows of viscous fluids, *Applied Numerical Mathematics*, 59, 251-271.
- Fekken, G. (1998). Numerical simulation of green water loading on the foredeck of a ship, *MSc-thesis*, August 1998.
- Fenner, R. (1983). The boundary integral equation (boundary element) method in engineering stress analysis, *Journal of Strain Analysis for Engineering Design*, 18(4), 199-205.
- Fletcher, C. A. J. (1991). *Computational techniques for fluid dynamics*, Springer: Berlin, 1991.
- Foss, M. M. (2007). *Introduction to LNG*, Center for Energy Economics, University of Texas, Austin.
- Frandsen J. B. (2004). Sloshing motions in excited tanks, *Journal of Computational Physics*, 196, 53-87.
- Frandsen, J. B. and Borthwick, A. G. L. (2003). Simulation of sloshing motions in fixed and vertically excited containers using a 2-D inviscid sigma-transformed finite difference solver, *Journal of Fluids and Structures*, 18(2), 197-214.
- Gavete, L., Gavete, M. L. and Benito, J. J. (2003). Improvements of generalized finite difference method and comparison with other meshless method, *Applied Mathematical Modelling*, 27, 831-847.
- Gavrilova, E. (2004). Coupled frequencies of a fluid-structure interaction cylindrical system, *Proceedings of the International Congress of Theoretical and Applied Mechanics (XXI)*, 15-21 Aug, Warsaw, Poland.
- Gedikli, A. and Erguven, M. E. (2003). Evaluation of sloshing problem by variational boundary element method, *Engineering Analysis with Boundary Elements*, 27(9), 935-943.
- Godderidge, B., Turnock, S., Earl, C. and Tan, M. (2009). The effect of fluid compressibility on the simulation of sloshing impacts, *Ocean Engineering*, 36(8), 578-587.

- Gotoh, H., Ikari, H., Memita, T. and Sakai, T. (2005). Lagrangian particle method for simulation of wave overtopping on a vertical seawall, *Coastal Engineering Journal*, 47(2-3), 157-181.
- Gotoh, H. and Sakai, T. (1999). Lagrangian simulation of breaking waves using particle method, *Coastal Engineering Journal*, 41(3-4), 303-326.
- Greaves, D. M. (2007). Viscous waves and wave-structure interaction in a tank using adapting quadtree grids, *Journal of Fluids and Structures*, 23, 1149-1167.
- Greco, M., Faltinsen, O. M. and Landrini, M. (2005). Shipping of water on a two-dimensional structure, *Journal of Fluid Mechanics*, 525, 309-332.
- Greco, M., Landrini, M. and Faltinsen, O. M. (2004). Impact flows and loads on ship-deck structures, *Journal of Fluids and Structures*, 19, 251-275.
- Griebel, M., Dornseifer, T. and Neunhoffer T. (1998). Numerical Simulation in Fluid Dynamics, *Society for Industrial and Applied Mathematics*.
- Grilli, S. T. and Svendsen, I. A. (1990). Corner problems and global accuracy in the boundary element solution of nonlinear wave flows, *Engineering Analysis with Boundary Elements*, 7(4), 178-195.
- Gu, H., Li, Y., Li, S. and Zhang, Q. (2005). The level set and particle level set method for tracing interface, *Journal of Hydrodynamics*, Series A, 20(2), 152-160.
- Guillot, M. J. (2006). Application of a discontinuous Galerkin finite element method to liquid sloshing, *Journal of Offshore Mechanics and Arctic Engineering*, 128, 1-10.
- Harlow, F. H. (1963). The particle-in-cell method for numerical solution of problems in fluid dynamics, in: *Proceedings of Symposia in Applied Mathematics*, 1963.
- Harlow, F. H. and Welch, J. E. (1965). Numerical Calculation of Time-Dependent Viscous Incompressible Flow of Fluid with Free Surface, *Physics of Fluids*, 8(12), 2182-2189.
- Haynes, W. M. ed. (2010). *CRC Handbook of Chemistry and Physics*, 91st Edition, CRC Press/Taylor and Francis, Boca Raton, FL.
- Hill, D. F. (2003). Transient and steady-state amplitudes of forced waves in rectangular basins, *Physics of Fluids*, 15(6), 1576-1587.
- Hirt, C. W. and Nichols, B. D. (1981). Volume of fluid (VOF) method for the dynamics of free boundaries, *Journal of Computational Physics*, 39, 201-225.
- Housner, G. W. (1957). Dynamic pressures on accelerated fluid containers, *Bulletin of the Seismological Society of America*, 47, 15-35.
- [http://en.wikipedia.org/wiki/Properties\\_of\\_water](http://en.wikipedia.org/wiki/Properties_of_water)
- <http://webbook.nist.gov/chemistry>

- <http://www.businesswire.com/multimedia/home/20081217005080/en/1735488/Exxon-Mobil-Technology-Yields-World%E2%80%99s-Largest-LNG-Carrier>
- Hu, C. H. and Kashiwagi, M. (2004). A CIP method for numerical simulations of violent free surface flows, *Journal of Marine Science and Technology*, 9(4), 143-157.
- Huang, S., Duan, W. and Zhu, X. (2010). Time-domain simulation of tank sloshing pressure and experimental validation, *Journal of Hydrodynamics*, 22(5), 556-563.
- Huang, Z. J. and Hsiung, C. C. (1996). Nonlinear shallow-water flow on deck, *Journal of Ship Research*, 40(4), 303-315.
- Huijsmans, R. H. M., Tritschler, G., Gaillardie, G. and Dallinga, R. P. D. (2004). Sloshing of partially filled LNG carriers, *Proceedings of the Fourteenth International Offshore and Polar Engineering Conference*, Toulon, France, May 23-28, 2004.
- Ibrahim, R. A. (2005). *Liquid sloshing dynamics: theory and applications*, New York, Cambridge University Press.
- Idelsohn, S. R., Onate, E. and Del Pin, F. (2004). The particle finite element method: a powerful tool to solve incompressible flows with free-surfaces and breaking waves, *International Journal for Numerical Methods in Engineering*, 61, 964-989.
- Idelsohn, S. R. and Onate, E. (2006). To mesh or not to mesh. That is the question..., *Computer Methods in Applied Mechanics and Engineering*, 195, 4681-4696.
- Idelsohn, S. R., Onate, E., Calvo, N. and Del Pin, F. (2003). The meshless finite element method, *International Journal for Numerical Methods in Engineering*, 58(6), 893-912.
- Idelsohn, S. R., Storti, M.A. and Onate, E. (2001). Lagrangian formulations to solve free surface incompressible inviscid fluid flows, *Computer Methods in Applied Mechanics and Engineering*, 191, 583-593.
- Ikegawa, M. (1974). Finite element analysis of fluid motion in a container, In: *Finite Element Methods in Flow Problem*. UAH Press, Huntsville, Alabama, 737-738.
- Johnson, N. L. (1996). The legacy and future of CFD at Los Alamos, *Proceedings of the 1996 Canadian CFD Conference*, Ottawa, Canada.
- Kershaw, D. S. (1978). The incomplete Cholesky-conjugate gradient method for the iterative solution of systems of linear equations, *Journal of Computational Physics*, 26, 43-65.
- Khayyer, A. and Gotoh, H. (2008). Development of CMPS method for accurate water-surface tracking in breaking waves, *Coastal Engineering Journal*, 50(2), 179-207.
- Khayyer, A. and Gotoh, H. (2009). Modified moving particle semi-implicit methods for the prediction of 2D wave impact pressure, *Coastal Engineering*, 56, 419-440.

- Kim, J. K., Koh, H. M., and Kwahk, I. J. (1996). Dynamic response of rectangular flexible fluid containers, *Journal of Engineering Mechanics-ASCE*, 122(9), 807-817.
- Kim, M. H., Lee, S. M., Lee, J. M., Noh, B. J. and Kim, W. S. (2010). Fatigue strength assessment of Mark-III type LNG cargo containment system, *Ocean Engineering*, 37(14-15), 1243-1252.
- Kim, Y., Nam, B. W., Kim, D. W. and Kim, Y. S. (2007). Study on coupling effects of ship motion and sloshing, *Ocean Engineering*, 34(16), 2176-2187.
- Kim, Y., Shin, Y. and Lee, K. H. (2004). Numerical study on slosh-induced impact pressures on three-dimensional prismatic tanks, *Applied Ocean Research*, 26, 213-226.
- Kim, Y., Shin, Y. S., Lin, W. M. and Yue, D. K. P. (2003). Study on sloshing problem coupled with ship motion in waves, *Proceedings of the Eighth International Conference on Numerical Ship Hydrology*, Busan, Korea.
- Kleefsman, K. M. T., Fekken, G., Veldman, A. E. P., Buchner, B., Bunnik, T. H. J. and Iwanowski, B. (2002). Prediction of green water and wave loading using a Navier-Stokes based simulation tool, *Proceedings 21th ASME Offshore Mechanics and Arctic Engineering*, American Society of Mechanical Engineers, paper 28480.
- Koh, C. G., Mahatma, S. and Wang, C. M. (1994). Theoretical and experimental studies on rectangular liquid dampers under arbitrary excitations, *Earthquake Engineering and Structural Dynamics*, 23, 17-31.
- Koh, C. G., Mahatma, S. and Wang, C. M. (1995). Reduction of structural vibrations by multiple-mode liquid dampers, *Engineering Structures*, 17, 122-128.
- Koh, H. M., Kim, J. K. and Park, J. H. (1998). Fluid-structure interaction analysis of 3-D rectangular tanks by a variationally coupled BEM-FEM and comparison with test results, *Earthquake Engineering and Structural Dynamics*, 27, 109-124.
- Koshizuka, S., Nobe, A. and Oka, Y. (1998). Numerical analysis of breaking waves using the moving particle semi-implicit method, *International Journal for Numerical Methods in Fluids*, 26(7), 751-769.
- Koshizuka, S. and Oka, Y. (1996). Moving-particle semi-implicit method for fragmentation of incompressible fluid, *Nuclear Science and Engineering*, 123(3), 421-434.
- Koshizuka, S., Tamako, H. and Oka, Y. (1995). A particle method for incompressible viscous flow with fluid fragmentation, *Computational Fluid Dynamic Journal*, 4(1), 29-46.
- Larese, A., Rossi, R., Onate, E. and Idelsohn, S.R. (2008). Validation of the particle finite element method (PFEM) for simulation of free surface flows, *Engineering Computations*, 25, 385-425.
- La Rocca, M., Sciortino, G., Adduce, C. and Boniforti, M. A. (2005). Experimental and theoretical investigation on the sloshing of a two-liquid system with free surface, *Physics of Fluids*, 17, 062101.

- Lee, C. J. K., Noguchi, H. and Koshizuka, S. (2007a). Fluid-shell structure interaction analysis by coupled particle and finite element method, *Computers and Structures*, 85(11-14), 688-697.
- Lee, D. H., Kim, M. H., Kwon, S. H., Kim, J. W. and Lee, Y. B. (2007b). A parametric sensitivity study on LNG tank sloshing loads by numerical simulations, *Ocean Engineering*, 34, 3-9.
- Lee, E. S., Moulinec, C., Xu, R., Violeau, D., Laurence, D. and Stansby, P. (2008). Comparisons of weakly compressible and truly incompressible algorithms for the SPH mesh free particle method, *Journal of Computational Physics*, 227, 8417–8436.
- Lee, S. J., Kim, M. H., Lee, D. H., Kim, J. W. and Kim, Y. H. (2007c). The effects of LNG-tank sloshing on the global motions of LNG carriers, *Ocean Engineering*, 34, 10-20.
- Lee, T., Zhou, Z. and Cao, Y. (2002). Numerical simulations of hydraulic jumps in water sloshing and water impacting, *Journal of Fluids Engineering*, 124, 215-226.
- Liszka, T. and Orkisz, J. (1980). The finite difference method at arbitrary irregular grid and its application in applied mechanics, *Computers and Structures*, 11, 83-95
- Liu, D. and Lin, P. (2008). A numerical study of three-dimensional liquid sloshing in tanks, *Journal of Computational Physics*, 227(8), 3921-3939.
- Liu, M. B., Xie, W. P. and Liu, G. R. (2005). Modeling incompressible flows using a finite particle method, *Applied Mathematical Modelling*, 29, 1252-1270.
- Lloyd's Register (2005). *Comparative sloshing analysis of LNG ship containment systems*.
- Lloyd's Register (2008). *Guidance on the Operation of Membrane LNG Ships to Reduce the Risk of Damage due to Sloshing*.
- Lo, E. Y. M. and Shao, S. D. (2002). Simulation of near-shore solitary wave mechanics by an incompressible SPH method, *Applied Ocean Research*, 24(5), 275-286.
- Lohner, R., Yang, C. and Onate, E. (2006). On the simulation of flows with violent free surface motion, *Computer Methods in Applied Mechanics and Engineering*, 195, 5597-5620.
- Losasso, F., Talton, J. O., Kwatra, N. and Fedkiw, R. (2008). Two-way coupled SPH and particle Level Set fluid simulation, *IEEE Transactions on Visualization and Computer Graphics*, 14(4), 797-804.
- Luo, Y. and Haussler-Combe, U. (2002). A generalized finite-difference method based on minimizing global residual, *Computer Methods in Applied Mechanics and Engineering*, 191, 1421-1438.

- Mendez, B. and Velazquez, A. (2004). Finite point solver for the simulation of 2-D laminar incompressible unsteady flows, *Computer Methods in Applied Mechanics and Engineering*, 193, 825-848.
- Mikelis, N. E. and Journee, J. M. J. (1984). Experimental and Numerical Simulations of Sloshing Behaviour in Liquid Cargo Tanks and its Effect on Ship Motions, *National conference on numerical methods for Transient and coupled problems*, Venice, Italy.
- Ming, P. and Duan, W. (2010). Numerical simulation of sloshing in rectangular tank with VOF based on unstructured grids, *Journal of Hydrodynamics*, 22(6), 856-864.
- Mitra, S. and Sinhamahapatra, K. P. (2005). Coupled slosh dynamics of liquid filled containers using pressure based finite element method, *Exploring Innovation in Education and Research@iCEER-2005 Tainan*, Taiwan, 1-5 March 2005.
- Modi, V. J., Akinturk, A. and Tse, W. (2003). A Family of Efficient Sloshing Liquid Dampers for Suppression of Wind-Induced Instabilities, *Journal of Vibration and Control*, 9(3-4), 361-386.
- Modi, V. J. and Seto, M. L. (1997). Suppression of flow-induced oscillations using sloshing liquid dampers: analysis and experiments, *Journal of Wind Engineering and Industrial Aerodynamics*, 67-8, 611-625.
- Molteni, D. and Colagrossi, A. (2009). A simple procedure to improve the pressure evaluation in hydrodynamic context using SPH, *Computer Physics Communications*, 180, 861-872.
- Monaghan, J. J. (1988). An introduction to SPH, *Computer Physics Communications*, 48(1), 89-96.
- Monaghan, J. J. (1994). Simulating free surface flows with SPH, *Journal of Computational Physics*, 110, 399-406.
- Nomura, T. (1994). ALE finite-element computations of fluid-structure interaction problems, *Computer Methods in Applied Mechanics and Engineering*, 112(1-4), 291-308.
- Nakayama, T. and Washizu, K. (1980). Nonlinear analysis of liquid motion in a container subjected to a forced pitching oscillation, *International Journal for Numerical Methods in Engineerings*, 15, 1207-1220.
- Nakayama, T. and Washizu, K. (1981). The boundary element method applied to the analysis of two-dimensional nonlinear sloshing problems, *International Journal for Numerical Methods in Engineerings*, 17, 631-1646.
- Ockendon, H. and Ockendon, J. R. (1973). Resonant surface waves, *Journal of Fluid Mechanics*, 59, 397-413.
- Oger, G., Doring, M., Alessandrini, B. and Ferrant, P. (2006). Two-dimensional SPH simulations of wedge water entries, *Journal of Computational Physics*, 213, 803-822.

- Onate, E., Idelsohn, S. R., Zienkiewicz, O. C., Taylor, R. L. and Sacco, C. (1996). A stabilized finite point method for analysis of fluid mechanics problems, *Computer Methods in Applied Mechanics and Engineering*, 139(1-4), 315-346.
- Onate, E., Sacco, C. and Idelsohn, S. R. (2000). A finite point method for incompressible flow problems, *Computing and Visualization in Science*, 3(1-2), 67-75.
- Osher, S. and Sethian, J. A. (1988). Fronts propagating with curvature-dependent speed: algorithms based on Hamilton–Jacobi formulations, *Journal of Computational Physics*, 79, 12–49.
- Pal, N. C., Bhattacharyya, S. K. and Sinha, P. K. (1999). Coupled slosh dynamics of liquid-filled composite cylindrical tanks, *Journal of Engineering Mechanics*, 491-495.
- Pal, N. C., Bhattacharyya, S. K. and Sinha, P. K. (2003). Non-linear slosh dynamics of liquid-filled laminated composite container: a two-dimensional finite element approach, *Journal of Sound and Vibration*, 261, 729-749.
- Pawell, A. (1997). Free surface waves in a wave tank, *International Series in Numerical Mathematics*, 124, 311-320.
- Perrone, N. and Kao, R. (1975). A general finite difference method for arbitrary meshes, *Computers and Structures*, 5, 45-58.
- Qian, L., Causon, D. M., Mingham, C. G. and Ingram, D. M. (2006) A free-surface capturing method for two fluid flows with moving bodies, *Proceedings of the Royal Society*, A8, 462(2065), 21-42.
- Radovitzky, R. and Ortiz, M. (1998). Lagrangian finite element analysis of Newtonian fluid flows, *International Journal for Numerical Methods in Engineering*, 43, 607-619.
- Ramaswamy, B. (1990). Numerical simulation of unsteady viscous free surface flow, *Journal of Computational Physics*, 90, 396-430.
- Ramaswamy, B. and Kawahara, M. (1987). Lagrangian finite element analysis applied to viscous free surface fluid flow, *International Journal for Numerical Methods in Fluids*, 7, 953-984.
- Ramaswamy, B., Kawahara, M. and Nakayama, T. (1986). Lagrangian finite element method for the analysis of two-dimensional sloshing problems, *International Journal for Numerical Methods in Fluids*, 6, 659-670.
- Rammerstofer, F. G., Scharf, K. and Fischer, F. D. (1990). Storage tanks under earthquake loading, *ASME Applied Mechanics Reviews*, 43(11), 261-283.
- Rognebakke, O. F., Hoff, J. R., Allers, J. M., Berget, K. and Berge, B. O. (2005). Experimental approaches for determining sloshing loads in LNG tanks, *Proceedings of the SNAME Maritime Technology Conference and Expo and Ship Production Symposium*, Houston Tx ETATS-UNIS, 113, 384-401.

- Romero, J. A., Ramirez, O., Fortanell, J. M., Maritinez, M. and Lozano, A. (2006). Analysis of lateral sloshing forces within road containers with high fill levels, *Proceedings of IMechE Part D: Journal of Automobile Engineering*, 220, 303-312.
- Shao, S. D. and Lo, E. Y. M. (2003). Incompressible SPH method for simulating Newtonian and non-Newtonian flows with a free surface, *Advances in Water Resources*, 26(7), 787-800.
- Shankar, K. and Balendra, T. (2002). Application of the energy flow method to vibration control of buildings with multiple liquid dampers, *Journal of Wind Engineering and Industrial Aerodynamics*, 90, 1893-1906.
- Shibata, K. and Koshizuka, S. (2007). Numerical analysis of shipping water impact on a deck using a particle method, *Ocean Engineering*, 34(3-4), 585-593.
- Shibata, K., Koshizuka, S. and Tanizawa, K. (2009). Three-dimensional numerical analysis of shipping water onto a moving ship using a particle method, *Journal of Marine Science and Technology*, 14, 214-227.
- Solaas, F. and Faltinsen, O. M. (1997). Combined numerical and analytical solution for sloshing in two-dimensional tanks of general shape, *Journal of Ship Research*, 41(2), 118-129.
- Soulaimani, A. and Saad, Y. (1998). An arbitrary Lagrangian-Eulerian finite element method for solving three-dimensional free surface flows, *Computer Methods in Applied Mechanics and Engineering*, 162, 79-106.
- Souto-Iglesias, A., Perez-Rojas, L. and Zamora Rodriguez, R. (2004). Simulation of anti-roll tanks and sloshing type problems with smoothed particle hydrodynamics, *Ocean Engineering*, 31(8-9), 1169-1192.
- Souto-Iglesias, A., Delorme, L., Perez-Rojas, L. and Abril-Perez, S. (2006). Liquid moment amplitude assessment in sloshing type problems with smooth particle hydrodynamics, *Ocean Engineering*, 33(11-12), 1462-1484.
- Stolbetsov, V. I. (1967). On oscillations of a fluid in a container having the shape of a rectangular parallelepiped, *Mekh Zhidk Gaza (Fluid Dynamics) N1*, 67-76 (in Russian).
- Strandberg, L. (1978). Lateral stability of road tanks, *National Road and Traffic research Institute*, Report No. 138A.
- Su, T. C., Lou, Y. K., Flipse, J. E. and Bridges, T. J. (1982). A Numerical Analysis of Large Amplitude Liquid Sloshing in Baffled Containers, *US Department of Transportation, Final Report*, MA-RD-940-82046.
- Sudharsan, N. M., Ajaykumar, R., Murali, K. and Kumar, K. (2004). A comparative study of dynamic mesh update methods used in the simulation of fluid-structure interaction problems with a nonlinear free surface, *Proceedings of the Institution of Mechanical Engineers 218 part C: Journal of Mechanical Engineering Science*, 283-300.

- Sueyoshi, M., Kashiwagi, M. and Naito, S. (2008). Numerical simulation of wave-induced nonlinear motions of a two-dimensional floating body by the moving particle semi-implicit method, *Journal of Marine Science and Technology*, 13(2), 85-94.
- Taylor, Sir Geoffrey (1953). An experimental study of standing waves, *Proceedings of the Royal Society of London, Series A, Mathematical and Physical Sciences*, 218(1132), 44-59.
- Tiwari, S. and Kuhnert, J. (2007). Modeling of two-phase flows with surface tension by finite pointset method, *Journal of Computational and Applied Mathematics*, 203, 376-386.
- Turnbull, M. S., Borthwick, A. G. L. and Eatock Taylor, R. (2003). Numerical wave tank based on a  $\sigma$ -transformed finite element inviscid flow solver, *International Journal for Numerical Methods in Fluids*, 42, 641-663.
- Tveitnes, T., Ostvold, T. K., Pastoor, L. W. and Sele, H. O. (2004). A sloshing design load procedure for membrane LNG tankers, *Proceedings of the Ninth Symposium on Practical Design of Ships and Other Floating Structures*, Luebeck-Travemuende, Germany.
- Valentine, D. T. and Frandsen, J. B. (2005). Nonlinear free-surface and viscous-internal sloshing, *Journal of Offshore Mechanics and Arctic Engineering*, 127, 141-149.
- Veletsos, A. S. and Tang, Y. (1986). Dynamics of vertically excited liquid storage tanks, *ASCE Journal of Structural Engineering*, 112(6), 1228-1246.
- Viccione, G., Bovolín, V. and Pugliese Carratelli, E. (2008). Defining and optimizing algorithms for neighbouring particle identification in SPH fluid simulations, *International Journal for Numerical Methods in Fluids*, 58, 625-638.
- Wang, C. Z. and Khoo, B. C. (2005). Finite element analysis of two-dimensional nonlinear sloshing problems in random excitations, *Ocean Engineering*, 32(2), 107-133.
- Wang, W., Li, J. F., and Wang, T. S. (2006). Damping computation of liquid sloshing with small amplitude in rigid container using FEM, *Acta Mechanica Sinica*, 22(1), 93-98.
- Wang, W., Wang, X., Wang, J., and Wei, R. (1996). Dynamical behavior of parametrically excited solitary waves in Faraday's water trough experiment, *Physics Letters A*, 219, 74-78.
- Webber, D. M., Gant, S. E. and Ivings, M. J. (2008). *LNG source term models for hazard analysis: a review of the state of the art and an approach to model assessment*, Health and Safety Laboratory Report, MSU/2008/24.
- Wu, C. H. and Chen, B. F. (2009). Sloshing waves and resonance modes of fluid in a 3D tank by a time-independent finite difference method, *Ocean Engineering*, 36(6-7), 500-510.

- Wu, G. X., Ma, Q. W. and Eatock Taylor, R. (1998). Numerical simulation of sloshing waves in a 3D tank based on a finite element method, *Applied Ocean Research*, 20(6), 337-355.
- Wu, G. X. and Eatock Taylor, R. (1994). Finite element analysis of two-dimensional non-linear transient water waves, *Applied Ocean Research*, 16, 363-372.
- Yan, G., Rakheja, S. and Siddiqui, K. (2009). Experimental study of liquid slosh dynamics in a partially-filled tank, *Journal of Fluids Engineering*, 131(7), 071303.
- Yi, W. and Natsiavas, S. (1990). Seismic response of anchored fluid-filled tanks using finite elements, *Proceedings of ASME Pressure Vessels and Piping Conference*, PVP-191, 25-30.
- Yoon, H. Y., Koshizuka, S. and Oka, Y. (1999). A particle-gridless hybrid method for incompressible flows, *International Journal for Numerical Methods in Fluids*, 30(4), 407-424.
- Zhang, S., Morita, K., Fukuda, K. and Shirakawa, N. (2006). An improved MPS method for numerical simulations of convective heat transfer problems, *International Journal for Numerical Methods in Fluids*, 51(1), 31-47.
- Zhang, X., Sudharsan, N. M., Ajaykumar, R. and Kumar, K. (2005). Simulation of free-surface flow in a tank using the Navier-Stokes model and unstructured finite volume method, *Proceedings of IMechE Part C: Journal of Mechanical Engineering Science*, 219, 251-266.
- Zhang, X., Teng, B. and Ning, D. (2004). Simulation of fully nonlinear 3-D numerical wave tank, *China Ocean Engineering*, 18(1), 59-68.



## Appendix A: CD for animation files and explanation note

The CD contains the CPM simulation animations for selected numerical examples. The video files for sloshing experiments in Chapter 5 are also included. Detailed summary of the files are listed as follows.

File name	Case name	Section	Corresponding figure
Dam_marin_w.avi	Dam break with $d / L_w = 0.5$	Sect. 4.5.2	Figure 4-29
Dam_marin_p.avi	Dam break with $d / L_w = 0.5$	Sect. 4.5.2	Figure 4-33
Dam_marin_v.avi	Dam break with $d / L_w = 0.5$	Sect. 4.5.2	Figure 4-34
Dam_Obstacle.avi	Dam break with obstacle	Sect. 4.5.3	Figure 4-37
Slosh_1_0.avi	Resonant water sloshing with $\omega / \omega_0 = 1$	Sect. 5.3.1.1	Figure 5-29
Slosh_1_1.avi	water sloshing with $\omega / \omega_0 = 1.1$	Sect. 5.3.1.2	Figure 5-34
Slosh_low.avi	Experiments of sloshing waves in low-filling tank	Sect. 5.3.2	Figure 5-49 to Figure 5-56
Slosh_breaking.avi	Experiments with sloshing wave impact on the tank ceiling	Sect. 5.3.3	Figure 5-61